A STUDY ON THE PERFORMANCE AND BOND BEHAVIOUR OF HIGH STRENGTH GEOPOLYMER CONCRETE

Submitted in partial fulfilment of the requirements

for the award of the degree of

DOCTOR OF PHILOSOPHY

in

CIVIL ENGINEERING

by

PADAKANTI RAKESH

(Roll No: 719021)

Supervisor

Dr. S. VENKATESWARA RAO

Professor

Co Supervisor

Dr. P. RATHISH KUMAR

Professor

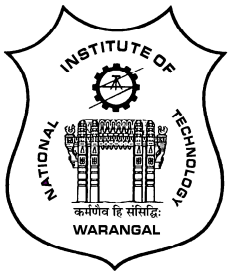

STRUCTURES DIVISION

DEPARTMENT OF CIVIL ENGINEERING

NATIONAL INSTITUTE OF TECHNOLOGY

WARANGAL- 506004 (T.S.) INDIA

December-2023

NATIONAL INSTITUTE OF TECHNOLOGY

WARANGAL

CERTIFICATE

This is to certify that the thesis entitled "**A STUDY ON THE PERFORMANCE AND BOND BEHAVIOUR OF HIGH STRENGTH GEOPOLYMER CONCRETE"** being submitted by **Mr. PADAKANTI RAKESH** for the award of the degree of **DOCTOR OF PHILOSOPHY** to the Department of Civil Engineering of **NATIONAL INSTITUTE OF TECHNOLOGY, WARANGAL** is a record of bonafide research work carried out by him under my supervision and it has not been submitted elsewhere for award of any degree.

Dr. S. VENKATESWARA RAO
Thesis Supervisor
Professor
Structures Division
Department of Civil Engineering
National Institute of Technology
Warangal (T.S.) – INDIA

Dr. P. RATHISH KUMAR
Thesis Co-Supervisor
Professor
Structures Division
Department of Civil Engineering
National Institute of Technology
Warangal (T.S.) – INDIA

APPROVAL SHEET

This dissertation work entitled "**A STUDY ON THE PERFORMANCE AND BOND BEHAVIOUR OF HIGH STRENGTH GEOPOLYMER CONCRETE**" by **Mr. PADAKANTI RAKESH** is approved for the degree of Doctor of Philosophy.

Examiners

_____

_____

_____

Supervisor

_____

Chairman

_____

Date:

Place: Warangal, India

DECLARATION

This is to certify that the work presented in the thesis entitled **"A STUDY ON THE PERFORMANCE AND BOND BEHAVIOUR OF HIGH STRENGTH GEOPOLYMER CONCRETE"** is a bonafide work done by me under the supervision of **Prof. S. VENKATESWARA RAO,** and the co-supervision of **Prof. P. RATHISH KUMAR** and was not submitted elsewhere for the award of any degree. I declare that this written submission represents my ideas in my own words and where others' ideas or words have been included, I have adequately cited and referenced the original sources. I also declare that I have adhered to all principles of academic honesty and integrity and have not misrepresented or fabricated or falsified any idea / data / fact /source in my submission. I understand that any violation of the above will be a cause for disciplinary action by the institute and can also evoke penal action from the sources which have thus not been properly cited or from whom proper permission has not been taken when needed.

_____

(Name of the Student: **PADAKANTI RAKESH**)

(Roll No: **719021**)

Date:

Place: Warangal, India

ACKNOWLEDGEMENTS

With great pleasure and proud privilege, I manifest my heartier thankfulness to my research supervisor, **Dr. S. Venkateswara Rao,** Professor, Department of Civil Engineering and research co-supervisor, **Dr. P. Rathish Kumar**, Professor, Department of Civil Engineering, for their invaluable suggestions, sagacious guidance, scholarly advice and comprehensive critical remarks in bringing out this research work with artistry.

I am perspicuous to divulge my sincere gratefulness to **Dr. P. Hari Krishna,** Professor in Department of Civil Engineering, Chairman of Doctoral Scrutiny Committee, for his enlightening guidance and immense help rendered in bringing out this work.

I am grateful to **Prof. G. Rajesh Kumar**, Professor (HAG) in Department of Civil Engineering, internal member of Doctoral Scrutiny Committee, **Dr. P. Hari Prasad Reddy**, Associate Professor in Department of Civil Engineering, internal member of Doctoral Scrutiny Committee, **Prof. N. Narasaiah**, Professor in Department of Electrical Engineering, external member of Doctoral Scrutiny Committee for their guidance and help during the investigation.

I am also thankful to Prof. M. Chandrasekhar Prof. D. Rama Seshu, Sri M. Sudhakar, Dr. T. D. Gunneswara Rao, Dr. D. Ravi Prasad, Dr. K. Gopi Krishna, Dr. M. V. N. Siva Kumar, Dr. T. P. Tezaswi, Dr. S. Anitha Priyadharshini, Dr. B. Kavitha, and Dr. B. Umesh,

I thank my friends and fellow scholars Dr. B Sagar, Dr. PVRK Reddy, Ms. Madhavi latha, Mr. Sateesh, Mr. Ravi kumar, Mr. Vivek, Ms. Renuka, and Mr. Ravinder, M.Tech. Structures students Mr. Ankush jain, and Mr. Rakesh Rathod, for their direct or indirect support throughout the period of my research work.

I am thankful to Sri A. Chandranarayana, Sri A. Laxman and Mr. Ahmad in Structural Engineering Laboratories, Sri Md. Hussain and Administrative staff for the help done during the research period.

I will be failing in my duty if I do not ventilate my gratefulness to my Wife, Mother, Brother in law, and sisters who strived for my excellence.

Finally, I thank everyone, who contributed either directly or indirectly in successful completion of this work.

Padakanti Rakesh

Dedicated to my father

Sri. Padakanti Ramesh (Late)

ABSTRACT

Geopolymer concrete (GPC) is a promising alternative to ordinary Portland cement (OPC), offering significant solutions to the issues of CO_2 emissions from cement production and the utilization of industrial byproducts. Rapid urbanization created a demand for high-rise structures, necessitating the use of high-strength concrete. In the present investigation, High-Strength Geopolymer Concrete (HSGPC) cured at ambient temperature is developed using particle packing concepts and multicomponent binder system. Also, investigated its strength properties along with resistance against chemical attack. The main aim of this work is to study the bond behaviour of HSGPC. In the present investigation, the experimental bond behaviour is determined through pullout and hinged beam tests. Finite element-based software ATENA V5.7.0p has been used to predict the bond behaviour of HSGPC.

The work is carried out in four different phases as described below.

Phase-I

Particle packing methods MTM and JDD are adopted to optimize the aggregate proportions. Binders such as flyash, GGBS, silica fume, alccofine, and OPC are used to develop high-strength geopolymer concrete. The mechanical characteristics such as compressive strength, flexural strength, and splitting tensile strength are determined as per IS 516: 2004. The modulus of elasticity and stress-strain behaviour is determined as per ASTM C469-02. Based on the experimental results, analytical models for the prediction of mechanical characteristics are proposed. A constitutional model for the prediction of stress-strain behaviour of HSGPC is included in the study. The influence of binder materials on microstructure properties is examined through microstructure characterization techniques such as SEM, XRD, FT-IR, EDS, and BSE.

Phase-II

The chemical resistance of high-strength GPC (60, 80 and 100 MPa) is investigated by exposing the specimens to HCl, H_2SO_4, $MgSO_4$, and NaCl. Parameters such as Dimension Loss Factor (DLF), Mass Loss Factor (MLF), Strength Loss Factor (SLF) and thus Acid Durability Loss Factor (ADLF) are evaluated. Rebound number and ultra-sonic pulse velocity assessment is done on the specimen before and after chemical exposure.

Phase-III

One of the important structural parameters, the bond behaviour of HSGPC is determined through the anchorage and flexural bond test. The anchorage bond behaviour is determined by employing the pullout test, while the flexural bond behaviour is determined by employing the hinged beam test. The pullout bond behaviour is determined by considering parameters such as bar diameter (12, 16, and 20 mm), embedment length (2.5D, 5D, and full depth), and grade of concrete (60, 80, and 100 MPa). The flexural bond behaviour is determined by considering parameters such as cover to concrete (16, 20, and 40 mm), bar diameter (12, 16, and 20 mm), and grade of concrete (60, 80, and 100 MPa). The pullout test is performed according to IS 2770: Part 1 and flexural bond behaviour is determined according to Rilem Feb ceb (1982)-RC5-TC9.

Phase-IV

The experimental bond behaviour of geopolymer concrete studied in Phase III is used to validate the numerical results from finite element software ATENA. Also, the parametric study is extended by considering variables such as type of bar (plain and ribbed), bar diameter (10, 12, 16 and 20 mm), embedment length (50, 75 and 100 for 10 mm and 12 mm bar diameter, 50, 75, 100 and 150 mm for 16- and 20- mm bar diameter) and compressive strength of concrete (20, 30, 40, 50, 60, 70, 80, 90, and 100 MPa) under pullout test. Also, the parameters like the ratio of embedment length to bar diameter (3, 5, 7, 9) and cover to bar diameter (1 to 5 at an increment of 0.5), compressive strength of concrete (20, 30, 40, 50, 60, 70, 80, 90, and 100 MPa) are considered for determining the flexural bond strength using beam end test.

Based on the experimental and numerical analysis it was concluded that there is a significant improvement in the microstructure and mechanical properties of HSGPC with the utilization of multi-component binders and particle packing models. The addition of alccofine in GPC mixes increased the compressive, splitting tensile and flexural strength of concrete. HSGPC of compressive strength 100 MPa was achieved at room temperature curing. From the microstructure analysis of GPC, it was noted that the addition of alccofine and silica fume increased the percentage of Ca bonds along with the Si bonds which led to dense microstructure attributed to polymerization and polycondensation. Analytical models for the prediction of modulus of elasticity, splitting, and flexural strength along with a constitutive model for the prediction of stress-strain behaviour of HSGPC is proposed. For an exposure period of 90 days of HCl, H_2SO_4, $MgSO_4$, and NaCl, 60 MPa concrete showed the highest chemical resistance

compared to 80 and 100 MPa by exhibiting lower loss factors, indicating that a higher percentage of siliceous compounds than calcium compounds increase the resistance of concrete to acid, sulfate and chloride attack. Pullout and flexural bond strength increased with an increase in the grade of concrete and decreased with an increase in bar diameter and embedment length. With the increase in cover concrete, the flexural bond strength has improved. Similarly, the slip corresponding to maximum bond stress decreased with increase in compressive strength, bar diameter, embedment length and cover to concrete. Based on the numerical analysis, analytical models for the prediction of bond behaviour of normal, standard and high-strength GPC are proposed. The proposed analytical models are compared with the available models in the literature and existing standards.

CONTENTS

LIST OF TABLES

LIST OF FIGURES

ABBREVIATIONS

GPC	Geopolymer Concrete
FEA	Finite Element Analysis
HSGPC	High Strength Geopolymer Concrete
GGBS	Ground Granulated Blast Furnace Slag
MTM	Modified Toufar Model
JDD	J D Dewar Model
NDT	Non-Destructive Test
CA	Coarse Aggregate
FA	Fine Aggregate
SEM	Scanning Electron Microscopy
EDX	Energy Dispersive X- Ray Spectroscopy
BSE	Back Scatter Electron
FT-IR	Fourier Transform Infrared Radiation
XRD	X-ray Diffraction Technique
DLF	Dimensional Loss Factor
MLF	Mass Loss Factor
SLF	Strength Loss Factor
ADLF	Acid Durability Loss Factor
LVDT	Linear Variable Differential Transducers
C-S-H	Calcium Silicate Hydrate
NASH	Sodium Aluminum Silicate Hydrate

NOTATIONS

Φ	Packing density
d_{char}	Characteristic diameter
f_{cc}	Compressive strength
f_{ct}	Splitting tensile strength
f_b or f_{cr}	Flexural strength
σ'	Peak stress
ϵ_0	Strain corresponding to peak stress
f_{cm}	Mean static compressive strength
E	Modulus of elasticity
f_{ae}	Compressive strength after exposure
f_{ae}	Compressive strength before exposure
τ_{max}	Maximum bond strength
τ_{bd}	Flexural bond strength
D	Diameter of bar
δ_{mslip}	Slip corresponding to maximum bond strength
l_e or l_d	Embedment length
C	Concrete cover

CHAPTER 1
INTRODUCTION

1.1 General

Concrete is one of the important construction material used globally. It is strong and has exceptional qualities to support the construction industry. By 2027, it is predicted that India's construction sector will require close to 500 million tonnes of cement; however, due to the observed trend in supply and demand, production will lag behind demand by 120 million tonnes (Singh et al., 2015). Additionally, the release of CO_2 gas during the manufacture of cement for concrete is a current issue of concern as it has significantly enhanced the greenhouse effect and is responsible for 7 to 8% of CO_2 emissions that cause global warming. It is known that the cement sector released close to 1.7 billion tonnes of CO_2 in 2022 (Alexander & Shashikala, 2022; Andrew, 2018; Kermeli et al., 2019). Cement manufacturing is a particularly energy and CO_2-intensive operation. One tonne of cement production results in the emission of 0.5-0.7 tonne of CO_2 (Xie et al., 2024).

Geopolymer concrete (GPC), a popular substitute for cement in concrete, provides a number of benefits over ordinary Portland cement concrete, including superior properties, fire and chemical resistance, reduced permeability, early compressive strength, etc., (Chindaprasirt et al., 2007; Diaz-Loya et al., 2011; Olivia & Nikraz, 2012; Samantasinghar & Singh, 2019; Shehab et al., 2016; Zhang et al., 2018). In numerous studies, it has been found that geopolymer concrete has all these advantages over regular Portland cement concrete. Alkali-activated concrete has recently been developed using the oven-cured GPC concept to overcome the drawbacks of flyash-based geopolymer concrete (Ling et al., 2019). Since geopolymer is a more recent area of study than traditional concrete, there are still many factors that are unknown to researchers that may have a significant impact on geopolymer concrete performance. Therefore, further study in the area of geopolymer concrete is required. An increase in urbanization created a demand for high–rise structures, necessitating the use of high-strength concrete. The development of high-strength concrete requires refinement in the microstructure properties of concrete (Jones et al., 2002; Karadumpa & Pancharathi, 2021; Kumar & Santhanam, 2003).

The void ratio is one of the prime factors which influences microstructural properties; refining the void ratio considerably improves the microstructural property and consequently, the mechanical properties of concrete (Jones et al., 2002). When there are more components to be blended, choosing the optimum balance of materials to improve concrete's properties through experimental trials is highly challenging. The packing density approach was used as the basis for a better method of determining the ideal combination of materials. This chapter covers the fundamentals of geopolymer concrete, the parameters that affect it, and the particle packing strategy.

Concrete is exposed to weathering throughout its lifespan. The severity of the weathering action depends on the region such as coastal and industrial areas. It is required to understand the behaviour of concrete under adverse weathering circumstances. As geopolymer concrete is an evolving material, it is felt necessary to study chemical resistance against acid, chloride and sulfate attack.

Concrete performs weak in tension despite being extremely resilient and robust in compression. Therefore, concrete is reinforced with materials like steel, fibre-reinforced polymer, carbon fibres, etc., to safely maintain tensile pressure and boost its flexural capacity. Due to its affordability, ductility, and ease of availability, steel is the most used reinforcing material in the construction sector. Because concrete is a composite material, all the components must function together for concrete to serve its intended purpose. This refers to the secure transmission of stress from steel to concrete, which is mostly reliant on the connection between concrete and steel. There are various parameters which influence the bond behaviour of reinforced geopolymer concrete that need to be studied. This chapter covers the fundamentals of bond behaviour like bond in concrete, types of bond, and elements that affect bond behaviour. However, it is not viable or productive to perform all experimental tests. Making use of finite-based software to predict the results of such tests is one of the best solutions which not only saves money but also time which can be gainfully used for further interpretation of results. There are various finite element-based software tools available which can simulate bond behaviour like Abaqus CAE, ANSYS Workbench, ATENA, DIANA FEA, etc., whose results are close to the results of experimental observations. ATENA v5.7.0p was used in the current work to simulate the bond behaviour between geopolymer concrete and steel reinforcement (Červenka et al., 2005). A brief introduction to ATENA v5.7.0p and Gid, along with the standard tests to determine bond strength has been added further.

1.2 Geopolymer Concrete

Geopolymer is a term coined by Davidovits in 1978 to materials which are formed by chains or networks of inorganic molecules (Davidovits, 1993; Davidovits, 1994). It is also known by the name of amorphous alkali aluminosilicate or alkali-activated cements. The mechanism involves the dissolution of Al and Si in an alkali medium, transportation (orientation) of dissolved species, followed by poly-condensation, forming a 3D network of silico-aluminate structures. Figure 1.1 illustrates the stages involved in the creation of geopolymeric gel. According to Davidovits (1994), these structures can be of three types: poly (sialate) (–Si–O–Al–O–), poly (sialate–siloxo) (Si–O–Al–O–Si–O) and poly (sialate–disiloxo) (Si–O–Al–O–Si–O–Si–O) (Ma et al. 2018) as presented in Figure 1.2.

The dissolution and hydrolysis reactions can be written as:

$Al_2O_3 + 3H_2O + 2OH^- \rightarrow 2[Al(OH)_4]^-$

$SiO_2 + H_2O + OH^- \rightarrow [SiO(OH)_3]^-$

$SiO_2 + 2OH^- \rightarrow [SiO_2(OH)_2]^{2-}$

Davidovits (Davidovits, 1999) proposed an empirical equation for determining the type of geopolymeric structure based on the Si/Al ratio and Na/ Al ratio.

$M_n(-(SiO_2)_z-AlO_2)_n, wH_2O$

Where M represents a cation such as potassium (K), or calcium (Ca); n is the degree of polycondensation; z=1, 2, 3 or higher, and w is the amount of binding water.

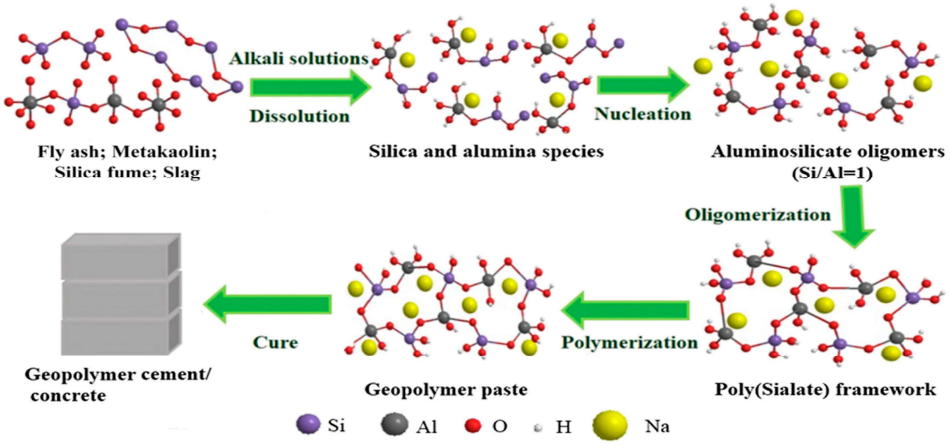

Figure 1.1: Schematic representation of the formation of geopolymer gel (Shariatmadari et al., 2021)

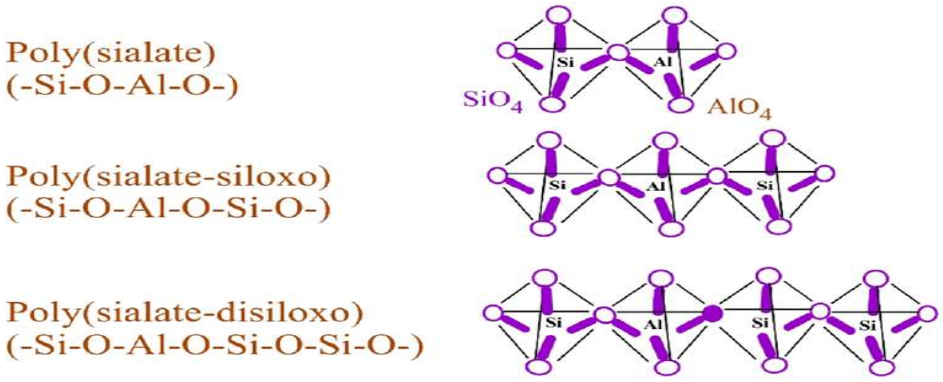

Figure 1.2: Different types of geopolymeric structure (Kabir et al., 2015)

In addition to the aluminosilicate source, the alkaline condition is also important for the dissolution and hydrolysis of the aluminosilicate source to form a polymeric chain. Basically, Sodium/Potassium Hydroxide and Sodium/Potassium Silicate solution are used as alkaline activators for the dissolution of aluminosilicate source (Davidovits, 1994).

1.2.1 Parameters affecting GPC

A large number of studies have been conducted to study the various parameters which influence the performance of geopolymer concrete; however, no unanimity has been met. The main parameters which influence the properties of geopolymer concrete are

1.2.1.1 Aluminosilicate source

Based on the type of aluminosilicate source, the properties of geopolymer concrete vary. The sources of aluminosilicate can be fly-ash, GGBS, Rice Husk Ash, and metakaolin, to name a few. The composition of the amount of Al_2O_3 and SiO_2 present in all these sources varies, affecting the various characteristics of geopolymer concrete (De Silva et al., 2007). For instance, the use of flyash as an aluminosilicate source would necessitate the use of temperature curing for geopolymer concrete to attain considerable strength (Pandurangan et al., 2018). However, the addition of GGBS in a suitable amount would result in the same geopolymer attaining comparable strength at ambient temperature (Nagajothi & Elavenil, 2021).

1.2.1.2 Curing condition

Polymerization reaction in geopolymer concrete which includes the dissolution of aluminosilicates in alkaline activators propagates only in the presence of heat. Since polymerization is not exothermic by nature unlike hydration reaction, it requires heat from an external source (Hardjito et al., 2004). Thus, the type of curing plays an important part wherein

temperature curing results in a faster polymerization reaction resulting in a rapid gain in strength compared to ambient curing condition (Verma & Dev, 2021).

1.2.1.3 Type of alkaline activator

The polymerization reaction of geopolymer concrete is affected by the basicity of the alkaline activator used. Since the basicity of alkaline activators differs depending upon the type, it has a considerable effect on geopolymer concrete. The basicity of potassium-based alkaline activators is more compared to sodium-based activators; thus, they produce dense polycondensation and hence, high strength (Bellum et al., 2020; Xin et al., 2014).

1.2.1.4 Combination and concentration of the alkaline activator

The ratio of sodium silicate to sodium hydroxide or any other alkaline activator affects the properties of geopolymer concrete. According to the literature, sodium hydroxide forms crystalline products while the addition of sodium silicate results in an amorphous product. Also, the quantity of sodium hydroxide is important for the dissolution of aluminosilicates. Thus, a balance in the combination of both substances is taken. Furthermore, an increase in the concentration of NaOH increases the rate of dissolution and consequently the strength. This increase in strength is limited to a certain extent of concentration only, after which the strength decreases as a result of an excess of OH^- ions in the solution (Bellum et al., 2020).

1.2.1.5 Alkaline activator to binder ratio

An increase in the alkaline activator-to-binder ratio decreases the compressive strength of geopolymer concrete due to the increase of water content in the mixture. Thus, balancing the alkaline activator to binder ratio is also of vital importance for geopolymer concrete (Haruna et al., 2020; Ou et al., 2022a).

1.2.1.6 Aggregate content and its subsequent proportioning

Various intrinsic properties of geopolymer concrete like modulus of elasticity, poission's ratio, and subsequently the mechanical properties depend upon the appropriate selection of the number of total aggregates present in the mixture. In addition to this, the ratio of fine and coarse aggregates also plays a major role in shaping the properties of geopolymer concrete as it directly affects the packing density of the mixture (Joseph & Mathew, 2012).

1.3 Particle Packing Theory for Mix Proportioning

As mentioned previously, aggregate content and its subsequent proportioning of fine and coarse aggregate influence the properties of geopolymer concrete. Furthermore, aggregate accounts for a majority of the concrete volume; thus, obtaining efficiently mixed aggregate is key to attaining good concrete properties. Efficiently mixed aggregate refers to a balance in the ratio of fine and coarse aggregates to obtain maximum packing density. Packing density indicates the amount of voids present in the concrete. It is defined as the volume of percentage of solids per unit volume. Attaining good packing density results in fewer overall voids, leading to dense concrete with high durability and strength. The requirement of less quantity of paste due to fewer voids is an added bonus which reduces the cost of concrete.

Due to such an advantage in attaining good packing density, various researches have been conducted to find a path of obtaining maximum packing density by varying the proportion of fine and coarse aggregates. Several models have been proposed, namely, the Modified Toufar Model (MTM) (Andersen, 1995), the Dewar model (Dewar, 1986) and the De Larrard model (De Larrard, 1999). They are based on the principle that the voids between the larger particles are filled by smaller particles thus reducing the total voids and attaining good packing density.

1.4 Bond in Concrete

To function together without slipping in a heavy reinforced structure, the link between steel and concrete is vital. The perfect bond between them ensures that the beam plane segment stays level even after bending, which explains how the bond contributes to the composite action of reinforced concrete and maintains strain compatibility. Bond in concrete is achieved through three mechanisms which are given below:

- Mutual adhesion between concrete and steel interfaces.
- Frictional resistance due to surface roughness.
- Mechanical interlock due to the presence of ribs only in case of deformed bars.

1.4.1 Mechanism of bond stress

The bond forces transfer, cracking, and damage mechanism is shown in Figure 1.3. In the initial stages, the bond forces are transferred purely by means of chemical adhesion between steel and concrete. After the failure of adhesion, the bond forces are transferred by mechanical interlock provided by the ribs. Also, frictional forces play an important role in the bond force transfer

mechanism. With an increase in the slip, the frictional forces are reduced leaving the bearing of the ribs as the only transfer mechanism of bond forces. The bearing forces are resolved into principal compressive and tensile stresses which are both perpendicular and parallel to reinforcement as shown in Figure 1.3 (a). Goto cracks as shown in Figure 1.3 (b) formed when the embedded bar was subjected to tension (pullout). When the spacing between the bar and concrete cover to bar is less, it fails as shown in Figure 1.3 (C) due to transverse cracks. While shear failure occurs along the bar surface as shown in Figure 1.3 (d), when a sufficient amount of spacing and concrete cover is maintained to delay the splitting of concrete, resulting in pullout failure.

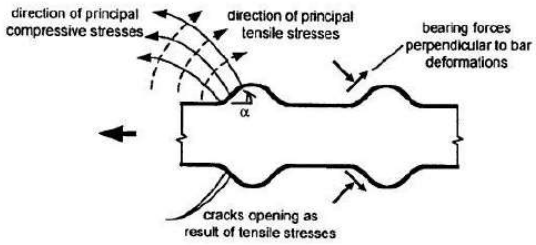

(a) side view of bar showing formation of Goto (1979) cracks

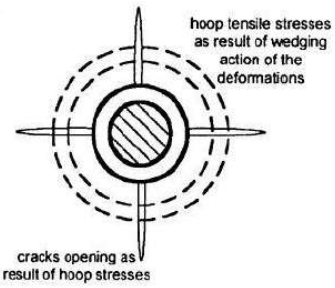

(b) end view of bar showing formation of splitting cracks

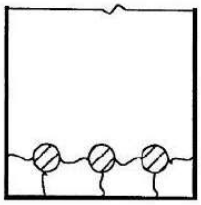

(c) end view of member showing splitting cracks between bar and through cover concrete

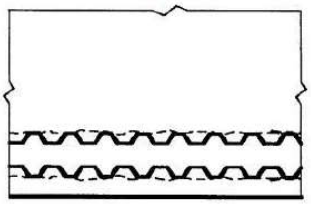

(d) side view of member showing shear crack and local crushing due to bar pull-out

Figure 1.3: Bond forces transfer, cracking, and damage mechanism (ACI 408R-03, 2003)

1.4.2 Bond stress

Bond stress is primarily the result of the shear interlock between the reinforcing element and the surrounding interfacial concrete. It can be defined as the development of shear stress along the interface of bar and concrete for the transfer of load. Bond stress can be calculated using Eq 1.1:

$$\tau_{bd} = \frac{q}{A_{contact}} = \frac{\delta f_s A_b}{\pi d} = \frac{d\,\delta f_s}{4} \qquad \text{Eq 1.1}$$

Where, q = Change of bar force over unit length

$A_{contact}$ = Contact area of bar and concrete of unit length = πd

δf_s = Stress variation in steel over unit length

A_b = Area of bar

d = Diameter of bar

1.4.3 Types of bond

The bond stress in a reinforced concrete member arises from two different loading situations. One from the anchorage of bars and the other from the change of tension force in the bar along its length due to a change in the bending moment. Based on these two loading conditions, the bond is classified as:

- Anchorage or Development Bond
- Flexure Bond

1.4.3.1 Anchorage or Development bond

For the safe transmission of bar force (F) to concrete in a reinforced concrete member, the bar is extended to a distance "L" beyond the section known as anchorage length, and the respective bond is known as anchorage bond as shown in Figure 1.4. A pullout test is generally performed to calculate the bond length.

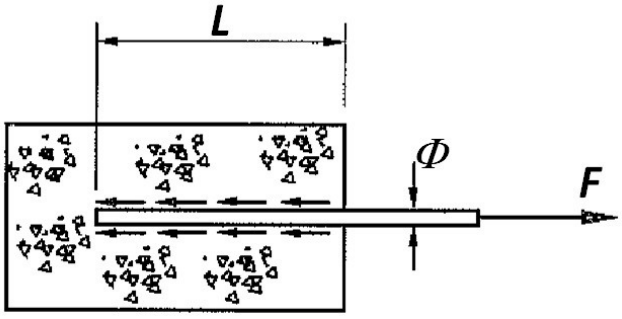

Figure 1.4: Anchorage bond stress

The anchorage length is given by Eq 1.2:

$$L = \frac{f_y \times \phi}{4 \times \tau_{bd}} \qquad \text{Eq 1.2}$$

Where,

L = Development Length

ϕ = Diameter of Bar

τ_{bd} = Bond Strength

1.4.3.2 Flexure bond

A flexure bond is one that results from a change in the bending moment over the length of the member, which causes a change in the tensile force carried by the bar along its length. A significant amount of shear occurs where it is acute. Local bond stress is another name for this bond since it happens in a specific localised area. Figure 1.5 shows the flexural bond stress distribution.

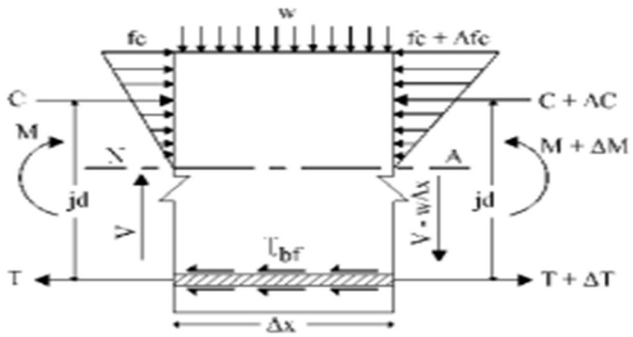

Figure 1.5: Flexural bond stress

The flexural bond stress is given by Eq 1.3:

$$\tau_{bd} = \frac{V}{j_d \times \pi \times d} \qquad \text{Eq 1.3}$$

Where,

V = Shear Force in the section

j_d = Lever Arm

d = Diameter of Bar

1.4.4 Factors affecting bond

The factors that affect the bond of steel to concrete are mainly divided into three categories, namely,

a) Structural Characteristics
    1. Concrete cover

2. Spacing of bars
3. Embedment length

b) Bar Properties
    1. Bar size
    2. Bar geometry
    3. Surface condition of bars

c) Concrete Properties
    1. Compressive strength
    2. Type and quantity of aggregate
    3. Concrete slump
    4. Addition of fibres

1.4.5 Tests for determining bond strength

IS 2770 Part 1 (IS: 2770-1: 1967(R2017), 1967) specifies the pullout test for the determination of bond strength between steel and concrete. It is the most widely used test for the evaluation of bond behaviour. The prime reason for the adoption of this method is the ease of fabrication of the specimen as well as the simple procedure applicable under any laboratory condition. The pullout test gives an approximation of bond behaviour. However, the pullout specimen does not simulate the actual construction condition. In a pullout test, the steel is in tension while the concrete is in compression. In practical scenarios, such a condition rarely occurs. Thus, in addition to the pullout test, some other test needs to be performed for proper access to bond strength in actual conditions. Few foreign codes incorporate various other tests in addition to the pullout test. ACI (2015) (ACI-2015, 2015) specifies four different types of test specimens for determining bond strength, namely,

a) Pull-out Specimen
b) Beam-end Specimen
c) Beam anchorage Specimen
d) Splice Specimen

The diagrammatic representation of the above-mentioned tests is shown in Figure 1.6.

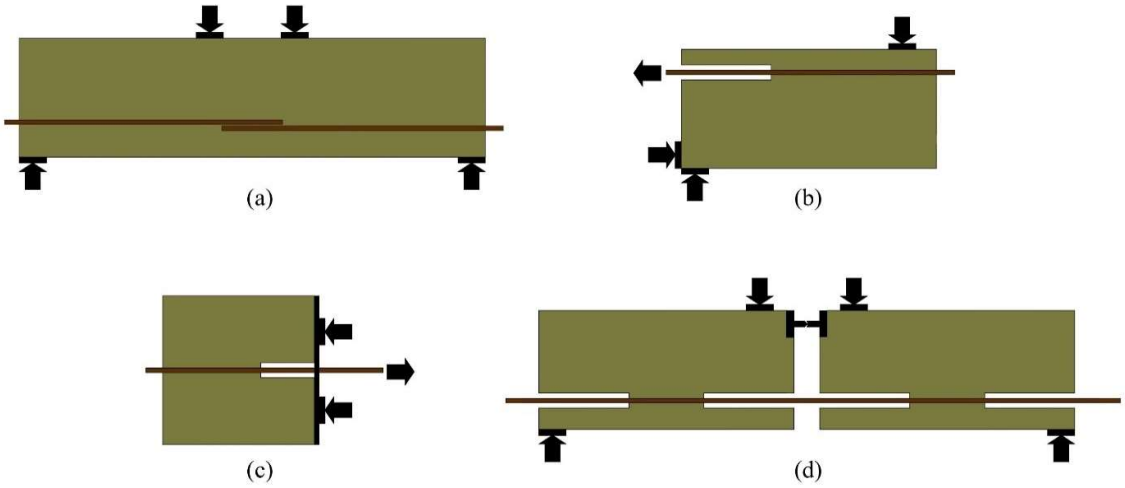

Figure 1.6 a) Spliced beam specimen b) Beam-end specimen c) Pullout specimen d) Hinged beam specimen

1.5 Need to Study the Bond Performance of GPC

The demand for concrete structures has grown significantly along with urbanization. This has resulted in a massive burden on the cement industry for production causing rapid depletion of limestone sources. Furthermore, it has resulted in the emission of a massive amount of CO_2. Keeping all these in mind, an alternative to cement concrete has been sought. Geopolymer concrete is one such alternative. Continuous research in this area is required to regulate the factors impacting geopolymer concrete. Since the success of reinforced geopolymer concrete as a two-phase building material depends on the ideal transmission of forces from steel to concrete, one of the key areas of research that requires our attention in this respect is the bond strength of geopolymer concrete. The various parameters related to the bond behaviour of reinforced geopolymer concrete need to be evaluated before it can be used for commercial construction purposes. Hence, research in the field of bond behaviour of geopolymer concrete is of vital importance.

1.6 Finite Element Analysis

Robust and reliable designs are prime requirements in all fields of engineering; it requires lots of experimentation, which is a time and resource-consuming process. Therefore, researchers are developing mathematical models to predict the behaviour of a real-world problem. Most real-world problems are complicated in nature. The finite element method is used for solving a differential or integral equation. Finite Element Analysis (FEA) is a numerical method of analysis which provides approximate solutions to complicated problems that would be

otherwise difficult to obtain. Several finite element software are available for performing the finite element analysis, which provides a platform to simulate the practical situations in the finite element environment. In the present research, FEA was carried out using finite element software ATENA-GiD to predict the bond behaviour of high-strength geopolymer concrete when subjected to loading.

Every finite element analysis consists of 3 stages:

- Pre-processing or modelling

This stage involves creating an input file which contains geometrical details, material details, interaction involved in the structural members, loads, boundary conditions, etc., for the finite element analyser (also called "solver"). The geometrical model of the physical problem is completely defined. The model is usually created graphically using GiD.

- Processing or FEA

In this stage, the ATENA solver solves the numerical problem defined in the model. For example, output files from a stress analysis problem include displacements and stresses that are stored in binary files and are ready for post-processing.

- Post-processing:

This stage is rendered stage, which generates reports, images, animations, etc., in the output data file.

1.6.1 ATENA-GiD

ATENA was developed by Cervenka Consulting, Czech Republic. ATENA is a user-friendly finite element-based software used for nonlinear analysis of concrete structures including cracking, crushing, and reinforcement yielding. The advantage of using ATENA is that it is a program specially developed for the analysis of concrete. It uses all the material properties based on cube strength using equations Fib model code 2010 and Bigaj model. Geometrical modelling of ATENA can be done using GiD. GiD is a graphical user interface for geometrical modelling and data input for different numerical simulations. GiD was developed by "the International Center for Numerical Methods in Engineering (CIMNE)". CIMNE is a research organization created in 1987 at the Technical University of Catalonia, Spain as a partnership between the Government of Catalonia and UPC, in cooperation with UNESCO.

1.6.2 Working with GiD

GiD is universal and adaptive pre and post-processor computer simulation in engineering and applied science (GiD). Using GiD, the model is to be numerically evaluated geometrically generated and assigned material properties. The boundary conditions are assigned to the geometrical model. The meshing of the model is done as per the requirement. This pre-processing information enables the solver to generate the results. In the present study, ATENA is employed as the solver. Finally, the results generated by the solver are read and visualised in the GiD post-process. The flow of work in ATENA-GiD is given in Figure 1.7.

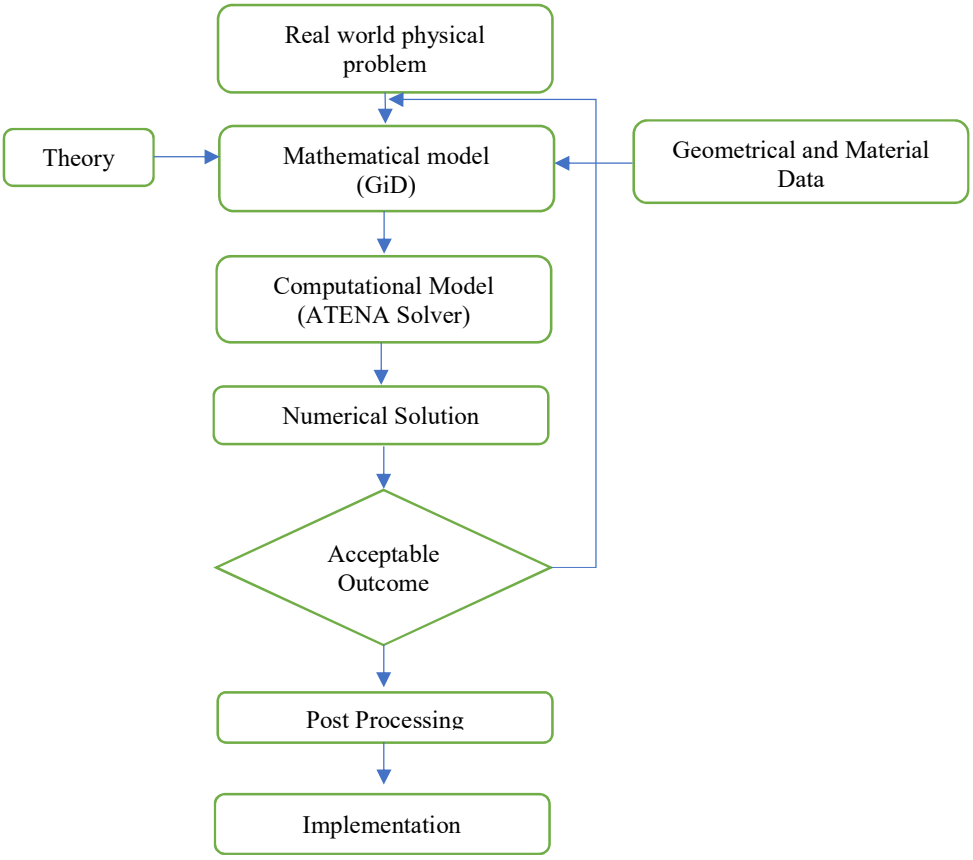

Figure 1.7: Numerical analysis methodology in ATENA

1.7 Need to Study the Performance of GPC under Chemical Attack

Concrete structures are intended for long-term operation. The chemical resistance of concrete plays a significant role in maintaining the design requirements for the design life period. The chemical resistance of concrete structures mainly depends on the chemical characteristics of raw materials and the degree of adverse nature of the environment. Adverse conditions are imposed by acidic rains, marine environment, deicing salts, increased carbon dioxide in the

environment, and industrial effluents. Hence, research in the field of chemical resistance of High Strength Geopolymer Concrete (HSGPC) is of vital importance. In the present study, simulation to the adverse environmental condition, HSGPC is subjected to acids, chlorides, and sulfates and investigation on the mechanical behaviour of HSGPC is taken up.

1.8 Scope of the Investigation

The scope of the present investigation includes the following:

- Developing multicomponent HSGPC by employing particle packing methods for optimising aggregate proportions under ambient curing conditions.
- Understanding the microstructure (SEM, XRD, EDS, FT-IR, and BSE) and strength (splitting tensile strength, flexural strength and modulus of elasticity) characteristics of ambient cured high-strength GPC along with its constitutive behaviour.
- Investigating the chemical resistance of high-strength GPC against acid, chloride and sulfate attack.
- Understanding the bond behaviour of multi-component binder-based high-strength geopolymer concrete experimentally by conducting pullout and hinged beam tests.
- Numerical modelling of the bond behaviour of geopolymer concrete to validate experimental results and evaluate the change in bond behaviour with change parameters affecting the same.
- Predicting the maximum bond stress with variables viz., ratio of cover to bar diameter (c/d), embedment length to bar diameter and compressive strength.

1.9 Objectives of the Investigation

The following objectives are defined for the present investigation.

- To develop High Strength Geopolymer Concrete (HSGPC) mixes using the particle packing approach and multicomponent binders.
- To study the chemical resistance of high-strength geopolymer concrete subjected to acid, chloride and sulfate attack.
- To evaluate the bond behaviour of high-strength geopolymer concrete based on pullout and flexural bond strength tests.
- To perform numerical modelling to evaluate the parameters influencing the bond behaviour of high-strength geopolymer concrete.

1.10 Research Methodology

To achieve the above-formulated objectives, a detailed experimental program was designed and carried out in four phases.

Phase-1

Particle packing models were used for optimizing the proportions of fine and coarse aggregate in the mix design of geopolymer concrete. Developing mix proportions for blending multiple component binders to develop high-strength geopolymer concrete can be done based on the literature available. Determining the strength characteristics such as compressive strength, flexural strength, splitting tensile strength, and modulus of elasticity. Constitutive behaviour is established. Analytical models for the prediction of mechanical characteristics are proposed. The influence of multicomponent binder materials on HSGPC is evaluated based on microstructure characterization techniques,

Phase -1 deals with the following aspects,

1) Particle packing Methods: Modified Toufar Model (MTM), J D Dewar Model (JDD)
2) Binder materials: flyash, GGBS, silica fume, alccofine, OPC
3) Test methods: compressive strength, splitting tensile strength, flexural strength, modulus of elasticity and stress-strain behaviour.
4) Microstructure techniques: SEM, XRD, EDS, FT-IR, and BSE

Phase-2

The chemical resistance of high-strength GPC was investigated by exposing it to HCl, H_2SO_4, $MgSO_4$, and NaCl. The dimensional loss factor, mass loss factor, and strength loss factor were determined.

Phase -2 deals with the following parameters,

1) Chemical: HCl, H_2SO_4, $MgSO_4$, and NaCl
2) Grade of concrete: 60, 80, 100 MPa
3) Exposure durations: 28, 56 and 90 days
4) Test methods: Dimensional loss factor, mass loss factor, strength loss factor, acid durability loss factor.

Phase-3

The bond behaviour of high-strength GPC is studied and the effect of parameters like bar diameter, development length, and cover to the bar are assessed by conducting pullout and hinged beam tests.

Phase -3 deals with the following parameters,

1) Grade of concrete: 60, 80, 100 MPa
2) Diameter of bar: 12, 16 and 20 mm
3) Embedment length: 2.5D, 5D and full depth of the specimen. (for pullout test)
4) Cover to bar: 16, 20 and 40 mm. (for hinged beam test)
5) Bond strength test: Pullout and hinged beam test

Phase-4

The bond behaviour of geopolymer concrete is studied using finite element software for both plain and ribbed bars by considering parameters such as bar diameter, development length, and cover to the bar, by using pullout and beam end test. The results of the ribbed bars are compared with the experimental results of the pullout test for validation. An analytical model is proposed to predict the bond stress in normal, standard and high-strength geopolymer concrete. The proposed analytical models are compared with available models in the literature.

Phase-4 deals with the following parameters,

1) Grade of concrete: 20, 30, 40, 50, 60, 70, 80, 90, and 100 MPa
2) Diameter of bar: 10, 12, 16 and 20 mm
3) Embedment length: 2.5D, 5D and full depth of the specimen (for pullout test); and for beam end l_e/d 3, 5, 7, and 9.
4) Cover to bar diameter ratio: 1 to 5 at an increment of 0.5 (for beam end test)
5) Bond strength test: Pullout and beam end test

The schematic diagram showing a detailed research methodology along with the variables involved in each phase of work and the output of the present investigation is given in Figure 1.8

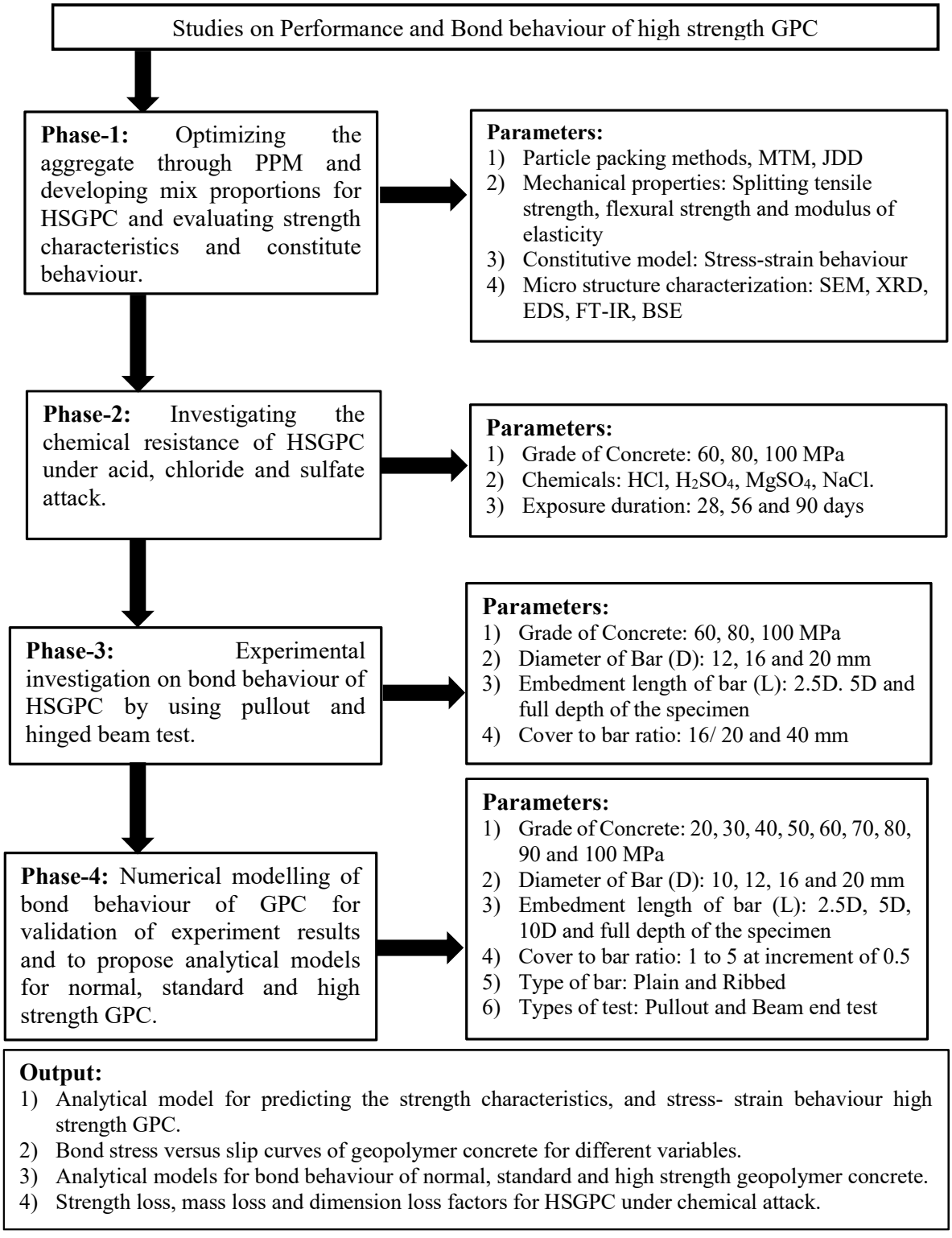

Figure 1.8: Methodology of the research work

1.11 Summary

In the present chapter, general information on geopolymer concrete, parameters affecting geopolymer concrete, and particle packing theory for mix proportioning are discussed. A brief introduction to the mechanism involved in bond stress, types of bond, factors affecting bond strength, and tests for determining bond strength of geopolymer concrete, are dealt with in detail. An introduction to numerical analysis on the bond behaviour of HSGPC has been discussed, including information about ATENA-GiD. Also, the importance of assessing the chemical resistance of HSGPC is discussed. The scope, objective and research methodology of the present research are presented. Based on the areas of research identified, a review of various works reported in the literature is discussed in Chapter 2.

CHAPTER 2
REVIEW OF LITERATURE

2.1 General

In the previous chapter, the significance of bond for the composite action of concrete, types of bond, and tests to perform the bond test were discussed along with an introduction to geopolymer concrete, factors affecting it, and particle packing theory for mix proportion. Furthermore, the significance of the chemical resistance of GPC along with the numerical simulation of bond behaviour were discussed. In the current chapter, a review of various works reported in the literature on geopolymer concrete, parameters affecting GPC, bond behaviour of GPC, and durability performance of GPC, are presented. The review of the literature is done in the following areas:

- Geopolymer concrete and its affecting parameters
- High Strength geopolymer concrete
- Particle Packing models
- Mechanical characteristics and constitutive behaviour of geopolymer concrete
- Bond behaviour of geopolymer concrete
- Numerical modelling of bond behaviour of concrete
- Durability performance of geopolymer concrete

2.2 Geopolymer Concrete and its affecting Parameters

De Silva et al., (2007) studied the early age reaction mechanism of geopolymer concrete. With sodium hydroxide and sodium silicate acting as an alkaline activator, metakaolin was used as an aluminosilicate source. The specimens were cured for 72 hours at 40°C, and the microstructural phase, setting time, and initial strength parameters were all extensively examined. It was found that the amount of alumina in the combination had a significant impact on how quickly the mixture was set. As the ratio of SiO_2/Al_2O_3 ratio increases, the setting time also increases. Additionally, it was observed that, up to a certain period the lateral strength increased with an increase in the ratio of SiO_2 to Al_2O_3. The extra alumina concentration caused a low-strength specimen when the ratio was increased beyond the optimum value. The research

ultimately led to the conclusion that maintaining an optimal ratio in accordance with the requirements is necessary since altering Al and Si content could have a substantial impact on the properties of geopolymer concrete (De Silva et al., 2007).

The effect of variations in aggregate content in geopolymer concrete was investigated by Joseph and Mathew (2012). Flyash was used as an aluminosilicate source, and NaOH and Na_2SiO_3 were used as alkali activators. The author also studied the effects of curing circumstances, alkaline activator type, combination, activator concentration, and the alkaline activator to binding ratio. It was observed that increasing compressive strength was positively impacted by curing temperatures up to 100 °C and that this progress ceased above 100 °C temperature. Furthermore, it was noted that curing the specimen at 100 °C resulted in gaining 96.4 % of 28 days strength in only 7 days. By raising the aggregate content, a rise in tensile strength was noticed. The splitting tensile strength improved by 45.5 % and the flexural strength by 30.6 %, respectively, with a change in the percentage of aggregate from 60 to 75 % in the concrete (Joseph & Mathew, 2012).

Deb et al., (2013) studied the behaviour of flyash-based Geopolymer concrete by replacing binder with proportions of GGBS varying from 10 to 20%, keeping the alkaline activator to binder ratio at 0.35 and cured at ambient temperature. The study was done to test compressive strength, drying shrinkage, sorptivity, and volume of permeable voids. The outcome of the study is that 20% flyash with GGBS gave better compressive strength and the addition of GGBS resulted in a decrease in sorptivity, drying shrinkage, and volume of permeable voids (Deb et al., 2013).

Nath and Sarker (2014) studied the effect of the addition of GGBS by varying its proportion from 0 to 30% to the total weight of the binder and examined the impact on the setting, workability, and early strength properties of flyash geopolymer concrete cured in ambient condition. The results showed that an increase of GGBS in the fly-ash-based geopolymer mixture reduces workability and setting time. The results show that with a replacement of GGBS up to 30%, compressive strength of 55 MPa was achieved in 28 days (Nath & Sarker, 2014).

Pavithra et al., (2016) studied the effect of Na_2SiO_3/NaOH ratio and NaOH molarity on the synthesis of flyash-based geopolymer mortar. In their study, the variation of Na_2SiO_3/NaOH ratio was taken in steps of 1, 1.5, 2, and 2.5 and the NaOH molarity was varied in steps of 10, 12, 14, 16, and 18 M. The influence of the variation was observed on the mechanical and

morphological properties of the geopolymer mix. According to the findings, compressive strength was high at a ratio of 1.5 of Na_2SiO_3 to NaOH. The compressive strength was found to rise with increasing NaOH molarity up to 16 M, after which it was shown to decrease with increasing NaOH molarity. The number of unreacted flyash particles in hardened mortar samples increases with an increase in Na_2SiO_3 to NaOH ratio, according to environmental scanning electron microscopy data (Pavithra et al., 2016b).

Hamidi et al., (2016) studied the effect of varying the concentration of sodium hydroxide from as low as 4 M to as high as 18 M on the properties of flyash-based geopolymer concrete with fixed curing of 60° for 1 day. The morphology properties were tested using Fourier Transform Infrared Spectroscopy (FT-IR) for structural elucidation; Scanning Electron Microscope (SEM) and for mechanical properties, flexural strength tests were done. From all tests, the common inference is that a value of 12 M NaOH solution is optimum for all the parameters tested (Hamidi et al., 2016).

Pavithra et al., (2016) proposed a mix design for geopolymer concrete with flyash**.** In their study correlation between alkaline activator solutions to binder ratios ranging from 0.4 to 0.8 and 28-day compressive strength was investigated to propose a conceptual mix design method for GPC. The proposed mix design was able to produce a geopolymer concrete with a compressive strength between 23-53 MPa and it can be observed that slump value increased with an increase in the ratio of alkaline activator solution to flyash ratio (Pavithra et al., 2016a).

Shadnia and Zhang (2017) performed a study on geopolymer concrete with Class F flyash and low calcium slag in different proportions. A number of specimens were cast to test compressive strength by changing the concentration of Sodium Hydroxide (NaOH) from 7.5 M, 10 M, and 15 M, and at curing times of 1, 2, 4, 7, 14, and 28 days. The findings of the study were that as GGBS proportion is increased, there is a corresponding increase in compressive strength and the same effect is with increasing the concentration of NaOH. 70% of final compressive strength is achieved in just 2 days and with no significant increase after 7 days (Shadnia & Zhang, 2017).

Particle packing theory was used by Chaitanya Thunuguntla and Gunneswara Rao (2018) to generate mix proportions for a targeted compressive strength of alkali-activated slag concrete (AASC). The alkaline solution-to-binder ratio, binder content, and sodium hydroxide concentration were all taken into consideration in the work. Alkaline activator solutions based on sodium silicate and sodium hydroxide are used to activate ground-granulated blast-furnace

slag. The optimal aggregate ratio for FA:CA that was determined through the experiment was 0.45:0.55. As a starting point for designing a mix, workability (slump) and average compressive strength at 28 days were determined. A set of alkaline solutions which included binder ratio, sodium hydroxide concentration, and binder content corresponding to a specific compressive strength was then determined by plotting it on compressive strength graphs and workability graphs (Thunuguntla & Gunneswara Rao, 2018).

Cui et al., (2020) studied the static correlation of the mechanical properties of flyash-based geopolymer concrete. Experimental tests were performed to measure the compressive strength, indirect tensile strength, and elasticity of modulus of flyash-based geopolymer concrete. The results were compared with the results of ordinary concrete by performing statistical hypothesis tests. It was observed that compressive and tensile strength, the elastic modulus of geopolymer concrete was lower than that of ordinary concrete. Also, the standard equations provided by codes for ordinary concrete to measure the modulus of elasticity cannot be applied to geopolymer concrete. Based on the experimental results and regression analysis, the author proposed an equation for the modulus of elasticity and tensile strength which predicted values for geopolymer concrete. The equation presented for evaluating the modulus of elasticity and tensile strength is given in Eq 2.1 and Eq 2.2 (Cui et al., 2020).

Modulus of Elasticity, $E = 874.5 \times f_{ck} \times 0.85$ Eq 2.1

Tensile strength, $t_e = 0.085 \times f_{ck} + 0.0585$ Eq 2.2

2.3 High Strength Geopolymer Concrete

Ambily et al., (2014) investigated the formation and determination of fresh and mechanical properties of ultra-high-performance geopolymer concrete under ambient curing condition. In this research, Portland cement was completely replaced as a binder by industrial by-products such as flyash and GGBS. Silica fume was also added to densify the concrete for increased performance. Ultra-high-performance concrete with and without steel fibres was evaluated wherein four mixtures with fibres and one mix without fibre addition were studied as UHPGPC mixtures. The parameters observed in the research were changing the proportion of flyash, GGBS, and silica fume, the type of alkaline activator, namely, sodium-based alkaline activator and potassium-based alkaline activator, the inclusion or exclusion of steel fibres with varying proportion and the length of steel fibre. It was observed from the initial trials that the inclusion of flyash decreased fresh density, flowability, and compressive strength for the same liquid-to-binder ratio. Furthermore, greater compressive strength was observed when binders were

activated with potassium-based alkaline activators. It was seen that the compressive strength was highest for 1% 6 mm and 2% 13 mm steel fiber with a value of 175 MPa while the value was 124 MPa for concrete without fibers. The flexural strength was 10.3-13.5 MPa for concrete with fibres and 9.1 MPa for concrete without fibres (Ambily et al., 2014).

Dong et al., (2017) developed a high-strength geopolymer mortar with a novel method of curing using solar energy. The binder material flyash was used as an aluminosilicate source. The mortar samples were coated on two different grey scales, namely, Solar Curing Black (SCB) and Grey (SCG 40% black). The mechanical properties were investigated. The microstructure behaviour was also investigated through microstructure characterization techniques. It was observed that a compressive strength of 92 MPa was achieved for SCB specimens. SCB and SCG specimens presented 17.8%, and 14.4% enhancement in strength compared with the control group. The degree of polymerization increased in the case of SCB specimens as the internal temperature increased to 65^{o}C. Microstructure characterization techniques revealed that SCB specimens presented more amount of C-A-S-H and N-A-S-H compounds. The SCG specimens showed a moderate enhancement in compressive and microstructure properties. Also, the constitute behaviour change was examined for SCG and SCB mortars (Dong et al., 2017).

Bharath et al., (2017) improved the compressive strength of low calcium flyash GPC with alccofine. The compressive strength of 73 MPa GPC cured at 90^{0} is achieved with the addition of 10% alccofine. Also, investigated the effect of parameters such as curing temperature, period of curing, flyash content, and alccofine content on the compressive strength of GPC. It was mentioned that GPC in the presence of alccofine can be used for the general purpose of concrete as required compressive strength can be achieved even at ambient curing temperature. An increase in the percentage of alccofine up to 10% increased the compressive strength of concrete to a certain percentage. Due to the early age reactivity of alccofine beyond an increase of 10%, the concrete loses its workability and compressive strength (Bharat et al., 2017).

Sakthidoss and Senniappan (2019) presented the production of high-strength geopolymer concrete with and without manufacturing sand. flyash and GGBS of equal quantity were used as aluminosilicate sources. Four mix proportions i.e., two with cement with and without M-sand, and two with GGBS and flyash, with and without M-sand were studied. Compressive strength and durability tests were performed. It was observed that there was an increase in compressive strength by 28% in HSCC (High Strength Cement Concrete) when M-sand was

used while it was 3.6% in HSGC (High Strength Geopolymer Concrete). Also, greater resistance to sulfate and acid attack was shown by HSGC compared to HSCC (Sakthidoss & Senniappan, 2020).

Bellum et al., (2020) investigated the influence of graphene oxide (GO) on the performance enhancement of flash-GGBS-based geopolymer concrete. The behaviour change in compressive strength and the modulus of elasticity with the addition of GO were evaluated. The microstructure characterization was performed through scanning electron microscopy. The chloride ion resistance of GPC was investigated through a Rapid Chloride Penetration Test (RCPT). It was observed that the microstructure was extra compacted and porosity decreased with the addition of GO. Enhanced compressive strength was observed only after the inclusion of GGBS. GO significantly improved the microstructure from porous nature to pore-filled morphology. The optimum mix proportion of 3% GO and 30% GGBS increased the compressive strength and modulus of elasticity by 38.51% and 28% respectively (Bellum et al., 2020).

Dong et al., (2020) compared the effect of alkaline activator sodium metasilicate pentahydrate against sodium silicate and sodium hydroxide solution. From the experimental study, it was observed that meta silicate improved the mechanical performance more than traditional liquid activators did up to the optimum dosage beyond which strength decreases and the risk of efflorescence increases. The microstructure characterization technique revealed that denser reaction products accumulated and the remaining metasilicate particles gradually dissolved under moisture ingression (Dong et al., 2020).

Liu et al., (2020) investigated the effect of steel fibre and micro silica on performance characteristics and fracture properties of ultra-high-performance concrete (UHGPC). The parametric study with a four-volume fraction of steel fibre and silica fume was considered. The correlation among the compressive, splitting, and modulus of elasticity was studied. The experimental results indicated that with an increase in steel fiber dosage, the fresh properties were affected though there was an improvement in the mechanical and fracture performance. The existing analytical models for predicting the elastic modulus of conventional concrete overestimated the behaviour of UHGPC. Silica fume presented a significant effect on the workability and mechanical properties and it depends on the amount that was utilised. The silica fume improved the performance and fracture properties for a dosage of more than 10%. With

an increase in silica fume content, the steel fibre dosage can be decreased without sacrificing performance and fracture properties (Liu et al., 2020).

Mayhoub et al., (2020) developed reactive powder geopolymer concrete (RPGPC) from GGBS. The mechanical and durability performance were examined under different curing techniques. Mechanical properties including compressive strength, sorptivity, and modulus of elasticity were determined. The microstructure behaviour was assessed using scanning electron microscopy. It was noticed that thermal curing provides more effective behaviour than other techniques for all RPGPC. It was concluded that RPGPC was successfully developed with satisfying engineering properties. It was also mentioned that the workability problem of RPGPC should be solved with superplasticizers (Mayhoub et al., 2021).

Amin et al., (2022) evaluated the behaviour under performance, durability, and microstructural aspects of flyash, metakaolin, and slag-based sustainable high-strength geopolymer concrete. The splitting tensile strength, flexural strength, and modulus of elasticity were measured. It was observed that the mix with 200 kg/m^3 of metakaolin, and 300 kg of slag showed the highest compressive, flexural, splitting tensile strength and modulus of elasticity of 82.6 MPa, 9.2 MPa, 6.2 MPa, and 37.68 GPa respectively. Also, with an increase in slag content, the coefficient of permeability decreased. The mixes with mineral additives showed decreased drying shrinkage. From the SEM analysis, the geopolymer matrix presented more dispersed pores than conventional concrete which indicates higher mechanical performance. It was mentioned that among the different parameters controlling the compressive strength of GPC, the percentage of Al_2O_3 is a significant parameter that affects the degree of polymerization. The reactivity of polymerization also depends on the provisions of non-calcium compounds and the lowest compressive strength was indicated in a higher percentage of metakaolin with a weak structured matrix. It was observed that flyash and metakaolin showed lower drying shrinkage than cement concrete by forming a high network alkali-activated matrix (Amin et al., 2022).

Kanagaraj et al., (2022) investigated the fire resistance of high and normal strength geopolymer concrete subjected to standard temperature exposure according to IS 834. The behaviour of GPC specimens was determined after their exposure to 821 ^oC, 925 ^oC, 986 ^oC, and 1029 ^oC with a rate of heating in accordance with ISO 834. The parameters of weight loss, strength loss, and visual and micro-level inspection were considered to determine the effect of temperature on GPC. From this study, it was observed that high-strength concrete is more prone

to temperature exposure. The specimens cured at room temperature showed more resistance against thermal exposure compared to oven-cured specimens. From the SEM analysis, phase changes were observed with dehydrated molecular structure and the strength of aggregate was considered as the parameter impacting degradation of GPC exposed to higher temperature. From the experimental dataset, it was observed that the aggregate crushing index of 8.1 % was an optimum value for retaining its strength after exposure to 821 ^{o}C (Kanagaraj et al., 2022).

Arunachelam et al., (2022) developed high-strength geopolymer concrete with silica fume and high-volume copper slag. The copper slag was used to replace fine aggregate in higher volumes to develop high-strength GPC. Different percentages of copper slag up to 100% replacement of natural sand were attempted to develop high-strength GPC. The traditional hybrid sodium-based alkaline activator was adopted with 12 M sodium hydroxide. GPC specimens were cured under ambient and steam atmospheres. The optimum mix with 2% silica fume showed the highest compressive strength of 79 MPa. From the test results, it was observed that the incorporation of copper slag significantly reduced the workability of concrete since copper particles are angular and irregular in shape. Up to 90% replacement showed an increment in mechanical properties with a slight reduction for complete replacement, which can be attributed to workability issues. From the results of performance characteristics, the optimum percentage of replacement of copper slag could be 100%. Steam-cured specimens showed a 55% increment in compressive strength compared to ambient-cured specimens. From SEM analysis it was observed that steam cured specimen presented fewer unreacted particles showing the requirement of heat for a high degree of polymerization (Arunachelam et al., 2022).

2.4 Particle Packing Models

De Larrard and Sedran (1994) held that the concept of achieving good packing density is a key to obtaining ultra-high-performance concretes. The authors discussed the parameters to be maximized during the mix design process. Reference was made to the concept of maximum paste, which leads to choosing fine sand for optimizing the compressive strength of cementitious material. Based on criteria such as fluid consistency, conventional components (such as common aggregate, sand, Portland cement, silica fume, superplasticizer, and water), and mild thermal curing, an ideal material is sought. Using a solid suspension model, a variety of blends was developed, and tests were run to determine the optimal mix. It was concluded from the study that the solid suspension model is a valuable tool for optimizing the high-packing density of cementitious material (de Larrard & Sedran, 1994).

Glavind and Pedersen (1999) reported that for selecting a concrete mix, it is desirable to compact aggregates as densely as possible, i.e., with maximum packing to minimize the amount of binder required to fill the cavities between the aggregates for constant concrete workability. Apart from an obvious economic benefit, the reduction in the binder results in less shrinkage and creep, enhancing the density and ensuring durable and strong concrete. The work presented as a packing model can be used to optimize the aggregate and arrive at the optimum quantity for the concrete mixes (Glavind & Pedersen, 1999).

Jones et al., (2002) studied different particle packing models, namely, the Dewar Model, Modified Toufar Model, and De Larrard Model to design a mix proportion of concrete with the least void ratio. The models used were compared with experimental results and other published works in the literature. The basic mathematics and principles used by each model were also discussed. The models were used for determining the proportion of both aggregates and cement phase and the result obtained with regard to of void ratio was compared with experimental results conducted in the laboratory. It was concluded from the research that these models had similar proportions of materials to obtain the least void ratio. Also, it was found that the proportioning of the aggregate phase resulted in a vast difference in the result void ratio compared to the cement phase where the improvement was minimal. However, the proportion of constituents using these models resulted in a harsher mix (Jones et al., 2002).

An investigation of the idea of particle packing and how it affects concrete performance was examined by Kumar and Santhanam (2003). When there are more components to combine, it becomes highly challenging to conduct experiments to determine the best percentage of materials to improve the quality of concrete. Improving the packing density of materials was a better strategy for achieving an ideal combination of materials. Various studies on this matter were presented in the review. The concept of discrete and continuous packing models was also presented. Furthermore, examples of mix proportion using LISA, software based on the Andreassen model was also provided in the study (Kumar & Santhanam, 2003).

Various experiments and theories on self-compacting concrete were explained by Brouwers and Radix in 2005. The "Chinese Method," which was created by Su et al., (2001) and modified for use in Europe, according to the authors, served as the foundation for the creation of new concrete mixes. Three types of sand (0-1 mm, 0-2 mm, and 0-4 mm), slag-mixed cement, gravel (4-16 mm), and a polycarboxylic ether-type superplasticizer were combined to create the mixes. These mixes were extensively tested, both in fresh and hardened

states and met all practical and technical requirements such as low cement and powder content (medium strength and low cost). It can be inferred from the study that the particle size distribution of all solids in the mix follows the grading line of the modified Andreasen model (1930). Using the packing theory of Andreasen (1930) and modifications by Funk and Dinger (1994), cheap SCC mixes can be composed to meet the standards and requirements in a fresh state. Furthermore, a carboxylic polymer-type superplasticizer was employed as a sole admixture (Brouwers & Radix, 2005).

Fennis (2011) studied the implementation of particle packing models to predict the mechanical properties of ecological concrete from its proportioning. The research looked at various works of literature focusing on the replacement of cement by various fillers and the impact on mechanical properties. Furthermore, various particle size distribution optimization methods were evaluated with regard to their advantages and disadvantages vis-a-vis ecological concrete mixture optimization. Particle characteristics, particle structure, and interparticle forces which impact packing density were also studied. Different particle packing models namely, the furnas model, toufar and modified toufar model, dewar model, linear packing density model, compressible packing model, schwanda model, and linear-mixture packing model were evaluated and compared. It was found that the compressible packing model was most flexible in accommodating several components to obtain a dense packing factor (Fennis, 2011).

Hatem et al., (2012) studied the influence of fineness modulus, cement paste volume based on slump test, and the properties of fresh and hardened concrete. The study on the applicability of two theoretical models, the toufar model and the 4C packing program for selecting suitable relative amounts of the concrete constituents, for obtaining the minimum void ratio, was undertaken by researchers. A comparison of the results was made using the theoretical models from the literature with experimental data. The models gave similar results and suggested similar combinations of material to give a minimum voids ratio. It was concluded that optimizing the composition of aggregate material in concrete was beneficial in terms of economy, strength, and durability. It was noted from the study that minimizing the voids ratio tends to raise the stiffness and also that the compressive strength is closely related to the moulding and fineness modulus (Hatem et al., 2012).

Mangulkar and Jamkar (2013) discussed in detail the fundamentals of particle packing theories which were categorized as discrete and continuous models. It was concluded that all the popular

packing models were based on the assumption that the particles are spherical. According to the study, the shape factor and convexity ratio are the most important shape parameters, and the mean size, specific gravity, and voids ratio are the most important size parameters that influence the packing of aggregates. According to this work, the concrete mix constitutes largely aggregate and its quality is hence dependent on the grading, size, and shape of the aggregates used (Mangulkar & Jamkar, 2013).

Karadumpa and Pancharathi (2021) studied the influence of particle packing methods on fresh, hardened, and microstructural properties of composite cement mortars. The Modified Toufar Model (MTM) and J. D. Dewar model (JDD) were considered for optimizing fine aggregate content in mortar specimens and compared with IS 383 and IS 650. The packing density of optimized aggregate proportions from JDD, MTM, IS 650:2008, and IS 383: 2016 methods was 0.6814, 0.6737, 0.6238, and 0.6008 respectively. MTM works on the principle of reducing the void content. Along with SEM, X-ray diffraction, Fourier transformation infrared radiation, thermogravimetric analysis, and differential thermal analysis were used to examine the effect of packing density on phase changes in microstructure characteristics. SEM analysis showed a significant improvement in the microstructure formation for increased packing density. The MTM method showed a better packing of particles compared to other methods and improved the compressive strength by 11.11% and 15.5 % than the specimens designed by IS 650:2008 and IS 383: 2016, respectively. For all curing ages, the MTM method showed better compressive strength behaviour (Karadumpa & Pancharathi, 2021).

2.5 Mechanical Characteristics and Constitutive Behaviour of Geopolymer Concrete

Nguyen et al., (2008) aimed to develop a framework for the constitutive modelling of concrete. Their research article presents the parameter identification and thermodynamic formulation for a non-local coupled damage-plasticity model. The calibration of the model parameters was the specific focus of this investigation. It was found that the experimental values can be used consistently and reliably to determine both local and non-local interactions controlling parameters. A novel method of parameter identification was developed by the division of total dissipation energy into additive components according to various dissipation mechanisms. In order to produce model responses that are compatible with the material's fracture energy, this research also discussed the link between local and non-local characteristics. In their research

paper, the model's application and calibration procedure was recommended. The numerical failure analysis of concrete structures was also explained through a series of existing structural tests, which demonstrated the model's effectiveness and the reliability of the suggested calibration technique (Nguyen et al., 2018).

Research on the tensile strength, Young's modulus, Poisson's ratio, and stress-strain equations for alkali-activated concrete that uses fly ash or ground granulated blast-furnace slag (GGBS) as the only binder was presented by Thomas et al., in (2015). In comparison to Portland cement concrete, alkali-activated concrete is shown to have lower Poisson's ratio and tensile properties. Alkali-activated concrete was predicted using equations of the same kind as those now used for OPC-based concrete, which depend on the compressive strength of the material, to determine the tensile strength and Young's modulus (Thomas & Peethamparan, 2015).

Noushini et al., (2015) experimentally studied the compressive strength, Young's modulus, and stress-strain characteristics of ambient and heat-cured GPC and OPCC. A total of 195 GPC cylinders and 210 OPCC cylinders were tested for the stated behaviour. Based on the experimental test outputs, constitutive model recitation of the whole stress-strain behaviour in uniaxial compression was established for low-calcium flyash-based GPC and the heat-cured Portland cement concrete (Noushini et al., 2016).

Investigations by Chitrala et al., (2017) mainly focused on the whole stress-strain properties of GPC with various fine aggregate blends. Granite fines were utilised in place of fine aggregates in this study. Sand and granite fines were mixed in a variety of weight ratios as fine aggregates. The compressive strength, stress-strain relationship, peak strain value, linearity of the stress-strain curve, ultimate strain, Young's modulus, and Poisson's ratio of GPC after 7, 28, and 90 days, were all tested under compression. According to the findings, a rising trend was seen in the behaviour when up to 40 % of GPC as the replacement of granite fines, at which point these values started to decline. Therefore, blending fine aggregate at a 60:40 ratio is ideal. Regression analysis was used to create new models based on the test findings to predict the stress-strain behaviour of GPC under compression. A comparison was made between the results of the proposed models to that of the experimental data to predict the equations based on various codes and past research (Chitrala et al., 2018).

Nath and Sarker (2017) investigated the flexural strength and elastic modulus of ambient cured low calcium flyash geopolymer concrete blended with OPC, hydrated lime, and GGBS. The results indicated that the density of ambient cured GPC and OPC specimens are equal. The

additives significantly improved the mechanical performance of low calcium flyash geopolymer concrete. The flexural strength of GPC was higher and the modulus of elasticity was lower compared with OPC concrete for the same grade of concrete. So, the existing equations for the prediction of the modulus of elasticity were not conservative for GPC, and a suitable analytical model was proposed (Nath & Sarker, 2017).

Cong et al., (2019) concentrated on describing the engineering properties of alkali-activated GGBS/FA concrete. Water-quenched slag (WQS) is regarded as a sand substitute in alkali-activated concrete to maximize the use of industrial by-products. The behaviour of the AAC under various loading scenarios, including in static compression, tension loads, and dynamic impact loads, is the specific emphasis of this work. Experimental research was done on the static compressive stress-strain relationship, direct tensile stress-strain relationship, Young's modulus, and dynamic response to impact loadings of ambient cured AAC. Additionally, by fitting the curves of the test results of AAC, constitutive models were created. The incorporation of additional material factors in the anticipated models results in more realistic behaviour and coherent equations for AAC than the current models recommended for OPC-based concrete. When compared to OPC concrete, it was discovered that AAC containing WQS particles exhibits enhanced deformability in the elastic range and ductility in the stress descending range (Cong et al., 2020).

Prachasaree et al., (2020) developed the performance characteristics models for flyash based geopolymer concrete. Based on the experimental test results and available data from the literature, analytical models of flexural strength, torsional strength, modulus of rupture, and elastic modulus were developed in terms of the compressive strength of concrete. Based on thin wall theory, an analytical model for predicting the cracking torsion strength was proposed based on critical stress $0.47\sqrt{f_c}$. It was observed that the proposed model for predicting the shear strength was similar to the ACI equation. Also, the interaction surface for combined loads, such as bending, shear, and torsion was established for the quarter-parabola bending-shear and torsion, and the quarter-circle torsion and shear interactions, with critical stresses of $f_b = 0.815\ f_c, f_s = 0.1s\ f_c, f_t = 0.3\ f_c$ respectively (Prachasaree et al., 2020).

Tang et al., (2019) conducted an experimental analysis to investigate the uniaxial compression behaviour of flyash-based geopolymer concrete incorporating GGBS and recycled aggregates. The parameters include percentage of recycled aggregates (0%, 50%, and 100%) and GGBS (0%, 10%, 20%, and 30% to the weight of the total binder content) in the analysis.

From the experimental results, it was observed that with an increase in the percentage of recycled aggregate, the stress-strain parameters such as elastic modulus, and peak stress decreased and with an increase in GGBS the stress-strain parameters increased. The reverse behaviour was observed for the ductility of flyash based geopolymer concrete (Tang et al., 2019).

Khalaf (2022) modelled Young's modulus of low calcium-based geopolymer concrete from nonlinear regression analysis. The author collected experimental results of 67 mix designs from the literature and divided them into two groups for the development and validation of the proposed analytical model for the prediction of modulus of elasticity. The proposed model showed a root mean squared error value of 3.11 GPa, and a mean absolute percentage error of 15% which indicates that the proposed model had a high correlation to experimental results. The coefficient of correlation with the experimental values was 0.88 (Khalaf & Kopecskó, 2022).

Ou et al., (2022) determined the influence of mix design parameters on static and dynamic compressive properties of slag-based geopolymer concrete with the addition of flyash. The parameters such as water-to-binder ratio, flyash content, and waterglass percentage were considered when carrying out experimental analysis. From the results, it was observed that the compressive strength varied from 50 MPa to 80 MPa. The increase in the water-to-binder ratio increased the workability and decreased compressive strength. The workability also increased with an increase in flyash content and waterglass. The percentage increase in waterglass increased the static compression behaviour and also the brittleness of concrete. The addition of 50% flyash imposed a sharp peak in dynamic compressive strength and dynamic increase factor. The constitutive models for static and dynamic compressive stress-strain behaviour were proposed (Ou et al., 2022b).

The constitutive models for GPC proposed in the literature are summarised in Table 2.1.

Table 2.1: Constitutive models proposed in the literature

AUTHOR	MODEL	PARAMETERS
Thomas et al. (Thomas & Peethamparan, 2015)	$\sigma = \sigma_0 \frac{\epsilon}{\epsilon_0}\left[\frac{n}{n-1+\left(\frac{\epsilon}{\epsilon_0}\right)^n}\right]$	$n = (0.4\times10^{-3})\sigma_0 + 1$ $\epsilon_0 = (2.7\times10^{-4})\sigma_0{}^{0.25}$ $E_c = 4400\sqrt{f_{cm}}$
Cong et al. (Cong et al., 2020)	$\sigma = f_{cm}\frac{\epsilon}{\epsilon_c}\left[\frac{m}{m-1+\left(\frac{\epsilon}{\epsilon_0}\right)^\beta}\right]$	$m = \frac{E_c}{19.5} + 2$ $\beta = 10\left(\frac{k}{f_{cm}}\right) + 5$ $E_c = 0.273(n+1)f_{cm} + 10$ $n = 0.08V_{WQS} - 0.03$
Noushini et al. (Noushini et al., 2016)	$\sigma = f_{cm}\frac{\epsilon}{\epsilon'_c}\left[\frac{n}{n-1+\left(\frac{\epsilon}{\epsilon_0}\right)^n}\right]$	$n = \left[1.02 - 1.17\frac{E_{sec}}{E_c}\right]^{-0.45} = n_1\ ;\ \epsilon_c \le \epsilon'_c$ $n = [n_1 + \omega + 28\zeta] = n_2\ ;\ \epsilon_c \ge \epsilon'_c$ $\zeta = 0.83exp\left(\frac{-911}{f_{cm}}\right)$ $\omega = 15(12.4 - 0.015f_{cm})^{-0.5}$ $E_c = -11400 + 4712\sqrt{f_{cm}}$

2.6 Bond Behaviour of Geopolymer Concrete

Sofi et al., (2007) investigated the bond performance of reinforcing bars in inorganic polymer concrete. Pullout tests and beam end tests were performed to evaluate the bond behaviour of reinforced geopolymer concrete. In that context, 23 beam-end specimens and 58 direct pullout type specimens were taken. In addition to that, 4 beam end specimens were made from OPC for comparison. The author observed that the result of the direct pullout test was more conservative with respect to the beam-end specimen test. It was concluded from the results that the bond performance of geopolymer concrete is on par with the performance of OPC concrete and thus it can be used as an alternative to OPC concrete in the construction industry (Sofi et al., 2007).

Sarker (2011) evaluated the bond strength of reinforced geopolymer concrete. To study the bond between the reinforcing bar and the concrete, a pullout test was performed on 24 beam-end specimens. To have a comparative study, the same number of specimens with OPC concrete was made and tested. The parameters included in the test were compressive strength, which varied from 25 MPa to 39 MPa, the diameter of the bar (20 mm and 24 mm), and the cover to the concrete where the cover-to-bar ratio was changed from 1.71 to 3.62. It was observed from the result that the bond strength of geopolymer concrete was higher than normal OPC concrete.

Additionally, the study found that applying analytical models and empirical formulas related to OPC concrete for geopolymer concrete would produce safe results even though the values would be more conservative (Sarker, 2011).

Castel and Foster (2015) investigated the bond strength of geopolymer concrete using a standard RILEM pullout test. The author obtained a blend of 85.2% flyash and 14.8% GGBS from the literature review. Two different curing procedures were used, namely, 2D curing and 7D curing. In 2D curing, the specimen was oven cured at 80^{o}C for 1 day and cured in an 80 ^{o}C water bath for a further 1 day. In 7D curing, the specimen was oven-cured at 40 ^{o}C for 1 day and had 80 ^{o}C water bath curing for a further 7 days. It was observed that in 2D curing there was a 10% increase in bond strength compared to OPC and a 25% increase in 7D curing for equivalent compressive strength. It was also observed that an extension of the duration of curing from 2 days to 7 days led to little increase in elastic modulus and tensile strength but increased bond strength by 25% (Castel & Foster, 2015).

Dogupparti (2015) presented an experimental investigation on the bond behaviour of geopolymer concrete. The bond behaviour of geopolymer concrete cubes of grade M35 reinforced with a 16 mm TMT bar was analysed. GPC was made by total replacement of cement with 60% flyash and 40% GGBS. NaOH & Na_2SiO_3 were used as alkaline activators. The bond strength test was carried out according to IS 2770-1997. The results indicated that the performance of reinforced geopolymer concrete with respect to bond was reliable enough to be used in the construction industry (Doguparti, 2015).

Topark-Ngam et al., (2015) investigated the setting time, strength and bond of high calcium fly ash geopolymer concrete. The findings showed that high calcium content in fly ash gives geopolymer concrete a quick setting time of 28–58 min. As the concentration of NaOH increases, the strength and elastic modulus increase. The splitting tensile strength values are lower than those of Portland cement concrete. The strength of the bonds was significantly influenced by NaOH content. The high calcium fly ash geopolymer concrete's (HCGC) improved bond strength properties as a result of the geopolymer matrix's excellent interfacial transition zone (ITZ) properties, which may have been helped by the inclusion of calcium and calcium silicate hydrate. HCGC's binding strength was marginally higher than that of geopolymer concrete made with low calcium fly ash (Topark-Ngarm et al., 2015).

Albitar et al., (2017) investigated the effect of corrosion of reinforcement on the bond behaviour of GPC through pullout testing. It needs to be mentioned that it is important to

understand the bond behaviour at the serviceability and ultimate limit state to simulate the behaviour of reinforced concrete structures. An experimental analysis was carried out on 102 pullout specimens considering various parameters like bar diameter, concrete cover-to-diameter ratio, compressive strength, and levels of corrosion. From the experimental analysis, the maximum bond strength increases as the degree of corrosion increases from 0 to 1%, and thereafter the bond strength decreases with increasing corrosion level. It was mentioned that the bond between the steel reinforcement and concrete is stronger in geopolymer concrete compared to OPC. The corrosion of reinforcement reduces the strength of reinforcement and also reduces bond strength which results in increased deflections, reduced strength, and ultimate failures. From the experimental database, a statistical model is proposed for corroded reinforcement and alternatively, the existing analytical models can be used as a safe lower bound for geopolymer concrete with corrosion levels of up to 30% (Albitar et al., 2017).

Zhang et al., (2018) conducted experiments to determine the effect of temperature on the bond behaviour of geopolymer concrete in comparison with OPC concrete. Bond behaviour was analysed when geopolymer concrete was subjected to 100, 300, 500, and 700^{o}C. Results showed that for up to 300^{o}C, the reduction in bond strength was insignificant. Upon increase in temperature, it was decreased. Under ambient and elevated temperatures, the bond performance of GPC was better than that of OPC. From the experimental dataset, it was observed that the rate of degradation of bond stress was similar to splitting tensile strength and higher than compressive strength. In the design of RC structures, as fire resistance is the main requirement, geopolymer concrete can be a practical alternative to OPC concrete (Zhang et al., 2018).

Al-Azzawi et al., (2018) investigated the bond strength of GPC with different fly ash (300, 400, and 500 kg/cm^3) based geopolymer concrete (FBGC). A total of 45 mix proportions with different fly ash and alkaline activators were prepared. The particle size and chemical compounds such as SiO_2, Al_2O_3, and CaO greatly influence the bond strength of FBGC. The findings showed that the binding strength between the FBGC and steel reinforcement increases greatly as the fly ash percentage in FBGC increases. In this investigation, fly ash from four different sources was used. The bond strength between FBGC and steel reinforcement increased between 16 and 36 % as fly ash content increased from 300 to 500 kg/m^3. The increase in brittleness also boosted the bond strength. Additionally, as the amount of SiO_2 in the alkaline activator increased, so did the bond strength. However, it was reduced as the overall amount of Na_2O in NaOH and Na_2SiO_3 increased (Al-Azzawi et al., 2018).

The impact of corrosion on the bond behaviour of fibre-reinforced geopolymer concrete was studied by Farhan et al., (2018). Due to reinforcement corrosion, the bond strength of geopolymer concrete with steel fibre reinforcement decreased; however, this decrease was less pronounced in steel fibre-reinforced geopolymer concrete specimens than in plain geopolymer concrete specimens. Steel bars that had been distorted corroded more quickly through an electrochemical approach. The embedded steel bars in concrete served as the anode for the direct current, which was applied to them. The galvanized mesh was used to create the cathode, which was wrapped around the specimens submerged in the salt solution. According to the compressive strength results, the average compressive strength of the geopolymer concrete increased by 6.3 %, 3.6 %, and 14.8 %, respectively, with the addition of MIS (micro steel fibre), DES (deformed steel fibre), and HYS (hybrid steel fibre) fibre content from 0 to 2 % by volume. Additionally, the splitting strength was raised by 37.8 %, 43.28 %, and 64.88 %, for MIS, DES, and HYS respectively. The specimens' corrosion resistance and chemical resistance were both greatly improved by steel fibre-reinforced geopolymer concrete, which also increased bond stress. The bond strength was enhanced by 38.27 %, 32.86 %, and 65.98 %, respectively, by the addition of 2 % MIS, 2 % DES, and 2 % HYS fibres by volume. Additionally, the presence of fibres significantly enhanced slip at the maximum bond stress. The bond strength of fibre-reinforced geopolymer concrete with 2% MIS, 2% DES, and 2% HYS fibres by volume decreased by 54.92 %, 60.54 %, and 38.84 %, respectively, as a result of the accelerated corrosion process (Farhan et al., 2018).

Z. Ma et al., (2023) performed a beam test to study the bond performance of epoxy-coated reinforcement geopolymer concrete. Experimental analysis was carried out on 13 beam specimens to investigate the effect of compressive strength of concrete, bar diameter, embedment length, and type of bar on the bond strength of geopolymer concrete. The bond strength decreased by 7.32% and 14.76% from increasing the bar diameter from 14 mm to 16 mm and 16 mm to 20 mm, respectively. By increasing the bar diameter and concrete strength, the mode failure shifted from pullout to splitting failure. For the medium embedment length and lower bar diameters, the mode of failure was pullout failure after concrete splitting. Based on the experimental test data a constitutive model for bond stress-slip was proposed that approximated the experimental results. Also, the analytical model for the prediction of ultimate bond strength for geopolymer concrete reinforced with epoxy-coated reinforcement was proposed (Z. Ma et al., 2023).

The analytical models and codal provisions proposed in the literature for the determination of bond behaviour are given in Table 2.2

2.7 Numerical Modelling of Bond Behaviour of Concrete

An effective approach to describe the bonding behaviour between the bar and the surrounding concrete was presented by Jendele and Cervenka (2006). The author conducted four analyses: a beam collapsing due to shear failure, a reinforcing bar pull-out experiment, a test of the shear strength of pre-stressed hollow core slabs, and a determination of the serviceability of a pre-stressed concrete slab. ATENA-GiD, a finite element modelling programme, was used. It was determined that the model produced accurate values for bond interaction between the surrounding concrete and the reinforcement (Jendele & Cervenka, 2006).

Issa and Masri (2015) numerically simulated the bond behaviour between steel reinforcement and concrete. The finite element software ABAQUS was used to develop a 3-dimensional nonlinear finite element pullout model for underwater concrete circumstances. The experimental results of 32 pullout specimens were implanted in a numerical model to investigate the effect of concrete cover, use of stirrups, the influence of bar diameter, and compressive strength of concrete. The interaction properties help in achieving accurate results in comparison with experimental results. The numerical analysis provided better feasibility to understand the stress distribution in each component of the model and helped in understanding the significance of stirrups in preventing the stress from reaching the side of the specimen (Issa & Masri, 2015).

Table 2.2: Bond models proposed in the literature and codal provisions

Model	Equation	Units	Test specimen
(Al-Jahdali et al., 1994)	$\tau_{max} = \left[-0.879 + 0.324 \left(\frac{C_{min}}{D}\right) + 5.79 \left(\frac{D}{L}\right)\right] \sqrt{f_{cy}}$	S.I	Modified pull-out
(Chapman & Shah, 1987)	$\tau_{max} = \left(3.5 + 3.4 \left(\frac{C_{min}}{D}\right) + 57 \left(\frac{D}{L}\right)\right) \sqrt{f_{cy}}$	Psi	Modified pullout
(Rangan, 1998)	$\tau_{max} = 4.9 \left(\frac{\frac{C_{min}}{D} + 0.5}{\frac{C_{min}}{D} + 3.6}\right) f_{ct}$ (for $f_{cy} < 50Mpa$ $\tau_{max} = 8.6 \left(\frac{\frac{C_{min}}{D} + 0.5}{\frac{C_{min}}{D} + 5.5}\right) f_{ct}$ (for $f_{cy} > 50Mpa$ $f_{ct} = 0.55 \sqrt{f_{cy}}$	S.I	Beam Splice
(Harajli, 1994)	$\tau_{max} = 0.75 \sqrt{f_{cy}} \left(\left(\frac{C_{min}}{D}\right)^{2/3} \right)$ (for $f_{cy} < 48$MPa) $\tau_{max} = 0.95 \sqrt{f_{cy}} \left(\left(\frac{C_{min}}{D}\right)^{2/3} \right)$ (for $f_{cy} > 48$MPa)	S.I	Beam Splice
(Kemp, 1986)	$\tau_{max} = 232.2 + \left(2.716 \left(\frac{C_{min}}{D}\right) \sqrt{f_{cy}}\right)$	S.I	Cantilever Stub
(Orangun et al., 1977)	$\tau_{max} = \left[1.22 + 3.23 \left(\frac{C_{min}}{D}\right) + 53 \left(\frac{D}{L}\right)\right] \sqrt{f_{cy}}$	Psi	Beam Splice
(ACI 408R-03, 2003)	$\tau_{max} = \left(1.22 + 3.13 \left(\frac{C_{min}}{D}\right) + 4.4 \left(\frac{D}{L}\right)\right)$	SI	Beam Splice
(CEBFIP, 2012)	$\tau_{max} = 2.5 \sqrt{f_{ck,cy}}$ $(for\ pullout\ failure)$ $\tau_{max} = 7.0 \left(\frac{f_{ck,cy}}{20}\right)^{0.25}$ $(for\ splitting\ failure)$	S.I	-
(AS 3600-2009, 2009)	$\tau_{max} = 0.265 \sqrt{f_{cy}} \left\{ \left(\frac{C_{min}}{D}\right) + 0.5 \right\}$	S.I	
(Dahou et al., 2016)	$\tau_u = 2.5 \sqrt{R_c}$	S.I	Pull-out
(Hadi, 2008)	$\tau_{max} = \left(22.8 - 0.208 \left(\frac{C_{min}}{D}\right) - 38.212 \left(\frac{D}{L}\right)\right) 0.083045 \sqrt{f_{cy}}$	S.I	Pull-out

The bond interaction between GFRP bars and flyash-based geopolymer concrete was researched by Tekle et al., (2017). Both GPC and OPC specimens were evaluated in a pullout test to assess the bond property. The pullout test specimens had a diameter of 100 mm and a height of 100 mm. The embedment length, concrete grade and bar diameter were factors taken into consideration when analysing bond behaviour. The concrete grades used were 25 MPa and 45 MPa, GFRP bar diameters were 12.7 mm and 15.9 mm, and the embedment length employed was 3, 6, and 9 times the diameter of the bar. The manner of failure, whether splitting failure or pullout failure, was recorded for each specimen. Additionally, the slip at the loaded and free ends as well as the average bond stress were noted. The findings showed that the bond strength between GFRP bars and geopolymer concrete and GFRP bars and OPC concrete was equivalent. For GPC concrete and OPC concrete, the average bond strength was 15.8 MPa and 14.3 MPa respectively. Additionally, it was observed that the link between the bar and the concrete weakened with increasing embedment length. The decreased bond strength was attributed to an increase in nonlinear forces (Tekle et al., 2017).

Siempu and Kumar Pancharathi (2022) conducted a numerical study on the pullout bond behaviour of plain and ribbed bars in self-compacting concrete. The parameters considered were the grade of concrete (20 MPa, 40 MPa, 60 MPa), bar diameter (10 mm, 12 mm, and 16 mm), and bar type (plain and ribbed) to assess the bond performance of self-compacting concrete. The numerical models were validated with experimental results. Numerical analysis showed that the bond strength of ribbed bars is twice the bond strength of plain bars and bond strength increases with the grade of concrete (Siempu & Kumar Pancharathi, 2022).

Dao et al., (2022) investigated the bond performance of flyash-based geopolymer concrete numerically and experimentally. Three concrete grades, concrete cover to bar diameter ratio (4.56 to 5.75), and two bar diameters D12 ribbed bar and D14 smooth bar were considered to assess the bond performance. ABAQUS software was used to simulate the bond behaviour of flyash based geopolymer concrete. The parametric study conducted from the numerical analysis revealed that the bond strength increased with an increase in concrete strength. The numerical results were close to experimental results (Dao et al., 2022).

Le et al., (2022) conducted studies on the bond behaviour of reinforced flyash-based geopolymer concrete numerically, experimentally and analytically. The experimental work was carried out on three grades of concrete (20, 30, and 40 MPa) and three bar diameters (12, 16, and 20 mm). The bond strength increased by 2.56 times with an increase in the grade of concrete

from 20.33 MPa to 41.2 MPa. It was mentioned that for concrete strength of 30 MPa and 40 MPa, with an increase in the ratio of cover-to-bar diameter, the bond strength increased whereas, for 20 MPa concrete, the bond strength decreased with an increase in cover-to-bar diameter ratio from 4.19 to 5.75. The bond stress-slip relation between the reinforcement and geopolymer concrete from the numerical simulation was in good correlation with experimental analysis with a coefficient of variation of 0.01. The experimental results were quite different from the analytical results from the fib model (Le et al., 2022).

2.8 Durability Performance of Geopolymer Concrete

Bakharev et al., (2004) investigated the performance of geopolymer concrete under sulfate attack. The geopolymer concrete made of flyash as binder and sodium hybrid solution as alkaline activator was subjected to sodium and magnesium sulfate attack at 5% concentration for a duration of 5 months. A few specimens were also subjected to a combined sodium and magnesium sulfate solution at 5% concentration. The geometrical changes with respect to dimensions and weight were tracked for exposure duration. When compared to magnesium sulfate solution, sodium sulfate solution caused more deterioration since the migration of alkalis into the solution has a more pronounced effect on concrete. The least strength changes were observed in case of a combined attack of sodium and magnesium sulfate. From the experimental analysis of all designed mixes, it was concluded that the sodium-hydroxide-based geopolymer concrete provided superior performance compared to other activators which is attributed to its stable cross-linked aluminosilicate polymer structures (Bakharev, 2005).

Vafaei et al., (2017) studied the durability of waste glass powder (WGP) and calcium aluminate cement (CAC) based geopolymer mortar subjected to acid solutions. The sodium-based hybrid alkaline activator was employed and cured under hydrothermal conditions. The experimental specimens were subjected to hydrochloric and sulfuric acids maintained at pH 1 for 6 months. After deterioration, the durability parameters such as residual compressive strength, and depth of deterioration were examined. The microstructure characteristics were analysed through x-ray diffraction, Fourier transformation infrared radiation spectroscopy, and scanning electron microscopy. The durability parameters showed that the deterioration in geopolymer concrete was lower than in the control specimen (WGP and CAC mortar samples). Gypsum rod-like structures were observed in SEM analysis and confirmed from XRD analysis. The rate of deterioration was higher in H_2SO_4 (pH 1) compared to HCl (pH 1) since the calcium compounds present in the mortar sample react with sulfates and form gypsum compounds. The

internal growth of gypsum crystal caused internal stresses that led to the cracking, and spalling of concrete (Vafaei & Allahverdi, 2017).

Mehtha and Siddique (2017) investigated the influence of sulfuric acid on flyash based geopolymer concrete blended with OPC. To investigate the long-term effect of H_2SO_4, GPC was exposed for 365 days at a 2% concentration of H_2SO_4. The durability behaviour was investigated based on mass and compressive strength loss, also the microstructural changes through SEM, XRD, and EDS. The addition of OPC improved the strength properties since it increases the calcium content addition to NASH gel. On the other hand, after exposure to a chemical attack, the OPC of 30% in GPC showed higher deterioration compared to flyash-based GPC due to the formation of additional calcium sulfate, which increased with an increase in calcareous compounds in the mixture. The microstructure characteristics also confirmed the presence of sulfur compounds, which were the main cause of deterioration (Mehta & Siddique, 2017).

Adak and Mandal (2019) modified the synthesis process of geopolymer concrete and determined its durability and strength characteristics. The alkaline activator was mixed with flyash and the mixture was heated for 45 min at 60^{o}C. The heated mixture was mixed with fine and coarse aggregate and filled in moulds. The specimens were cured at ambient temperature until testing. The process-modified geopolymer concrete showed enhanced mechanical and durability properties than conventional heat-cured geopolymer concrete. Also, the microstructure characteristics were analysed and it was observed that process-modified geopolymer concrete showed enhanced interaction between the flyash and alkaline activator at early ages resulting in phase changes from amorphous to crystalline (Adak & Mandal, 2019).

Cevik et al., (2018) studied the influence of nano-silica on the durability and mechanical performance of flyash-based geopolymer concrete. Two different sources of flyash were considered for the mix design of concrete with and without nano-silica. A hybrid sodium-based alkaline activator was employed for alkaline activation. GPC and OPC concrete were subjected to H_2SO_4, $MgSO_4$ with a concentration of 5%, and NaCl with a concentration of 3.5%. The durability was assessed based on visual appearance, weight changes of concrete and strength loss with respect to compressive, splitting, and flexural strength changes before and after chemical exposure. From the experimental analysis, it was observed that GPC showed superior performance than OPC concrete due to low calcium content. H_2SO_4 showed higher deterioration compared to $MgSO_4$ and NaCl. The almost initial condition was maintained by

GPC after exposure to $MgSO_4$ and NaCl. The addition of nano-silica significantly improved the mechanical and durability performance of flyash-based GPC due to decreased porosity and more dense microstructure. The performance characteristics decreased after exposure to chemicals in the order of H_2SO_4 > $MgSO_4$ > NaCl (Çevik et al., 2018).

Jena et al., (2019) investigated the influence of silica fume on the mechanical and durability properties of flyash geopolymer concrete. NaOH with 14 M and Na_2SiO_3 solution were used as alkaline activators. Silica fume was varied with mass fractions of 5%, 10%, and 15%. The durability performance under chemical exposure to sulfuric acid and magnesium sulfate with a concentration of 2% and sodium chloride with a 5% concentration was measured. With the addition of silica fume, a maximum compressive strength of 42.6 MPa was achieved. The addition of silica fume in flyash-based GPC significantly improved the resistance to chemical attack. The addition of 5% silica fume resulted in 81.67%, 59%, and 65% higher than the control mix which was subjected to acid, sulfate, and chloride attacks respectively (Jena et al., 2019).

Bellum et al., (2022) investigated the effect of slag on the strength and durability properties of flyash GPC. The rapid chloride penetration test and accelerated corrosion test were performed to understand its durability performance. The addition of slag significantly decreased the pore structure. The chloride ion permeability decreased with an increase in slag content and results showed that the highest permeability was observed in a 100% flyash mixture. Accelerated corrosion tests also showed that the addition of slag enhanced resistance against corrosion attack. It was mentioned that GPC produced with a combination of FA and GGBS enhances mechanical and durability performance (Bellum et al., 2020).

Ganeshan and Venkataraman (2021) evaluated the durability performance of self-compacting flyash based geopolymer concrete. To eliminate the constraint of heat curing for class F flyash geopolymer concrete, class C flyash was added. Durability performance was assessed by using parameters like acid resistance, sulfate resistance, water absorption, sorptivity, rapid chloride penetration test, and accelerated corrosion tests were performed. From the experimental results, it was observed that the inclusion of class C flyash did not show any significant detrimental effect on adverse environmental conditions. Sorptivity and water absorption tests proved that there was lower water ingression for class C flyash concrete when compared with control class F flyash. Flash setting properties of class C flyash provide efficient polymerization resulting in minimum chloride permeability. The accelerated corrosion test

provided results in line with the chloride penetration test. SEM analysis results recommended a blend of class C flyash with class F flyash to provide enhanced mechanical and durability performance at ambient curing conditions (Ganeshan & Venkataraman, 2021).

2.9 Summary

In the present chapter, a review of literature on the parameters affecting geopolymer concrete, particle packing model, bond behaviour of geopolymer concrete, numerical modelling of bond behaviour of concrete, and durability performance of GPC is dealt with. It can be seen that the ratio of binder to alkaline activator ratio, a combination and concentration of the activator, curing condition, and aluminosilicate source play a vital role in improving the performance of geopolymer concrete. Furthermore, the mix design procedure for geopolymer concrete is also discussed. The various factors affecting bond strength in geopolymer were addressed to a certain extent. Also, the constitutive parameters required for the numerical modelling of bond behaviour using the finite element method were discussed. The influence of different alumino-silicate sources on the durability performance of GPC was discussed. However, the field of bond strength in geopolymer concrete has not been discussed in previous research on geopolymer concrete in detail. The influence of multi-component systems on the chemical resistance of GPC was not explored. Thus, further investigation in these fields is needed.

2.10 Gaps in the Literature

Research on parameters affecting geopolymer concrete such as the ratio of binder to the alkaline activator, combination and concentration of the activator, curing condition, and aluminosilicate source has been done in sufficient numbers. There are very few studies on the bond behaviour of geopolymer concrete. The studies on the bond behaviour of flyash-based geopolymer concrete exhibited a higher bond strength compared to OPC which led the researchers to investigate its performance in detail and propose identical models for assessing the bond strength of GPC. There is limited work on the bond behaviour of high-strength geopolymer concrete made with fly ash, GGBS, silica fume, OPC and alccofine combined as an aluminosilicate source which is significant since the addition of different aluminosilicates influence microstructure properties and thereby strength properties of GPC. It is understood that in case of high-strength concrete, failure takes place through the aggregate phase which may differ from the crack propagation behaviour in the geopolymer matrix due to the bond forces. So, this is considered as a potential area of investigation. Also, few studies are available

on the flexural bond behaviour which has a load distribution similar to real-time application. Furthermore, the literature on numerical modelling of bond behaviour between reinforcing bars and geopolymer concrete is very scarce which is required for the production of data set by varying dependent parameters. The behaviour of GPC under chemical attack is also limited and is significant for understanding its behaviour under adverse environmental conditions.

CHAPTER 3
DEVELOPMENT OF HIGH-STRENGTH GEOPOLYMER CONCRETE

3.1 General

The importance of high-strength geopolymer concrete cured at ambient temperature was discussed and certain objectives were laid down in Chapter 1. An experimental program (Phase -1) designated to develop high-strength geopolymer concrete for attaining strength under ambient curing condition is presented in this chapter. The major factors that can contribute to high-strength concrete are the packing density of the mixture, the volume of reactive binder materials, and the volume of aggregate proportions. The performance of concrete is greatly affected by the type and degree of packing of its constituents. Thus, knowledge of particle packing and its influence on concrete performance is required. In the current chapter, a basic overview of packing density and various models used to optimize the packing density for the mix proportion have been presented. Furthermore, two-particle packing models namely, the Modified Toufar Model (MTM) and J D Dewar Model (JDD) have been discussed in detail and made use of proportioning of aggregates in the geopolymer concrete. Based on the literature, the weight percentage of multi-component binder has been considered and trial mixes are performed to ensure high compressive strength at ambient temperature. The hardened properties like compressive strength, splitting tensile strength, modulus of elasticity and flexural strength are determined and suitable analytical models were proposed for the hardened properties of HSGPC. The constitutive behaviour is analysed and an analytical model is proposed to predict the stress-strain behaviour. The proposed analytical models are compared with the existing analytical equations and codal provisions. The causes for improvement in the strength of high-strength mixes are determined by performing the microstructure characteristic techniques such as SEM, XRD, FT-IR, EDS and BSE.

3.2 Raw Materials

Different materials are used in geopolymer concrete making in the present work and these include flyash, GGBS, silica fume, alccofine 1203, cement, fine aggregate, coarse aggregate,

sodium hydroxide, sodium silicate and superplasticizer. The details of these materials such as chemical compositions, and physical and mechanical properties are discussed in the subsequent sections.

3.2.1 Flyash

Flyash was procured from a local thermal power station. The specific gravity of fly ash is found to be 2.10. The chemical characteristics of flyash from the XRF analysis are given in Table 3.1. Figure 3.1 shows the SEM analysis along with the XRD of flyash**.** This indicates the crystalline phases of quartz, mullite, and mellite. The flyash particles are spherical and the presence of cenospheres are evident. The flyash conformed to Class F, according to ASTM C618-03 (ASTM C618-03, 2003)

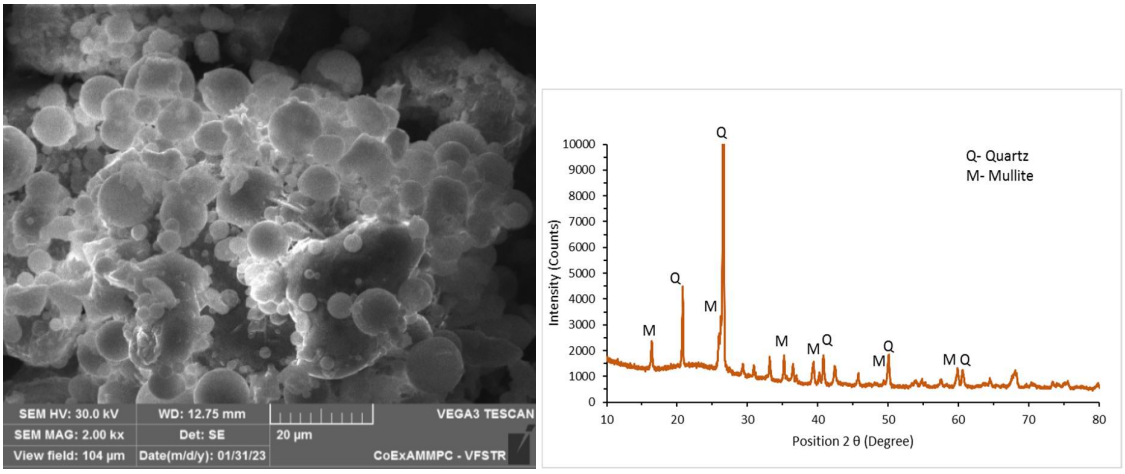

Figure 3.1: SEM and XRD of flyash

3.2.2 GGBS

The source of Ground Granulated Blast Furnace Slag (GGBS) is steel industries. The specific gravity is found to be 2.85, and it is conformed to IS-12089-1987 (IS:12089, 1987). Figure 3.2 shows the SEM and XRD analysis of GGBS. This is representative of the amorphous nature of the material. The chemical characteristics of GGBS from XRF analysis are given in Table 3.1.

3.2.3 Silica fume

Silica fume is a micro-fine material having an average particle size of 157 nm - 349.2 nm acquired from ferrosilicon alloy plants. The specific gravity is found to be 2.25. The chemical composition examined from XRF analysis is given in Table 3.1 and conformed to IS: 15388 (IS:15388, 2003). SEM image and XRD analysis of silica fume are shown in Figure 3.3. The

XRD analysis is representative of lower crystalline phases showing the presence of reactive silica.

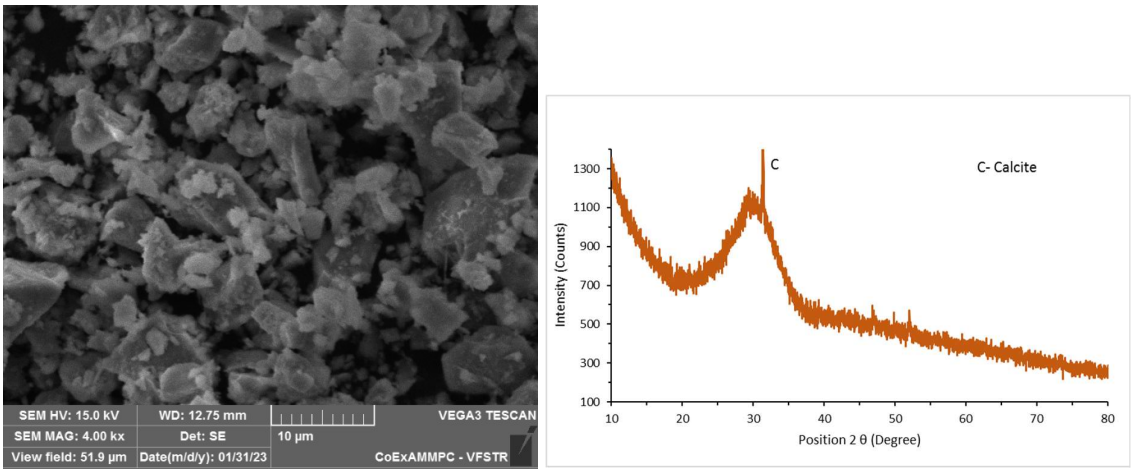

Figure 3.2: SEM and XRD of GGBS

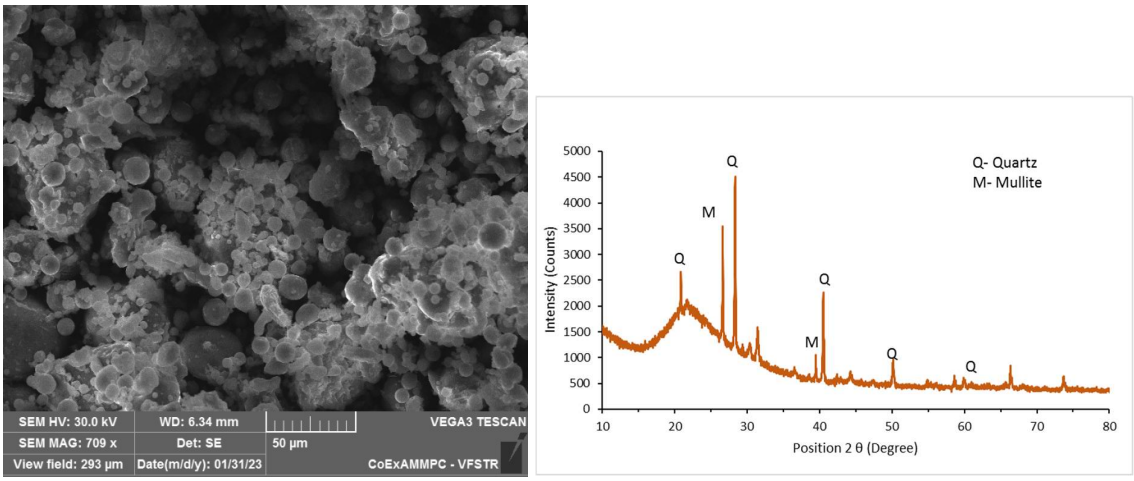

Figure 3.3: SEM and XRD of silica fume

3.2.4 Alccofine

Alccofine is a micro-fine material having a particle range of 0.1 to 17 microns and an average particle size of 4 microns. The specific gravity is found to be 2.84. The chemical composition examined from XRF analysis is given in Table 3.1 and it is indicative of the presence of calcium and silicate compounds. XRD analysis and SEM image are shown in Figure 3.4. XRD analysis shows the amorphous nature of the material with fewer peaks with calcite. Alccofine is used in the present work for achieving early-age strength and to improve GPC properties.

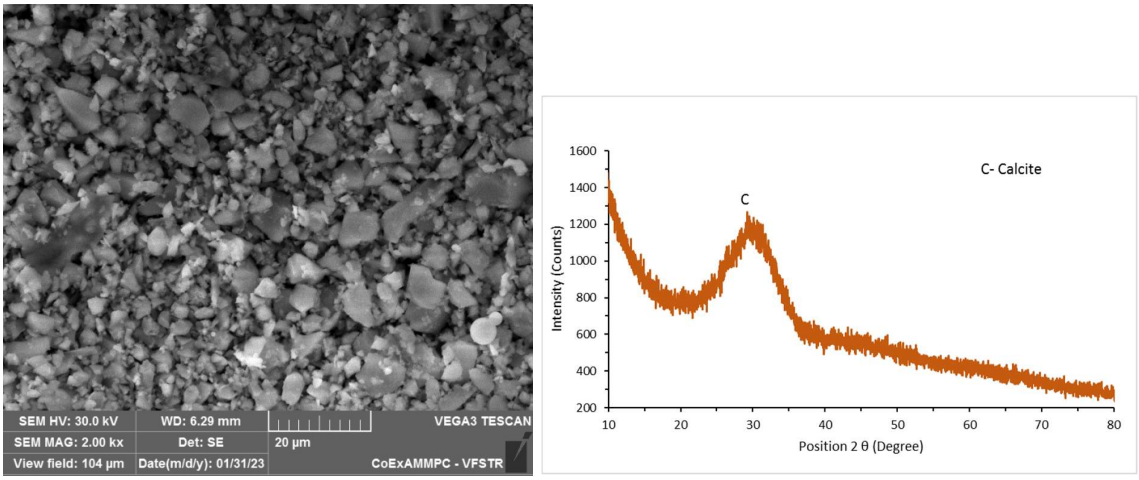

Figure 3.4: SEM and XRD of alccofine

3.2.5 Cement

Ordinary Portland Cement (OPC) conforms to IS: 12269-2013 (IS: 12269, 2013). The chemical composition of XRF is presented in Table 3.1. XRD analysis and SEM images are shown in Figure 3.5. The specific gravity is found to be 3.1

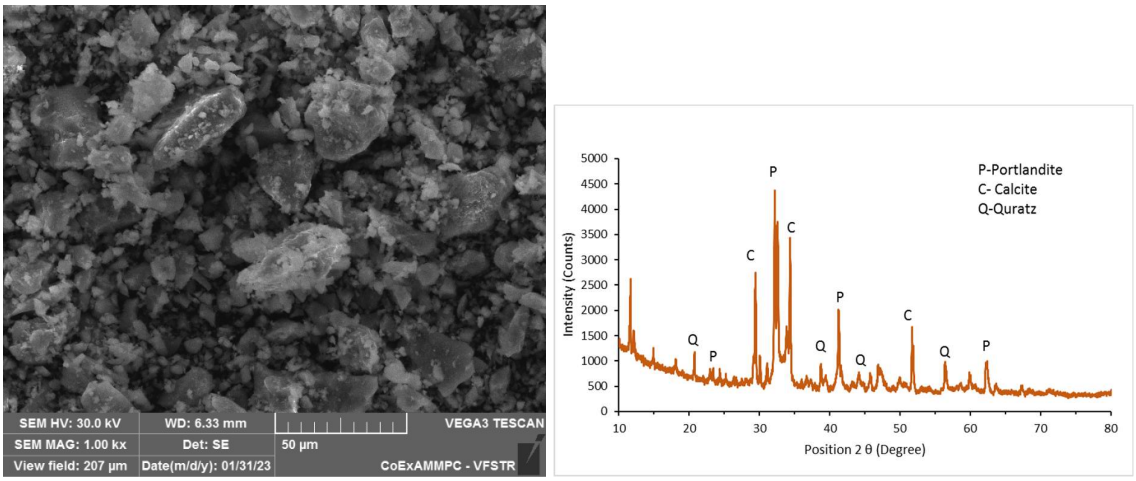

Figure 3.5: SEM and XRD of OPC

3.2.6 Fine and coarse aggregate

The fine aggregate confirmed to zone II in accordance with IS 383-2016 (IS:383, 2016) was used in the present work. The particle size distribution for coarse and fine aggregates is presented in Figure 3.6, while Table 3.2 shows the physical properties. Crushed granite is used as coarse aggregate in accordance with the graded aggregate of IS 383-2016 (IS:383, 2016).

Table 3.1: Chemical composition of source material

Material	SiO_2 (%)	Al_2O_3 (%)	Fe_2O_3 (%)	CaO (%)	MgO (%)	SO_3 (%)	Na_2O (%)	K_2O (%)	L.O.I (%)	Specific surface area (m^2/kg)
Flyash	63.46	24.34	4.55	4.86	1.17	0.25	0.13	0.003	1.96	322.3
GGBS	34.02	14.28	0.51	39.6	9.0	0.34	0.7	0.8	0.26	410.27
Silica fume	90.25	5.98	2.10	-	-	0.21	0.51	-		20000
Alccofine	36.31	22.42	1.21	32.21	6.17	0.11	0.032	0.68	0.85	1200
OPC	21.02	3.43	4.32	64.57	1.80	3.42	-	0.754	1.42	300

Table 3.2: Physical properties of coarse and fine aggregates

Aggregate	Water absorption (%)	Fineness modulus	Porosity	Specific gravity	Void ratio	Bulk density (kg/m^3)
Fine aggregate (FA)	0.72	2.68	0.47	2.67	0.68	1617
Coarse aggregate (CA)	0.64	6.24	0.58	2.74	0.82	1457

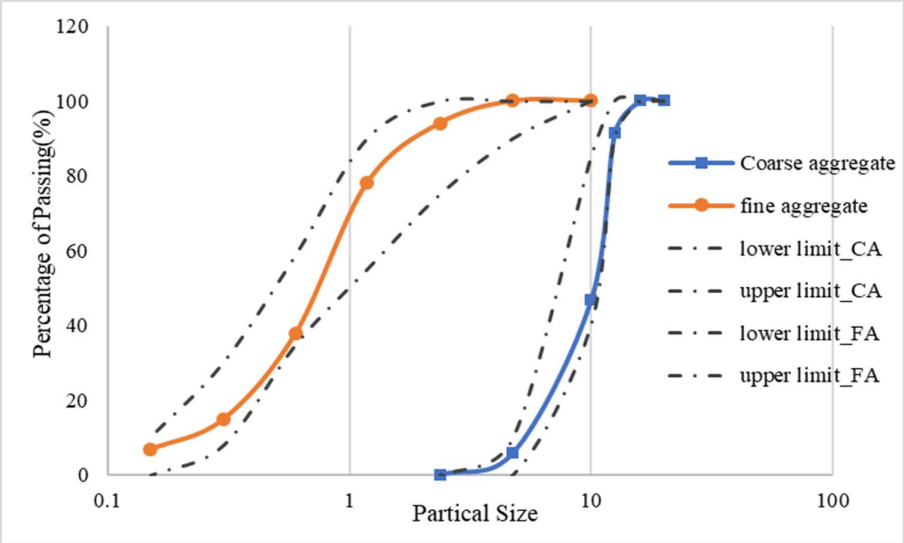

Figure 3.6: Particle size distribution for fine and coarse aggregate

3.2.7 Alkaline activator

Sodium silicate or water glass (Na_2SiO_3) and sodium hydroxide (NaOH) alkaline activators are used for polymerization. The molarity of NaOH is 14 M / 16 M and the ratio of Na_2SiO_3 to NaOH was taken as 2.5. The molar index (SiO_2/Na_2O) for Na_2SiO_3 is 2.19 with a specific gravity of 1.55 and pH is 11. Based on preliminary studies, the alkaline activator to binder ratio (AA/Bi) is kept constant at 0.38. For the synthesis of GPC, NaOH is prepared 24 hours before

the casting and allowed to cool at room temperature. Na_2SiO_3 is mixed with NaOH before 2-3 hours of casting, and allowed to cool at room temperature.

3.2.8 Superplasticizer

Sodium silicate is a glass material which has higher viscosity than water so GPC is more sticky and cohesive. To improve its workability, sulfonated naphthalene formaldehyde (SNF)-based water-reducing admixture conplast SP430 was used and it is conformed with IS 9103-1999 (IS 9103, 1999) and BS: 5075 Part 1.

3.2.9 Water

Potable water was used as additional water for GPC mixes.

3.3 Particle Packing

Particle packing describes how dense particles are packed into a given volume. The most common unit of measurement is packing density (Φ), which is defined as the proportion of the solid volume of the particles (V_p) to the bulk volume that the particles occupy (V_b). The packing density is given by:

$$\Phi = \frac{V_p}{V_b} \quad \text{Eq 3.1}$$

Void ratio (e) is defined as the ratio of the volume of voids (V_v) to the solid volume of particles (Vp). Thus,

$$e = \frac{V_v}{V_p} \quad \text{Eq 3.2}$$

From Eq 3.1 and Eq 3.2, it can be deduced that

$$\Phi = \frac{1}{1+e} \quad \text{Eq 3.3}$$

3.3.1 Concept of particle packing theory

The particle packing model works on the principle that the voids created by larger particles in the mixture are filled by relatively smaller particles in the group thus reducing the overall void ratio. Depending upon the type of blend i.e., binary or ternary or some other proportion, the amount of filler group which fills the voids of the larger group in the mixture was determined and the process continued. Thus, varying the proportion of different sizes of particles converged to an optimum proportion, which is compact and highly dense. The concept of particle packing has been illustrated in Figure 3.7

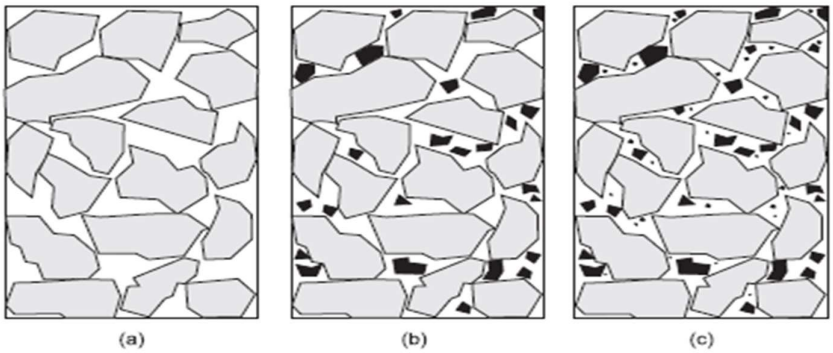

Figure 3.7: Concept of particle packing

3.3.2 Classification of particle packing models

Based on the continuity of different sizes of aggregate assumed in the model, the particle packing model has been classified into two types. They are:

3.3.3 Discrete models

In this model, the sizes of aggregate present in the mixture are discrete i.e., all the sizes of aggregates in a particular range of aggregates were not present. The largest size of aggregate makes the core while the voids of these particles were filled by smaller particles and the process went on. It is assumed in this approach that all the sizes of aggregates pack to their maximum density in the available volume. Discrete models are further classified into three types, namely, binary, ternary and multimodal, based on the particle size participating in the distribution.

3.3.4 Continuous models

In this approach, it is assumed that there is no gap between the sizes of aggregate in the overall range of aggregates. There are no gaps between size classes and all potential sizes are present in the particle distribution system, which uses a discrete method with neighbouring size class ratios that are close to 1:1. This model is more suitable for concrete mix design as it incorporates more and varying sizes of aggregates which give more freedom to fill the voids. The categorization of the particle packing model has been presented in Figure 3.8.

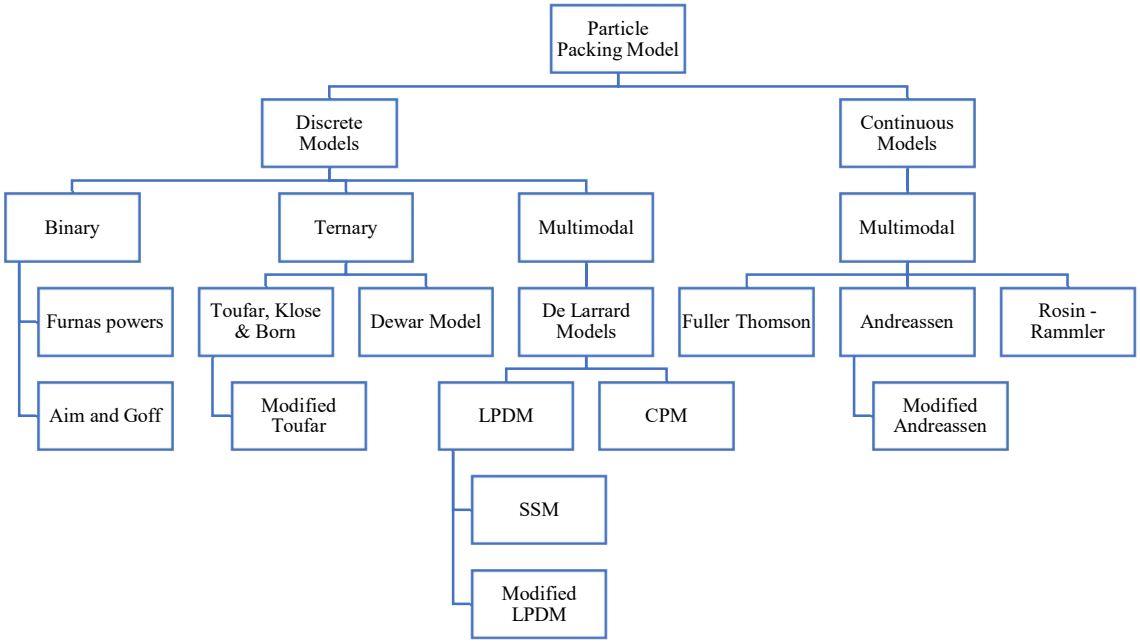

Figure 3.8: Classification of particle packing models

3.3.5 Modified Toufar Model (MTM)

In MTM, the packing densities of particle combinations are determined by using the packing density and characteristic diameter of each material, d_{char}. The model is initially used to determine d_{char}, and a combination of the two materials for multi-particle computations. In order to integrate the first combination with subsequent constituent material, this model is used. This process is repeated until all constituent materials have been incorporated, at which point the total packing density of the mix is computed. The formulation of the individual packing density of the material and subsequently the formulation of the packing density of the mixture based on research of Fennis (2011) (Fennis, 2011) has been discussed in the following section.

3.3.5.1 Calculation of particle density for mono-dispersed sized particles

For the overall estimation of the packing density of the mixture, it is important to calculate the packing density of individual materials involved in the mixture. The packing density (Φ) for mono-dispersed sized particles is given in Eq 3.4:

$$\Phi = \frac{\rho_i}{\gamma_i \times \rho_w} \qquad \text{Eq 3.4}$$

Where,

Φ = Packing density of specified individual material

ρ_i = Bulk density of specified individual material

γ_i = Relative density of an individual material

ρ_w = Density of water

3.3.5.2 Calculation of combined packing density

After the computation of individual packing density and characteristic diameter of each material, the following set of empirical equations i.e., Eq 3.5 – Eq 3.10 were used to maximize the packing density of the binary mixture (Fennis, 2011).

$$\Phi_{binary} = \frac{1}{\left\{\left(\frac{Y_1}{\Phi_1}\right) + \left(\frac{Y_2}{\Phi_2}\right) - Y_2\left(\frac{1}{\Phi_2} - 1\right) \times K_d \times K_s\right\}} \quad \text{Eq 3.5}$$

Where,

$$K_d = \frac{d_2 - d_1}{d_1 + d_2} \quad \text{Eq 3.6}$$

$$K_s = \frac{x}{x_0} \times k_o \quad \text{Eq 3.7}$$

$$= 1 - \frac{(1+x)}{(1+x)^4} \quad \text{for } x > x_0 \quad \text{Eq 3.8}$$

Here, $x_o = 0.4753$ $k_0 = 0.3881$ Eq 3.9

And $x = \frac{\left(\frac{Y_1}{Y_2}\right) \times \left(\frac{\Phi_1}{\Phi_2}\right)}{(1 - \Phi_2)}$ Eq 3.10

d_{char} = Characteristic diameter = $\sqrt{d_i \times d_j}$

d_i = Smallest size in the individual range of particle

d_j = Largest size in the individual range of particle

d_1, d_2 = Characteristic diameter of fine and coarse sizes of the binary mixture

Y_1, Y_2 = Volume fractions of fine and coarse sizes of the binary mixture

Φ_1, Φ_2 = Packing density of fine and coarse size of the binary mixture

K_d = Diameter ratio factor

K_s = Statistical factor

The packing density for the ternary blend is obtained similarly to binary blending. The binary packing density of the two subsequent largest particles in the mixture is evaluated using the above formulas, the results of which are used as the packing density of the next coarser material

while the next particle size is considered as finer size in the binary combination. This process is repeated until all the particle sizes are covered and the final resulting packing density is the optimum packing density.

3.3.5.3 Observations and results from MTM

MTM was used to design binary and ternary blend volumes of aggregates. The size range of aggregates used in the design are (12.5-10) mm, (10-4.75) mm and (4.75-0.15) mm. The packing densities for the respective mono-sized range of aggregates are calculated using equation 3.4, which is shown in Table 3.3.

Table 3.3: Packing density of mono-sized aggregates

Aggregate Size (mm)	12.5-10	10-4.75	4.75-.15
Characteristic Diameter (d_{char})	11.18	6.89	0.84
Bulk Density (Kg/m^3)	1426	1384	1578
Specific Gravity	2.7	2.7	2.65
Packing Density (Φ)	0.528	0.513	0.595

3.3.5.4 Binary blending of aggregates

For the binary blend of aggregates, excel sheets were made considering equations 3.5-3.9. The Excel sheets are presented in APPENDIX-I. The binary combination of aggregates using MTM shows that the optimum aggregate proportion is CA-55 & FA- 45 for the combination (12.5 – 10) mm & (4.75-0.15) mm with a maximum packing density of 0.69 while it is CA-50 & FA-50 for the combination (10-4.75) mm & (4.75-0.15) mm with a maximum packing density of 0.67. The volume fraction and packing degree for binary blending of aggregate are shown in Table 3.4. Also, a graph between the void ratio and the percentage of smaller particles is presented in Figure 3.9 and 3.10.

Table 3.4: Volume fraction and packing degree for binary blending of aggregate by MTM

S.N	Sieve Size Combination	Volume Fraction		Packing Degree (Φ_{max})
		Y1	Y2	
1	12.5-10 mm & 4.75-0.15 mm	55	45	0.69
2	10-4.75 mm & 4.75-0.15 mm	50	50	0.67

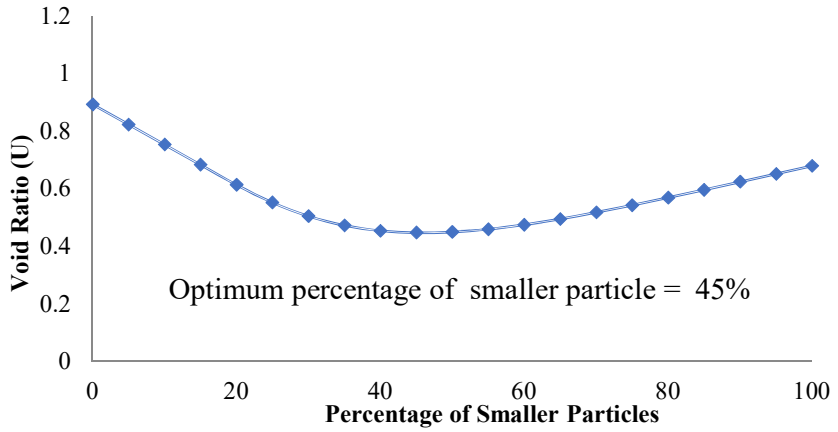

Figure 3.9: Binary combination of (12.5 – 10) mm & (4.75-0.15) mm

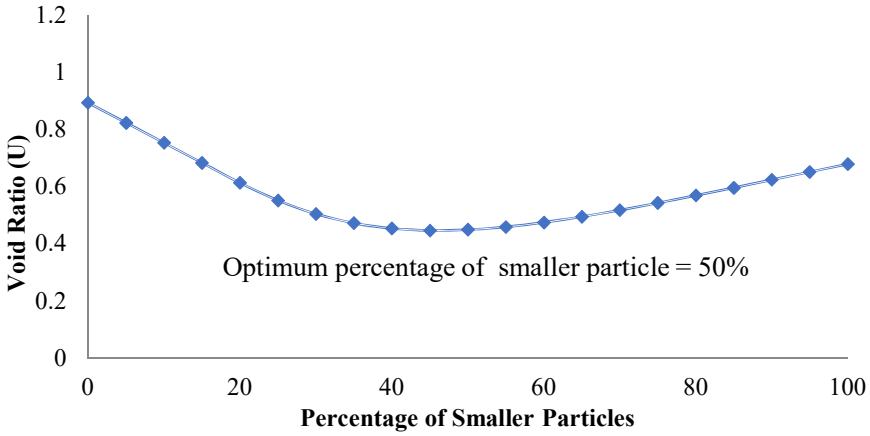

Figure 3.10: Binary combination of (10-4.75) mm & (4.75-0.15) mm

3.3.5.5 Polydispersed packing density

For the polydispersed packing density, the number of trials of binary packing density using equation 3.5-3.10 was performed in a sequential manner with coarser particles participating in the first trials. Excel sheets for performing the trials are presented in Appendix I. It has been observed from the trials that the optimum aggregate content for the mixing of CA & FA was in the ratio of 55:45 respectively with a maximum packing density of 0.712. The optimized aggregate content for polydispersed mixes of 12.5 mm nominal size using MTM has been presented in Table 3.5.

Table 3.5: Optimization of polydispersed mixes of 12.5 mm nominal size using MTM

Trial	Group 1 (mm)	Proportion	Group 2 (mm)	Proportion	Φ
Coarse Aggregate					
1	12.5 - 10	0.65	10 - 4.75	0.35	0.552
Fine Aggregate					
2	4.75 - 2.36	0.6	2.36 - 0.15	0.4	0.636
Coarse Aggregate & Fine Aggregate					
3	12.5 - 4.75	0.55	4.7 - 0.15	0.45	0.712
Size	CA/FA	12.5 - 10	10 - 4.75	4.75 - 2.36	2.36 - 0.15
12.5 mm	55/45	0.3575	0.1925	0.27	0.18

3.3.6 J D Dewar Model (JDD)

This model takes an approach to minimize the void ratio of a blend of aggregates. It gives a good approximation of the packing degree for binary and ternary aggregate combinations. The relation to the link between the void ratio and the packing degree is given by equation (3.11). The procedure to calculate a blend of aggregates giving maximum packing density or the least void ratio is as follows:

1) Calculation of log mean diameter (d_m) and void ratio for each size class of aggregates. For this, equations 3.11 and 3.12 were used:

$$log(d_i) = \frac{log(d_{upper}) + log(d_{lower})}{2} \quad \text{Eq 3.11}$$

$$U_i = \frac{\gamma_i \times \rho_w}{\rho_i} - 1 \quad \text{Eq 3.12}$$

Where,

d_i = log mean particle size between two sieve sizes

d_{upper} = diameter of the largest particle in the group

d_{lower} = diameter of the smallest particle in the group

U_i = void ratio of i^{th} group

ρ_i = bulk density of i^{th} group

γi = relative density of i^{th} group

ρ_w = density of water

2) Once the void ratios and log mean diameters for each aggregate group are calculated, the void ratio of a binary blended combination is minimized using the theory of particle

mixtures. The theoretical prediction of the combined void ratio is done as per equations 3.13-3.17:

$$U_n = nU_0^{"} \quad \text{Eq 3.13}$$

$$n = \frac{U_0^{"}}{1+U_0^{"}+U_1^{"}} \quad \text{Eq 3.14}$$

$$U_0^{"} = (1+U_0)(1+mr)^3 - 1 \quad \text{Eq 3.15}$$

$$U_1^{"} = \frac{(1+U_1)U_0^{"}}{(1+U_0^{"})-(1+Z)^3} \quad \text{Eq 3.16}$$

$$Z = k_{int} + [(1+U)^{1/3} - 1 - K_{int}]r^{K_p} \quad \text{Eq 3.17}$$

Where,

U_n = Void ratio of combined gradation

n = fine material volume fraction

$U_0^{"}$, $U_1^{"}$ = effective void ratio of coarse and fine aggregate particles respectively after blending

m = spacing factor; (Table 3.6)

r = ratio of log-mean diameter of fine aggregate to coarse aggregate

Z = notional width factor

K_{int}, K_p = empirical factors; (Table 3.6)

Table 3.6: Empirical factors

Points on void ratio diagram	Spacing factor (m)	Empirical factor (K_{int})	Empirical factor (K_p)
A	0	-	-
B	0.3	0.12	0.6
C	0.75	0.06	0.65
D	3	0.015	0.8
E	7.5	0.0	0.9
F	∞	-	-

The complete procedure for mixing the full range of coarse aggregates with fine aggregates was carried out as per the following steps with the results shown in Table 3.7 and 3.8, and the calculations are shown in Appendix I**.**

1) In the first step, the finer groups of coarse aggregate 10 mm-4.75 mm and 12.5 mm-10 mm are blended using binary combinations and void ratios are calculated for various

aggregate proportions. For the void ratios calculated, the packing degree is determined and the maximum packing degree gives optimized aggregate proportions.

2) This step explains the ternary blending of 10 mm-4.75 mm, 12.5 mm-10 mm and 16 mm-12.5 mm (if available, dependent on the size class considered). The maximum packing degree was obtained along with optimized aggregate proportions from different aggregate groups.
3) The blending procedure is continued for fine aggregates, where the finer groups of fine aggregate were considered initially for binary blending. The minimum void ratio and optimized aggregate proportions were calculated for aggregate groups '0.36 mm - 0.15 mm' and '4.75 mm-0.36 mm'.
4) From the maximum packing densities of obtained groups '12.5-4.75 mm' and '4.75-0.15 mm', the binary blending procedure was repeated to obtain the optimized proportions for coarse and fine aggregates, which is shown in Table 3.8. Excel sheets for performing the trials are presented in Appendix I.

Table 3.7: Mono-sized natural aggregates characteristics

Aggregate Size	12.5-10	10-4.75	4.75-0.15	4.75-2.36	2.36-0.15
d_{char} (mm)	11.180	6.890	0.840	3.348	0.595
Bulk Density	1349	1300	1578	1377	1418
Sp. Gravity	2.700	2.700	2.650	2.650	2.650
Φ	0.500	0.481	0.595	0.520	0.535

Table 3.8: Optimized aggregate proportions from the JDD model

Step	Group 1	Proportion	Group 2	Proportion	Φ
Coarse Aggregate					
1	12.5-10	0.55	10-4.75	0.45	0.515
Fine Aggregate					
2	4.75-2.36	0.55	2.36-0.15	0.45	0.623
Coarse Aggregate & Fine Aggregate					
3	12.5-4.75	0.57	4.7-0.15	0.43	0.688
Size	CA/FA	12.5-10	10-4.75	4.75-2.36	2.36-0.15
Proportion	57/43	0.314	0.257	0.237	0.194

3.4 Mix Design Procedure

Based on the guidelines by Ambily et al. (2013) and the results of the particle packing model (MTM), mix proportions for trial mixes are prepared. 13 trial mixes were prepared with the notation D1 to D13 with varying percentages of flyash, GGBS and silica fume. D1 to D4

consisted of a total aggregate volume of 70% while trial mixes D5 to D13 consisted of a total aggregate volume of 65%. The general steps followed for the mix design procedure have been presented below.

Step 1: Consider the wet density of geopolymer concrete to be 2400 kg/m^3

Step 2: Mass of combined aggregate = 70% of the mass of concrete

= (70x2400/100) = 1680 kg/m^3

Step 3: Mass of Binders and the alkaline liquid = 2400-1680 = 720 kg/m^3

Step 4: Alkaline liquid to Binders ratio by mass = 0.38

Step 5: Mass of fly ash + GGBS + silica fume = 720/ (1+0.38) = 521.74 kg/ m^3

Mass of GGBS = 43% of Binder = (43x521.74/100) = 224.35 kg/ m^3

Mass of fly ash = 33% of Binder = (33x521.74/100) = 172.18 kg/ m^3

Mass of silica fume = 24% of Binder = (24x521.74/100) = 125.28 kg/ m^3

Step 6: Mass of alkaline liquid = 720 – 521.74 = 198.26 kg/ m^3

Step 7: Ratio of sodium silicate to sodium hydroxide solution = 2.5

Step 8: Mass of sodium hydroxide solution = 198.26/ (1+2.5) = 56.65 kg/ m^3

For 1 molar sodium hydroxide solution, 40 g of sodium hydroxide pellets are dissolved in 1 litre of water.

i.e., for 1 molar: 40 g pellets → 1000 g or 1000 ml of water.

For 14 molar: 14 x 40 g of pellets → 1000 g or 1000 ml of water.

Total sodium hydroxide solution= (14 X 40+1000) =1560 g

% of sodium hydroxide solids in NaOH Solution = (560/ (1000+560))*100 = 35.89 %

In sodium hydroxide solution, solids = 0.3589 x 56.65 = 20.3 kg,

and water = 56.65 – 20.3 = 36.27 kg.

Step 9: mass of sodium silicate solution = 198.26 – 56.65 =141.6 kg/ m^3

Step 10: Water content in sodium silicate solution=55.9%

In sodium silicate solution, water = 0.559 x 141.6 = 79 kg, and solids = 141.43 – 79 = 62.43 kg.

Therefore, total mass of water = 62.43+36.27= 98.7 kg,

Step 11: Coarse aggregate=0.55 X 1680 = 924 kg/ m^3

Step 12: Fine aggregate= 0.45 X 1680 = 756 kg/ m^3

3.5 Synthesis of Geopolymer Concrete

The mix proportion for the 13 mixes is given in Table 3.9. Mixes are developed aiming at 100 MPa compressive strength. Silica fume, alccofine and OPC 53 grade were used to improve the early-age compressive strength. Aggregate proportions were optimized using MTM packing methods in which the CA/FA ratio was 55/45 with a packing density of 0.712 (Table 3.5). The sodium silicate and alkaline activator-to-binder ratios were 2.5, and 0.38 respectively. Alccofine is limited to 10% (Parveen et al., 2018) as beyond this percentage, the mix becomes uneconomical. Very little amount of OPC at 10% is used in some mixes.

Table 3.9: Mix proportions of GPC

For 1 m^3 of concrete (in Kg)	**D1**	**D2**	**D3**	**D4**	**D5**	**D6**	**D7**	**D8**	**D9**	**D10**	**D11**	**D12**	**D13**
Aggregate: Total volume	70:100	70:100	70:100	70:100	65:100	65:100	65:100	65:100	65:100	65:100	65:100	65:100	65:100
Fly ash	172.18 (33%)	0%	104.35 (20%)	104.35 (20%)	243.48 (40%)	213.05 (35%)	213.05 (35%)	213.05 (35%)	152.18 (25%)	152.18 (25%)	152.18 (25%)	152.18 (25%)	158.53 (25%)
GGBS	224.35 (43%)	313.04 (60%)	206.87 (50%)	208.7 (40%)	365.22 (60%)	273.92 (45%)	273.92 (45%)	273.92 (45%)	304.35 (50%)	273.92 (45%)	273.92 (45%)	304.35 (50%)	273.92 (45%)
Silica fume	125.28 (24%)	208.7 (40%)	156.52 (30%)	208.7 (40%)	0%	121.74 (20%)	121.74 (20%)	121.74 (20%)	121.74 (20%)	121.74 (20%)	121.74 (20%)	121.74 (20%)	121.74 (20%)
Alccofine	0%	0%	0%	0%	0%	0%	0%	0%	30.44 (5%)	60.87 (10%)	60.87 (10%)	0%	0%
OPC/Alccofine	0%	0%	0%	0%	0%	0%	0%	0%	0%	0%	0%	30.44 (5%)	60.87 (10%)
Fine aggregate (kg/m^3)	756 (45%)	756 (45%)	756 (45%)	756 (45%)	702 (45%)	702 (45%)	702 (45%)	702 (45%)	702 (45%)	702 (45%)	702 (45%)	702 (45%)	702 (45%)
Coarse aggregate (kg/m^3)	924 (55%)	924 (55%)	924 (55%)	924 (55%)	858 (55%)	858 (55%)	858 (55%)	858 (55%)	858 (55%)	858 (55%)	858 (55%)	858 (55%)	858 (55%)
AA/Bi (alkaline activator) (kg/m^3)	0.38 (206.5)	0.38 (206.5)	0.38 (206.5)	0.38 (206.5)	0.38 (231.3)	0.47 (286)	0.38 (231.3)	0.38 (231.3)	0.38 (231.3)	0.38 (231.3)	0.38 (231.3)	0.38 (231.3)	0.38 (231.3)
NaOH (kg/m^3)	56.65 (14 M)	56.65 (14 M)	56.65 (14 M)	56.65 (14 M)	66.09 (16 M)	66.09 (14 M)	66.09 (14 M)	66.09 (16 M)	66.09 (16 M)	66.09 (14 M)	66.09 (16 M)	66.09 (16 M)	66.09 (16 M)
Na_2SiO_3 (kg/m^3)	141.6	141.6	141.6	141.6	165.2	165.2	165.2	165.2	165.22	165.2	165.22	165.2	165.2
Na_2SiO_3/NaOH	2.5	2.5	2.5	2.5	2.5	2.5	2.5	2.5	2.5	2.5	2.5	2.5	2.5
Sp= 2% (kg/m^3)	10.44	10.44	10.44	10.44	12.2	12.2	12.2	12.2	12.2	12.2	12.2	12.2	12.2
Water (kg/m^3)	15.66 (3%)	15.66 (3%)	15.66 (3%)	15.66 (3%)	0%	0%	0%	0%	0%	0%	0%	0%	0%

3.6 Mechanical Properties

The basic mechanical properties like compressive strength, splitting tensile strength, flexural strength, modulus of elasticity and stress-strain behaviour are determined at different days of curing. The procedure for testing specimens is detailed in the subsequent sections.

3.6.1 Compressive strength, flexural strength and splitting tensile strength

Concrete cubes of 100 mm size for compressive strength, beams of size 100 x 100 x 500 mm for flexural strength, and cylinders of size 100 mm diameter and 200 mm height for splitting tensile strength, were cast. All the specimens were allowed to cure at an ambient temperature of 27 ± 2°C. The compression, flexural, and tensile strengths were determined as per IS 516: Part 1: Sec 1: 2021. The loading rates for compressive, flexural and tensile strength were maintained at a rate of 140 kg/(cm^2/min), 1.2 to 1.4 (N/mm^2/min), and 180 (kg/min) respectively as per IS 516. The compressive strength, splitting tensile strength, and flexural strength are calculated using equations 3.18, 3.19, and 3.20 respectively.

$$f_{cc} = \frac{P}{b \times w} \quad \text{Eq 3.18}$$

$$f_{ct} = \frac{2P}{\pi d_s l} \quad \text{Eq 3.19}$$

$f_b = \frac{Pl}{bd^2}$ when a is greater than 13.3 cm, Eq 3.20(a)

$f_b = \frac{3Pl}{bd^2}$ when a is less than 13.3 cm Eq 3.20(b)

Where,

P= Maximum load taken by the specimens, kN

b= Breadth of the specimen, mm

w= Width of the specimen, mm

d_s= Diameter of the specimen, mm

l= Length of the specimen, mm

d= Depth of the specimen, mm

a= Distance between the line of fracture and the nearest support, measured on the tension side of the specimen, cm

3.6.2 Static Young's modulus and stress-strain behaviour

Young's modulus and stress-strain behaviour under static loading conditions were investigated as per ASTM C 469-02 (ASTM C469-02, 2006) under a displacement-control machine at a strain rate of 1 mm/min. Strain gauges were installed on the surface of the cylinder with a gauge length of 30 mm to measure deformation with respect to load. The load applied to the specimen was measured using a load cell of 2 MN. Two Linear Variable Differential Transducers (LVDT) were also attached to the test specimen as shown in Figure 3.11 to measure axial deformation. DAQ (Data Acquisition System) with a sensitivity of 40 Hz was used to collect the data.

Figure 3.11: Test setup for Young's modulus and stress-strain curve

3.7 Microstructure Characterization Studies

Microstructure characterization was carried out on the high-strength GPC specimens to investigate the compound phase changes due to different binders and concentrations of NaOH and also to assess the phases of high-strength GPC when cured at ambient temperature.

3.7.1 Energy Dispersive X-ray spectroscopy (EDX) and Scanning Electron Microscopy (SEM) analysis

SEM and EDX were performed on a representative sample of a 10-mm cube to determine its morphology, mineral identification, and quantification. SEM and EDX were performed on the instrument OXFD3SEM of OXFORD at an acceleration voltage of 6- 21 kV. SEM images were visualised when the sample was scanned with the electron beam and backscattered electron. As GPC is a nonconductive material, gold sputtering was done for better visualization and quantification of elemental compounds present in the specimen.

3.7.2 Back Scatter Electron microscopy (BSE)

BSE images were used to understand the extent of reacted and unreacted binder portions. Backscatter images work on the basis of contrast of different materials with different compositions. The higher atomic number elements appear brighter, while the lower atomic number elements appear dark. Usually, individual elements have higher atomic numbers before the chemical reaction than in the compound state, so unreacted elements appear brighter than reacted elements. Grey contrast of BSE is also affected by the Ca/Si ratio (Scrivener, 2004). With an increase in calcium compounds, grey contrast becomes brighter while with increasing silica compounds, it becomes darker. BSE images can be collected from SEM and EDX instruments with a special separate detector.

3.7.3 Fourier Transform Infrared Radiation (FT-IR) Spectroscopy

FT-IR technique measures the infrared radiation absorbed by the specimen. When infrared radiation passes through the specimen, some radiation is absorbed while the remaining passes through the specimen. A spectrum was created based on this output signal. The spectrum for each molecule is unique and different. Chemical bonds present in specimens are identified based on this spectrum. This spectrum is used to identify the chemical bonds in the specimen. Upon identification of chemical bonds, the chemical compounds in the specimen can be detected. FT-IR was used to identify polymeric, inorganic, and organic phases in the material. For performing FT-IR analysis, the GPC powdered sample which passed through a 75-micron sieve was collected and mixed with potassium bromide (kBr) to form a pellet.

3.7.4 X-ray Diffraction Technique (XRD)

XRD analysis was used to identify the crystalline and amorphous nature of the material. The specimen was subjected to an X-ray beam with wavelength λ. The scattered X-ray beam was detected and recorded as spectra. This spectrum is unique for every element and compound. The power diffraction database was used to identify the elements and compounds. To perform XRD analysis, a representative GPC powdered sample passing through a 90 μm sieve was used. The samples were subjected to x-ray under a diffractometer with a speed of 2^{o}/minute, 0.02^{o} step size and radiation of Cu-Kα at 60 kC/55 mA.

3.8 Results of Mechanical Properties

The strength performance of GPC through mechanical properties such as compressive strength, splitting tensile strength, flexural strength and Young's modulus are discussed in the following sections.

3.8.1 Compressive strength

The compressive strength of all 13 mixes is shown in Figure 3.12. It can be observed that mixes with 35% binder content in a total volume of concrete showed increased compressive strength compared to mix with 30% binder content. From the mixes (D7, D9, and D11), it can be observed that with an increase in alccofine, the compressive strength of concrete increased. This behaviour is supported by SEM and EDS analysis where it was observed that with an increase in alccofine, the microstructure became denser with fewer voids and cracks due to the formation of additional C-S-H and C-A-S-H gel along with the N-A-S-H (Figure 3.23-3.25). An increase in the percentage of alccofine content increased the reactivity of binder material and utilised most of the free Na available from the alkaline activator for polymerization which can be observed in Table 3.10. A similar observation is mentioned in the research conducted by Parveen et al., 2017 where it was mentioned that an increase in alccofine up to 10%, improved the compressive strength and beyond that the mix lost its workability and strength (Bharat et al., 2017; Diksha et al., 2023). Also, the mix D11 (10 % alccofine and 16 M NaOH) has shown the highest compressive strength of 103 MPa. From mixes D7- D8 and D10- D11, it can be observed that with an increase in molarity of NaOH from 14 M to 16 M, there is an increase in compressive strength. The addition of 5%-10% OPC triggered the rate of polymerization and provided a 14.93% and 29.07% increase in compressive strength for mixes D12 and D13 respectively relative to mix D7(0% OPC). OPC provided ettringite and CH gels (Figure 3.26) as additional strengthening elements to the polymeric gel. To assess the mechanical and microstructural behaviour of HSGPC, mix D7 (> 60 MPa concrete), D9, D10, and D13 (> 80 MPa concrete) and D11 (> 100 MPa) concrete samples were considered.

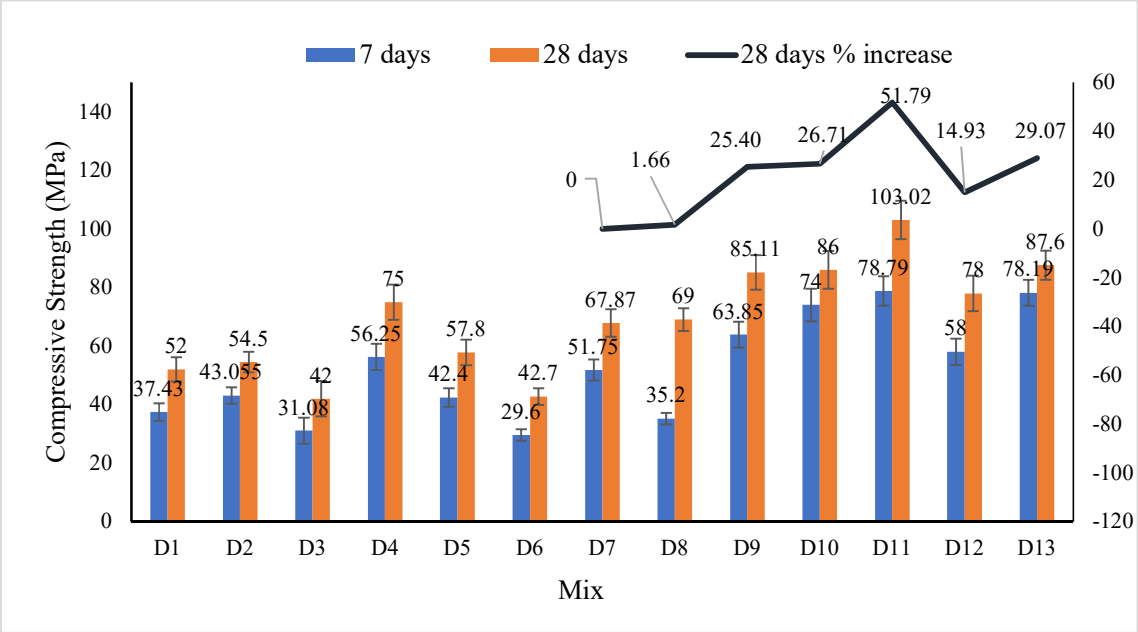

Figure 3.12: Compressive strength of GPC

3.8.2 Splitting tensile strength

Figure 3.13 shows the splitting tensile strength for the considered mixes. An increase in alccofine (D9 and D11) from 5 to 10% increased the splitting tensile strength by 11%. Similarly, with an increase in alccofine, the morphology (D9 and D11) became stronger by eliminating the micro-cracks and unreacted particles which can be observed in Figure 3.23 and 3.25. The mix D11 has shown the highest splitting tensile strength of 5.81 MPa in all mixes. Also, from the XRD analysis (Figure 3.30), Mix D11 presented the highest counts for C-S-H and quartz which provides better strength properties. The use of 10% alccofine in mix D11 increased the splitting tensile strength by 66% compared to a mix without alccofine (D7). The use of 10% OPC increased it by 46%. The addition of alccofine and OPC increased the reactivity of the binder for early age strength and thereby increased the splitting tensile strength of the concrete. An analytical equation was proposed based on the experimental results, as shown in Equation 3.21:

$$f_{ct} = 0.4(f_{ck})^{0.56} \quad \text{Eq 3.21}$$

The studies by researchers who established relationships between the tensile and compressive strength of concrete are summarized below:

(Arioglu et al., 2006) $f_{ct} = 0.39(f_{ck})^{0.63}$ Eq 3.22

(Xu & Shi, 2009) $f_{ct} = 0.21(f_{ck})^{0.83}$ Eq 3.23

(Ramadoss & Nagamani, 2008) $f_{ct} = 0.485(f_{ck})^{0.56}$ Eq 3.24

(ACI 318-11, 2011) $$f_{ct} = 0.56(f_{ck})^{0.5}$$ Eq 3.25

Where f_{ck} is the characteristic compressive strength of concrete and f_{ct} is splitting tensile strength. Figure 3.14 shows the failure surface of the cylindrical specimen under splitting tensile stress. This shows that the failure was through the aggregate rather than ITZ, exhibiting stronger ITZ in 60 MPa, 80 MPa, and 100 MPa HSGPC. Similar results are observed by the researchers (Ahmet et al., 2018; Thomas & Peethamparan, 2015). A comparison of the various analytical models and experimental results along with proposed models from the researchers and code provisions is shown in Figure 3.15. The results of the OPC-based models showed higher values than the experimental results of high-strength GPC.

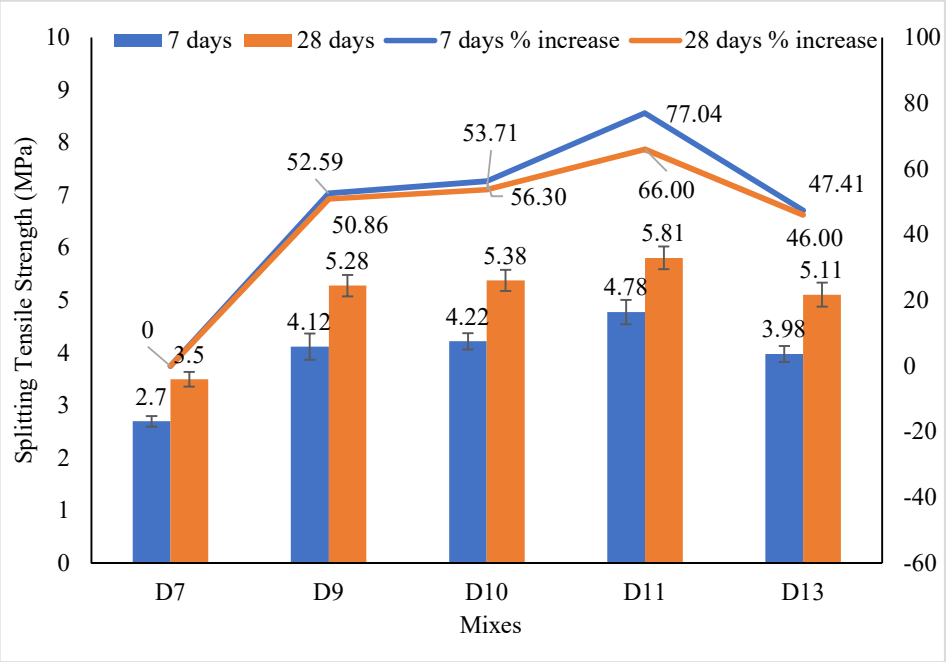

Figure 3.13: Splitting tensile strength of GPC

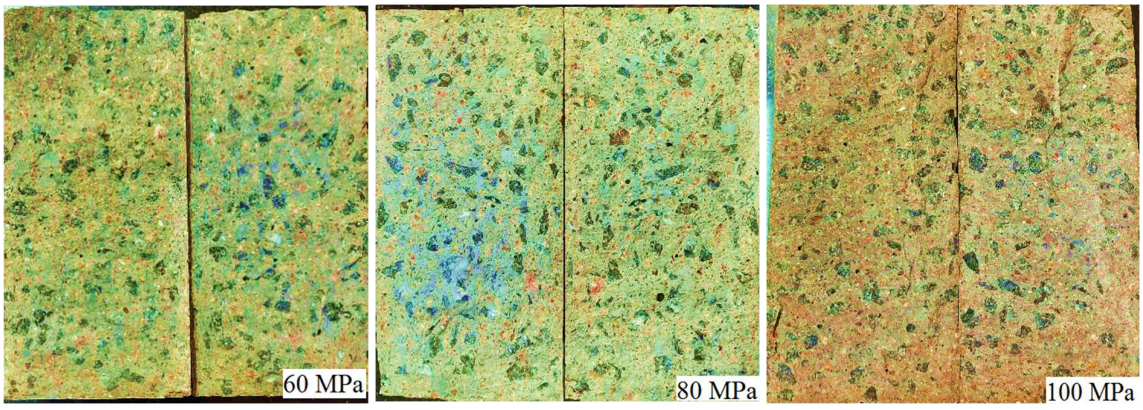

Figure 3.14: Splitting failure of typical cylinders for a) 60 MPa b) 80 MPa c) 100 MPa compressive strength mixes

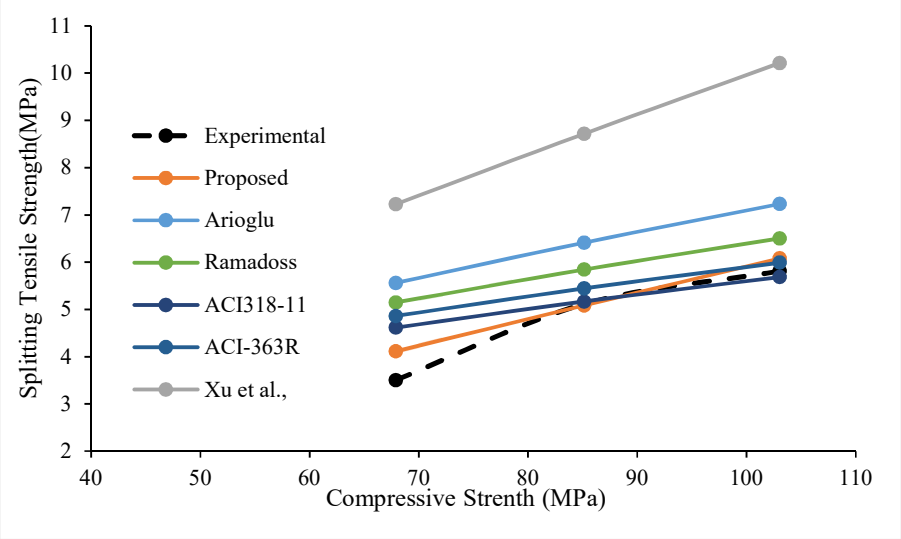

Figure 3.15: Relationship between compressive strength and splitting tensile strength of GPC.

3.8.3 Flexural strength

The results of the flexural strength test of considered GPC mixes are shown in Figure 3.16. An increase in the alccofine (D9 and D11) from 5 to 10%, increased the flexural bond strength by 5.2%. It can be observed that, with the use of 10% alccofine, the flexural strength increased by 9.36% compared to the mix without alccofine. Mix D11, showed the highest flexural strength of 8.06 MPa. The incorporation of OPC increased the flexural strength by 6.38% compared to the mix without OPC. It can also be observed that, for mixes D10- D11, with an increase in the molarity from 14 M to 16 M, the flexural strength increased by 4.5%. BSE analysis also mentioned that with an increase in molarity, the unreacted particles become less and provide stronger ITZ (Figure 3.29). From this, it can be concluded that the addition of alccofine and OPC increased the flexural strength of HSGPC.

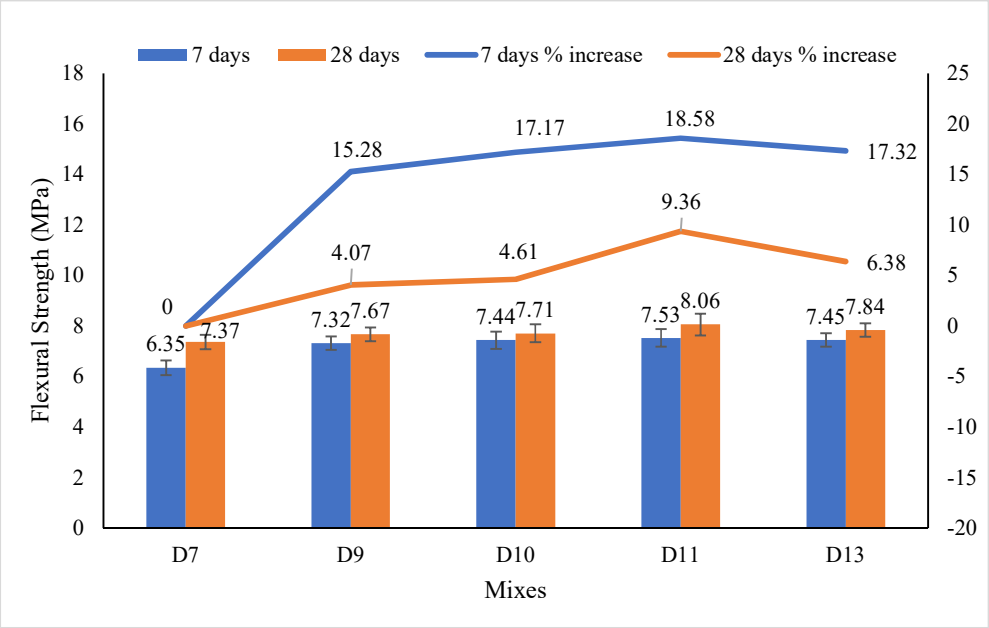

Figure 3.16: Flexural strength of HSGPC mixes

An analytical model for the determination of the flexural strength of concrete based on the experimental data set is proposed and given in Equation 3.26:

$$f_{cr} = 3.57(f_{ck})^{0.177} \quad \text{Eq 3.26}$$

Some of the other models showing the relationship between the flexural and compressive strength are summarized below:

(Nath & Sarker, 2017)	$f_{cr} = 0.93(f_{ck})^{0.5}$	Eq 3.27
(Diaz-Loya et al., 2011)	$f_{cr} = 0.69(f_{ck})^{0.5}$	Eq 3.28
(AS 3600-2009, 2009)	$f_{cr} = 0.6(f'_{ck})^{0.5}$	Eq 3.29
(ACI 318-11, 2011)	$f_{cr} = 0.62(f'_{ck})^{0.5}$	Eq 3.30

Where f_{ck} is the characteristic compressive strength of concrete in MPa and f_{cr} its flexural strength in MPa.

Figure 3.17 shows the experimental results and a comparison with the proposed model. It can be seen that all the OPC-based models yield lower results than experimental ones. The model proposed by Nath and Sarkar (Nath & Sarker, 2017) is close to experimental values which are proposed based on the results of GPC. From Figure 3.17, it can be seen that the flexural strengths from OPC models are lower compared to experimental results of GPC, a similar observation can be seen in the research conducted by Nath and Sarkar, 2017; Prachasaree et al., 2020.

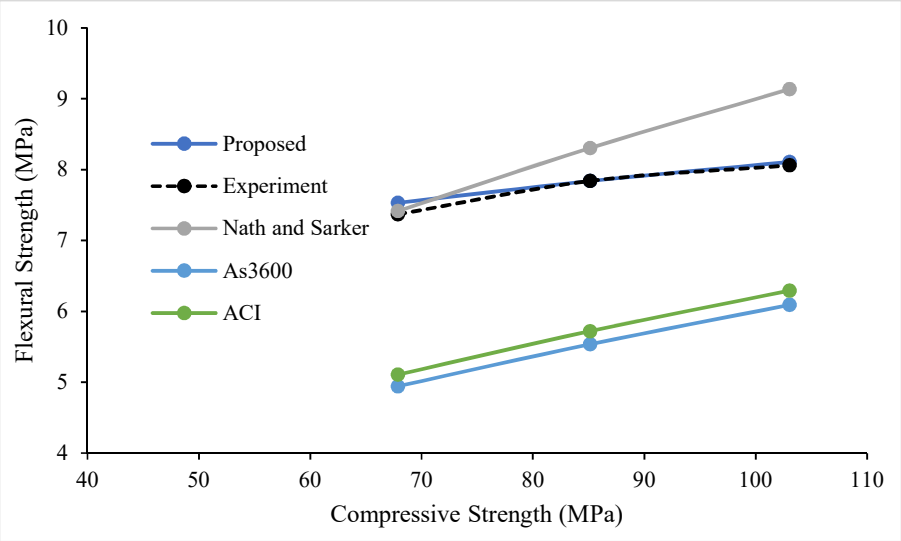

Figure 3.17: Relationship between compressive strength and flexural strength of GPC

3.8.4 Static modulus of elasticity and stress-strain behaviour

The results of the static modulus of elasticity are shown in Figure 3.18. The modulus of elasticity increased with an increase in the compressive strength of concrete with a maximum value of 21.09 GPa for mix D11. An increase in the alccofine from 5% to 10% increased the modulus of elasticity by 3.7%. The addition of 10% alccofine increased the modulus of elasticity by 21.6% compared to a mix without alccofine. The addition of 10% OPC increased the compressive strength by 21% compared to a mix without OPC which is similar to the observation made in compressive strength. From the stress-strain behaviour (Figure 3.20), it can be observed that the initial stiffness is low for all mixes, indicating the reduced modulus of elasticity. The cylinder compressive strength was approximately 80% of the cube compressive strength. Based on the experimental results, an analytical equation is developed to determine the modulus of elasticity based on regression analysis and is given by Equation 3.31

$$E = 2391.85(fck)^{0.476} \quad \text{Eq 3.31}$$

Some of the other established models from the literature are summarized below:

(Lee & Lee, 2013) $E = 5300\sqrt[3]{fck}$ Eq 3.32

(Diaz-Loya et al., 2011) $E = 0.037\ \rho^{1.5}\sqrt{fck}$ Eq 3.33

(AS 3600-2009, 2009) $E_c = \rho^{1.5}\ X\ \left(0.024\sqrt{f_{ck}} + 0.012\right)$ Eq 3.34

(BS EN 12390-13:2021, 2021) $E_c = 20000 + 0.2f_{ck}$ Eq 3.35

Where f_{ck} is the compressive strength of concrete at 28 days in MPa, E is the modulus of elasticity in MPa and ρ the density of concrete in kg/m^3.

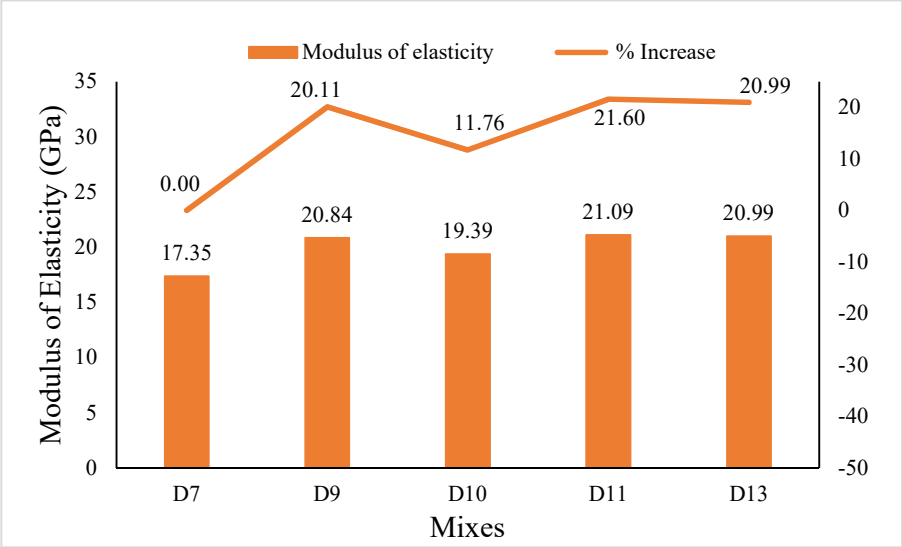

Figure 3.18: Modulus of elasticity of the GPC mixes

Figure 3.19 shows a comparison of experimental results with existing analytical equations. It can be seen that the values from AS 3600 (AS 3600, 2009) are more than the values determined from experimental results, indicating that the modulus of elasticity for HSGPC was lower compared to OPC concrete. The modulus of elasticity values are in line with the results of Lee and Lee's (Lee & Lee, 2013) in which the modulus of elasticity of alkali-activated concrete is investigated.

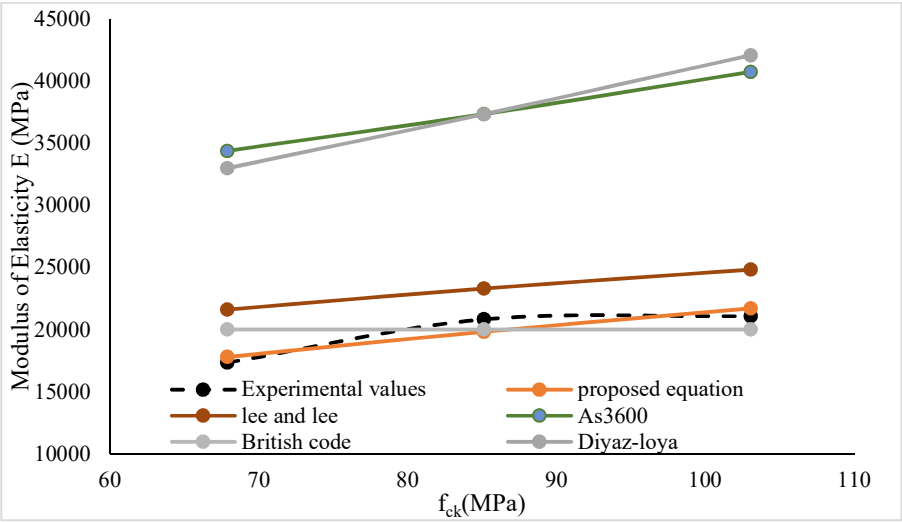

Figure 3.19: Relationship between compressive strength and modulus of elasticity of GPC

Figure 3.20 shows the stress-strain behaviour of HSGPC mixes. It can be seen that the addition of 10% alccofine improved the stress-stain behaviour of GPC compared to other mixes with a stress of 86.46 MPa. The incorporation of OPC also provided better performance than the

D7 mix. D9 and D10 mixes showed better behaviour as both were synthesized with alccofine but with different molarities and percentages.

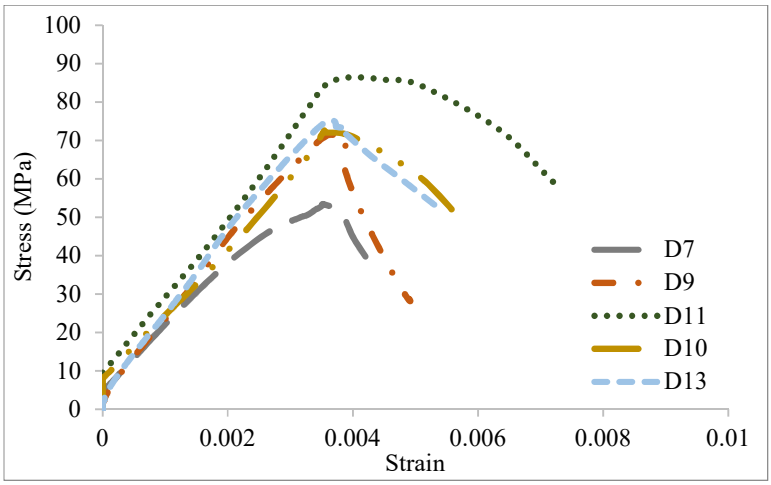

Figure 3.20: Stress-strain behaviour of the GPC mixes

A constitutive model is developed to predict the stress-strain behaviour of HSGPC, and is shown in Equation 3.36:

$$\sigma = \sigma' \frac{\epsilon}{\epsilon_0}\left[\frac{A}{A-1+\left(\frac{\epsilon}{\epsilon_0}\right)^B}\right] \quad \text{Eq 3.36}$$

Where,

$A = \frac{Ec}{262792.3} + 6.45$

$E_c = 2391.85 \times (f_{ck})^{0.476}$

$\epsilon_0 = 6.161 \times 10^{-4} \times \sigma'^{0.424}$

$B = \frac{2768.633}{\sigma' - 29.55}$

f_{ck}= 28 days compressive strength of concrete

σ'= Peak stress

ϵ_0= Strain corresponding to peak stress

Cong et al., 2020 (Cong et al., 2020) proposed a constitutive model for predicting the performance of alkali-activated concrete given by Equation 3.37:

$$\sigma = f_{cm} \frac{\epsilon}{\epsilon_o}\left[\frac{m}{m-1+\left(\frac{\epsilon}{\epsilon_o}\right)^\beta}\right] \quad \text{Eq 3.37}$$

Where,

$m = \frac{Ec}{19.5} + 2$

where, $E_c = 0.273\ (n+1) f_{cm} + 10$, $n = 0.08 V_{WQS} - 0.03$, $\beta = 10\left(\frac{k}{f_{cm}}\right) + 5$

V_{WQS} = Volume percentage of WQS in fine aggregates

f_{cm} = Mean static compressive strength

Thomas et al., 2015 (Thomas et al., 2015) developed an analytical model to determine the stress-strain behaviour of geopolymer concrete that is given by Equation 3.38:

$$\sigma = \sigma_0 \frac{\epsilon}{\epsilon_o}\left[\frac{n}{n-1+\left(\frac{\epsilon}{\epsilon_o}\right)^n}\right] \quad \text{Eq 3.38}$$

Where,

$$n = (0.4 \text{ x } 10^{-4})\sigma_0 + 1,\ \epsilon_0 = (2.7 \text{ x } 10^{-4})\sigma_0{}^{0.25}$$

Figure 3.21(a, b and c) shows a comparison of the experimental stress-strain behaviour with the constitutive model developed from the literature. It can be seen that the developed model has a good relation with experimental results. The model proposed by Thomas et al. (Thomas & Peethamparan, 2015), depends on the maximum stress in the stress-strain curve, while the one proposed by Cong et al. (Cong et al., 2020) depends on the maximum values of strain corresponding to the maximum stress and modulus of elasticity. It was seen that, at higher compressive strength of concrete, the proposed model was closer to the experimental results.

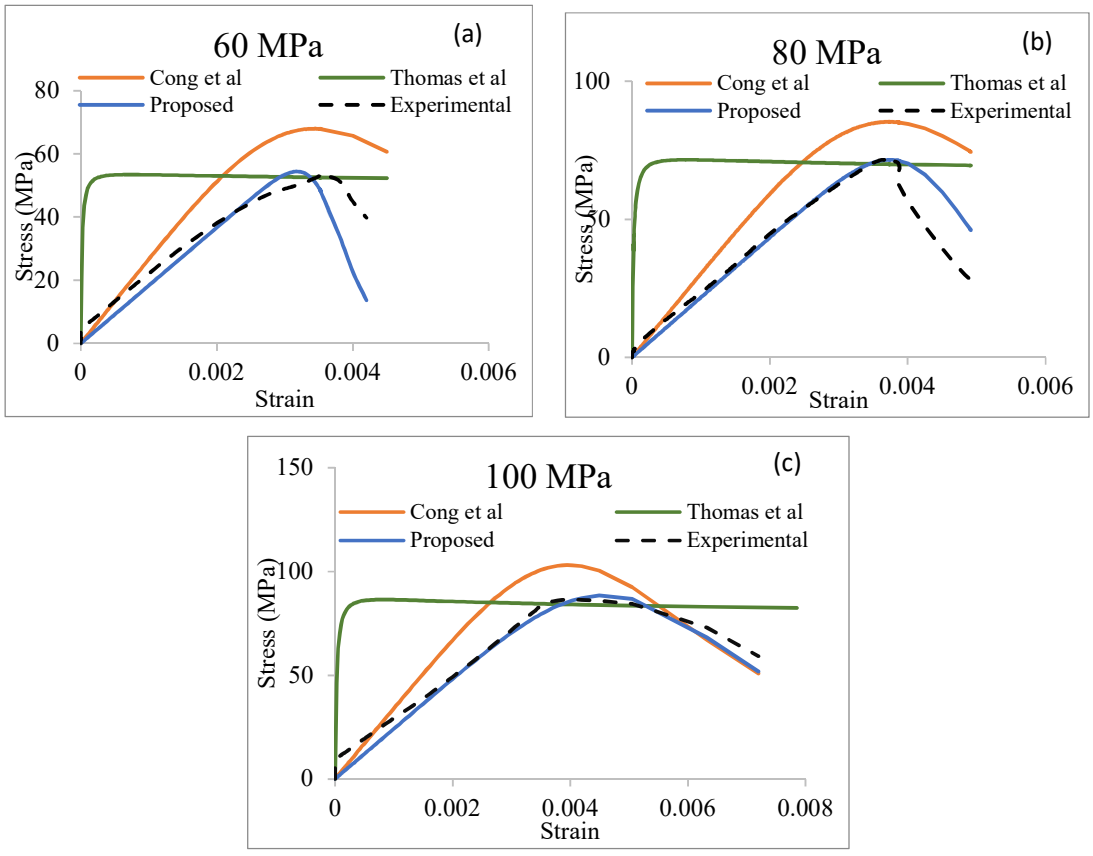

Figure 3.21: Experimental and predicted stress-strain behaviour of (a) 60 MPa (b) 80 MPa (c) 100 MPa GPC

3.9 Results of Micro-structure Characterization Studies

The microstructure characteristics of multicomponent binder-based geopolymer concrete are discussed with the SEM, FT-IR, XRD, EDS, and BSE techniques.

3.9.1 Scanning electron microscopy

Figure 3.22 to 3.26 shows the SEM images of high-strength GPC mixes. It can be observed that all the mixes showed dense and heterogeneous phases, indicating good cohesion between the binder phase and aggregate matrix. From the SEM images of mix D7, it can be noted that the voids are more and the mix is less dense than others. Cracks are also evident in mix D7, which resulted in lower mechanical strength compared to other mixes. The presence of unreacted fly ash particles is also evident in mix D7. The D9 (16 M NaOH and 5% alccofine) mix showed similar gel formation but with a lower number of unreacted particles. Mix D10 (14 M NaOH and 10% alccofine) has a higher formation of CSH gel than mix D7 (0% alccofine), clearly indicating that the incorporation of alccofine increased the volume of CSH. In case of mix D11 (10% alccofine and 16 M NaOH), the morphology was dense and compact, indicating polymerization and polycondensation of a large volume of binder, resulting in higher compressive, splitting and flexural strength among all other mixes. The increase in alccofine (D7, D9 and D11) decreased the voids and cracks, exhibiting good adhesion between the reacted and unreacted particles resulting in higher compressive strength. From Figure 3.26, it can be seen that there is evidence of the formation of ettringite needle-like structures and CH plate structure elements in mix D13. This implies that there is a beneficial effect of the use of OPC in geopolymer concrete.

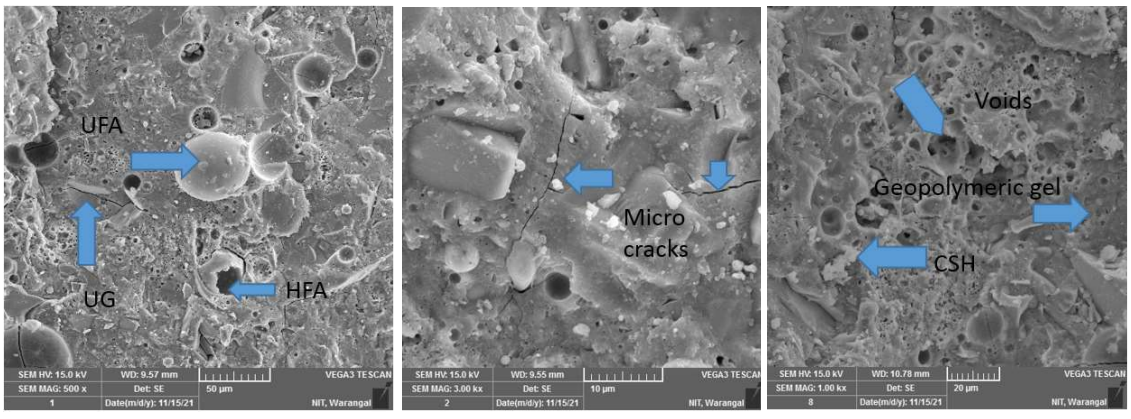

Figure 3.22: SEM of mix D7

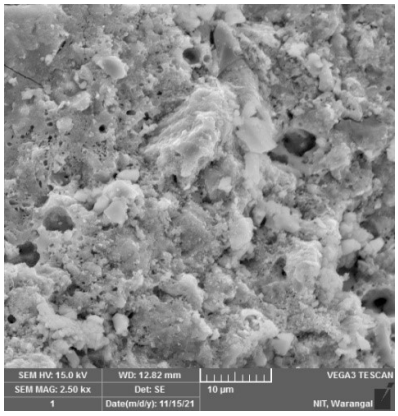

Figure 3.23: SEM of mix D9

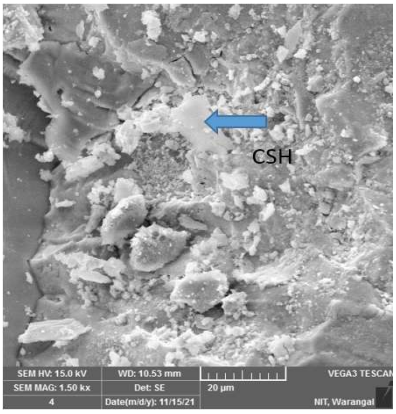

Figure 3.24: SEM analysis of mix D10

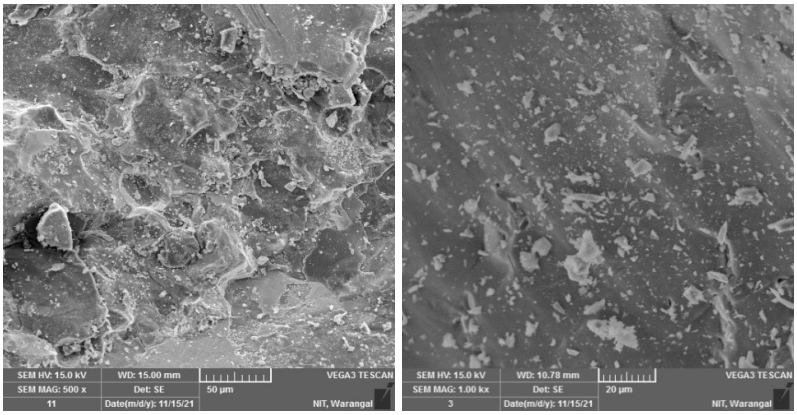

Figure 3.25: SEM analysis of mix D11

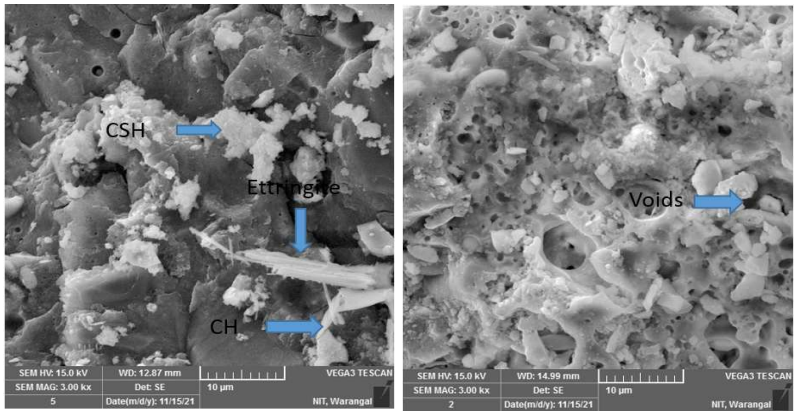

Figure 3.26: SEM analysis of mix D13

3.9.2 Energy dispersive X-ray spectroscopy

EDX analysis was used to identify and quantify the elements. Davidovits (Davidovits, 1999) proposed an empirical equation for determining the type of geopolymeric structure based on Si/Al ratio and Na/ Al ratio, $M_n(-(SiO_2)_z\text{-}AlO_2)_n$, wH_2O, where M represents a cation such as potassium (K), or Calcium (Ca); n is the degree of polycondensation; Z=1, 2, 3 or higher, and w is the amount of binding water.

Based on the ratio of Si/Al and Na/Al, three types of geopolymer structures were formulated. The ratio extends from 1-3 and 0.4-1 for Si/Al and Na/Al respectively:

1. Poly (Sialate), i.e., Na_n-(-Si-O-Al-O-)$_n$-
2. Poly (Sialate-siloxo), i.e., Na_n-(-Si-O-Al-O-Si-O)$_n$-
3. Poly (Silate-disiloxo). i.e., - Na_n-(--Si-O-Al-O-Si-O-Si-O-)$_n$-

The identification of C-S-H and Calcium Hydroxide (CH) can be estimated based on Eq. 3.39 and 3.40:

C-S-H: $0.8 \leq Ca/Si \leq 2.5$, $(Al+Fe)/Ca \leq 0.2$ Eq 3.39

CH: $Ca/Si \geq 10$, $(Al+Fe)/Ca \leq 0.4$, $S/Ca \leq 0.04$ Eq 3.40

In case of higher calcium ions, there is a possibility of the formation of calcium silicate hydrate (C-S-H) gels in the geopolymer system. In case of fly ash-based geopolymer, there will be the formation of NASH aluminosilicate gel. In case of FA-GGBS-based geopolymer, the C-S-H and C-A-S-H gel forms additionally due to the presence of calcium ions from GGBS over Na ions until all available calcium ions are exhausted. Hence, the geopolymer system has both N-A-S-H and C-A-S-H in case of FA-GGBS binders.

Figure 3.27 (a) and Table 3.10 show the element percentage at the selected region (D7/a) in mix D7. It can be observed that the atomic percentage of Si, Al, and Na is higher while calcium's is low. This can be attributed to the presence of aluminosilicate gel (NASH). From the EDX analysis of mix D7 (D7/b), as shown in Figure 3.27 b) and Table 3.10, it can be observed that unreacted sodium is present on the flyash particles showing an atomic percentage of 6.34% of Na ion. From Table 3.10 (D7/c) and Figure 3.27 c), it can be seen that the geopolymer gel consists of a Si/Al ratio of 5.96 and Na/Al ratio of 2.87, from which it can be confirmed that three types of geopolymeric structures were formed. It can also be observed that Ca, Na, K, Mg, Al, and Si elements were present.

For mix D9, the EDX analysis is shown in Figure 3.27 d) and Table 3.10. It can be observed that the Si/Al ratio was 7.42 and the Na/Al ratio was 0.6. The Si/Al ratio is higher in the case of D9 than in D7, which provides evidence of strong Si-Al bonds leading to better mechanical properties than D7. The EDX analysis of the D10 mix also showed similar behaviour to that of mix D9, which can also be noted from Table 3.10 and Figure 3.27 (e). As there is a higher percentage of alccofine, there is a slight increase in the atomic percentage of Ca.

EDX analysis for mix D11 is given in Figure 3.27 f) and Table 3.10. It can be observed that the atomic percentages of Al, Si, and Ca are higher. The Si/Al ratio is 0.94 and Na/Al is 0.12. This is conclusive of three types of geopolymeric gel and CASH and CSH gel as it includes GGBS and alccofine. This provides a dense and compact microstructure and higher Si-Al bond and Ca-Al bonds, leading to better mechanical performance than other GPC mixes. Similar observations can be noted from compressive strength results. The EDX analysis for mix D13 is shown in Table 3.10 and Figure 3.27 g). It can be observed that the atomic percentage of silica is low while calcium is high and hence forms more Ca-Al bonds than Si-Al bonds. In addition, as Si-Al bonds form double bonds and Ca-Al bonds form single bonds, mix D11 has higher compressive strength than mix D13.

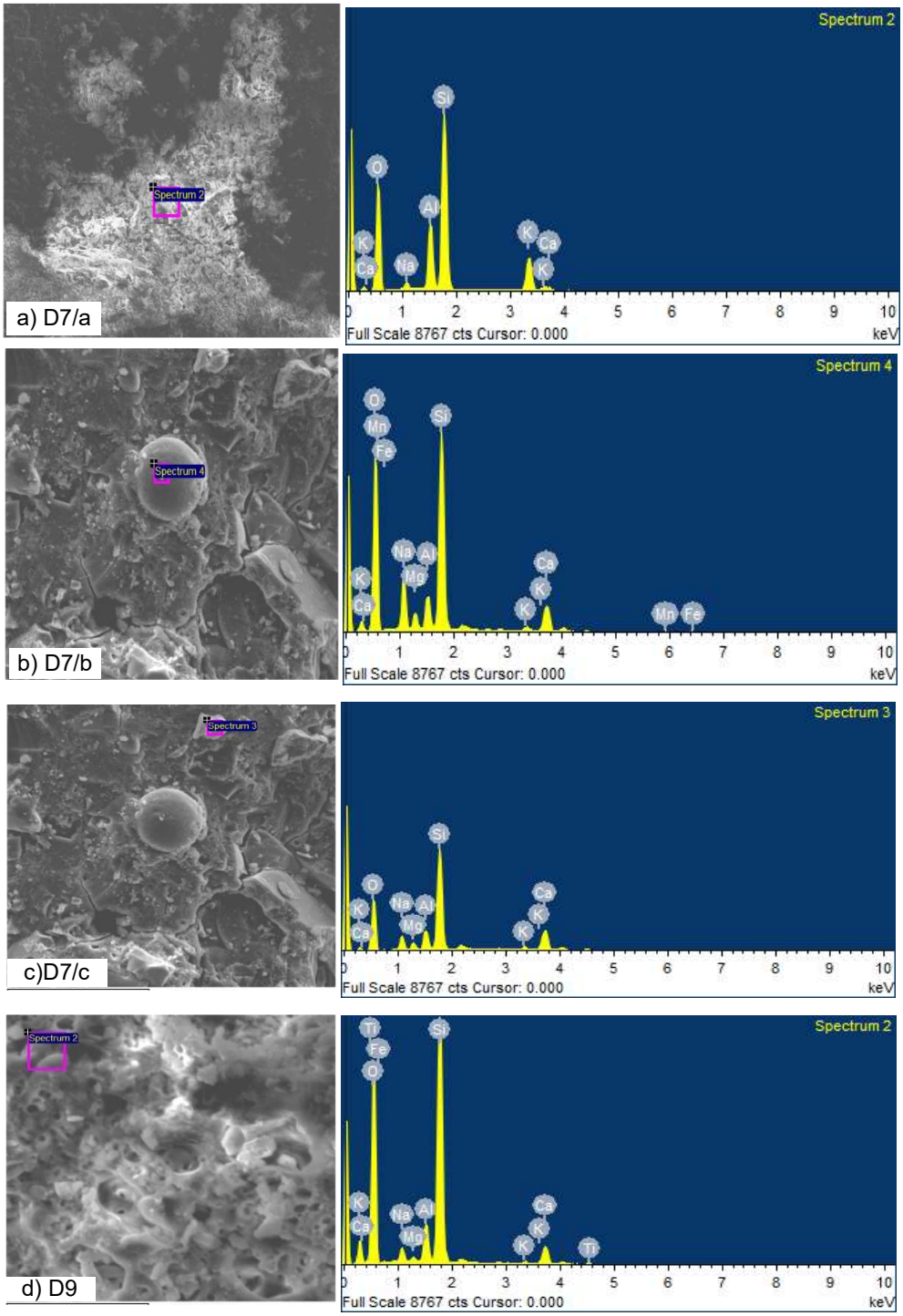
Spectrum 2
Si
O
Al
K
Ca
Na
Full Scale 8767 cts Cursor: 0.000
keV
a) D7/a
Spectrum 4
O
Mn
Fe
Si
Na
Al
Mg
Ca
K
Full Scale 8767 cts Cursor: 0.000
keV
b) D7/b
Spectrum 3
Si
O
Na
Al
Mg
Ca
K
Full Scale 8767 cts Cursor: 0.000
keV
c)D7/c
Spectrum 2
Ti
Fe
O
Si
K
Ca
Na
Al
Mg
Ti
Full Scale 8767 cts Cursor: 0.000
keV
d) D9

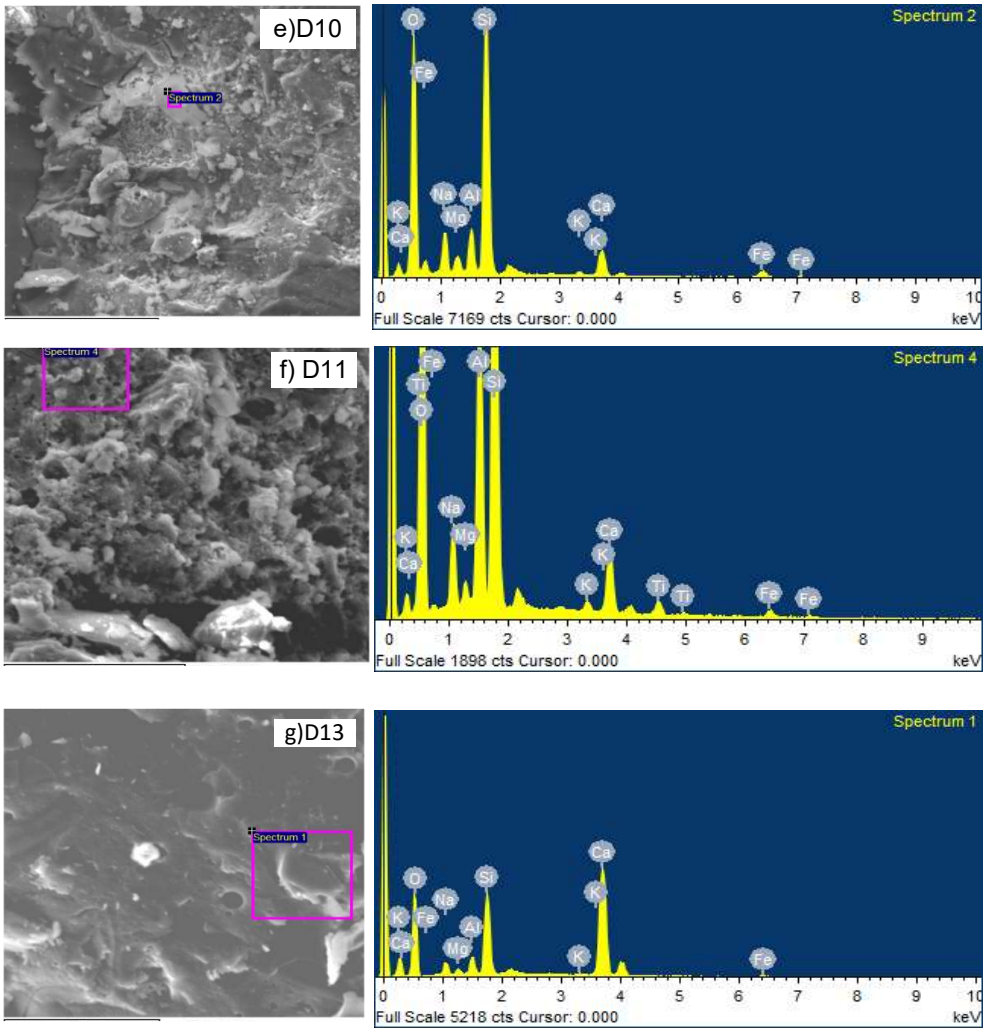

Figure 3.27: EDX analysis of mixes a) D7/a b) D7/b c) D7/c d) D9 e) D10 f) D11 g) D13

Table 3.10: Percentage of elements in the selected region of GPC mixes

Sample	O	Na	Mg	Al	SI	K	Ca	Fe
	Atomic percentages							
D7/a	65.69	1.18	-	6.6	20.80	5.27	0.44	-
D7/b	68.31	6.34	1.50	2.62	16.99	0.45	3.40	0.27
D7/c	62.21	4.19	1.46	3.55	21.15	0.86	4.17	0.40
D9	72.37	1.56	0.27	2.75	20.40	0.25	2.15	0.16
D10	69.50	2.28	1.34	2.71	17.84	0.38	2.60	1.66
D11	65.89	2.266	0.44	8.12	19.8	0.33	2.14	0.61
D13	69.58	2.12	0.60	1.66	8.55	0.22	17.01	0.27

3.9.3 Fourier transformation infrared spectroscopy analysis

Figure 3.28 shows the infrared radiation (IR) response for mixes D7, D11 and D13. The range covered for the IR is 4000-400 cm^{-1}. The intense signals at 3459, 3443, and 3436 cm^{-1} correspond to stretching vibrations of H-O groups belonging to $Mg(OH)_2$ and water molecules and the same

is confirmed from XRD analysis (Perná et al., 2014). The weak absorption bands at 2923 and 2857 cm^{-1} on D11 and D13 mixes correspond to –CH groups indicating the presence of organic compounds from OPC and fly ash (Perná et al., 2014). The absorption band at 1638, 1644, and 1642 cm^{-1} of mixes D7, D11, and D13 respectively were stretching and bending vibrations of O-H bonds, indicating the presence of water molecule and alkaline activation products in geopolymer network (Fine & Stolper, 1986). The broad absorption band at 1110, 1048, and 1040 cm^{-1} of mixes D7, D11, and D13 respectively are attributed to symmetric and asymmetric vibrations of Si-O-X (X=Al or Si) bond, related to geopolymer network (Rees et al., 2007). These wave numbers are on the higher side of around 1000 cm^{-1} due to the inclusion of calcium ions into the tetrahedral site or silica substances from micro silica resulting in the extension of the geopolymer network (Kaze et al., 2018; Yip et al., 2005). The bands at 779, 776, and 776 cm^{-1} of D7, D11, and D13 respectively were due to the stretching vibrations of the Al(VI)-O bond (Yunsheng et al., 2010). The lower absorption bands from wave number 699 to 535 cm^{-1} of all IR spectrum of mixes correspond to stretching and bending vibration modes of Si-O-X (X= Si or Al) bonds (Hsu & Nacu, 2005) responsible for polymerization (CASH and NASH) and hydration (CSH) (Al-Majidi et al., 2016; Samantasinghar & Singh, 2019). In addition, the bands at 451 and 463 cm^{-1} of mix D11 and D13 were linked to the stretching vibration of Mg-O (Hsu & Nacu, 2005). The bands at 1120, 1646, and 3420 cm^{-1} indicate the presence of ettringite in mix D13. The FT-IR response is in line with the results from the XRD analysis. The stretching vibrations at 1062 cm^{-1} in mix D7 were not observed in mixes D11 and D13, as the addition of calcium substances from CSH and NASH gel using Al changes in polymerization and improves the mechanical properties. The band 2360 cm^{-1} in mix D7 and D11 is due to C=O bond stretching vibration, which is evidence of CO_2 formation.

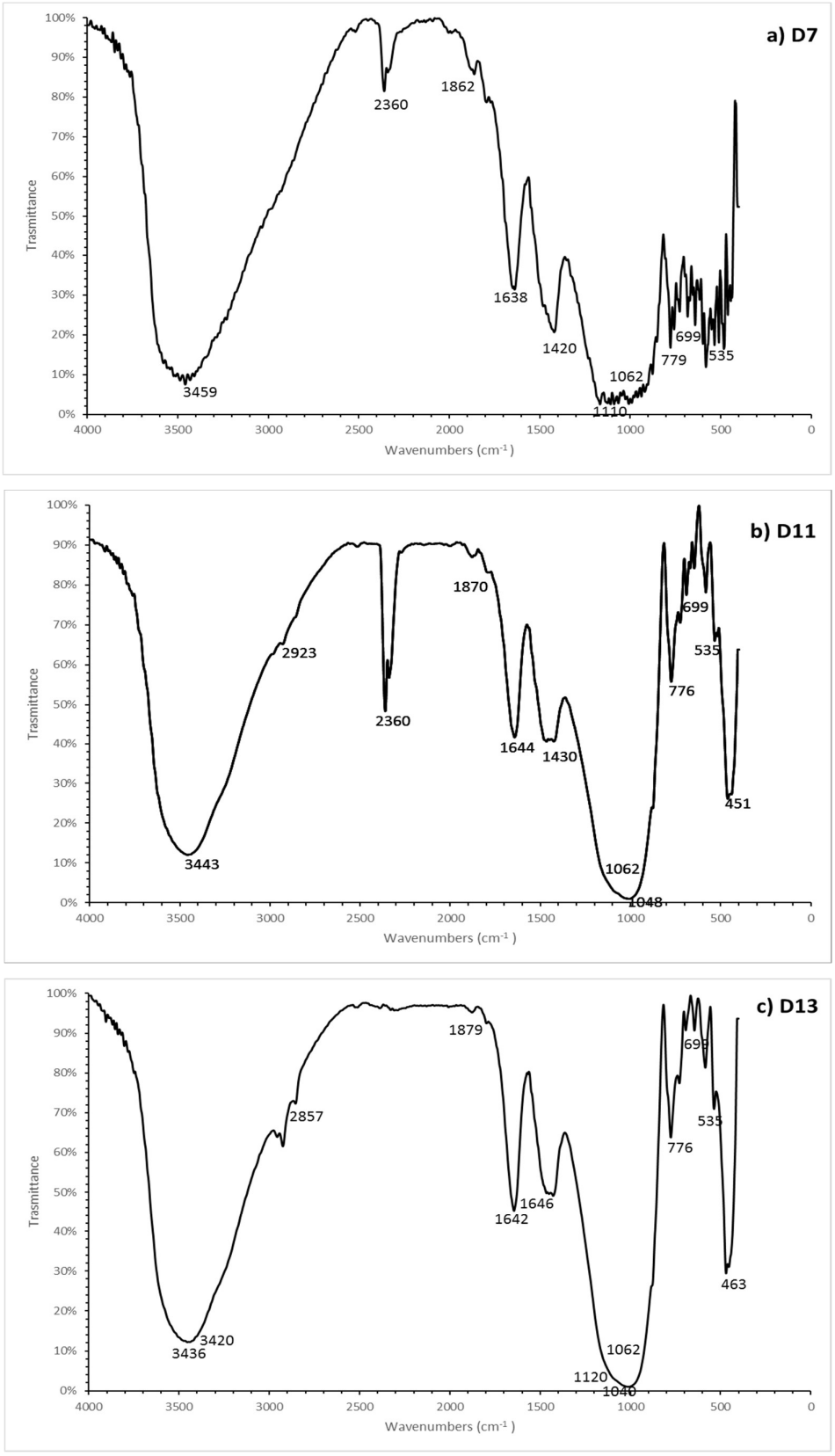

Figure 3.28: FT-IR spectrum of mixes a) D7 b) D11 c) D13

3.9.4 Backscattered electron microscopy

Figure 3.29 shows the BSE images of mixes D7, D9, D11, and D13. It can be seen that the image of the D13 mix is brighter than that of all other mixes, as it has higher quantities of C-A-S-H and C-S-H gel. Mix D7 is darker than mix D10 as it has higher silica content. Mix D9 is darker than mix D10 as the molarity is high, which leads to more reactivity and a lower volume of unreacted particles, resulting in lower atomic numbers and hence, darker images. Similar observations can be noted in case of compressive strength results. Mix D13 showed the brightest image compared to all other mixes since it had a higher amount of calcium content and higher molarity. A similar observation can be drawn from EDX analysis.

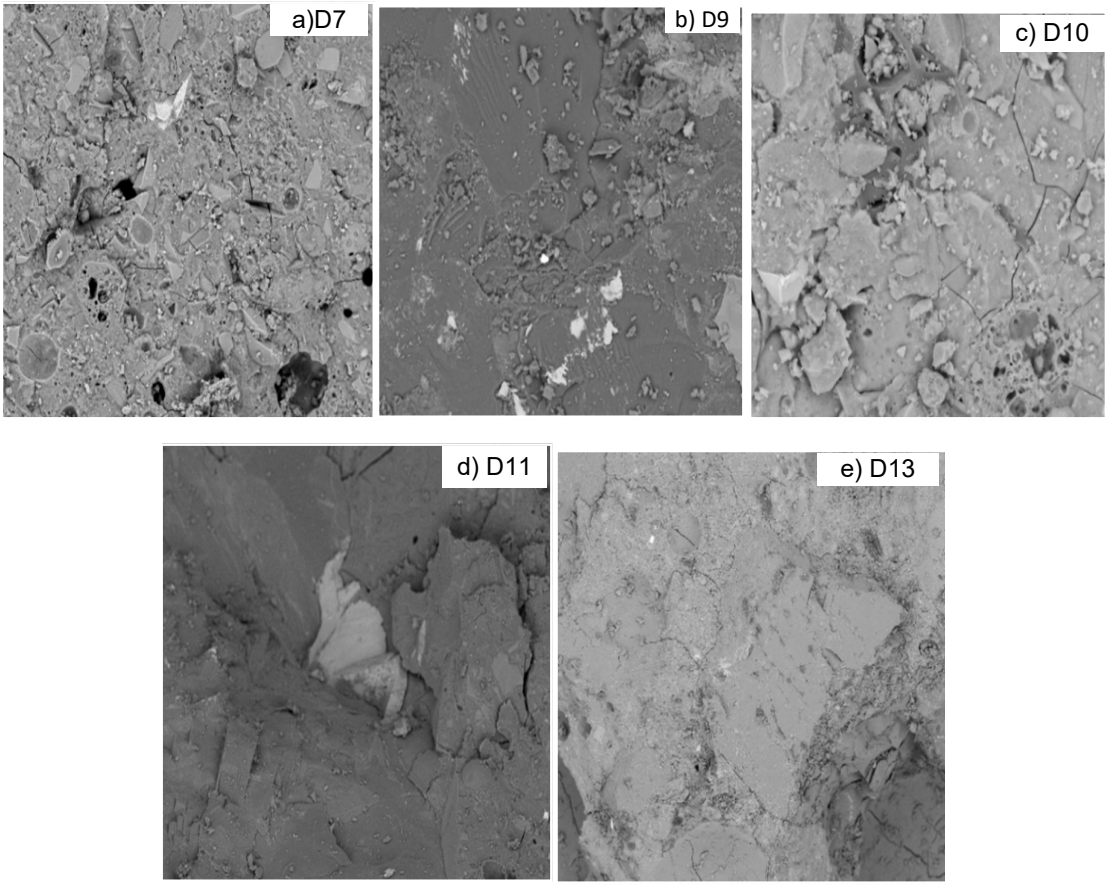

Figure 3.29: BSE images of mixes a) D7 b) D9 c) D10 d) D11 e) D13

3.9.5 X-ray diffraction analysis

Samples of mixes D7, D11, and D13 were considered to evaluate the diffraction response through XRD analysis. Figure 3.30 shows this analysis. It is evident that there is a change in material chemistry due to the reaction in an alkaline solution. The presence of amorphous

(NASH), low crystalline (CSH), quartz (SiO_2), calcite ($CaCO_3$), and margarite (CASH-amorphous) is evident. These compounds lead to the formation of three types of polymeric products viz poly (sialate), poly (sialate-siloxo), and poly (silate-disiloxo). In all the mixes, aluminosilicate substances N-A-S-H and C-A-S-H (2θ = 25-32°) were responsible for initial polymerization as amorphous compounds dissolve easier than crystalline compounds.

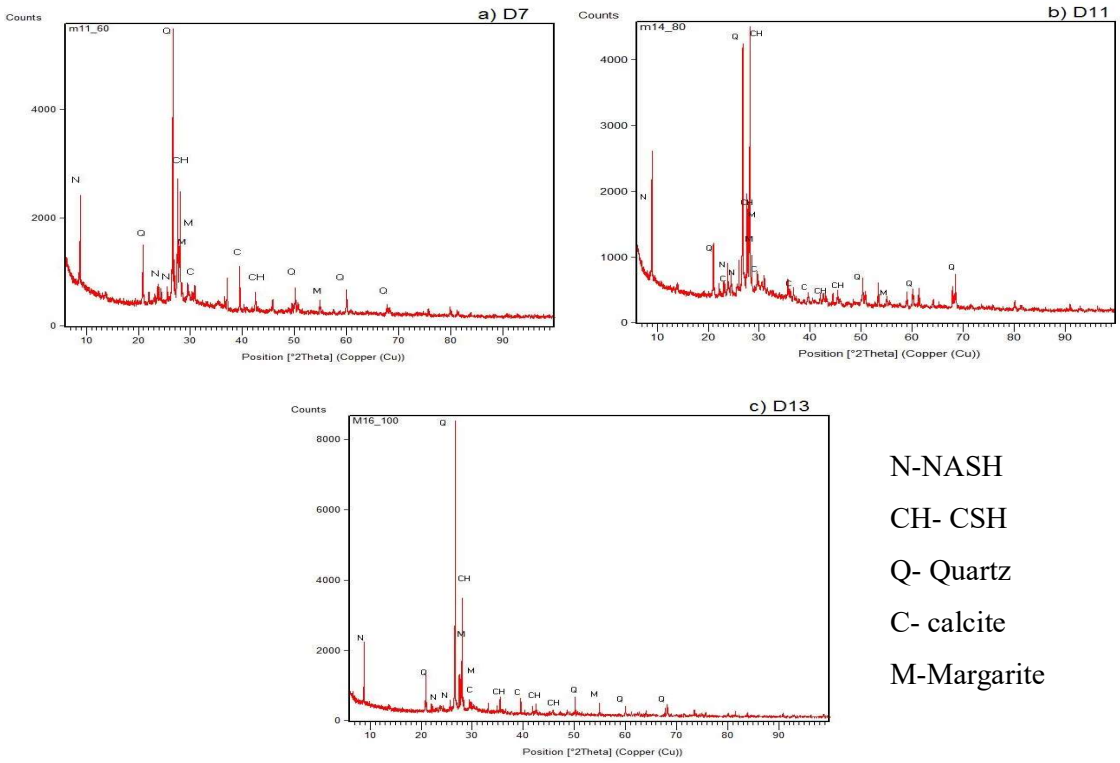

Figure 3.30: XRD analysis of mixes a) D7 b) D11 c) D13

Mostly, broad peaks were observed in the region 2θ =19-32°. It can be observed that mix D13 showed a large peak corresponding to C-S-H, in case of mixes D7 and D11, where large peaks of quartz were noted. The quartz peaks at 2θ = 27° in mix D7 shifted from 5000 counts to 9000 in mix D11, which indicates higher consumption of quartz leading to better mechanical properties than other mixes. A higher volume of binder was converted into crystalline form in mix D11, as more peaks were observed compared to those in mixes D7 and D13. Amorphous silica and aluminosilicates in the silica fume and alccofine led to the formation of aluminosilicate gel that increased the homogeneity and compactness of the microstructure at ambient temperature. Even C-S-H for mix D11 showed nearly 4500 counts, whereas, in the case of mix D7, it was 3500 counts, evidencing that the incorporation of alccofine improved the intensity of silicate and calcium substances. The peaks for calcite were mostly observed in

mix D13 and were due to the incorporation of OPC. Amorphous calcium substances in OPC led to the formation of a high amount of C-S-H and resulted in higher compressive strength at ambient temperatures than mix with 0% OPC.

3.10 General Remarks

A detailed study on the effect of the addition of multi-component binders along with a lower quantity of OPC on the strength and microstructure properties of high-strength geopolymer concrete resulted in the following findings:

- A maximum compressive strength of 103 MPa is achieved with 10% alccofine along with other binders, indicating that alccofine is contributed to increased compressive strength, at room temperature curing condition.
- A splitting tensile strength of 5.81 MPa and a flexural strength of 8.06 MPa were achieved using 10% alccofine along with other mineral admixtures. A correlation was established between the experimental values with those obtained from various codes and there was a good correlation.
- A constitutive model for the prediction of stress-strain behaviour of multicomponent binder-based high-strength GPC is established. It can be concluded that the 'E' of GPC is lower than that of conventional concrete.

$$\sigma = \sigma' \ \frac{\epsilon}{\epsilon_0}\left[\frac{A}{A - 1 + \left(\frac{\epsilon}{\epsilon_0}\right)^B}\right]$$

Where, A= $\frac{\text{Ec}}{262792.3} + 6.45$, $E_c = 2391.85 \text{ x } (f_{ck})^{0.476}$, $\epsilon_0 = 6.161 \text{ x } 10^{-4} \text{ x } \sigma'^{0.424}$ and B = $\frac{2768.633}{\sigma' - 29.55}$

- From SEM analysis, it is evident that GPC samples (alccofine along with other binders) exhibited a dense structure. This can be attributed to polymerisation and polycondensation, resulting in higher compressive strength. An increase in molarity from 14 M to 16 M increased the reactivity of binders and lowered the unreacted particles.
- From the elemental composition, based on the ratio of Si to Al and Na to Al, it is possible to form a 3D network of polysialate-siloxo and polysialate-disiloxo.
- It is evident from the backscatter electron analysis that mix D11 has fewer bright regions with a grey contrast indicating higher reactivity due to higher molarity of 16 M. The mix with 14 M (D7) had unreacted substances and it was brighter.

- N-A-S-H and C-A-S-H gels are the primary causes of higher compressive strength. This is evident from XRD studies. The addition of OPC altered the phases of GPC from amorphous to crystalline.
- Micro binders like silica fume, alccofine and OPC have higher surface area and reactivity. The dissolution of calcareous, siliceous and aluminous substances from the materials facilitated GPC formation and led to a dense microstructure.
- FT-IR spectrum also confirmed the presence of C-A-S-H and N-A-S-H gel in the geopolymer network responsible for improved strength properties at ambient temperature. The ettringite and C-S-H gels indicate the hydration of OPC in geopolymer concrete, which contributes to the improvement in the mechanical and microstructure properties of high-strength GPC.

CHAPTER 4
CHEMICAL RESISTANCE OF HIGH-STRENGTH GEOPOLYMER CONCRETE

4.1 General

In the previous chapter, HSGPC was developed and the strength properties are investigated. The present chapter discusses the chemical resistance of high-strength geopolymer concrete. To realise the second objective defined in Chapter 1, the chemical resistance of HSGPC was determined under acid, chloride and sulfate attack. The developed high-strength concrete mixes, namely, D7, D9 and D11 were considered as 60, 80 and 100 MPa concrete respectively for investigation of their performance under chemical attack such as HCl, H_2SO_4, $MgSO_4$ and NaCl. Non-destructive testing such as rebound hammer, and ultrasonic pulse velocity, are used to assess the chemical resistance of HSGPC.

4.2 Materials

The details of the materials used such as flyash, GGBS, silica-fume, alccofine, sodium hydroxide, sodium silicate, and superplasticizers were already discussed in the previous chapter. The same materials are used in this phase of work too.

4.3 Mix Proportions

Among the high-strength concrete developed in the previous chapter, D7, D9 and D11 mixes were considered under 60, 80, and 100 MPa concrete and are now designated as GP60, GP80 and GP100 for further discussion. The mix proportions of these mixes are presented in Table 4.1.

4.4 Deterioration Characteristics

Chemical resistance is assessed by understanding parameters such as dimensional loss factor, mass loss factor, strength loss factor, and finally acid durability loss factor which are discussed in detail below.

Table 4.1: Mix proportions of HSGPC

Materials / Mixes	GP60	GP80	GP100
Flyash	213.05 (35%)	152.18 (25%)	152.18 (25%)
GGBS	273.92 (45%)	304.35 (50%)	273.92 (45%)
Silica fume	121.74 (20%)	121.74 (20%)	121.74 (20%)
Alccofine	0%	30.44 (5%)	60.87 (10%)
OPC/Alccofine	0%	0%	0%
Fine aggregate (kg/m^3)	702 (45%)	702 (45%)	702 (45%)
Coarse aggregate (kg/m^3)	858 (55%)	858 (55%)	858 (55%)
AA/Bi (alkaline activator) (kg/m^3)	0.38 (231.3)	0.38 (231.3)	0.38 (231.3)
NaOH (kg/m^3)	66.09 (14M)	66.09 (16M)	66.09 (16M)
Na_2SiO_3 (kg/m^3)	165.2	165.22	165.22
SP= 2% (kg/m^3)	12.2	12.2	12.2

4.4.1 Dimensional loss factor

Dimensional Loss Factor (DLF) determines the dimensional difference between the exposed and control specimen i.e., decrease or increase in diagonal dimension. It can be determined from equation 4.1.

$$\text{DLF} = \frac{\delta_1 - \delta_2}{\delta_1} \times 100 \qquad \text{Eq 4.1}$$

Where,

δ_1= length of the diagonal before exposure

δ_2= length of the diagonal after immersion

4.4.2 Mass loss factor

Mass Loss Factor (MLF) elucidates the mass difference due to chemical exposure i. e. increase or decrease in the mass of the specimen after exposure. It can be determined from equation 4.2.

$$\text{MLF} = \frac{m_1 - m_2}{m_1} \times 100 \qquad \text{Eq 4.2}$$

Where,

m_1 = weight of the specimen before exposure

m_2 = weight of the specimen after exposure

4.4.3 Strength loss factor

The strength loss factor (SLF) corresponds to a variation of compressive strength due to a chemical attack i.e., loss or gain of strength after exposure. The compressive strength test procedure is explained in detail in section 4.6 and can be determined from equation 4.3.

$$\text{SLF} = \frac{f_{ae}}{f_{be}} \times \frac{M}{D} \times 100 \qquad \text{Eq 4.3}$$

Where

f_{ae}= Compressive strength after exposure

f_{ae}= Compressive strength before exposure

M= Maximum duration of exposure,

D= Duration at which the durability factor is required

4.4.4 Acid durability loss factor

The Acid Durability Loss Factor (ADLF) is the multiplication of the dimensional loss factor, mass loss factor, and strength loss factor. It can be determined from equation 4.4

$$\text{ADLF} = DLF \times MLF \times ASLF \qquad \text{Eq 4.4}$$

4.4.5 Rebound hammer test

For the control specimens and specimens exposed to various chemicals, the rebound hammer number is determined as per the specifications provided by IS: 13311-2 (1992) at every age of exposure (IS 13311 (Part 2), 1992).

4.4.6 Ultrasonic pulse velocity test

The quality of the exposed samples is compared with control samples at every age of chemical exposure using ultrasonic pulse velocity as per IS: 516 (Part-5): 2018 (IS: 516 Part 5, 2018).

4.5 Experimental Program

In the present chapter, the deterioration behaviour under chemical attack was discussed by exposing the concrete to 5% concentrated HCl, H_2SO_4, $MgSO_4$ and NaCl for a duration of 28, 56 and 90 days for GP60, GP80 and GP100 concrete specimens. The residual compressive strength after exposure to a reagent for respective durations is determined as explained in section 3.6. Also, DLF, MLF, SLF and ADLF were determined for respective exposure duration

for all grades of concrete. The details of the number of test specimens considered are given in Table 4.2.

Table 4.2: Details of specimens cast for chemical resistivity analysis of HSGPC

S.No.	Strength of concrete (MPa)	Duration of exposure	HCl	H_2SO_4	$MgSO_4$	NaCl
1	60	28 days	3	3	3	3
		56 days	3	3	3	3
		90 days	3	3	3	3
2	80	28 days	3	3	3	3
		56 days	3	3	3	3
		90 days	3	3	3	3
3	100	28 days	3	3	3	3
		56 days	3	3	3	3
		90 days	3	3	3	3
Number of specimens in each case			27	27	27	27
Total Number of Specimens			108			

4.6 Results and Discussions

The chemical resistance of HSGPC subjected to 5% concentrated HCl, H_2SO_4, $MgSO_4$ and NaCl are discussed through deterioration characteristics in the subsequent sections.

4.6.1 DLF and MLF of high-strength GPC subjected to chemical exposure

Figure 4.1 shows the DLF and MLF of HSGPC with respect to the age of exposure for HCl, H_2SO_4, $MgSO_4$, and NaCl. It can be observed that with an increase in exposure period, DLF is increased in case of acids, sulfate, and chloride exposure. Whereas MLF increased with an increase in the duration of exposure in case of acids exposure, while weight gain (negative values of MLF) is observed in case of sulfate and chloride exposure. The DLF and MLF are higher in case of acid exposure due to H_2SO_4 compared to other chemicals. The order of higher DLF and MLF in case of high-strength GPC is H_2SO_4 > HCl > $MgSO_4$ > NaCl. Acids showed lower chemical resistance compared to sulfate and chloride since acids provide a much lower pH environment than sulfate and chloride. It is also observed that with an increase in the grade of GPC, the DLF increased in case of HCl, $MgSO_4$, and NaCl. In case of H_2SO_4, for exposure duration up to 56 days, the GP60 mix showed higher DLF and MLF compared to GP80 and GP100. As the exposure duration increased to 90 days, the GP60 showed lower DLF and MLF indicating that a higher percentage of the siliceous and a lower percentage of the calcium compounds increased the acid resistance at a longer exposure period compared to mixes having

a higher percentage of calcium compounds and a lower percentage of siliceous compounds. This is similar to the findings of Mehta & Siddique, 2017 and Vafaei & Allahverdi, 2017 who mentioned that calcium compounds generate calcium salts ($CaSO_4$ and $CaCl_2$) additionally when exposed to chemical reagents. In all the exposure conditions beyond 56 days, the difference between GP80 and GP100 mixes in DLF and MLF is not significant showing that improved compressive strength due to the additional calcium compounds does not contribute to the acid, chloride and sulfate resistance beyond 56 days of chemical exposure.

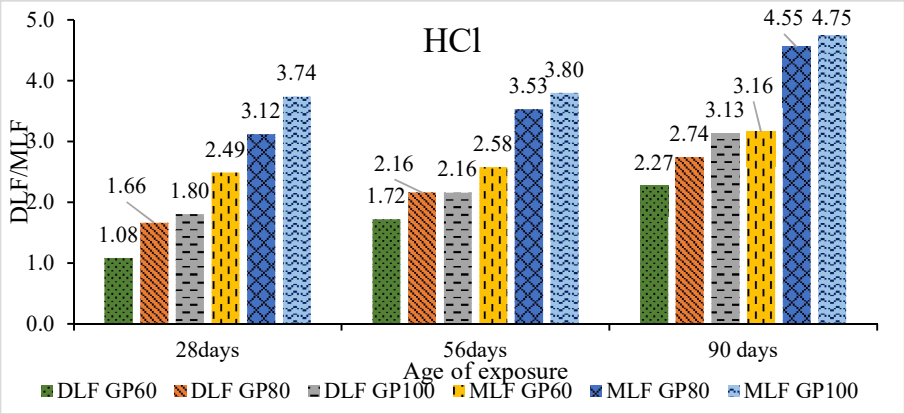

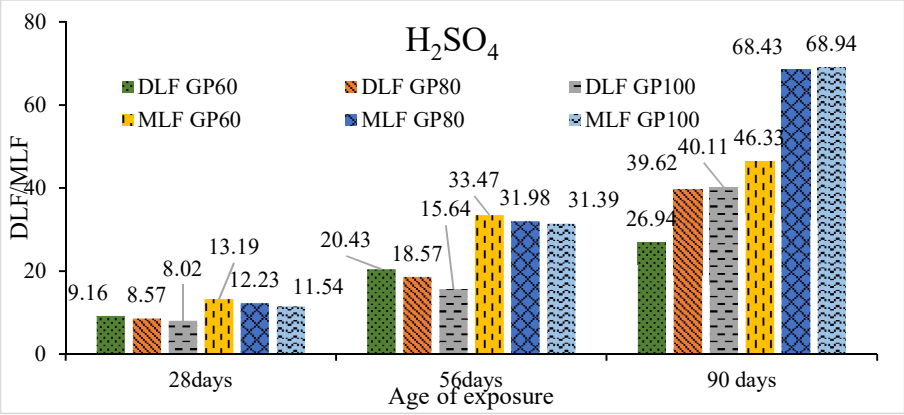

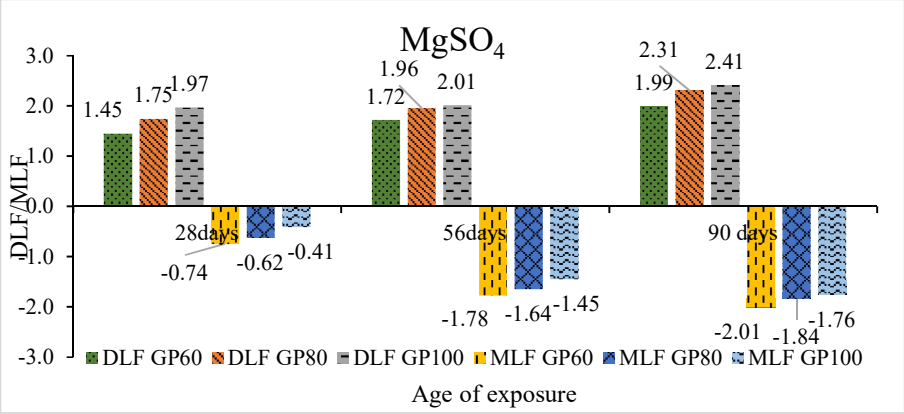

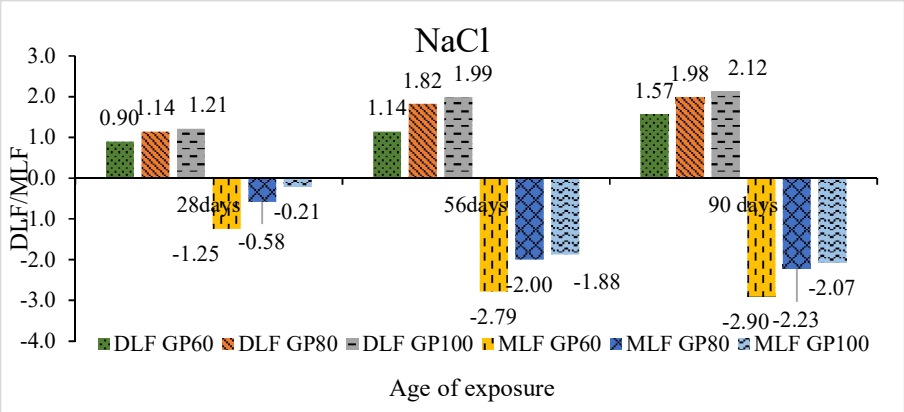

Figure 4.1: DLF and MLF of HSGPC with respect to exposure period for 5% concentrated a) HCl b) H_2SO_4 c) $MgSO_4$ d) NaCl exposure

4.6.2 SLF of high-strength GPC subjected to chemical exposure

Figure 4.2 shows the SLF of HSGPC with age of exposure for HCl, H_2SO_4, $MgSO_4$, and NaCl. It can be observed that similar to DLF, with an increase in exposure period, SLF is increased in case of acids, sulfates, and chlorides. The SLF is higher in case of exposure to H_2SO_4 compared to other chemicals. The magnitude of SLF varied from 30.9 to 64.9 in exposure condition HCl, 47.24 to 74.83 in case of H_2SO_4, 12.8 to 37.4 in case of $MgSO_4$, and 6.6 to 31.6 in case of NaCl. The order of higher SLF is H_2SO_4 > HCl > $MgSO_4$ >NaCl. It is also observed that with an increase in the grade of GPC, the SLF is increased in case of HCl, $MgSO_4$, and NaCl exposure. In case of H_2SO_4, for an exposure duration of up to 28 days, the GP60 mix showed higher SLF compared to GP80 and GP100. As the exposure duration increased to 56 and 90 days, GP60 showed lower SLF indicating that a higher percentage of siliceous and lower percentage of calcium compounds increased acid resistance compared to mixes having a higher percentage of calcium compounds and lower percentage of siliceous compounds, which is similar to the findings of Mehta & Siddique, 2017 and Vafaei & Allahverdi, 2017.

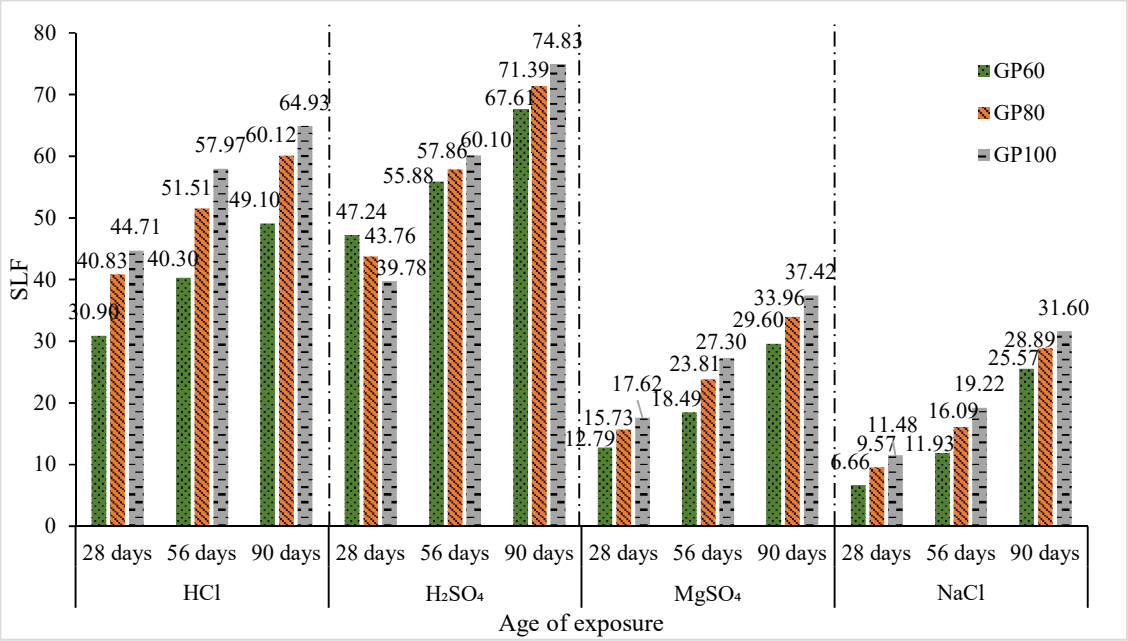

Figure 4.2: SLF of HSGPC with respect to exposure duration for 5% concentrated a) HCl b) H_2SO_4 c) $MgSO_4$ d) NaCl exposure

4.6.3 ADLF of high-strength GPC subjected to chemical exposure

Figure 4.3 shows the ADLF of HSGPC with respect to the exposure period for HCl, and H_2SO_4. ADLF applies to acid exposure conditions. It can be observed that similar to DLF and SLF, with an increase in exposure period, ADLF increased showing that for increased duration of exposure, the chemical resistance of HSGPC is decreased. ADLF was higher in case of acid exposure due to H_2SO_4 compared to HCl. The magnitude of ADLF varied from 83.2 to 964.9 for exposure to HCl, and 5708.47 to 206949.1 for H_2SO_4. It was also observed that with an increase in the grade of GPC, ADLF increased in case of HCl. In case of H_2SO_4, for an exposure duration of up to 56 days, the GP60 mix showed higher ADLF compared to GP80 and GP100. With exposure to 90 days, GP60 showed lower SLF indicating that a higher percentage of siliceous and lower percentage of calcium compounds increased acid resistance compared to mixes having a higher percentage of calcium compounds and a lower percentage of siliceous compounds.

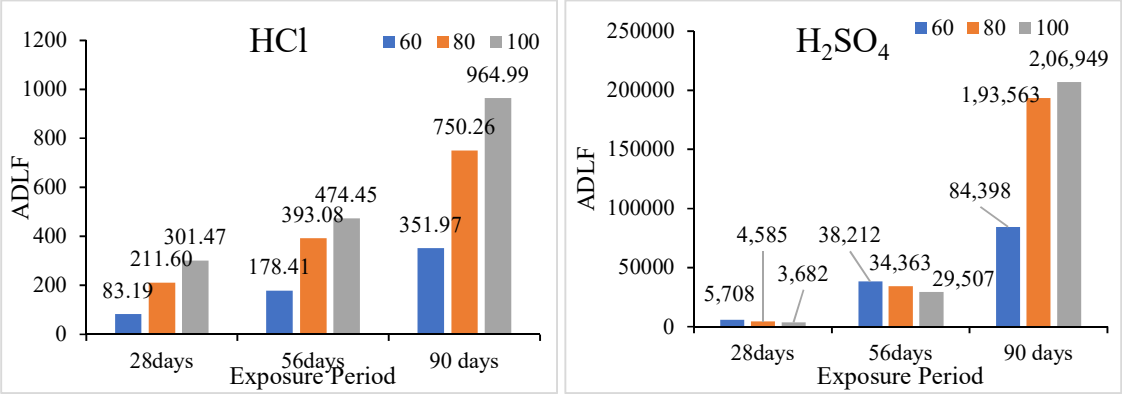

Figure 4.3: ADLF of HSGPC with respect to exposure duration for 5% concentrated a) HCl b) H_2SO_4 exposure

4.6.4 Rebound number of high-strength GPC subjected to chemical exposure

To examine the MLF, DLF, SLF and ADLF, the rebound number for exposed concrete is investigated and the results are given in Figure 4.4. It can be observed that the rebound number decreased with an increase in exposure duration which is similar to the behaviour of DLF and SLF. In case of H_2SO_4, for an exposure period of 90 days, the concrete didn't show any rebound number indicating low residual compressive strength; similar behaviour can also be observed from SLF response. The rebound number varied from 46.52 to 16 for exposure to HCl, 46.52 to 0 for H_2SO_4, 46.52 to 32 for $MgSO_4$, and 46.52 to 36 for NaCl. The rebound number for different exposures followed the order NaCl>$MgSO_4$>HCl>H_2SO_4. It can also be observed that in all exposure conditions, after the exposure duration of 56 days, the mix GP60 concrete showed a higher rebound number than GP80 and GP100 indicating a lower loss of strength after chemical exposure; similar behaviour can also be observed from SLF and DLF response analysis.

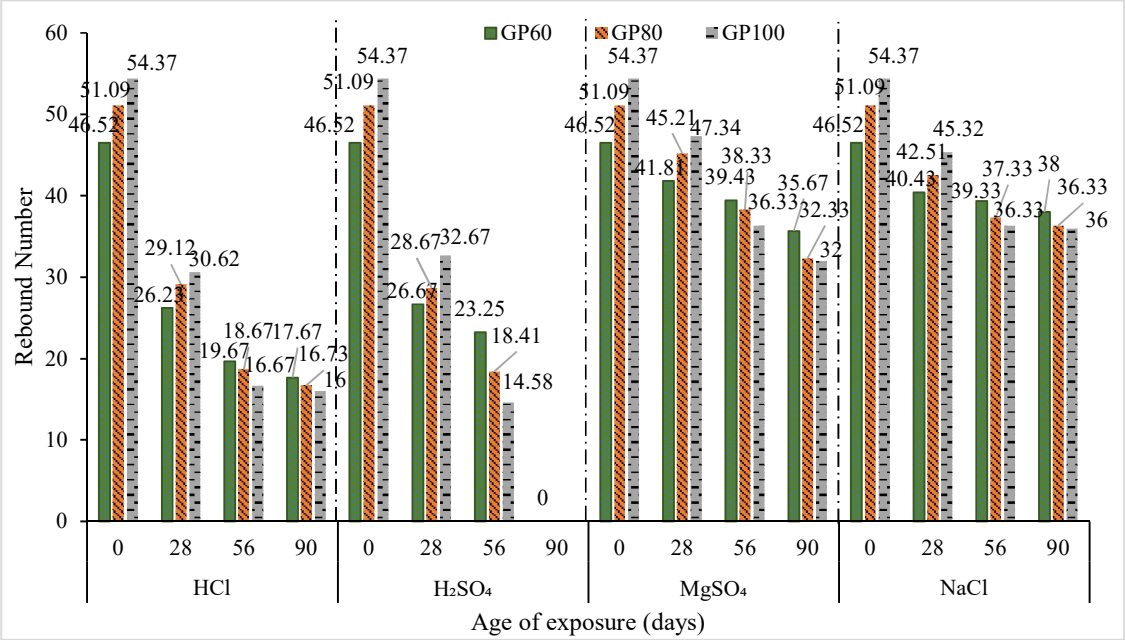

Figure 4.4: Rebound number with respect to exposure duration for 5% concentrated a) HCl b) H_2SO_4 c) $MgSO_4$ d) NaCl exposure

4.6.5 UPV response of high-strength GPC subjected to chemical exposure

Along with the rebound number, the UPV test was performed to examine the loss factor. Figure 4.5 shows the ultrasonic pulse velocity of HSGPC exposed to chemicals with respect to exposure duration. It can be observed that with increasing exposure period in all exposure conditions, UPV decreased showing the deterioration of concrete, similar to the behaviour observed from DLF, SLF and rebound analysis. In case of H_2SO_4, the concrete does not allow infrared rays as the surface of the concrete deteriorated showing the low residual compressive strength, similar behaviour can also be observed in SLF response. The velocity of exposed specimens varied from 3.8 to 2.1 for exposure condition to HCl, 3.8 to 0 for H_2SO_4, 3.8 to 3.24 for $MgSO_4$, and 3.8 to 3.36 for NaCl. The UPV number follows the order NaCl>$MgSO_4$>HCl>H_2SO_4. It can also be observed that in all exposure conditions excluding H_2SO_4 after exposure duration of 56 days, GP60 concrete mix showed higher velocity indicating lower loss of strength after chemical exposure; similar behaviour can also be observed with SLF and DLF response analysis.

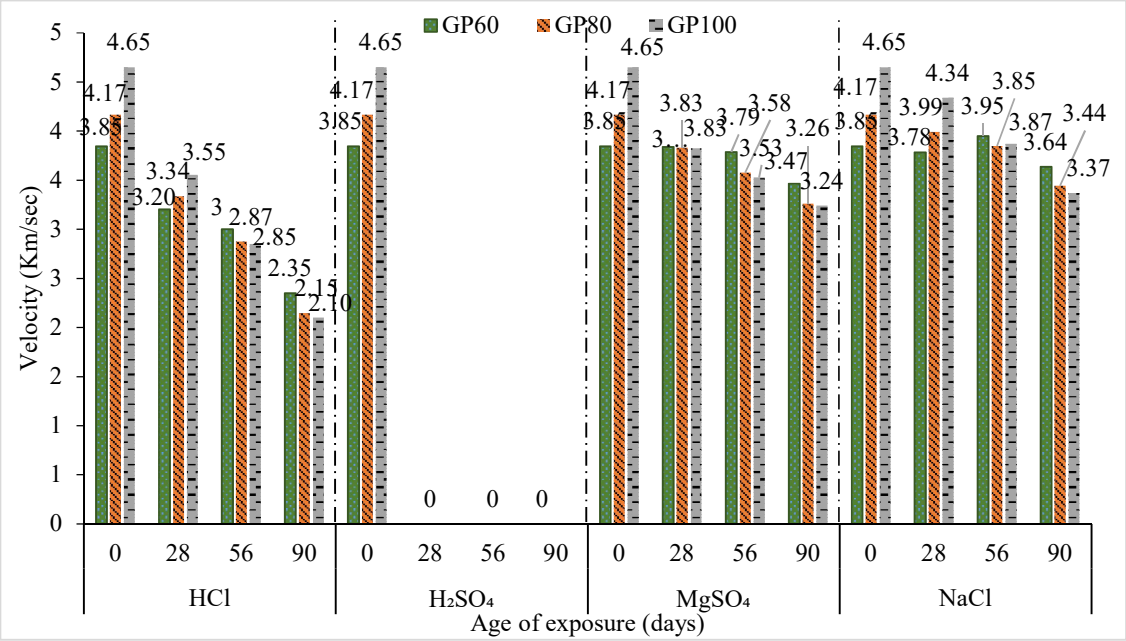

Figure 4.5: Ultrasonic pulse velocity with respect to exposure duration for 5% concentrated a) HCl b) H_2SO_4 c) $MgSO_4$ d) NaCl exposure

4.7 General Remarks

Based on the experiments on chemical resistance of HSGPC subjected to 5% concentrated HCl, H_2SO_4, $MgSO_4$, and NaCl for 28, 56 and 90 days of exposure, the following conclusions can be drawn.

- Dimensional Loss Factor (DLF), Mass Loss Factor (MLF), and Strength Loss Factor (SLF) of HSGPC increased with increasing exposure period in case of HCl, H_2SO_4, $MgSO_4$ and NaCl chemicals.
- The DLF, MLF, SLF, and Acid Durability Loss Factor (ADLF) increased with the grade of concrete for a definite exposure period and different chemical exposure conditions.
- For an exposure period of 90 days of HCl, H_2SO_4, $MgSO_4$ and NaCl, 60 MPa concrete showed lower chemical resistance compared with 80 and 100 MPa by exhibiting lower DLF, MLF, SLF, and ADLF values, indicating that a higher percentage of siliceous compounds than calcium compounds increase the resistance of concrete to acid, sulphate and chloride.
- In all exposure conditions, for exposure durations of 56 and 90 days, DLF, MLF, SLF, and ADLF values of 80 and 100 MPa HSGPC did not show significant difference

indicating improved compressive strength due to additional calcium compounds which does not contribute to acid, sulfate resistance beyond 56 day of chemical exposure.

- The extent of deterioration due to exposure condition follows the order H_2SO_4 > HCl >$MgSO_4$ > NaCl.
- The rebound number and USPV results are in line with deterioration characteristics such as DLF, SLF, and MLF.

CHAPTER 5
BOND BEHAVIOUR OF HIGH-STRENGTH GEOPOLYMER CONCRETE

5.1 General

In the previous chapter, the performance of multicomponent-based HSGPC under chemical exposure was explained. The present chapter deals with the experimental bond behaviour of HSGPC. To realise the third objective defined in Chapter 1, various parameters that affect the bond behaviour like concrete strength (60, 80, and 100 MPa), bar diameter (D= 12, 16 and 20 mm), and embedment length (2.5D, 5D, and full depth), type of test (Pullout and Hinged beam test) and cover of concrete (16, 20 and 40 mm) were considered and the experimental program was carried out (Phase III).

5.2 Materials

Materials like cement, flyash, GGBS, silica fume, alccofine, and superplasticizers which are used in the preparation of concrete as already discussed in Chapter 4, were used in the experiment.

5.3 Mix Proportions

Among the high-strength concretes developed earlier, D7, D9 and D11 were considered for 60, 80, and 100 MPa concretes and designated as GP60, GP80 and GP100 for further discussion. The mix proportions of these mixes are presented in Table 4.1.

5.4 Pullout Test

The pullout test is considered to determine the anchorage bond behaviour of HSGPC. Three concrete mixes (GP60, GP80 and GP100), three bar diameters (D=10, 12 and 16 mm) and three embedment lengths (L =2.5D, 5D and full depth of the specimen) are the parameters chosen for the study. According to IS: 2770:1967 part 1, cube sizes of 100 X 100 X 100 mm for 12 mm bar diameter bars, and 150 X 150 X 150 mm for 16- and 20-mm bar diameter were chosen for the pullout test. The details of the specimens cast for the pullout test for HSGPC are shown in Table 5.1. The experimental setup for the test is shown in Figure 5.1. For distributing the stress

uniformly, a steel plate 20 mm thick and 20 mm wide was placed over the specimen. The load was applied at a rate of 2250 kg/min. The bond stress was calculated as the load per unit contact area between steel and concrete. For the calculation of bond stress, Equation 5.1 was used.

$$\tau_{max} = \frac{P_{max}}{\pi D l} \quad \text{Eq 5.1}$$

P_{max}= is the maximum load taken by the specimen i.e., load corresponding to failure of the specimen, kN

D= Diameter of the bar, mm

l= embedment length, mm

Table 5.1: Details of the test specimens cast for the pullout test of HSGPC

S.No.	Concrete strength	Diameter of bar (D) (mm)	Embedment length (mm)	Cube specimen size (mm)	Number of specimens
1	60/80/100 MPa	12	30	100	3
2			60		3
3			100		3
4		16	40	150	3
5			80		3
6			150		3
7		20	50	150	3
8			100		3
9			150		3
Total number of specimens = 27 x 3					81

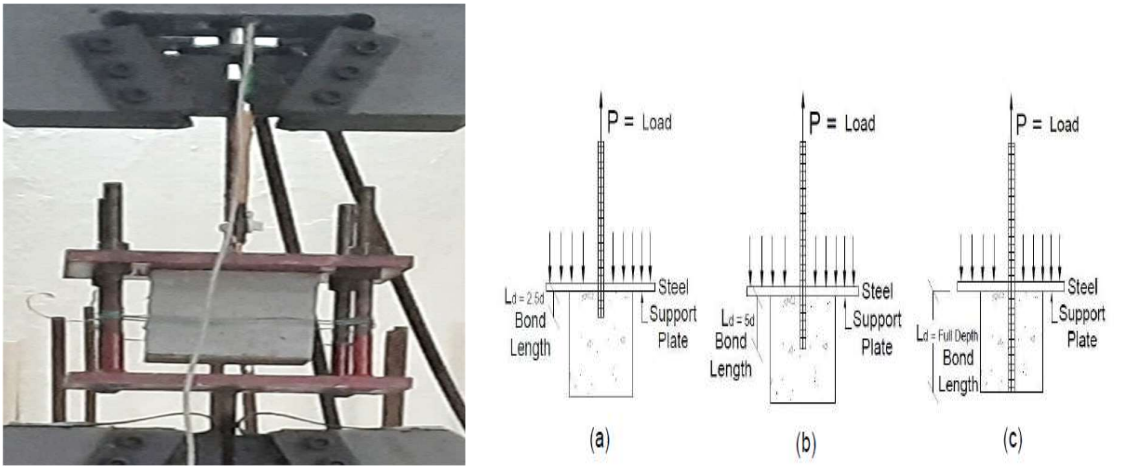

Figure 5.1: A) experimental test setup B) force distribution in pullout specimen-a) 2.5D b) 5D c) Full depth of the specimen

5.5 Flexural Bond Test

Flexure bond results from a change in bending moment throughout the length of the member, which causes a change in the tensile force carried by the bar along its length. Since this bond occurs at a particular localised place, it is also called local bond stress. In the present study, a hinged beam test proposed by RILEM Fip-Ceb-RC5-TC9 (Rilem-Fip-Ceb-RC5-TC9, 1973) was adopted to assess the bond behaviour of HSGPC. The specimens and reinforcement details given by RILEM are shown in Figure 5.2 for Type A (for up to 16 mm bar diameter) and for Type B (for above 16 mm bar diameter) shown in Figure 5.3. It consists of two rectangular half beams connected by a reinforcement at the bottom and a hinge at the top to transfer the force equally to half beams. The free-body diagram of force distribution in the RILEM beam is shown in Figure 5.4 (a). The details of the test specimens considered in the present study are given in Figure 5.2 and Figure 5.3. The stress-strain behaviour of 12, 16, and 20 mm steel bars is shown in Figure 5.4 (b). The tensile stresses in the flexural reinforcement are calculated by Equation 5.2. The flexural bond strength is calculated by Equation 5.3.

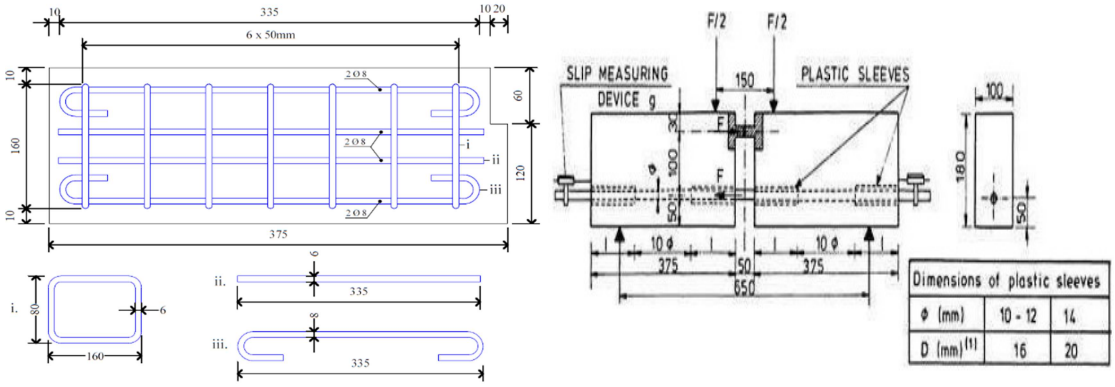

Figure 5.2: Specimen dimensions and reinforcement details of hinged beam for type A.

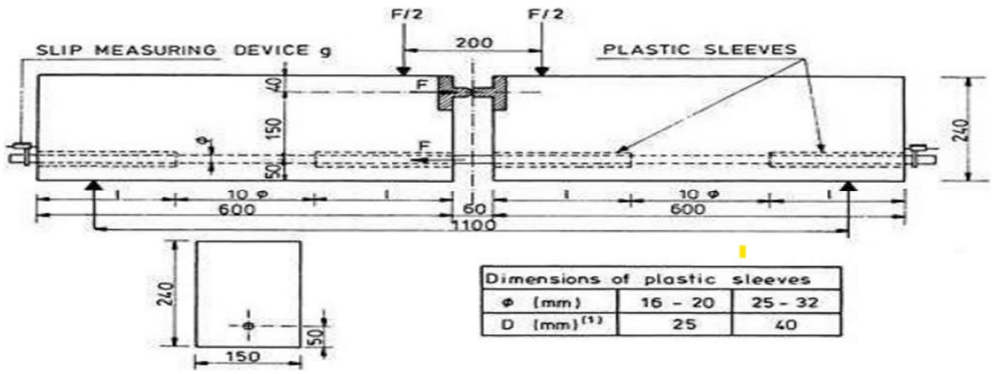

Figure 5.3: Specimen dimensions and reinforcement details of hinged beam for type B.

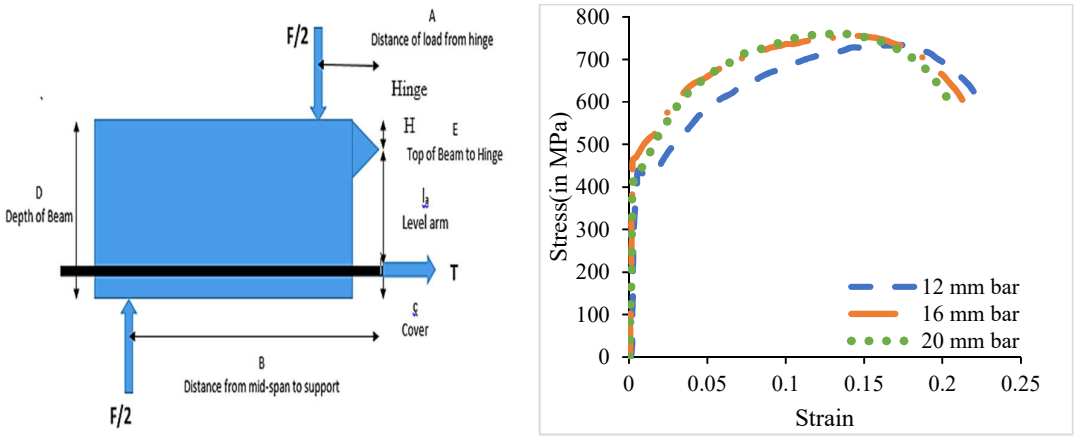

Figure 5.4: a) Free body diagram of Rilem hinged beam b) Stress-Strain behaviour of 12, 16 and 20 mm HYSD bar

$$\sigma_s = \frac{k \times P}{A_s} \qquad \text{Eq 5.2}$$

$$\tau_{bd} = \frac{\sigma_s \times A_s}{\pi \times \Phi \times l_d} \qquad \text{Eq 5.3}$$

Where, $K = F \times \frac{B-A}{2 \times l_a}$ (from Figure 5.4)

P = Load applied on the beam

A_s = Area of steel

Φ = bar diameter

l_a = Lever arm= (D-E-C) (from Figure 5.4)

The hinged beam specimens were tested under a displacement-controlled testing machine (Figure 5.5) with a 0.016 mm/sec loading rate. The slip of the bar at two ends of the rectangular beam was measured using Linear Variable Differential Transducers (LVDT) and the measurements were recorded using a data acquisition system continuously. The load was applied symmetrically to the mid-span onto the two half beams.

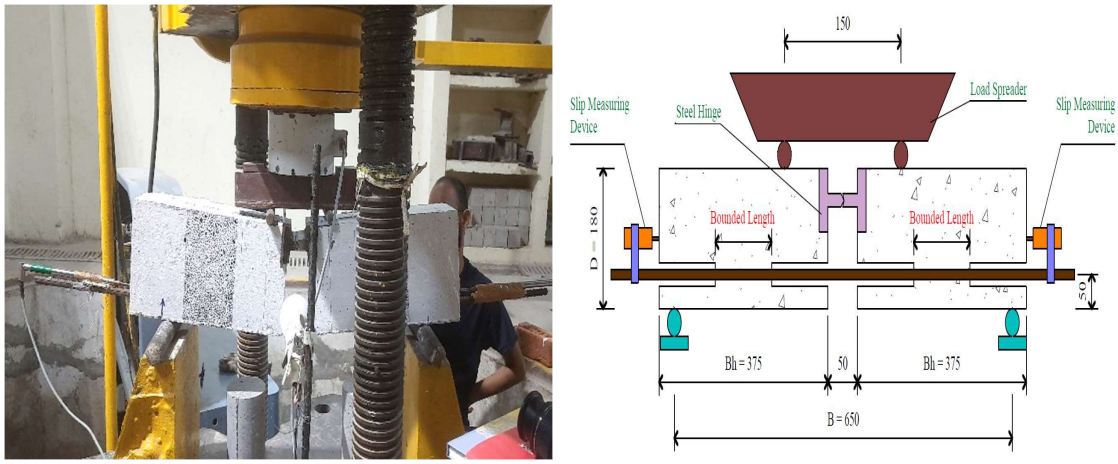

Figure 5.5: Test setup Configuration a) Experimental test setup b) 2D test setup

5.6 Anchorage Bond Behaviour of HSGPC through Pullout Test

In the present research, the influence of concrete compressive strength, bar diameter (D) and embedment length (l_d) on the anchorage bond strength of HSGPC was investigated experimentally based on 81 pullout specimens. The details of the test specimens are given in Table 5.2.

Table 5.2: Details of the flexural specimens for experimental investigation.

Specimen identification	Compressive strength of concrete (MPa)	Cover to bar (C) (mm)	Bar diameter (D) (mm)	Embedment length (l_d) = 10 Φ (mm)	Factor k
GP60C16D12	67.87	16	12	120	0.977
GP80C16D12	85.11	16			
GP100C16D12	103.02	16			
GP60C40D12	67.87	40			1.2
GP80C40D12	85.11	40			
GP100C40D12	103.02	40			
GP60C16D16	67.87	16	16	160	0.992
GP80C16D16	85.11	16			
GP100C16D16	103.02	16			
GP60C40D16	67.87	40			1.225
GP80C40D16	85.11	40			
GP100C40D16	103.02	40			
GP60C20D20	67.87	20	20	200	1.32
GP80C20D20	85.11	20			
GP100C20D20	103.02	20			
GP60C40D20	67.87	40			1.5
GP80C40D20	85.11	40			
GP100C40D20	103.02	40			

5.6.1 Influence of compressive strength on anchorage bond behaviour of HSGPC

The anchorage bond stress-slip curves with respect to changes in compressive strength of concrete are shown in Figure 5.6 - 5.8**.** The notation 12-FD-100 indicates the bond stress-slip curve for a 12 mm bar diameter with full embedment length for the 100 MPa concrete. Similar notations were used to indicate other parameters considered in the test specimen. It can be observed that with an increase in the compressive strength of concrete, the anchorage bond strength increased; also, there was a decrease in slip corresponding to maximum bond strength (δ_{mslip}) keeping other parameters as constant. The reason could be that with increased compressive strength, the splitting tensile strength increased and also the ITZ between aggregate and geopolymeric gel became very dense which resulted in increased radial tensile resistance caused by the pulling of the bar which is in line with the results of Topark-Ngarm et al., 2015. Table 5.3 and 5.4 show the maximum anchorage bond strength and δ_{mslip} variations with respect to change in compressive strength of concrete. The average percentage of increase

in the maximum bond strength decreased, while the average δ_{mslip} decreased with increase in the grade of concrete. The reason could be attributed to an increase in compressive strength, the adhesion between the reinforcement and concrete increases delaying the slipping of the bar. The average percentage increase in bond strength with an increase in grade of concrete from 60 MPa to 80 MPa was 10.42% and the average decrease in δ_{mslip} was 10.29%. The maximum bond stress (τ_{max}) was normalised with respect to equivalent cube compressive strength (f_{cc}) i.e., $\frac{\tau max}{\sqrt{fcc}}$. The variation of normalised maximum bond stress with concrete strength from Figure 5.16 is given in Table 5.10. The statistical value of closeness i.e., the coefficient of determination is also given in Table 5.10. From this table, it is quite evident that there exists a close relation between the compressive strength and normalised maximum bond stress. The closeness of the regression line was as good as 85% to 99%. The regression equation and value of regression for maximum slip and concrete strength from Figure 5.15 is given in Table 5.9 and it can be observed that there exists a good relation between slip and concrete strength. The value of regression varies between 0.87 and 0.99.

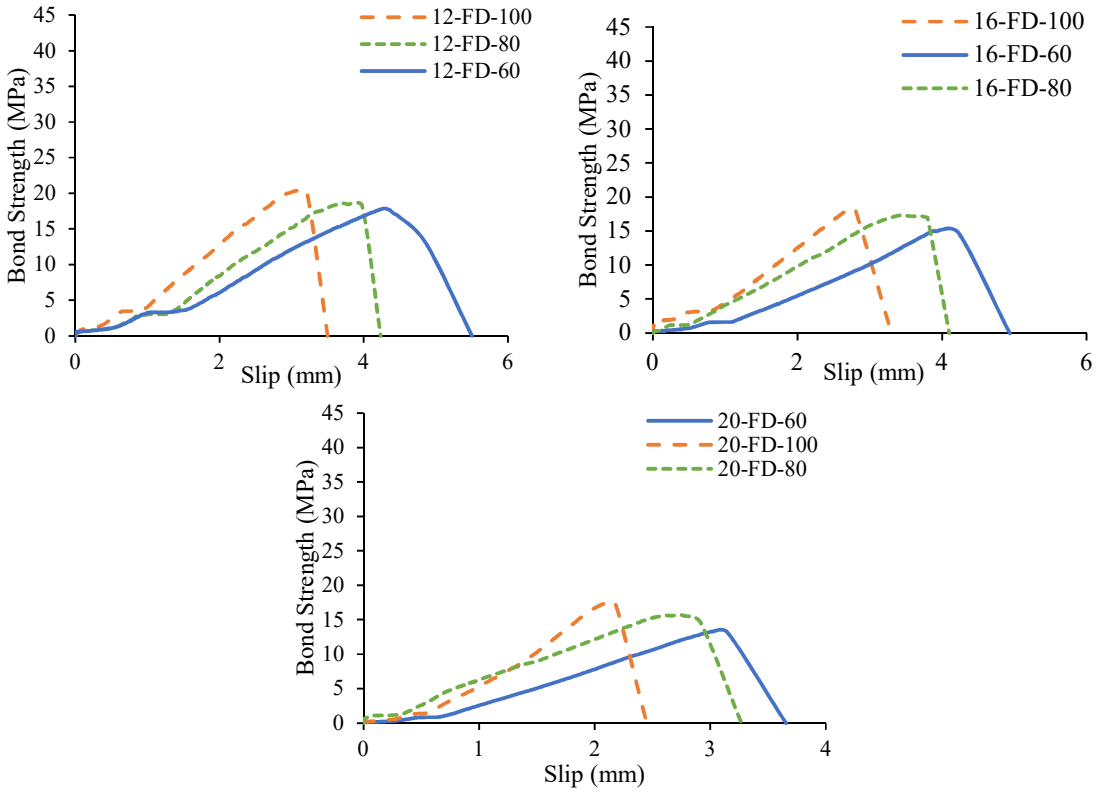

Figure 5.6: Bond stress-slip curves of HSGPC with respect to the compressive strength of concrete for full embedment length

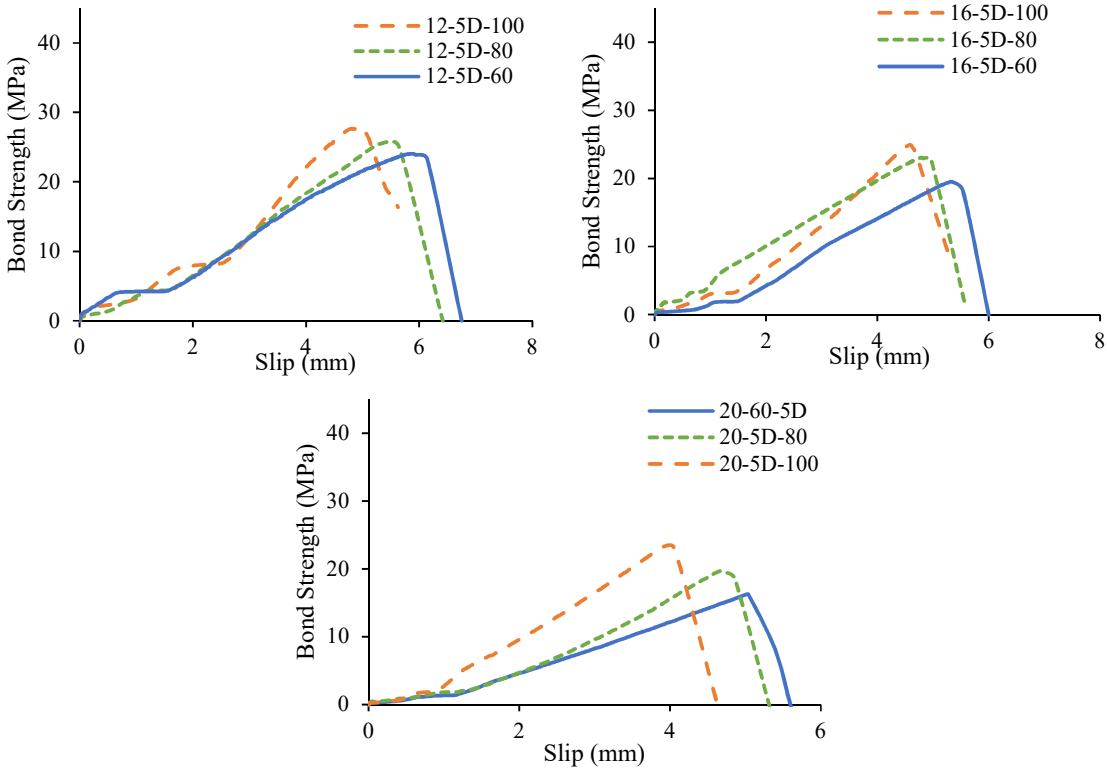

Figure 5.7: Bond stress-slip curves of HSGPC with respect to the compressive strength of concrete for 5D embedment length

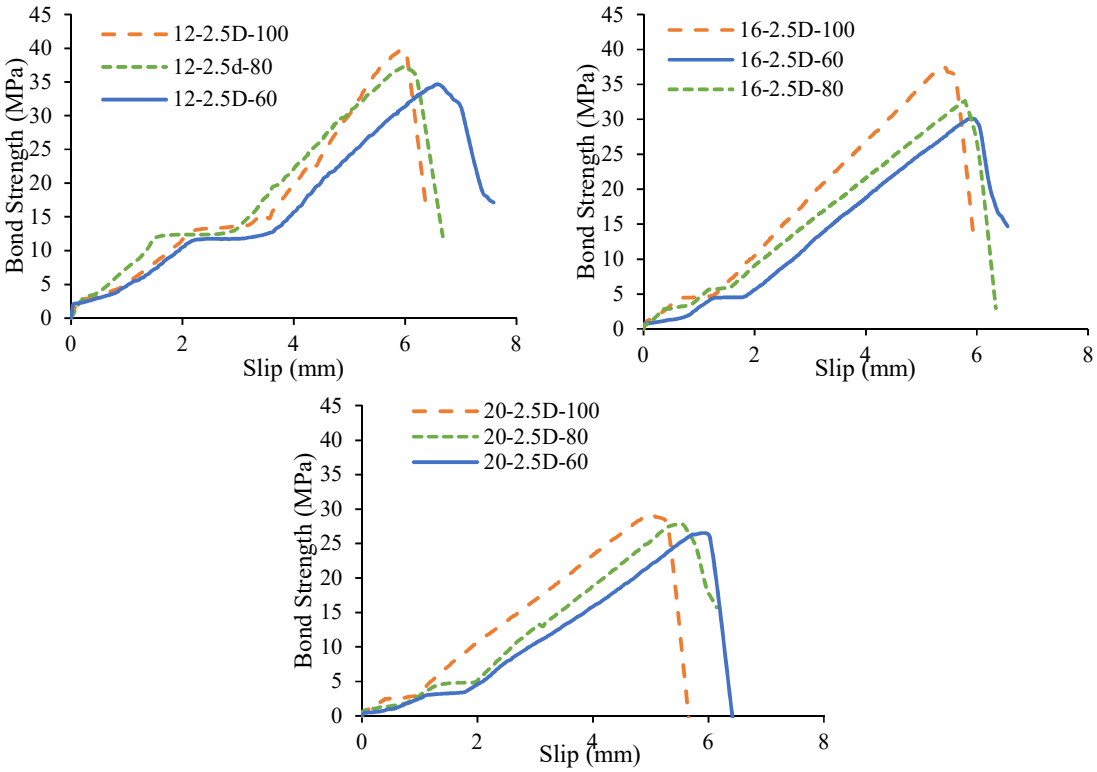

Figure 5.8: Bond stress-slip curves of HSGPC with respect to the compressive strength of concrete for 2.5D embedment length

Table 5.3: Maximum anchorage bond strength with respect to change in compressive strength of concrete

D (mm) -L (mm)	Maximum bond strength (MPa)			% Increase	
	60 MPa	80 MPa	100 MPa	60 to 80 MPa	80 to 100 MPa
12-30	34.66	37.24	39.68	7.43	6.55
12-60	24.06	25.47	27.84	5.90	9.28
12-100	17.87	18.59	20.32	4.01	9.31
16-40	30.08	32.61	37.50	8.40	14.97
16-80	19.52	23.07	24.94	18.16	8.12
16-150	15.03	15.69	17.42	4.44	10.98
20-50	26.32	27.87	29.14	5.92	4.55
20-100	16.24	19.68	23.10	21.18	17.37
20-150	13.26	15.69	17.42	18.32	10.98
Average				10.42	10.24

Table 5.4: Variation of δ_{mslip} with respect to change in compressive strength of concrete

D (mm) -L (mm)	δ_{mslip} (mm)			% Decrease	
	60 MPa	80 MPa	100 MPa	60 to 80 MPa	80 to 100 MPa
12-30	6.56	6.01	5.90	8.48	1.82
12-60	5.86	5.32	4.98	9.29	6.28
12-100	4.27	3.72	3.06	13.03	17.82
16-40	5.90	5.78	5.39	2.16	6.75
16-80	5.33	4.79	4.58	10.05	4.36
16-150	3.89	2.74	2.18	29.60	20.53
20-50	5.72	5.53	5.00	3.43	9.61
20-100	5.04	4.67	4.05	7.40	13.16
20-150	3.02	2.74	2.18	9.17	20.53
Average				10.29	10.21

5.6.2 Influence of embedment length on anchorage bond behaviour of HSGPC

The anchorage bond stress-slip curves with respect to various embedment lengths of the bar are shown in Figure 5.9 – 5.11. It can be observed that with an increase in the embedment length of the bar, the anchorage bond strength of concrete decreased; also, there was a decrease in slip corresponding to the maximum bond strength (δ_{mslip}) when keeping other parameters as constant. The reason could be that with increased embedment length, the non-uniformity of stress distribution along the bar increases, which results in reduced bond strength. Similar observations are reported in the research of Dahou et al., 2016 and Z. Ma et al., 2023. Table 5.5 and 5.6 show the maximum anchorage bond strength and δ_{mslip} variations with respect to

various embedment lengths. The average percentage of decrease in the maximum bond strength decreased with an increase in the embedment length while the average δ_{mslip} increased with increase in embedment length. The reason could be attributed to the fact that with increased embedment length, the contact area is high to resist pullout load which retards the movement of the bar along the direction of load. The average percentage decrease in bond strength with an increase in embedment length 2.5D to 5D and 5D to FD was 30.68 and 26.58% respectively while the average decrease in δ_{mslip} was 12.58 and 31.94% respectively for 12 mm bar diameter.

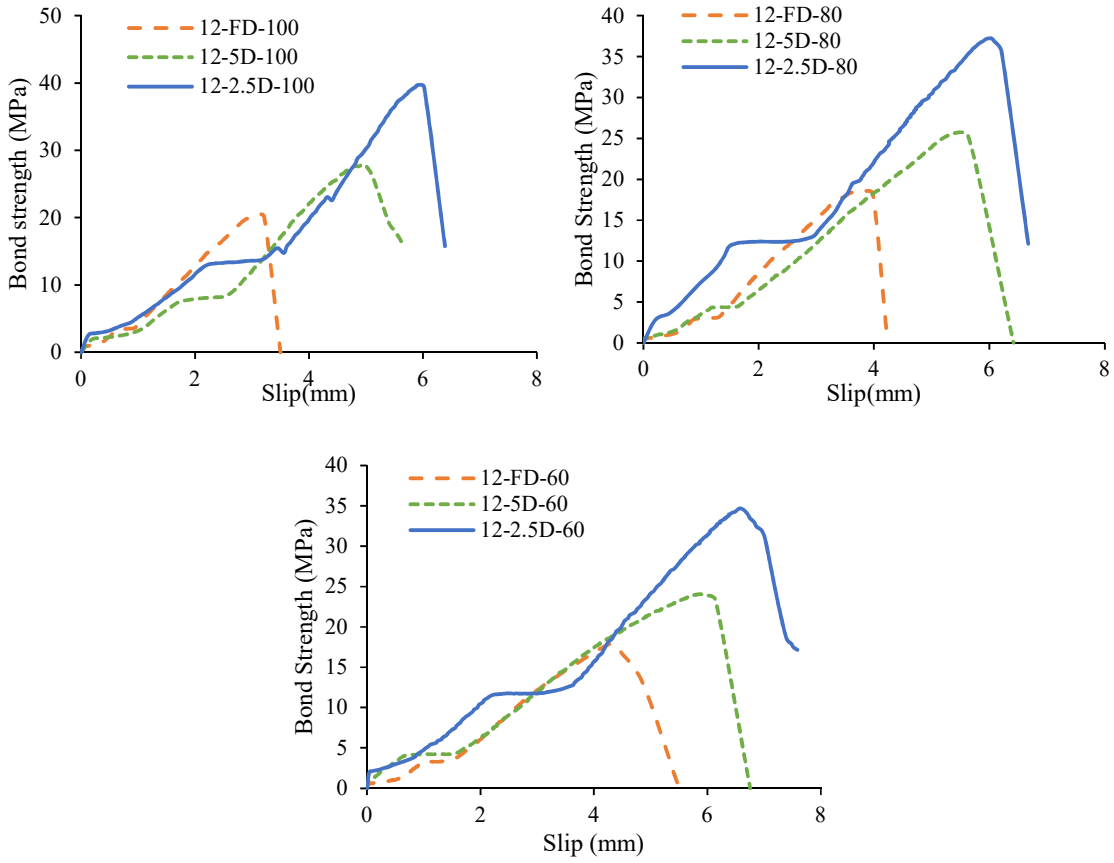

Figure 5.9: Bond stress-slip curves of HSGPC with respect to various embedment lengths for 12 mm bar diameter

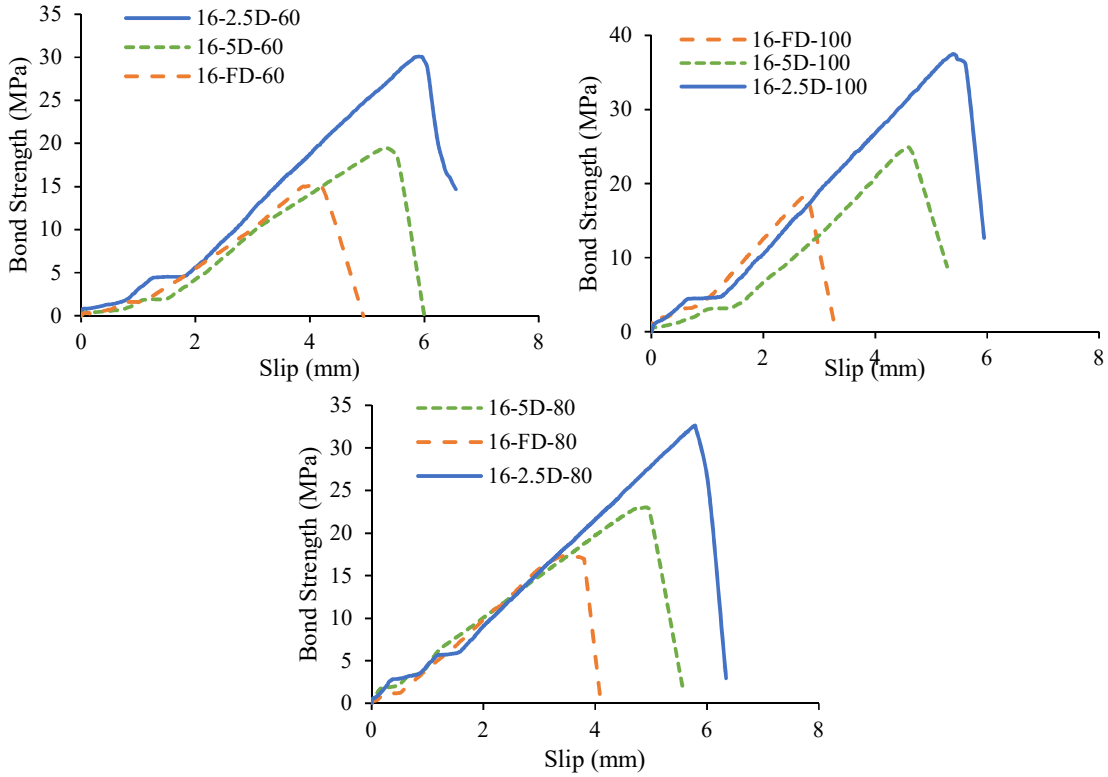

Figure 5.10: Bond stress-slip curves of HSGPC with respect to various embedment lengths for 16 mm bar diameter

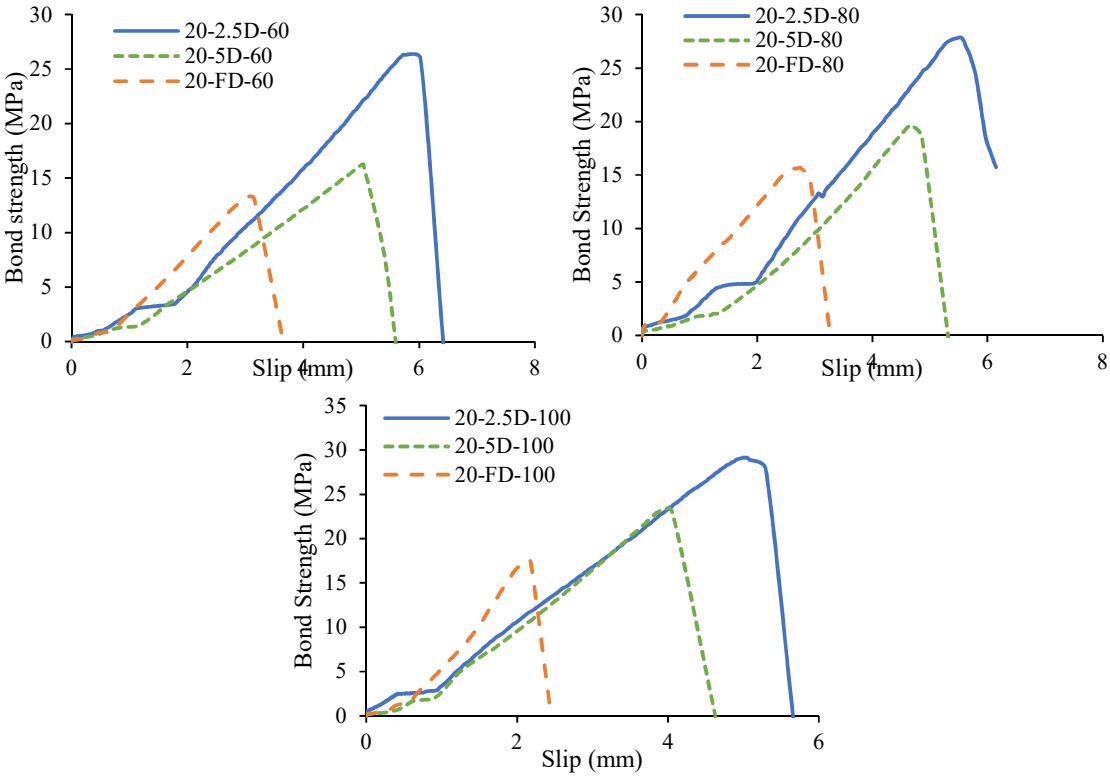

Figure 5.11: Bond stress-slip curves of HSGPC with respect to various embedment lengths for 20 mm bar diameter.

Table 5.5: Maximum anchorage bond strength with respect to various embedment lengths of bar

D (mm)	L (mm)	Maximum bond strength (MPa)			Average %
		60 MPa	80 MPa	100 MPa	
12	30	34.66	37.24	39.68	
12	60	24.06	25.47	27.84	
12	100	17.87	18.59	20.32	
%Decrease in bond stress	30-60	30.60	31.59	29.84	30.68
	60-100	25.71	27.03	27.01	26.58
16	40	30.08	32.61	37.50	
16	80	19.52	23.07	24.94	
16	150	15.03	17.33	18.19	
%Decrease in bond stress	40-80	35.11	29.27	33.49	32.62
	80-150	23.03	24.88	27.05	24.99
20	50	26.32	27.87	29.14	
20	100	16.24	19.68	23.10	
20	150	13.26	15.69	17.42	
%Decrease in bond stress	50-100	38.28	29.39	20.73	29.47
	100-150	18.34	20.27	24.61	21.07

Table 5.6: Variation of δ_{mslip} with respect to various embedment lengths of bar

D (mm)	L (mm)	δ_{mslip} (mm)			Average %
		60 MPa	80 MPa	100 MPa	
12	30	6.56	6.01	5.90	
12	60	5.86	5.32	4.98	-
12	100	4.27	3.72	3.06	
% Decrease in δ_{mslip}	30-60	10.71	11.50	15.52	12.58
	60-100	27.06	30.07	38.69	31.94
16	40	5.90	5.78	5.39	
16	80	5.33	4.79	4.58	-
16	150	3.89	3.46	2.73	
% Decrease in δ_{mslip}	40-80	9.82	17.09	14.97	13.96
	80-150	26.92	27.85	40.49	31.75
20	50	5.72	5.53	5.00	
20	100	5.04	4.67	4.05	-
20	150	3.02	2.74	2.18	
%Decrease in δ_{mslip}	50-100	11.99	15.61	18.93	15.51
	100-150	40.13	41.27	46.26	42.55

5.6.3 Influence of bar diameter on anchorage bond behaviour of HSGPC

The anchorage bond stress-slip curves with respect to different bar diameters are shown in Figure 5.12-5.14**.** It can be observed that with an increase in bar diameter, the anchorage bond strength decreases, and there is a decrease in slip corresponding to the maximum bond strength

(δ_{mslip}) keeping other parameters constant. The reason could be that with increased bar diameter, the non-uniformity of stress distribution increases which results in reduced bond strength. Table 5.7 and 5.8 show the maximum anchorage bond strength and δ_{mslip} variations with respect to different bar diameters. The average percentage of decrease in maximum bond strength increased with an increase in bar diameter and the average δ_{mslip} decreased with increase in bar diameter. The average percentage decrease in bond strength with an increase in bar diameter from 12 to 16 mm and 16 to 20 mm, was 10.38 and 16.45% respectively while the average decrease in δ_{mslip} was 7.51% and 4.88% respectively for a 2.5D embedment length.

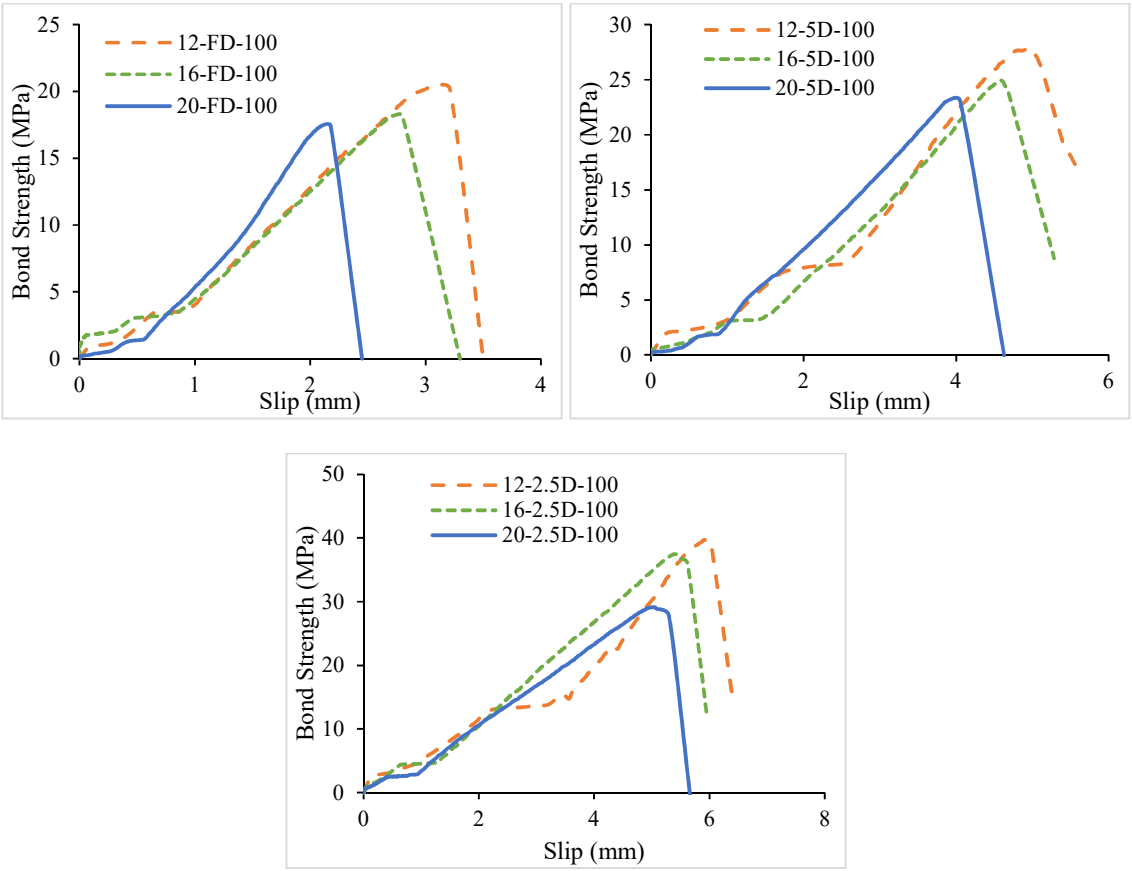

Figure 5.12: Bond stress-slip curves of 100 MPa HSGPC with respect to different bar diameters

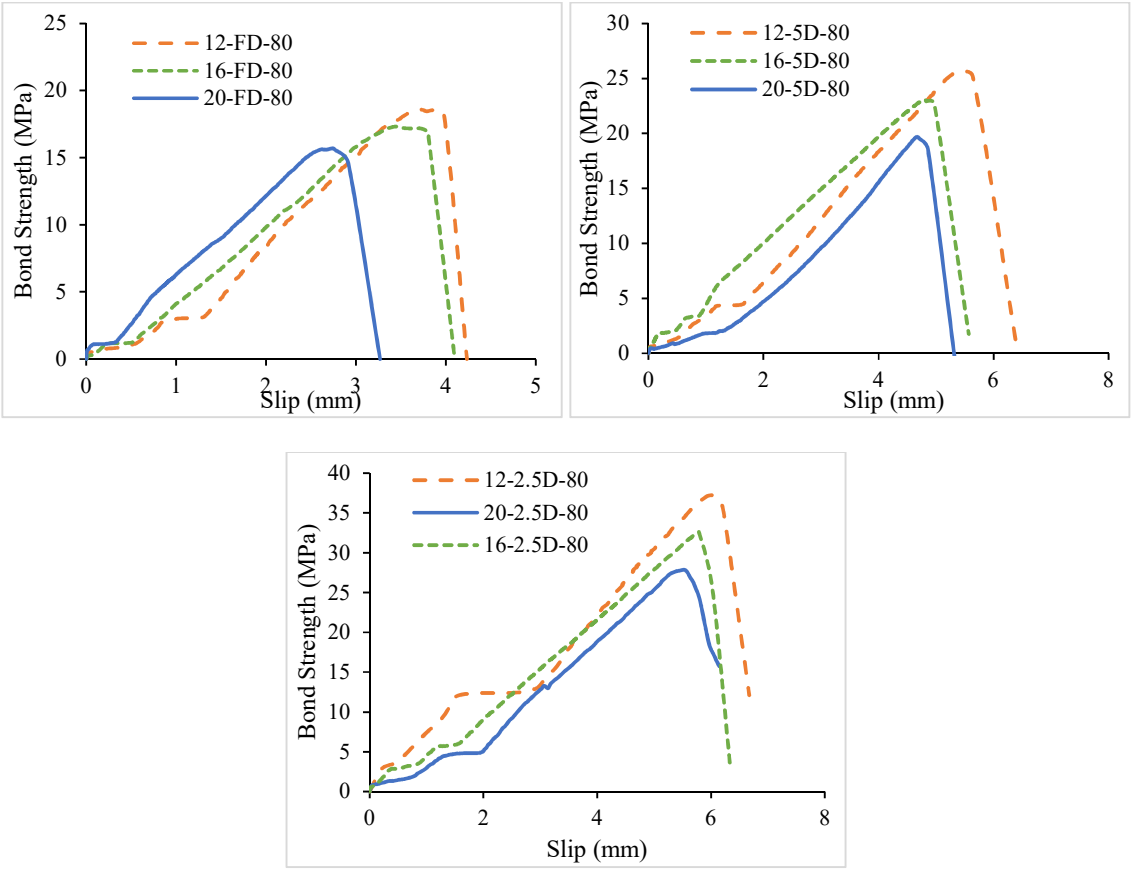

Figure 5.13: Bond stress-slip curves of 80 MPa HSGPC with respect to different bar diameters

Table 5.7: Maximum anchorage bond strength with respect to different bar diameter

L (mm)	D (mm)	Maximum Bond Stress (MPa)			Average %
		60 MPa	80 MPa	100 MPa	
2.5D	12	34.66	37.24	39.68	
	16	30.08	32.61	37.50	
	20	26.32	27.87	29.14	
%Decrease in bond stress	12-16	13.21	12.42	5.50	10.38
	16-20	12.53	14.53	22.28	16.45
5D	12	24.06	25.47	27.84	
	16	19.52	23.07	24.94	
	20	16.24	19.68	23.10	
%Decrease in bond stress	12-16	18.85	9.45	10.41	12.91
	16-20	16.80	14.68	7.37	12.95
FD	12	17.87	18.59	20.32	
	16	15.03	17.33	18.19	
	20	13.26	15.69	17.42	
%Decrease in bond stress	12-16	15.93	6.78	10.47	11.06
	16-20	11.73	9.44	4.27	8.48

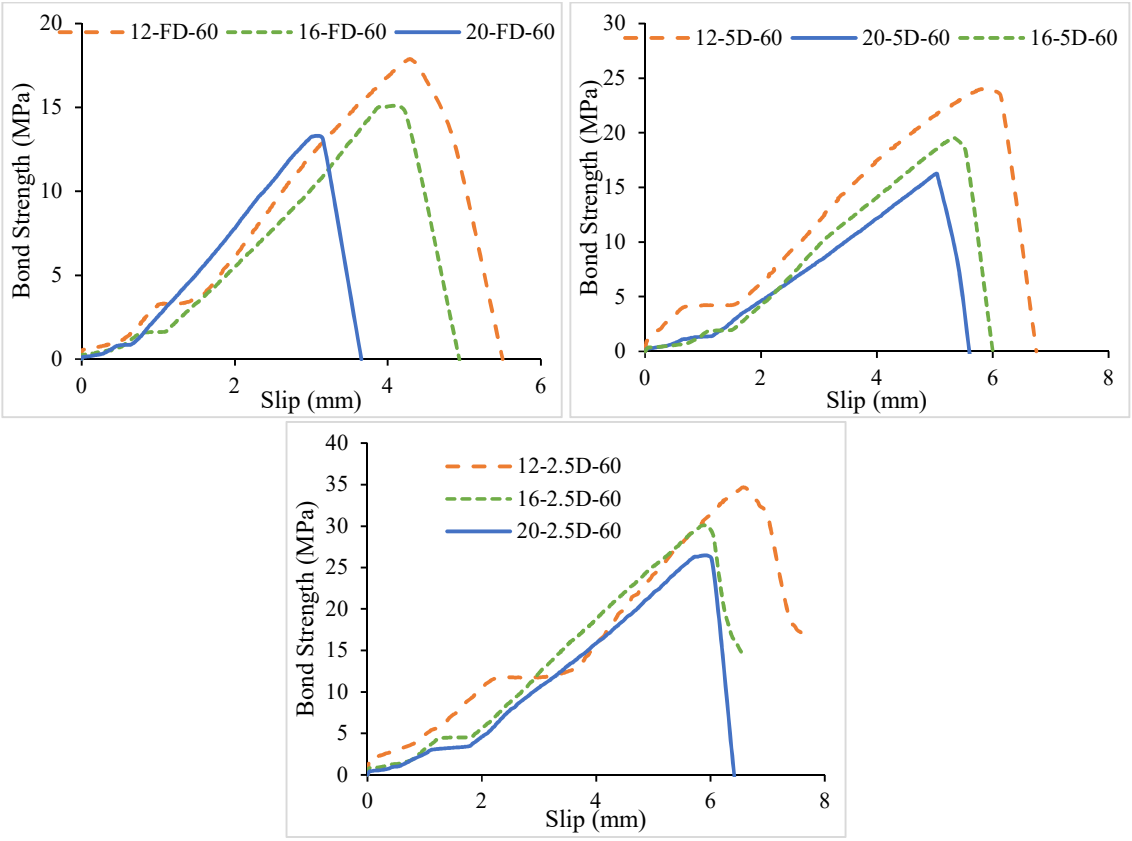

Figure 5.14: Bond stress-slip curves of 60 MPa HSGPC with respect to different bar diameters

Table 5.8: Variation of δ_{mslip} with respect to different bar diameter

L (mm)	D (mm)	δ_{mslip} (mm)			Average %
		60 MPa	80 MPa	100 MPa	
2.5D	12	6.56	6.01	5.90	
	16	5.90	5.78	5.39	
	20	5.72	5.53	5.00	
%Decrease in δ_{mslip}	12-16	10.04	3.83	8.66	7.51
	16-20	3.06	4.32	7.25	4.88
5D	12	5.86	5.32	4.98	
	16	5.33	4.79	4.58	
	20	5.04	4.67	4.05	
%Decrease in δ_{mslip}	12-16	9.14	9.91	8.06	9.04
	16-20	5.40	2.61	11.57	6.52
FD	12	4.27	3.72	3.06	
	16	3.89	3.46	2.73	
	20	3.02	2.74	2.18	
%Decrease in δ_{mslip}	12-16	8.96	7.04	10.76	8.92
	16-20	22.49	20.73	20.14	21.12

Table 5.9: Relation between δ_{mslip} and concrete strength of HSGPC

D (mm)- L(mm)	Relation between δ_{mslip} and concrete strength and coefficient of determination (R^2) value	
	Equation	R^2
12-30	Y = -0.0166x+7.4884	0.8693
12-50	Y = -0.022x+7.1428	0.9812
12-100	Y = -0.0305x+6.1217	0.9975
16-40	Y = -0.0129x+6.7248	0.921
16-80	Y = -0.0186x+6.387	0.9397
16-150	Y = -0.0429x + 6.3649	0.9397
20-50	Y = -0.0182x + 6.8716	0.9339
20-100	Y = -0.0247x + 6.5583	0.9804
20-150	Y = -0.021x+4.3223	0.9627

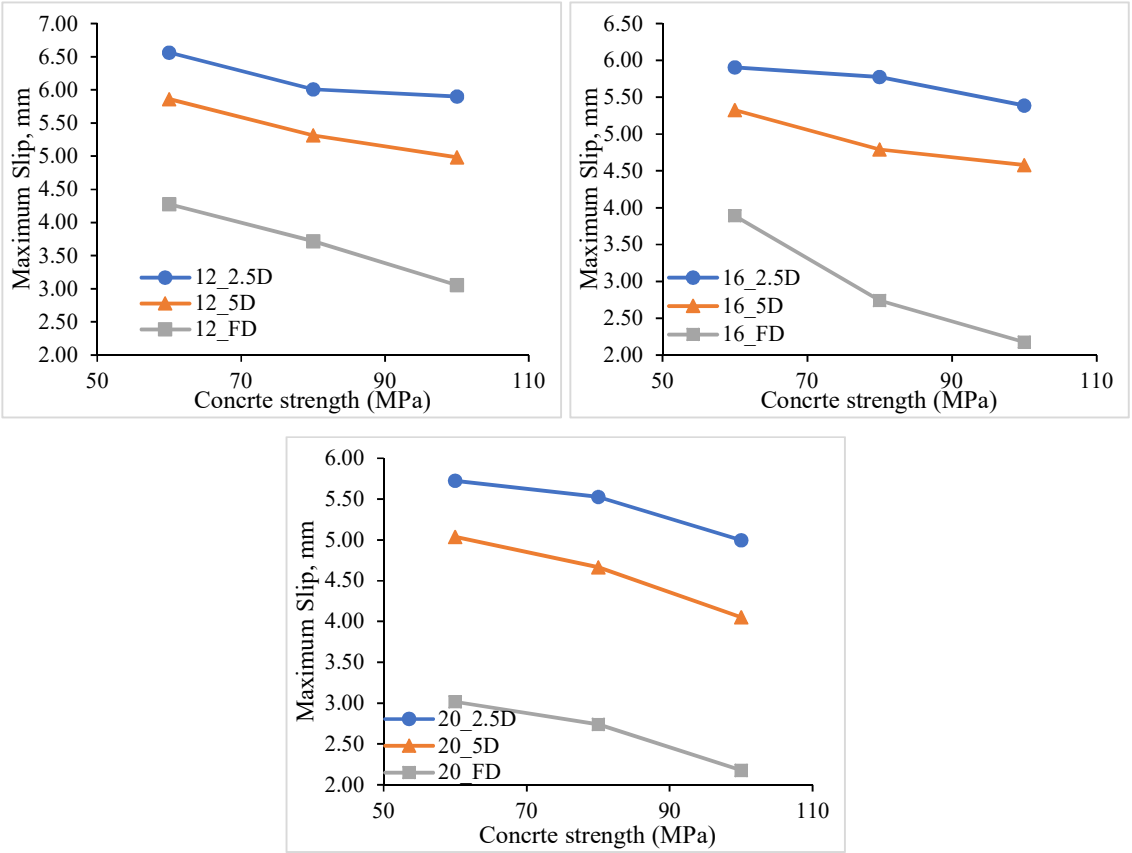

Figure 5.15: Variation of maximum slip with concrete strength for 12, 16, and 20 mm diameter bar

Table 5.10: Relation between normalised maximum bond strength and concrete strength of HSGPC

D (mm)- L(mm)	Relation between normalised maximum bond strength and concrete strength and coefficient of determination (R^2) value	
	Equation	R^2
12-30	Y = -0.0075x+4.6477	0.9928
12-50	Y = -0.0044x+3.1625	0.8278
12-100	Y = -0.0042x+2.3967	0.8075
16-40	Y = -0.0011x+3.5421	0.9664
16-80	Y = -0.0022x+2.2672	0.9387
16-150	Y = -0.0027x + 1.9627	0.9648
20-50	Y = -0.0081x + 3.6752	0.9984
20-100	Y = -0.0076x + 1.5179	0.9987
20-150	Y = -0.0026x+ 1.4636	0.8532

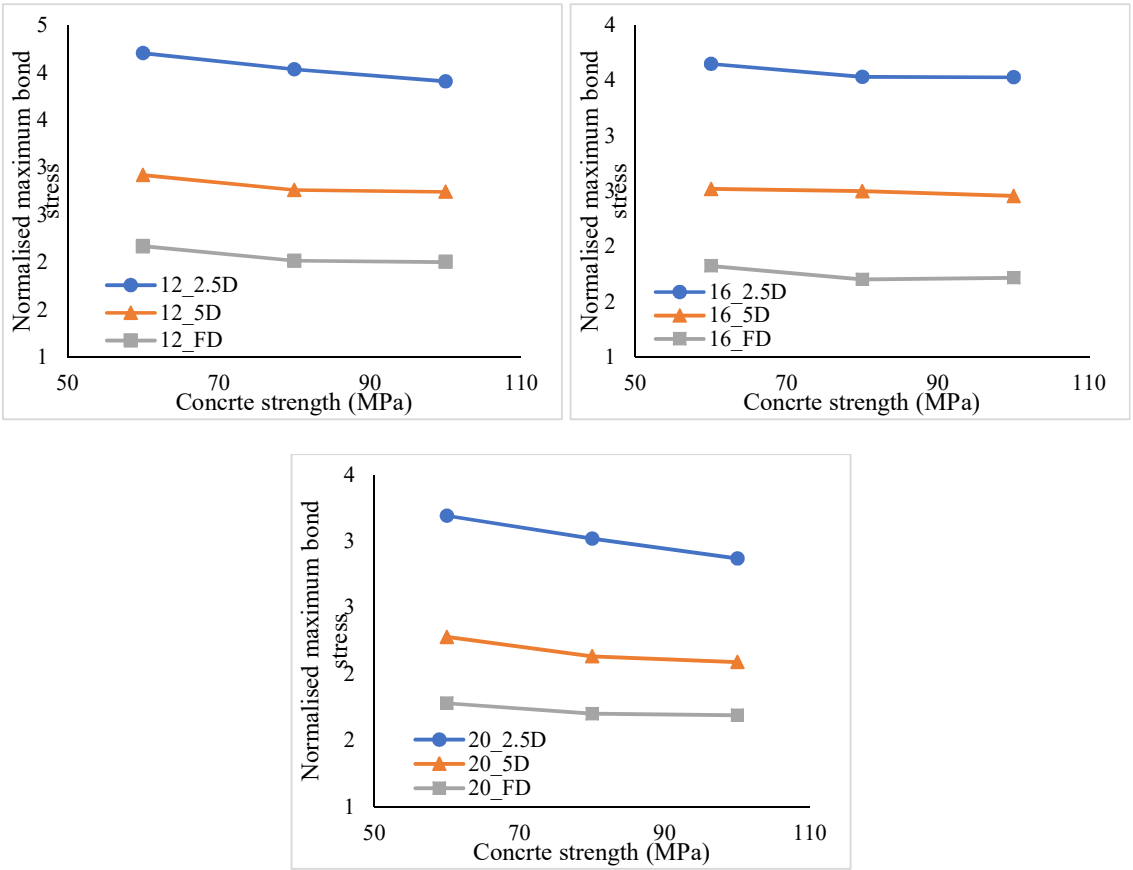

Figure 5.16: Variation of normalised maximum bond stress with strength of HSGPC

5.6.4 Fracture energy response of HSGPC

Fracture energy is defined as the ability of a material to absorb post-crack energy. Fracture energy is defined as the area under the bond stress versus slip curves (Figure 5.6 – 5.8)

determined using the trapezoidal rule. Fracture energy was calculated for concrete strength of 60, 80 and 100 MPa with 12, 16, and 20 mm bar diameter (D) and three embedment lengths (L= 2.5D, 5D and full depth of specimen). The comparison plots of fracture energy for different parameters of the study are drawn (Figure 5.17). From these plots, it can be noted that lower-grade concrete exhibited higher fracture energy. Since an increase in concrete strength increases bond strength and decreases the slip, it decreases fracture energy. The reason could be that with an increase in concrete strength, the brittle nature increases and there is less post-crack behaviour. The increase in embedment length leads to decreased bond strength and slip which result in decreased fracture energy. For longer embedment lengths, splitting failure occurs which is brittle in nature. Similarly, the fracture energy decreased with an increase in bar diameter. The percentage increase in fracture energy of HSGPC is given in Table 5.11. The average percentage decrease in fracture energy from 60 to 80 MPa and 80 to 100 MPa concrete was 12.45%, and 6.53% respectively.

The regression equation and value of regression for fracture energy and concrete strength from Figure 5.18 is given in Table 5.12 and it can be concluded that there exists a good relation between the slip and concrete strength. The regression value varies between 0.84 and 1.

Table 5.11: Fracture energy of different compressive strengths of HSGPC

D (mm) -L (mm)	Fracture energy			% Decrease	
	60 MPa	80 MPa	100 MPa	60 MPa to 80 MPa	80 MPa to 100 MPa
12-30	129.26	124.62	111.93	3.59	10.18
12-60	84.61	77.85	73.37	7.98	5.76
12-100	47.43	37.77	34.73	20.37	8.05
16-40	117.02	99.76	95.59	14.75	4.18
16-80	52.70	48.67	48.10	7.65	1.16
16-150	33.55	19.99	17.99	40.42	9.98
20-50	75.22	72.92	70.50	3.07	3.31
20-100	40.90	38.79	36.38	5.15	6.21
20-150	21.97	19.99	17.99	9.02	9.98
Average				12.45	6.53

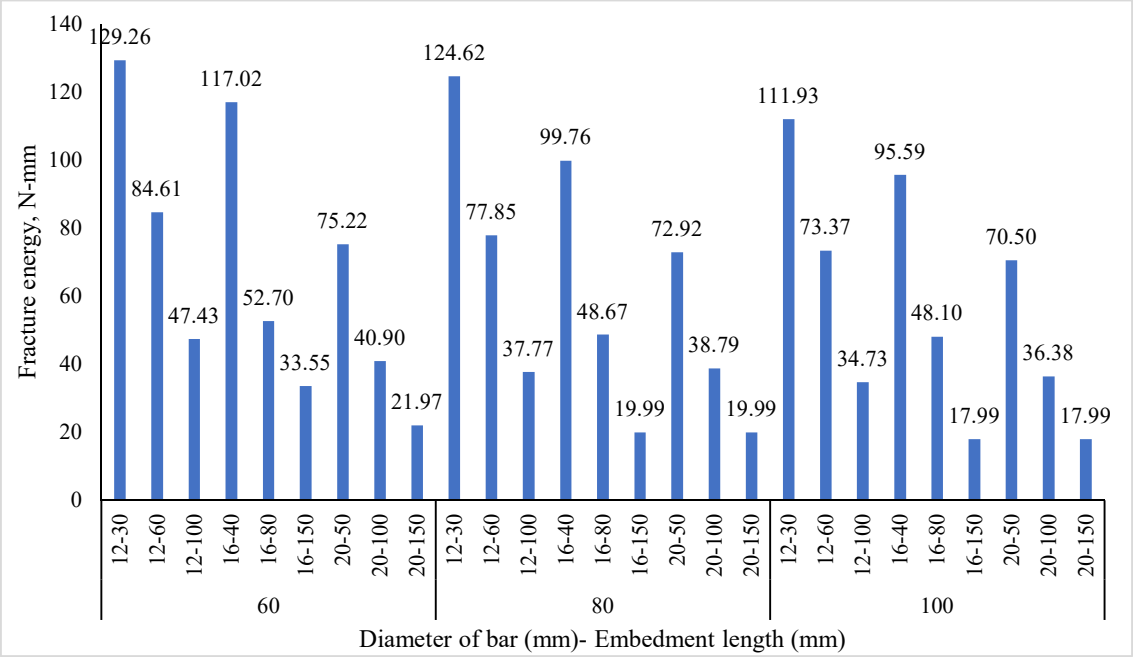

Figure 5.17: Plots of comparison of fracture energy of HSGPC for 60, 80 and 100 MPa concrete

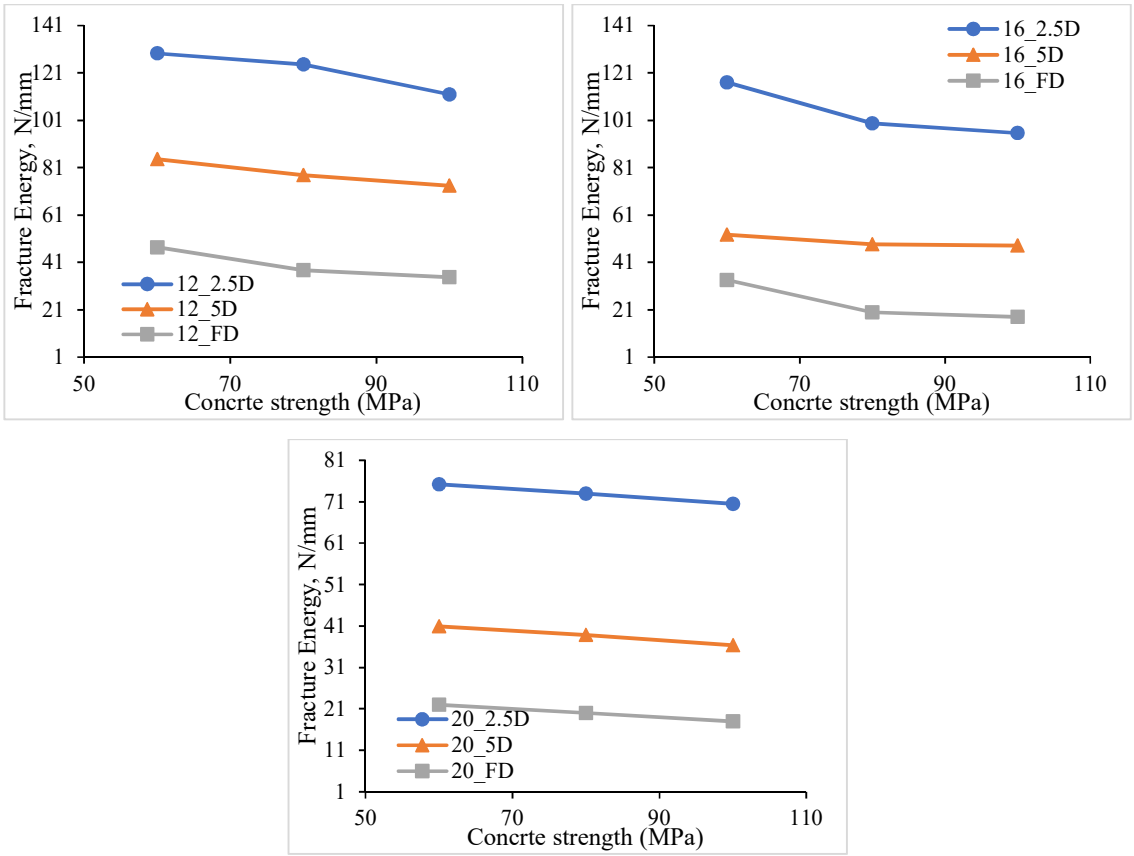

Figure 5.18: Variation of fracture energy with concrete strength of HSGPC

Table 5.12: Relation between fracture energy and concrete strength of HSGPC

D (mm)- L(mm)	Relation between fracture energy and concrete strength and coefficient of determination (R^2) value	
	Equation	R^2
12-30	Y = -0.4331x+156.58	0.9329
12-50	Y = -0.281x+101.09	0.9866
12-100	Y = -0.3175x + 65.373	0.9169
16-40	Y = -0.5359x + 147	0.8894
16-80	Y = -0.1149x + 59.013	0.8404
16-150	Y = -0.3889x + 54.955	0.8444
20-50	Y = -0.118x + 82.323	0.9998
20-100	Y = -0.1128x + 47.717	0.9985
20-150	Y = -0.0994x+ 27.935	1

5.6.5 Failure modes of HSGPC

Failure of pullout specimens takes place in two types i) pullout failure (Figure 5.20 a) and ii) splitting failure (Figure 5.20 b). The bond failure modes of HSGPC for the considered parameters are given in Table 5.13. Bar from the cube specimen pulls out in case of pullout failure when the maximum bond resistance provided by the chemical adhesion, mechanical interlock of ribs and frictional resistance reaches a maximum value (Figure 5.19). The second mode of failure i.e., splitting failure occurs when the principal radial tensile forces developed while pulling the bar from the specimen reaches the splitting tensile strength of concrete. The concrete around the bar splits abruptly and the bar pulls out from the specimen. Before reaching the maximum bond resistance offered by concrete adhesion, friction and mechanical interlock of ribs (in case of ribbed bars), concrete maximum splitting tensile strength will be achieved. From Table 5.13 it can be observed that in lower-grade concrete, more splitting failure can be observed because of lower splitting tensile strength. With an increase in the grade of concrete, the failure mode shifts from splitting failure to pullout failure. Also, with increasing the bar diameter and embedment length, the mode of failure shifted from pullout failure to splitting failure, as the applied load on the specimen increases with an increase in contact area and tends to reach the tensile strength of concrete. Similar type of failure modes can be noted in the research work of Kim & Park, 2014.

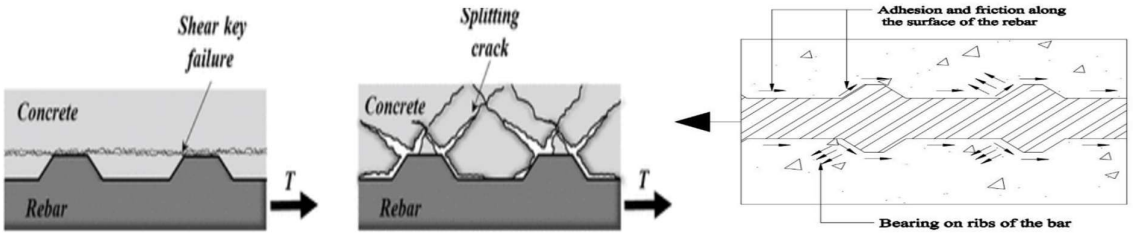

Figure 5.19: Distribution of forces along the bar in pullout specimen (Kim & Park, 2014)

Figure 5.20: a) Pullout failure b) splitting failure

Table 5.13: Pullout failure modes of HSGPC

D (mm) - L (mm)	Failure mode: Splitting (S) and Pullout (P)		
	60 MPa	80 MPa	100 MPa
12-30	P	P	P
12-60	S	S	P
12-100	S	S	S
16-40	P	P	P
16-80	S	S	P
16-150	S	S	S
20-50	S	P	P
20-100	S	S	S
20-150	S	S	S
total number of splitting failures			18
total number of pullout failures			9

5.7 Flexural Bond Behaviour of HSGPC through Hinged Beam Test

In the current research, the influence of concrete compressive strength, cover-to-bar diameter (C), bar diameter (d) and embedment length (l_d) on the flexural bond behaviour of HSGPC was investigated experimentally based on 18 hinged beam specimens.

5.7.1 Influence of compressive strength on flexural bond behaviour of HSGPC

The flexural bond stress-slip behaviour of HSGPC of different grades is shown in Figure 5.21-5.22. It can be observed that with an increase in the compressive strength of concrete, the flexural bond strength increases. The highest bond strength of 17.17 MPa was noted in the 100 MPa concrete with a 16 mm cover and 18.01 MPa for a 40 mm cover of the same grade. The radial principal compressive and tensile stress caused by flexural loading of specimens generates delayed cracks with an increase in compressive strength, enabling increased bond strength. Table 5.14 gives the maximum bond strength with respect to the compressive strength of HSGPC. The average percentage increase in bond strength decreased from 15.14% to 8.94 % when strength increased from 60-80 MPa concrete to 80-100 MPa concrete. The reason can be attributed to the fact that with an increase in the grade of concrete due to the brittle nature of concrete, there is an impact on radial tensile resistance which leads to lower bond loads. This indicates that as the compressive strength of concrete increased, the average percentage increase in bond strength declined. The slip corresponding to the maximal bond strength (δ_{mslip}) is shown in Table 5.15. The minimum δ_{mslip} is recorded for 100 MPa concrete. It can be observed that with an increase in the grade of concrete, δ_{mslip} decreased. The reason could be that in case of higher grade of concrete, the cohesion between the steel bar and concrete increases due to dense ITZ and therefore a reduced δ_{mslip}. Also, the average decrease in δ_{mslip} decreased with an increase in the grade of concrete. The average percentage decrease in δ_{mslip} for 60 MPa to 80 MPa and 80 MPa to 100 MPa is 25.85 %, and 13.25 % respectively in case of 16 mm cover while it was 12.54% and 11.60% in case of 40 mm cover. The percentage decrease in slip decreased with an increase in the grade of concrete, similar to maximum bond strength as the brittle nature affects the radial tensile resistance of concrete and propagates micro-cracks easily.

Table 5.14: Flexural bond strength of HSGPC of different compressive strengths

Bar dia	16/20 mm cover					40 mm cover				
	Maximum bond strength (MPa)			%Increase		Maximum bond strength (MPa)			%Increase	
	60 MPa	80 MPa	100 MPa	60 to 80	80 to 100	60 MPa	80 MPa	100 MPa	60 to 80	80 to 100
12	13.98	15.80	17.17	12.98	8.73	16.36	17.38	18.01	6.23	3.60
16	13.54	15.52	16.97	14.62	9.36	15.34	17.11	17.71	11.55	3.5
20	12.96	15.27	16.61	17.83	8.74	14.94	16.41	17.23	9.84	4.97
Average				15.14	8.94				9.21	4.03

Table 5.15: Slip corresponding to the maximum bond strength of HSGPC

Bar diameter (mm)	16/20 mm cover					40 mm cover				
	δ_{mslip} (mm)			% Decrease		δ_{mslip} (mm)			% Decrease	
	60 MPa	80 MPa	100 MPa	60 to 80	80 to 100	60 MPa	80 MPa	100 MPa	60 to 80	80 to 100
12	1.06	0.82	0.73	22.53	11.10	0.42	0.38	0.36	11.53	4.91
16	0.75	0.58	0.48	23.03	17.97	0.31	0.27	0.24	12.21	12.32
20	0.58	0.39	0.35	32.00	10.67	0.28	0.25	0.20	13.88	17.58
Average				25.85	13.25				12.54	11.60

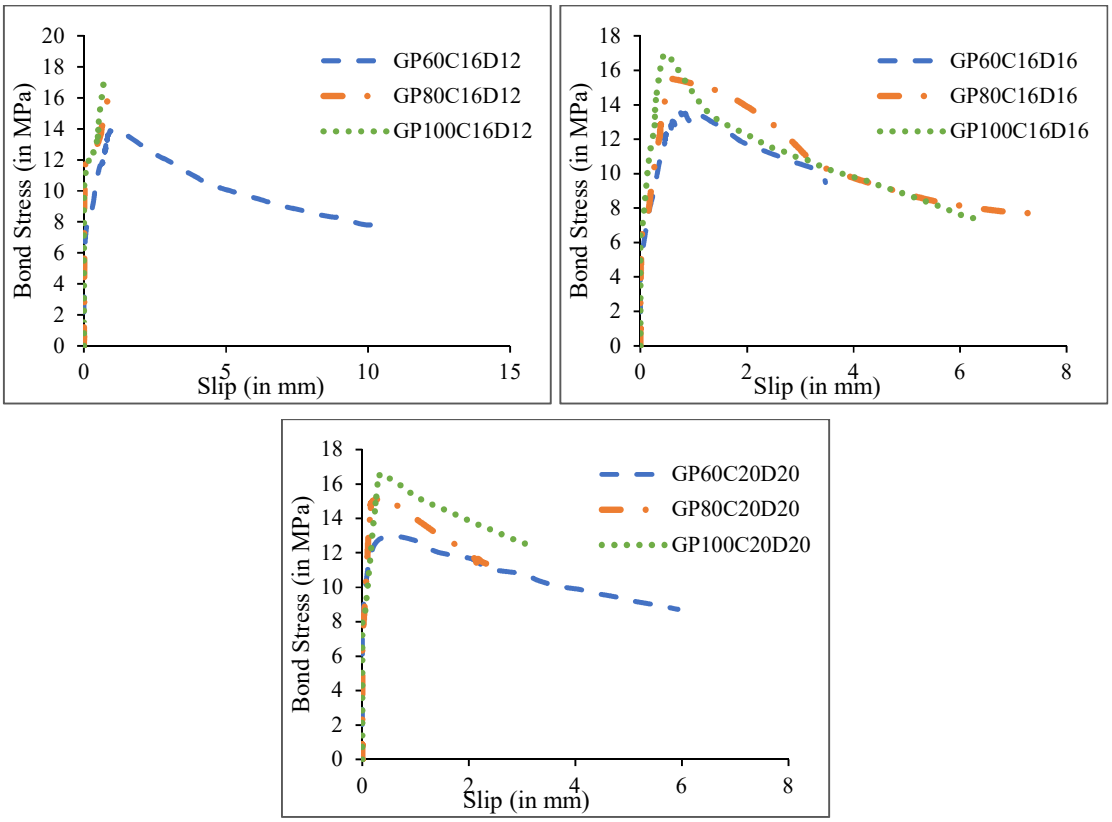

Figure 5.21: Flexural bond behaviour of HSGPC for 16/20 mm cover

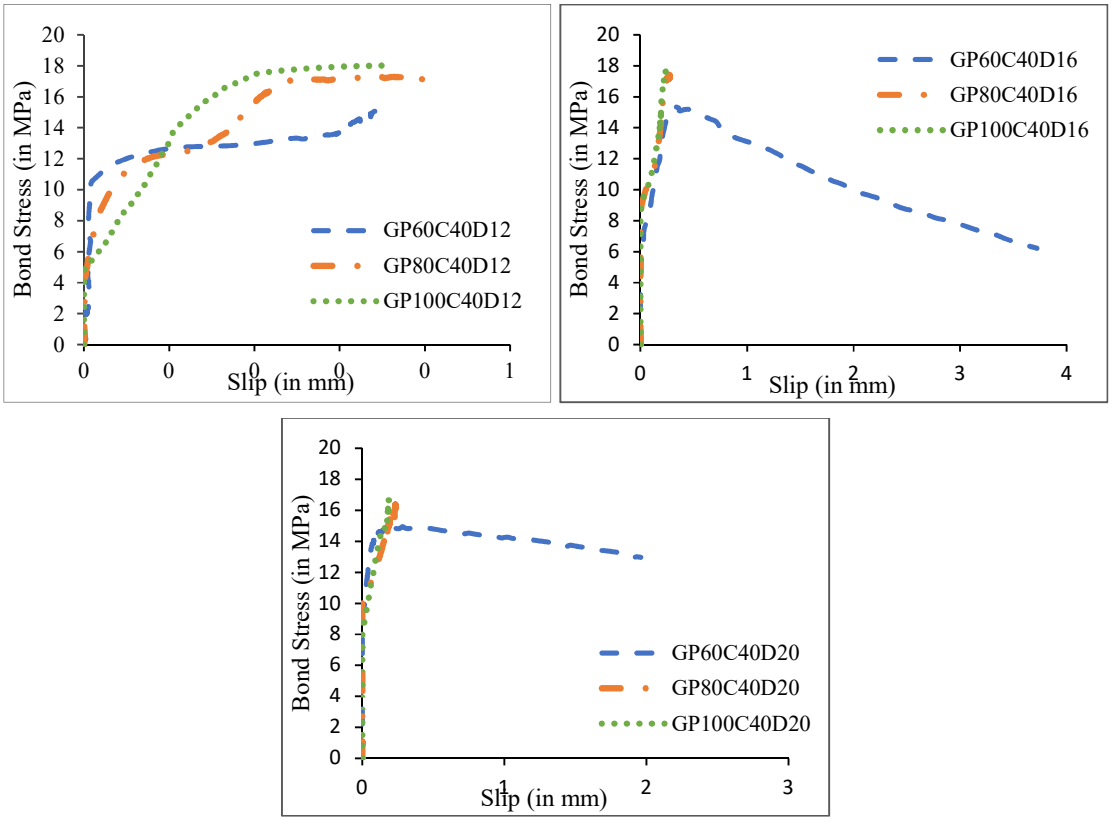

Figure 5.22: Flexural bond behaviour of HSGPC for 40 mm

5.7.2 Influence of cover to reinforcement on flexural bond behaviour of HSGPC

The flexural bond stress-slip behaviour of HSGPC with respect to the cover of concrete can be observed in Figure 5.23 - 5.25. It can be noted that with an increase in concrete cover, the flexural bond strength increased. The highest bond strength of 18.01 MPa was observed for a 40 mm cover. An increase in cover provides passive confinement in addition to the confinement provided by the stirrups. This delays the formation of transverse cracks caused due to principal tensile forces around the bar. Table 5.16 shows the maximum bond strength with different concrete covers. The percentage increase decreased with an increase in the grade of concrete highlighting the effect of passive confinement becoming stable at higher grades of concrete. The highest percentage increase in flexural bond strength was observed in lower-grade concrete (60 MPa) and it was 15.30% in case of 20 mm bar. The average increase in bond strength was 9.81%. The slip corresponding to maximum bond strength (δ_{mslip}) behaviour with respect to changes in the cover of concrete is given in Table 5.17. An increase in the cover of concrete decreased δ_{mslip}. The percentage decrease in slip was observed to be 50.87.

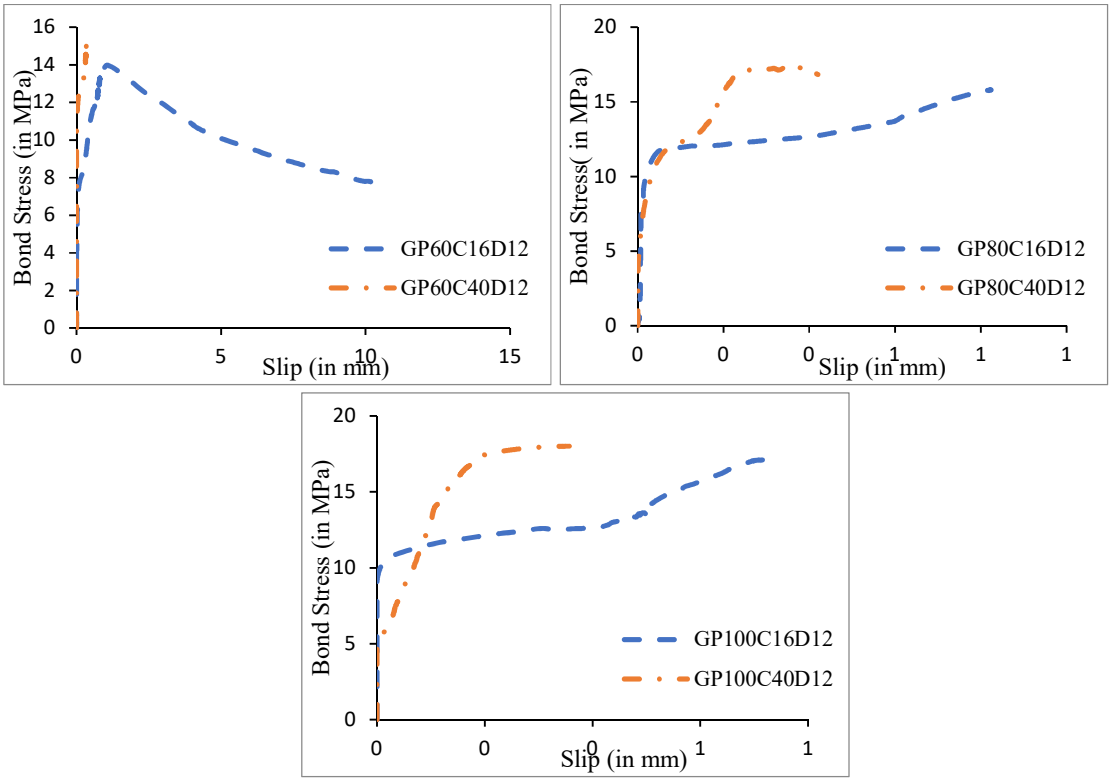

Figure 5.23: Flexural bond stress-slip behaviour of HSGPC of a) 60 MPa b) 80 MPa c) 100 MPa for 12 mm bar dia.

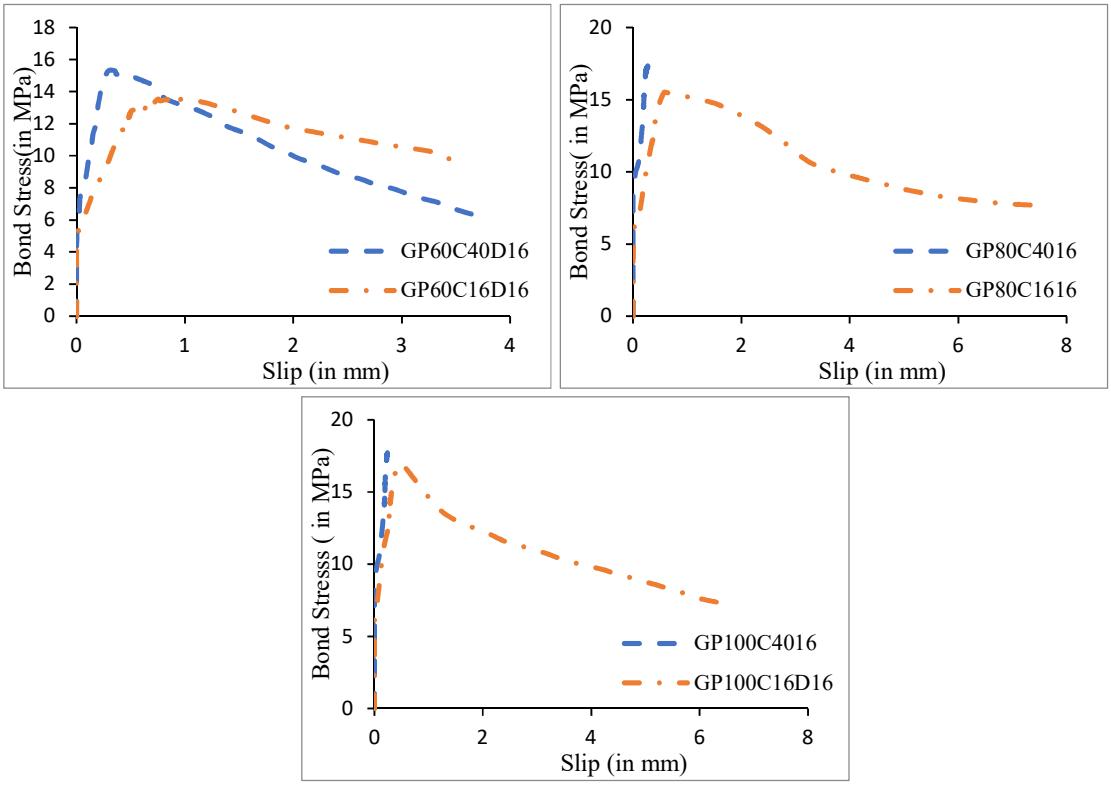

Figure 5.24: Flexural bond stress-slip behaviour of HSGPC of a) 60 MPa b) 80 MPa c) 100 MPa for 16 mm bar dia.

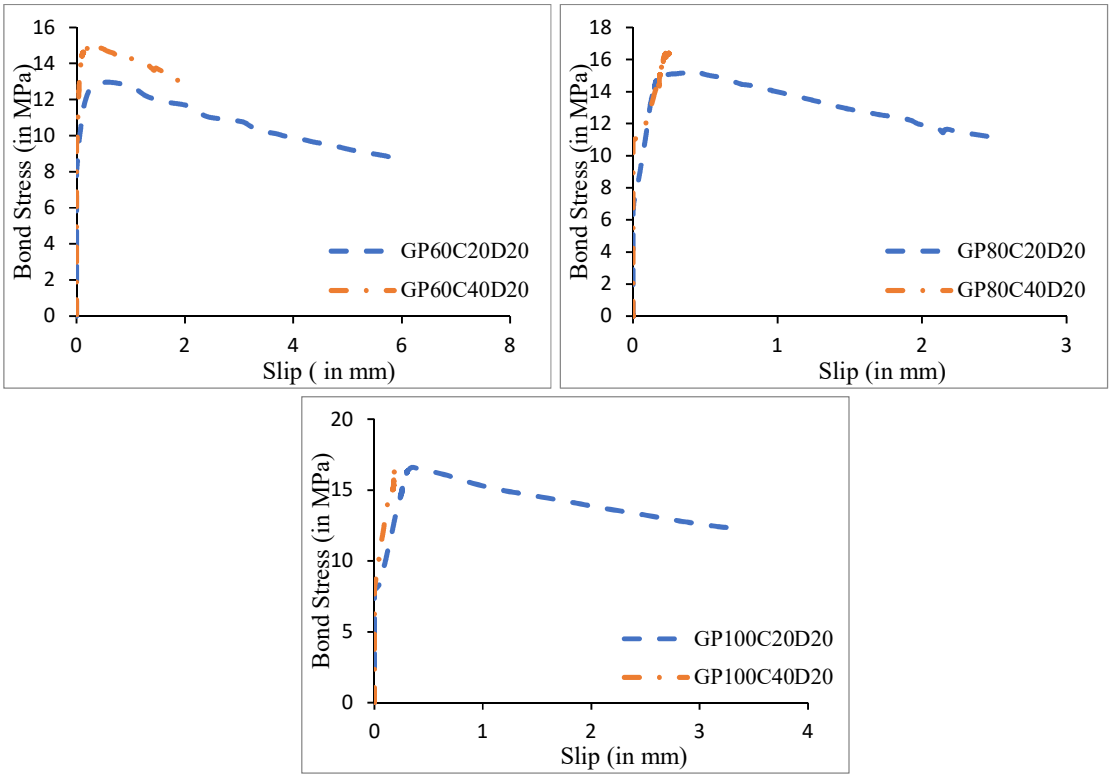

Figure 5.25: Flexural bond stress-slip behaviour of HSGPC of a) 60 MPa b) 80 MPa c) 100 MPa for 20 mm bar dia.

Table 5.16: Maximum flexural bond strength with respect to change in concrete cover

D (mm)-F_c (MPa)	Maximum bond strength (MPa)		% Increase
	16 mm	40 mm	16/20 to 40
12-60	13.98	16.36	17.05
12-80	15.80	17.38	10.06
12-100	17.17	18.01	4.87
16-60	13.54	15.34	13.29
16-80	15.52	17.11	10.26
16-100	16.97	17.71	4.35
20-60	12.96	14.94	15.30
20-80	15.27	16.41	7.47
20-100	16.61	17.23	3.74
average			9.81

Table 5.17: The slip corresponding to maximum bond strength with respect to change in concrete cover.

D (mm)- f_c (MPa)	δ_{mslip} (mm)		% Decrease
	16/20 mm	40 mm	16/20 to 40
12-60	1.06	0.42	60.07
12-80	0.82	0.38	54.39
12-100	0.73	0.36	51.22
16-60	0.75	0.31	58.84
16-80	0.58	0.27	53.06
16-100	0.48	0.24	49.82
20-60	0.58	0.28	50.63
20-80	0.39	0.25	37.47
20-100	0.35	0.20	42.30
average			50.87

5.7.3 Influence of bar diameter on flexural bond behaviour of HSGPC

The flexural bond stress-slip behaviour of HSGPC with respect to different bar diameters can be observed in Figure 5.21 – 5.25. It can be noted that with an increase in bar diameter, the flexural bond strength decreased. An increase in bar diameter provides a non-uniform stress distribution over the contact area. Due to this, the formation of transverse cracks due to principal tensile forces around the bar becomes more prone. Table 5.18 shows the maximum bond strength with different bar diameters. The percentage decrease increased with an increase in bar diameter highlighting the effect of non-uniform stress distribution. The percentage decrease in flexural bond strength was 2.67 for a change in bar diameter from 16 to 20 mm and 2.02 for 12 to 16 mm. The slip corresponding to maximum bond strength (δ_{mslip}) behaviour with respect to bar diameter is given in Table 5.19. An increase in bar diameter decreased δ_{mslip}. The percentage decrease in slip was observed to be 31.16, 29.12 for change in bar diameter from 12 to 16 mm in 16 mm and 40 mm cover of concrete. There was an average percentage decrease in δ_{mslip}, which decreased with an increase in the bar diameter. The behaviour of δ_{mslip} with respect to change in the bar diameter is shown in Figure 5.27. It can be observed that with increase in concrete strength, δ_{mslip} decreased which was more pronounced at higher bar diameter. The relation between the δ_{mslip} and compressive strength shown in Figure 5.27 is given in Table 5.21. It can be observed that there is good correlation ranging between 0.883 to 0.999.

For eliminating the effect of compressive strength, flexural bond strength is normalised with respect to cube compressive strength (fcc) and is determined by $\frac{\tau_{max}}{\sqrt{f_{cc}}}$. The normalised flexural bond response with respect to bar diameter is shown in Figure 5.26. It can be observed with an increase in the compressive strength of concrete the normalised flexural bond strength decreased which is as shown in Table 5.14. Similar behaviour was observed in 12, 16, and 20 mm bars for 16- and 40-mm covers. The relation of normalised compressive strength of concrete with normalised flexural bond strength (Figure 5.26) is given in Table 5.20. It was observed that there was a good correlation between the normalised flexural bond strength and compressive strength of concrete, which varied between 0.93 to 0.99.

Table 5.18: Maximum flexural bond strength with respect to different bar diameters.

Grade of concrete (MPa)	16/20 mm cover					40 mm cover				
	Maximum bond strength (MPa)			% Decrease		Maximum bond strength (MPa)			% Decrease	
	12	16	20	12 to 16	16 to 20	12	16	20	12 to 16	16 to 20
60	13.98	13.54	12.96	3.15	4.27	16.36	15.34	14.94	6.26	2.58
80	15.80	15.52	15.27	1.74	1.59	17.38	17.11	16.41	1.57	4.08
100	17.17	16.97	16.61	1.17	2.14	18.01	17.71	17.23	1.66	2.71
Average				2.02	2.67				3.16	3.12

Table 5.19: Slip corresponding to maximum bond strength with different bar diameters.

Grade of concrete (MPa)	16/20 mm cover					40 mm cover				
	δ_{mslip} (mm)			% Decrease		δ_{mslip} (mm)			% Decrease	
	12	16	20	12 to 16	16 to 20	12	16	20	12 to 16	16 to 20
60	1.06	0.75	0.58	29.04	23.49	0.42	0.31	0.28	26.86	8.22
80	0.82	0.58	0.39	29.49	32.41	0.38	0.27	0.25	27.43	9.96
100	0.73	0.48	0.35	34.94	26.39	0.36	0.24	0.20	33.08	15.36
Average				31.16	27.43				29.12	11.18

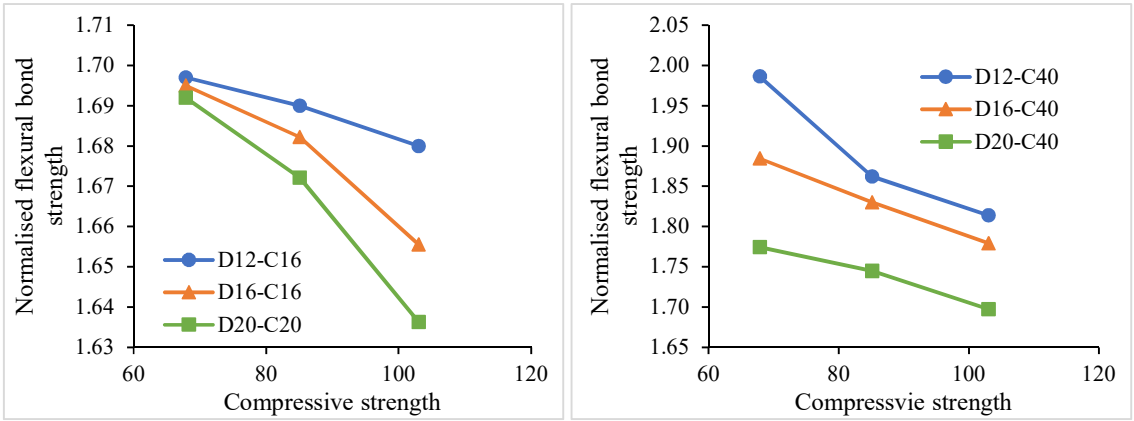

Figure 5.26: Relation between the normalised flexural bond strength and compressive strength of concrete for a) 16 mm b) 40 mm of concrete cover

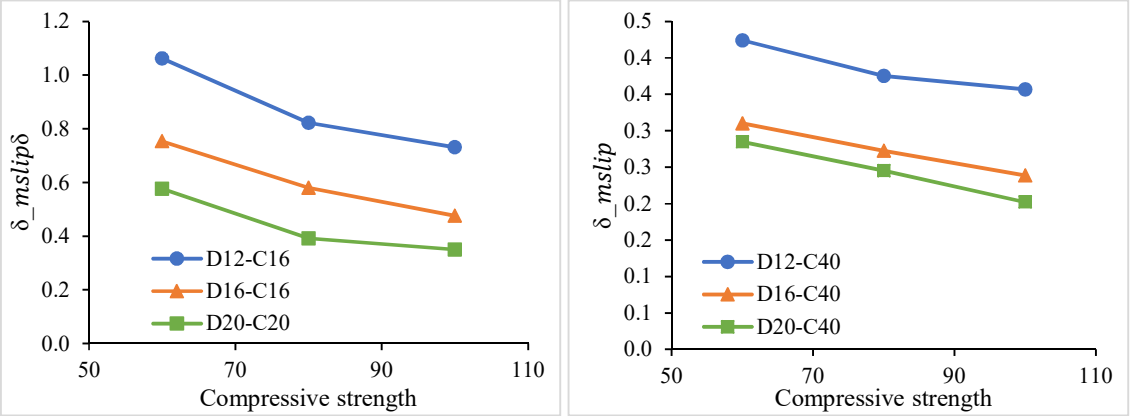

Figure 5.27: Relation between the δ_{mslip} and compressive strength of concrete with respect to bar diameter for a)16 mm cover b) 40 mm cover

Table 5.20: Correlation between the normalised flexural bond strength and compressive strength of concrete

D (mm)- C (mm)	Relation between normalised flexural bond strength and concrete strength	
	Equation	R^2
12-16	Y = -0.0005x + 1.7304	0.9921
12-40	Y = -0.0049x + 2.3048	0.9333
16-16	Y = -0.0011x + 1.7737	0.9641
16-40	Y = -0.003x + 2.0865	0.9991
20-20	Y = -0.0022x + 1.9257	0.9766
20-40	Y = -0.0247x + 6.5583	0.9852

Table 5.21: Correlation between the δ_{mslip} and compressive strength of concrete

D (mm)- C (mm)	Relation between δ_{mslip} and concrete strength	
	Equation	R^2
12-16	Y = -0.0083x + 1.5335	0.9374
12-40	Y = -0.0017x + 0.52	0.936
16-16	Y = -0.0069x + 1.1589	0.9797
16-40	Y = -0.018x + 0.4166	0.9988
20-20	Y = -0.0057x + 0.8923	0.883
20-40	Y = -0.0057x + 0.8923	0.9994

5.8 Comparison of Direct Pullout and Flexural Bond Strength

The maximum bond stress values through pullout and flexural bond strength are given in Figure 5.28. It can be observed that in case of flexural bond strength, magnitudes were lower than pullout bond strength. This was due to load distribution in the specimen. In case of the pullout specimen, the concrete surrounding the rebar was under compression whereas in case of flexural bond strength the concrete surrounding the rebar was in tension. As concrete is weak in tension and strong in compression, the concrete in the hinged beam specimen provides lower resistance

to bond strength and this scenario of load distribution is more realistic in practical application. So, it's significant to consider this effect while analyzing reinforced structural elements. The percentage reduction in maximum flexural bond strength compared to pullout bond strength was around 55.

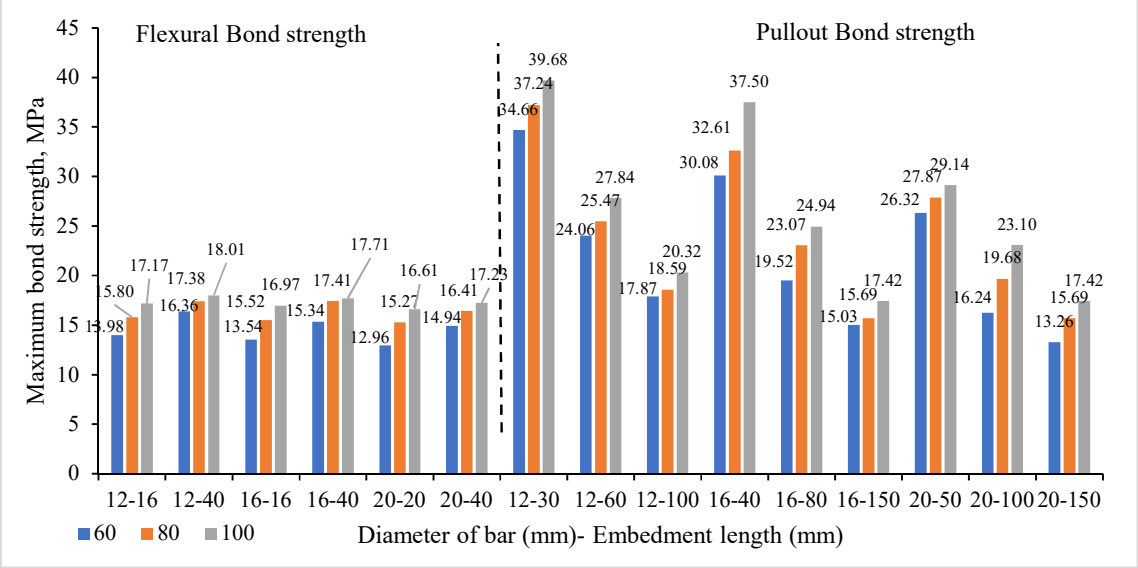

Figure 5.28: Comparison plots of maximum flexural and pullout bond strength of HSGPC

5.9 General Remarks

The bond performance of HSGPC through pullout and hinged beam tests was investigated in this phase of work. The parameters such as concrete compressive strength (60, 80, and 100 MPa), bar diameter (D = 12, 16 and 20 mm) and embedment length (2.5D, 5D and full depth of the specimen) were considered for studying the anchorage bond behaviour. Concrete compressive strength (60, 80 and 100 MPa), bar diameter (D = 12, 16 and 20 mm) and cover of concrete (16, 20 and 40 mm) were considered for flexural bond behaviour. From this phase of work, the following observations can be drawn.

- An increase in the strength of concrete improved the direct pullout bond strength. The average percentage increase in bond strength for 60 to 80 MPa, and 80 to 100 MPa concrete was 10.42% and 10.24 % respectively. This means improved compressive strength provides stronger ITZ between concrete and aggregate, resulting in improved bond strength.
- An increase in concrete strength decreased the slip corresponding to maximum bond strength. The average percentage decrease in slip corresponding to the maximum bond

strength for 60 to 80 MPa, and 80 to 100 MPa concrete was 10.29 % and 10.21% respectively. Improved adhesion resulted in delayed slip propagation.

- As the embedment length increases, the bond strength decreases. The average percentage decrease in bond strength for 2.5D to 5D and 5D to FD embedment length was 30.68 %, and 26.58% respectively in case of 12 mm bar. The reason for the decrease could be due to non-uniform stress distribution along the length of the bar, which is more significant in case of higher embedment lengths.
- An increase in embedment length decreased the slip corresponding to maximum bond strength. The average decrease in slip for 2.5D to 5D, and 5D to FD embedment length is 12.6 % and 31.9% respectively in case of a 12 mm bar. The reason could be due to a greater amount of area available to resist forces causing the propagation of slip.
- Similar to embedment length, the effect of bar diameter on bond strength is similar. The average percentage decrease in bond strength for 12 to 16 mm and 16 to 20 mm bar diameter is 10.38 and 16.45% respectively for 2.5D embedment length. For the same, the average percentage decrease in slip was 7.51 to 4.88%.
- High-strength geopolymer concrete specimens exhibited predominant splitting failure indicating higher brittleness and lower splitting tensile strength of concrete.
- The fracture energy which indicates the ability of materials to absorb post-crack energy, decreases with an increase in the compressive strength of concrete, bar diameter and embedment length. The percentage decrease in fracture energy decreases with an increase in the grade of concrete and bar diameter.
- The failure mode shifted from pullout failure to splitting failure for lower-grade concrete, higher bar diameter, and longer embedment lengths. This provides higher radial tensile stresses than the splitting tensile strength of concrete.
- Similar to direct pullout bond strength, the flexural bond strength increases with an increase in the grade of concrete and decreases with an increase in bar diameter. Also, the increase in cover concrete improved bond strength.
- With an increase in the cover of concrete, bond strength increased by 10% while the slip corresponding to maximum bond stress decreased by 50%.

- The magnitude of bond strength of the pullout test was higher when compared to the hinged beam test, since, the concrete around reinforcement in the pullout test is in compression while in the case of the hinged beam test, it is under tension.

CHAPTER 6
NUMERICAL ANALYSIS OF BOND BEHAVIOUR OF HIGH-STRENGTH GEOPOLYMER CONCRETE

6.1 General

In the previous chapter, various parameters that affect bond behaviour such as concrete strength (60, 80, and 100 MPa), bar diameter (D= 12, 16 and 20 mm), and embedment length (2.5D, 5D, and full depth), type of test (Pullout and hinged beam test) and cover to concrete (16/20 and 40 mm) were considered and experimental programs were carried out (Phase III). The present chapter deals with the numerical simulation of the bond behaviour of HSGPC, including the validation of experimental work. To realise the fourth objective listed in Chapter 1, parameters such as compressive strength of concrete (20, 30, 40, 50, 60, 70, 80, 90, and 100 MPa), bar diameter (10, 12, 16 and 20 mm bar diameter), embedment length (50, 75, 100, and 150 mm) are considered under pullout test and the parameters such as compressive strength of concrete (20, 30, 40, 50, 60, 70, 80, 90, and 100 MPa), bar diameter (10, 12, 16 and 20 mm bar diameter), cover to bar diameter ratio (1 to 5 at an increment of 0.5), embedment length to bar diameter ratio (3, 5, 7 and 9), are considered under beam end test. Based on the numerical data set analysed through finite element software ATENA-GiDv5.7.0p, multiple non-linear regression analysis is performed and an analytical model for maximum bond behaviour of normal, standard and high-strength geopolymer concrete is proposed. The modelling of the pullout and beam end mechanism in ATENA-GiD and the associated discussion of results obtained are taken up in the following sections and in Appendix II.

6.2 Modelling in ATENA-GiD

Modelling of the pullout and beam end mechanisms is done using ATENA-GiD software (ATENA V5.7.0p, GiD v15.1.3). The procedure for modelling of pullout and beam end model using ATENA - GiD is briefed below. The procedure involves different steps listed:

Step-1: Geometrical modelling for pullout and beam end model.

Step-2: Assigning material properties to the pullout and beam end model.

Step-3: Defining boundary conditions and displacement of the pullout and beam end model.

Step-4: Defining points to monitor applied displacement and the response.

Step-5: Generate mesh properties and select the suitable interval data for the solver.

Step-6: Run the model using solver "ATENA" and analyse the results.

The details are given in Appendix II.

6.2.1 Specifications for the numerical model.

The analytical simulation is taken up in two phases:

Phase-A: In this phase, the numerical modelling of the standard pullout test was done with cube specimens in accordance with IS 2770-1 (1967) (IS: 2770-1: 1967(R2017), 1967) for the different parameters viz, reinforcement bar (plain and ribbed), diameter of bar (10 mm, 12 mm and 16 mm), embedment length (150 mm, 100 mm, 75 mm, 50 mm) and varying grade of concrete (20, 30, 40, 50, 60, 70, 80, 90, and 100 MPa). As per IS 2770-1 (1967) (IS: 2770-1: 1967(R2017), 1967), cube specimens of size 150 x 150 x 150 were modelled for rebar size greater than 12 mm and 100 x 100 x 100 mm of rebar size less than or equal to 12 mm. The geopolymer concrete is simulated by the user-defined material model cementitious2 which is present in the material models of ATENA. The solid concrete portion of the pullout specimen is modelled using hexahedral solid element and the bar is modelled in the specimen using linear structured element. Material properties obtained from section 3.6 were used for material simulation into finite element analysis. Direct application of load on a linear element does not produce a converging solution; to avoid this, the wrap of the discreet element was modelled with a semi-structured tetrahedral solid element and applied on it, as it will not deform during the analysis but transferred the load uniformly to the bar. To simulate the boundary conditions, the top surface of the test cube was restrained against translation and rotation in X, Y, and Z directions. The wrap element was restrained in the X and Y direction while displacement was applied at the top node of the wrap. Reaction forces and displacements are to be measured at the points of strategic importance; so, for this monitoring points were assigned to the specific nodes. To perform analysis accurately, the size of the elements was limited to 10 mm.

Phase-B: From the literature, a direct pullout test for evaluating the bond strength of concrete yields high conservative values and so the same set of tests with different parameters was also simulated on a beam-end specimen based on the American Society for Testing and Materials ASTM- A944 (ASTM-A944, 2004). The modelled specimen was 600 mm in length, 360 mm in depth and 250 mm in width with reaction plates at top-back end and bottom-front end. The

bar was placed with varying cover-to-bar diameter ratios of 1, 1.5, 2, 2.5, 3, 3.5, 4, 4.5 and 5, embedded such that the embedment length-to-diameter ratios were 3, 5, 7 and 9 in concrete with varying grades of concrete (20, 30, 40, 50, 60, 70, 80, 90, and 100 MPa). These specimens are able to simulate actual field conditions, wherein, the concrete engulfing the rebar is also in tension unlike in case of the direct pullout test specimens. Similar to phase A, solid concrete is modelled as a hexahedral solid element, and the reinforcement present in the specimen is modelled using a linear structured element. In this analysis also, the wrap was used for the application of load. The mesh size of solid and linear elements was limited to 10 mm.

An analytical equation is proposed from the results of Phase-B (i.e., Beam end specimen analysis) by performing multiple non-linear regression analysis, which incorporates the effect of embedment length to rebar diameter ratio, concrete cover to rebar diameter ratio and compressive strength of concrete. Further, the existing analytical equation and empirical formulas proposed by various researchers and standards are compared with the results of numerical analysis. The numerical models used for Phase A and Phase B are shown in Figure 6.1.

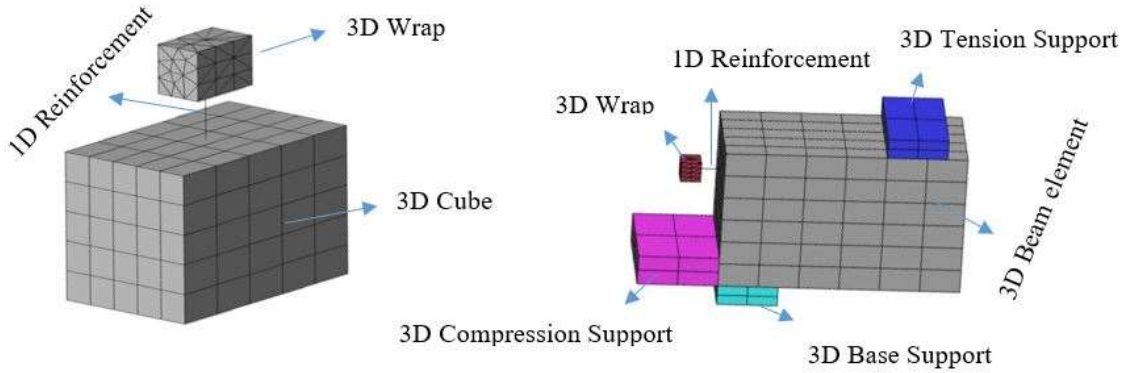

(a) (b)

Figure 6.1: Numerical Model for a) Pullout and b) Beam end specimen.

6.3 Results and Discussion on Numerical Analysis of Bond Behaviour of GPC

The results are discussed in two phases, phase A discusses the bond behaviour of GPC through pullout test and Phase B discusses the bond behaviour of GPC through beam end test as follows.

6.3.1 Phase-A: Pullout bond behaviour

The results of phase A are discussed through the influencing parameters of bond behaviour such as compressive strength, bar diameter and embedment length.

6.3.1.1 Influence of change in compressive strength of concrete on bond behaviour of GPC.

To study the effect of compressive strength on the bond strength of geopolymer concrete, a simulation was done keeping the diameter of the bar and embedment length constant while the compressive strength of the concrete was varied. The effect of variation in bond strength of GPC is represented in Figure 6.2 - 6.5 for different diameters of ribbed bar and for plain bars it is shown in Figure 6.6 - 6.9. Similar curves were obtained for normal and standard grade concrete and details are provided in Appendix-II. The percentage change in the bond stress was noted. For example, with an increase in the grade of concrete from 60 to 70, 70 to 80, 80 to 90, and 90 to 100 MPa for different embedment lengths and diameter of ribbed bars, the bond strength increased by 7.38%, 6.23%, 5.47% and 3.91% respectively and for plain bars it was 8.48%, 7.22%, 6.54% and 6.03% respectively. For different combinations, the results are presented in Table 6.1 for ribbed bars and for plain bars in Table 6.2. Similarly, for the normal and standard grades of GPC, the maximum bond strength variations can be observed in Appendix II.

The frictional forces offered from the surface of the bar also play an essential role in the bond transfer mechanism. With an increase in slip, the resistance offered by mechanical interlock reduces, leaving the frictional force as the only transfer mechanism of bond forces, also called residual forces. These residual forces are approximately equal in magnitude in both ribbed and plain bars. Thus, the ascending and descending portions of the curves (Figure 6.2 to Figure 6.5) are purely offered by the mechanical interlock (Ribs) of deformed bars. The residual forces continued till the failure of specimens. The trend as seen in the results depicts that with an increase in the grade of geopolymer concrete, the bond stress increased. The reason behind this may be an increase in tensile strength with an increase in compressive strength. As the bar causes principal compressive and tensile forces in the radial direction, the principal stresses reach their maximum capacity and the specimen fails by crushing.

Table 6.1: Effect on maximum bond stress of ribbed bars with change in compressive strength of HSGPC

D (mm) - L (mm)	Maximum bond stress (MPa)					% increase			
	60 MPa	70 MPa	80 MPa	90 MPa	100 MPa	60 to 70 MPa	70 to 80 MPa	80 to 90 MPa	90 MPa to 100 MPa
10 - 50	26.90	28.96	30.60	32.58	34.13	7.66	5.67	6.48	4.76
10 - 75	23.39	24.79	26.70	27.86	28.92	5.99	7.71	4.35	3.81
10 - 100	20.88	22.65	23.95	25.23	26.17	8.48	5.74	5.35	3.73
12 - 50	26.13	28.89	30.13	31.44	32.65	10.57	4.30	4.35	3.85
12 - 75	21.70	23.27	24.54	26.13	27.06	7.24	5.46	6.48	3.56
12 - 100	19.30	20.49	21.81	23.01	23.66	6.17	6.45	5.51	2.83
16 - 50	21.09	22.64	24.18	25.63	27.14	7.35	6.81	6.00	5.90
16 - 75	18.72	20.05	21.27	22.54	23.48	7.11	6.09	5.98	4.18
16 - 100	17.18	18.55	19.84	20.83	21.55	7.98	6.96	4.99	3.46
16 - 150	15.34	16.50	17.53	18.53	19.07	7.57	6.25	5.71	2.92
20-50	20.35	21.70	22.93	24.00	24.87	6.64	5.67	4.67	3.63
20-75	18.59	19.84	21.09	22.02	22.54	6.70	6.31	4.42	2.37
20-100	17.25	18.38	19.65	20.71	21.56	6.56	6.91	5.40	4.11
20-150	13.87	14.89	15.92	17.02	17.97	7.36	6.92	6.91	5.59
Average (%)						7.38	6.23	5.47	3.91

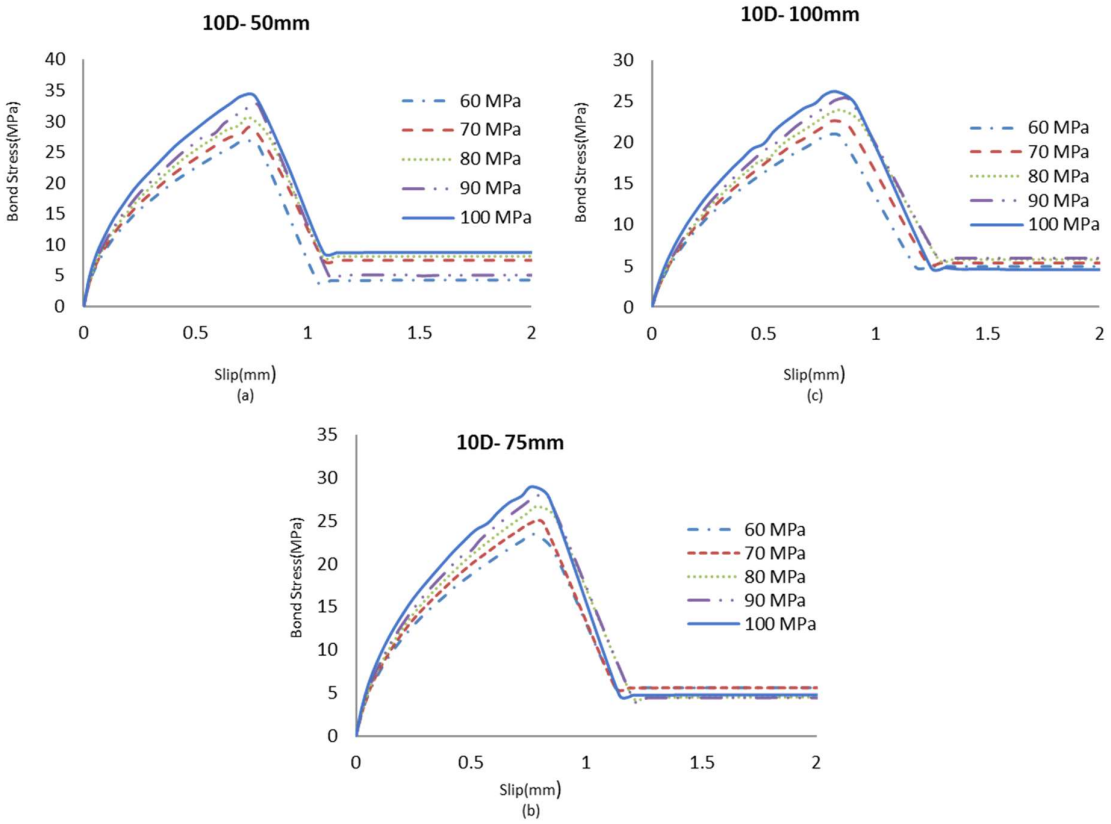

Figure 6.2: Bond vs slip of 10 mm diameter ribbed bar with different grades of concrete

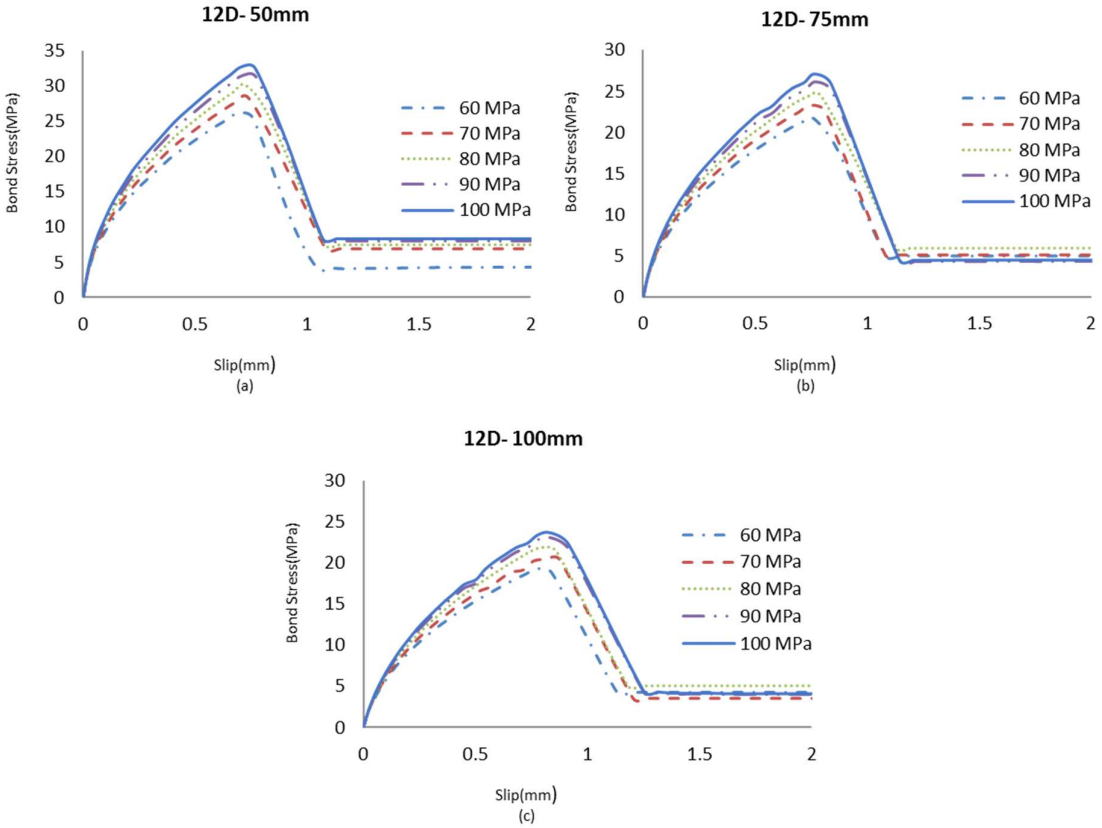

Figure 6.3: Bond vs lip of 12 mm diameter ribbed bar with different grades of concrete

Table 6.2: Effect on maximum bond stress of plain bars with change in compressive strength of HSGPC

D (mm)-L (mm)	Maximum bond stress (MPa)					% increase			
	60 MPa	70 MPa	80 MPa	90 MPa	100 MPa	60 to 70 MPa	70 to 80 MPa	80 to 90 MPa	90 to 100 MPa
10 - 50	5.09	5.51	5.86	6.19	6.54	8.26	6.36	5.64	5.66
10 - 75	4.46	4.78	5.13	5.41	5.66	7.18	7.33	5.46	4.63
10 - 100	4.05	4.34	4.64	4.9	5.35	7.17	6.92	5.61	9.19
12 - 50	4.69	5.08	5.43	5.71	6.00	8.32	6.89	5.16	5.00
12 - 75	3.87	4.19	4.46	4.73	4.99	8.27	6.45	6.06	5.50
12 - 100	3.46	3.72	3.97	4.2	4.44	7.52	6.73	5.80	5.72
16 - 50	3.34	3.6	3.85	4.07	4.26	7.79	6.95	5.72	4.67
16 - 75	2.94	3.17	3.39	3.6	3.77	7.83	6.95	6.20	4.73
16 - 100	2.74	2.96	3.17	3.36	3.55	8.03	7.10	6.00	5.66
16 - 150	2.54	2.75	2.93	3.11	3.23	8.27	6.55	6.15	3.86
20-50	2.22	2.36	2.52	2.79	2.97	6.31	6.78	10.72	6.46
20-75	1.85	2.06	2.28	2.39	2.51	11.36	10.68	4.83	5.03
20-100	1.57	1.68	1.77	1.94	2.12	7.01	5.30	9.61	9.29
20-150	1.37	1.58	1.74	1.89	2.06	15.33	10.13	8.63	9.00
Average (%)						8.48	7.22	6.54	6.03

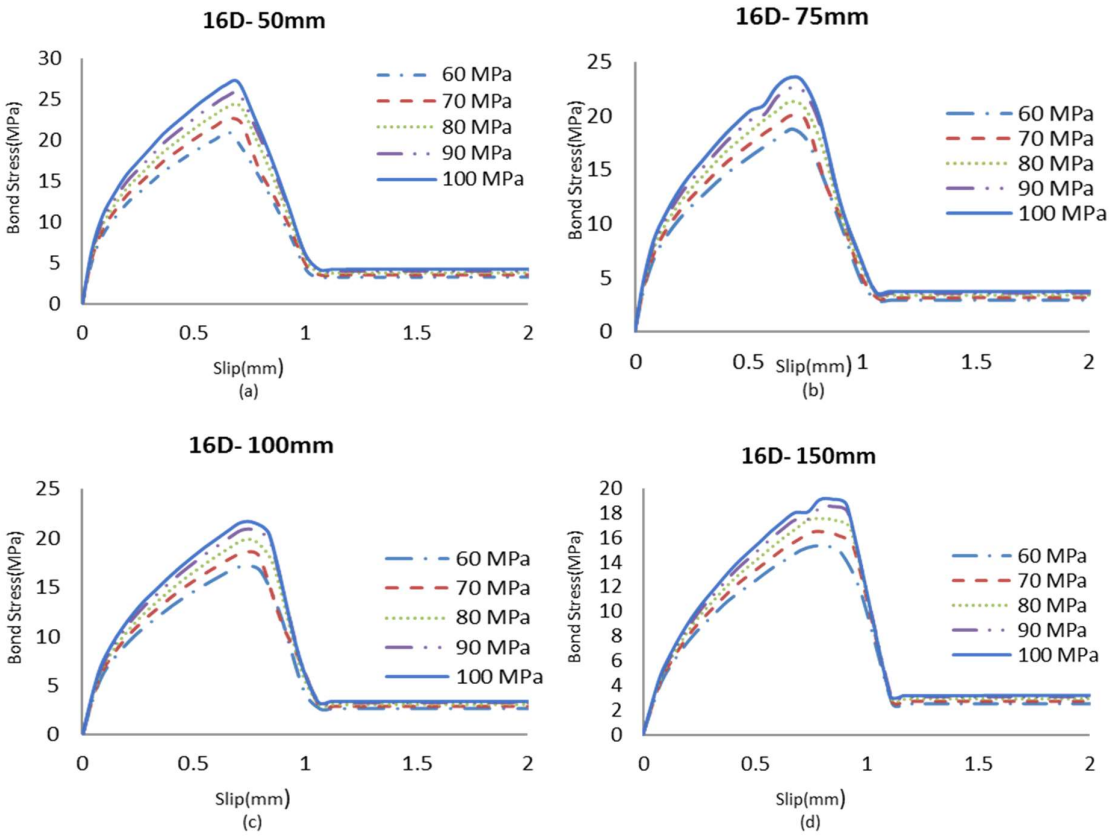

Figure 6.4: Bond vs Slip of 16 mm diameter ribbed bar with different grades of concrete

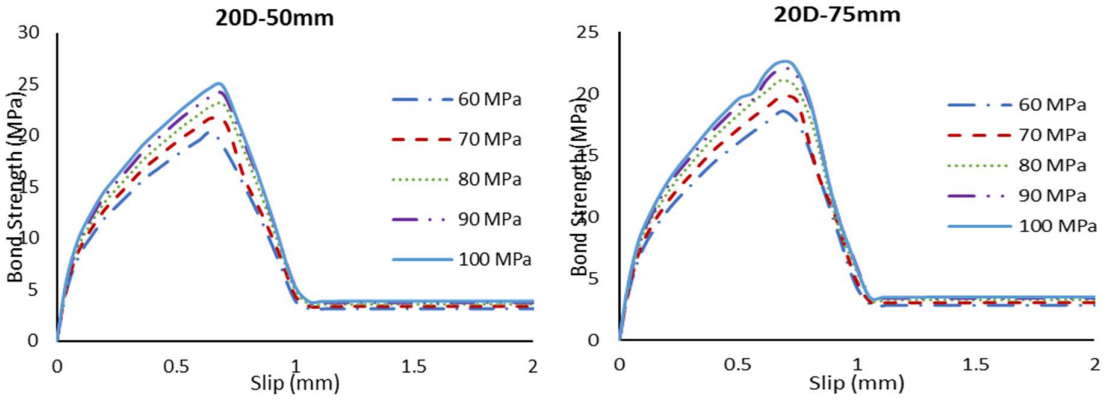

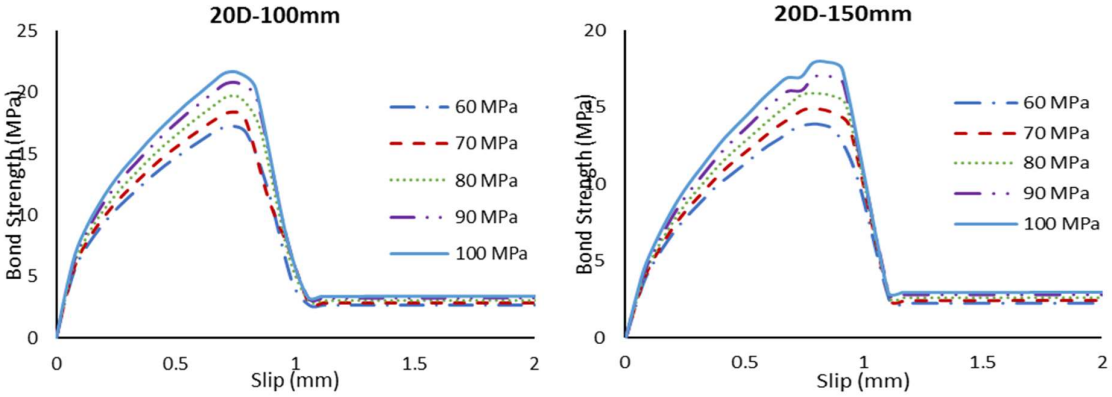

Figure 6.5: Bond vs Slip of 20 mm diameter ribbed bar with different grades of concrete

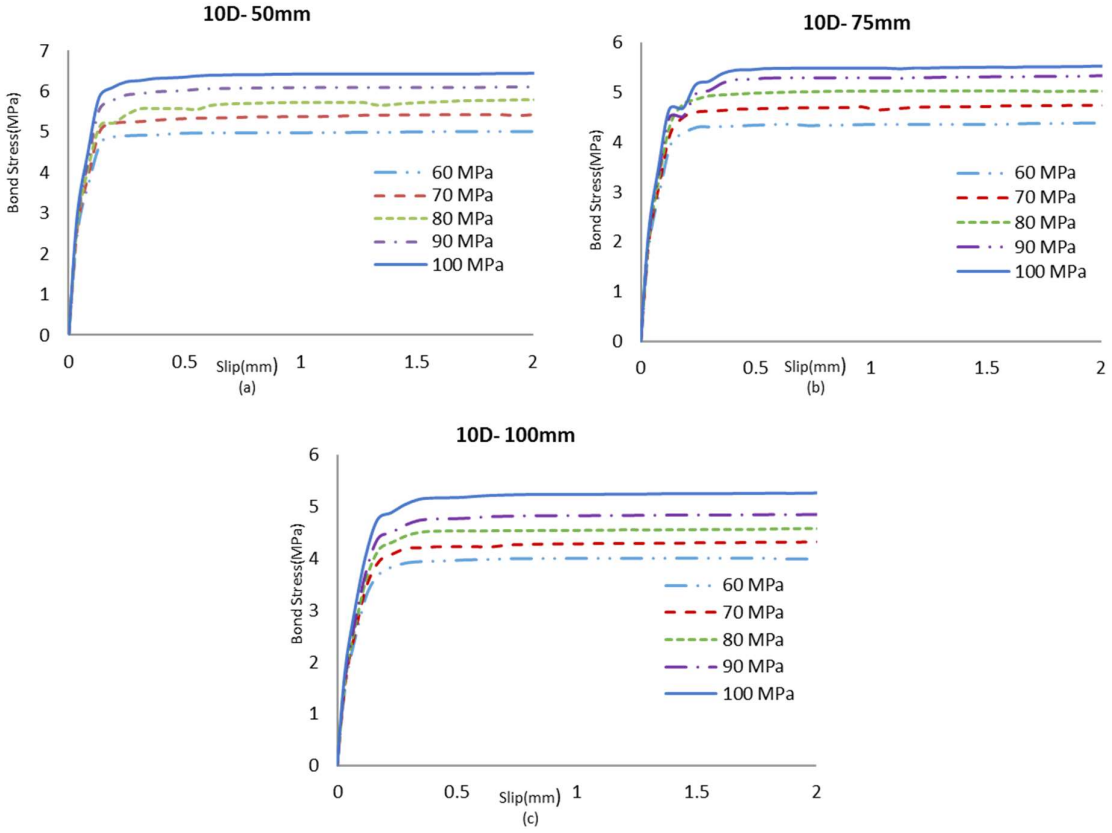

Figure 6.6: Bond vs Slip of 10 mm diameter plain bar with different grades of concrete

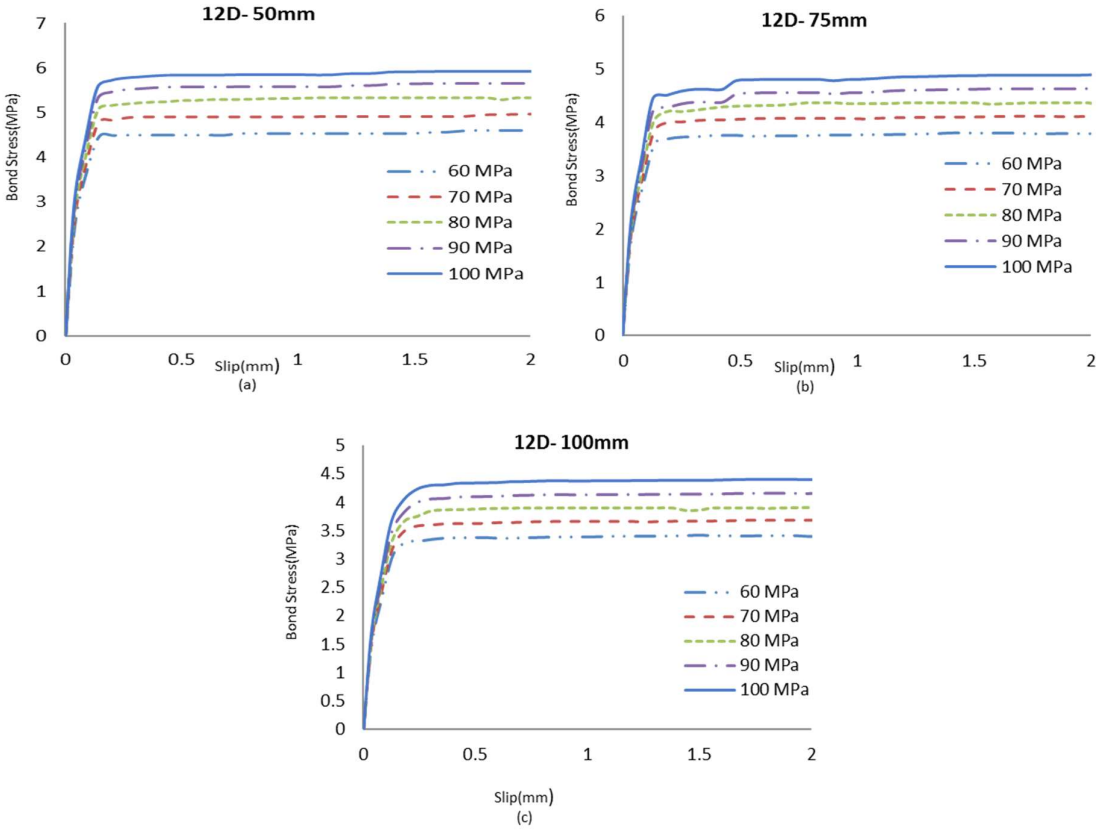

Figure 6.7: Bond vs Slip of 12 mm diameter plain bar with different grades of concrete

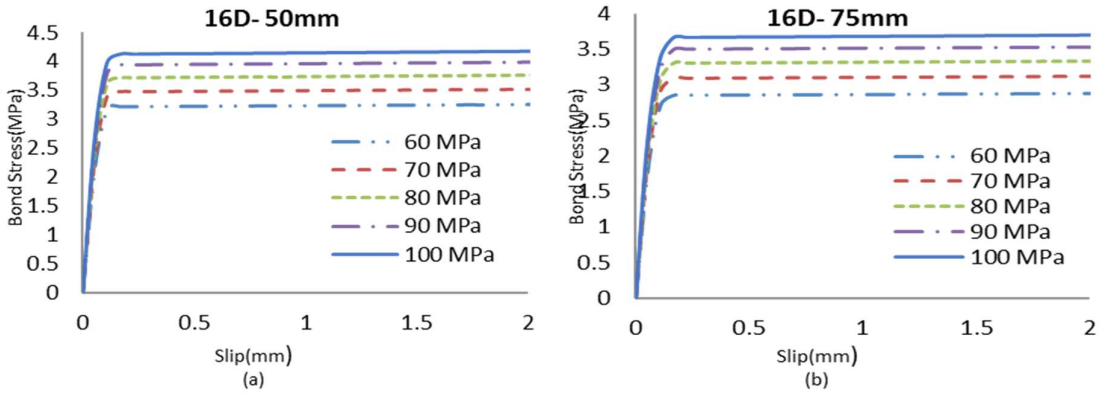

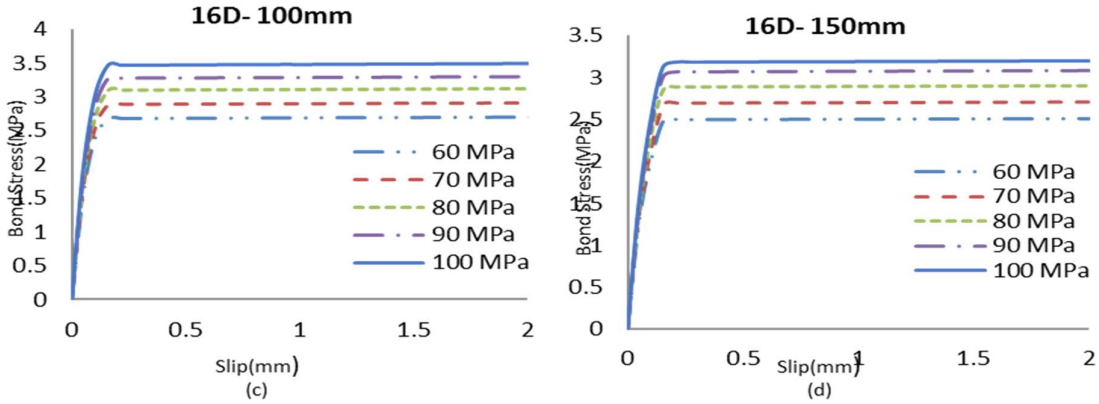

Figure 6.8: Bond vs Slip of 16 mm diameter plain bar with different grades of concrete

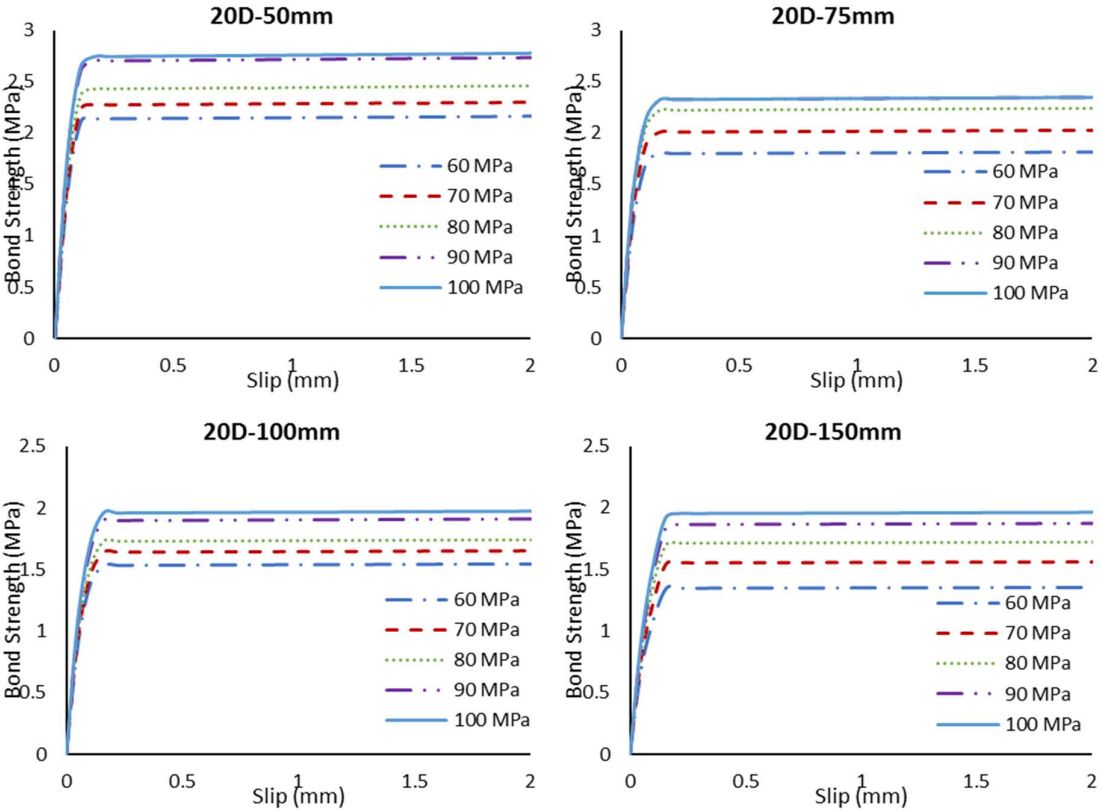

Figure 6.9: Bond vs Slip of 20 mm diameter plain bar with different grades of concrete

6.3.1.2 Influence of embedment length of the bar on bond behaviour of GPC.

The maximum bond strength and percentage change in bond strength with embedment length for the same diameter of the ribbed bar and grade of concrete are presented in Table 6.3. From the results obtained from modelling different embedment lengths, it was perceived that the increase in embedment length decreased the bond strength. With an increase in embedment length from 50 mm to 75 mm and then 75 mm to 100 mm for a 10 mm diameter bar, the average

percentage decrease in maximum bond stress was 14 % and 9.7% respectively. Similarly, for the 12 mm diameter bar, the average percentage decrease in maximum bond stress was 17.84% and 11.76% respectively while it was 12.17%, 7.34% and 10.54% for 50 to 75 mm, 75 to 100 mm and 100 to 150 mm change in embedment length respectively for 16 mm bar diameter and for 20 mm bar diameter, it was 8.59%, 6.32%, and 18.42% respectively. Also, similar behaviour was observed in the case of results in the plain bar shown in Table 6.4. With an increase in embedment length, more length of the bar had surface contact with the surrounding concrete. This results in nonlinear stress distribution in the concrete in contact with the bar causing it to fail quickly. This is the main reason for the decrease in bond stress with an increase in embedment length. Similar behaviour was observed for normal and standard-grade concrete and discussed in Appendix II.

Table 6.3: Effect on maximum bond stress of ribbed bars with change in embedment length of rebars

D (mm)	L (mm)	Maximum bond stress (MPa)					Average %
		60 MPa	70 MPa	80 MPa	90 MPa	100 MPa	
10	50	26.9	28.96	30.6	32.58	34.13	-
10	75	23.39	24.79	26.7	27.86	28.92	
10	100	20.88	22.65	23.95	25.23	26.17	
% Decrease	50 to 75	13.05	14.4	12.75	14.49	15.27	14
	75 to 100	10.74	8.64	10.3	9.45	9.51	9.7.
12	50	28.89	30.13	31.44	5.71	32.65	-
12	75	23.27	24.54	26.13	4.73	27.06	
12	100	20.49	21.81	23.01	4.2	23.66	
% Decrease	50 to 75	19.46	18.56	16.89	17.17	17.13	17.84
	75 to 100	11.95	11.13	11.95	11.21	12.57	11.76
16	50	22.64	24.18	25.63	4.07	27.14	-
16	75	20.05	21.27	22.54	3.6	23.48	
16	100	18.55	19.84	20.83	3.36	21.55	
16	150	16.5	17.53	18.53	3.11	19.07	
% Decrease	50 to 75	11.44	12.04	12.06	11.55	13.49	12.116
	75 to 100	7.49	6.73	7.59	6.67	8.22	7.34
	100 to 150	11.06	11.65	11.05	7.45	11.51	10.54
20	50	20.35	21.7	22.93	24	24.87	-
20	75	18.59	19.835	21.085	22.015	22.535	
20	100	17.25	18.38	19.65	20.71	21.56	
20	150	13.87	14.89	15.92	17.02	17.97	
% Decrease	50 to 75	8.65	8.6	8.05	8.28	9.39	8.59
	75 to 100	7.21	7.34	6.81	5.93	4.33	6.32
	100 to 150	19.6	18.99	18.99	17.82	16.66	18.42

Table 6.4: Effect on maximum bond stress of plain bars with change in embedment length of rebars

D (mm)	L (mm)	Maximum bond stress (MPa)					% Average
		60 MPa	70 MPa	80 MPa	90 MPa	100 MPa	
10	50	5.09	5.51	5.86	6.19	6.54	-
10	75	4.46	4.78	5.13	5.41	5.66	
10	100	4.05	4.34	4.64	4.9	5.35	
% Decrease	50 to 75	12.38	13.25	12.46	12.61	13.46	12.832
	75 to 100	9.2	9.21	9.56	9.43	5.48	8.576
12	50	4.69	5.08	5.43	5.71	5.995	-
12	75	3.87	4.19	4.46	4.73	4.99	
12	100	3.46	3.72	3.97	4.2	4.44	
% Decrease	50 to 75	17.49	17.52	17.87	17.17	16.77	17.364
	75 to 100	10.6	11.22	10.99	11.21	11.03	11.01
16	50	3.34	3.6	3.85	4.07	4.26	-
16	75	2.94	3.17	3.39	3.6	3.77	
16	100	2.74	2.96	3.17	3.36	3.55	
16	150	2.54	2.75	2.93	3.11	3.23	
% Decrease	50 to 75	11.98	11.95	11.95	11.55	11.51	11.788
	75 to 100	6.81	6.63	6.49	6.67	5.84	6.488
	100 to 150	7.3	7.1	7.58	7.45	9.02	7.69
20	50	2.22	2.36	2.52	2.79	2.97	-
20	75	1.85	2.06	2.28	2.39	2.51	
20	100	1.57	1.68	1.769	1.939	2.119	
20	150	1.37	1.58	1.74	1.89	2.06	
% Decrease	50 to 75	16.67	12.72	9.53	14.34	15.49	13.75
	75 to 100	15.14	18.45	22.42	18.88	15.58	18.094
	100 to 150	12.74	5.96	1.64	2.53	2.79	5.132

6.3.1.3 Influence of bar diameter on bond behaviour of GPC.

The influence of the diameter of the bar on the bond strength was evaluated by modelling ribbed bars of size 10 mm, 12 mm and 16 mm. The maximum bond stress and percentage change in bond stress for different diameters of ribbed bars with a constant grade of concrete and embedment length are shown in Table 6.5. From these results, it can be perceived that an increase in bar diameter causes a reduction in the maximum bond stress of the bar. The average percentage decrease in the maximum bond stress was 2.50%, 19.21% and 5.51% following an increase in diameter from 10 mm to 12 mm, 12 mm to 16 mm and 16 mm to 20 mm, respectively for 50 mm embedment length. Similarly, the average percentage decrease was 6.82%, 13.58%, and 1.80% for 75 mm embedment length and 8.89%, 11.68, and 1.56% for 100 mm embedment length. Also, similar behaviour was observed in a plain bar which can be seen in Table 6.6. The decrease in bond stress with an increase in the diameter of the bar is due to the presence of

larger ITZ in concrete with higher-diameter bars. As the ITZ is in a weak phase in the surrounding portion of the aggregate and the bar, it decreases the overall bond strength in concrete. In case of normal and standard-grade concrete, the effect of bar diameter is not significant with respect to bond strength, which can be observed from the bond strength-slip curves shown in Appendix II.

Table 6.5: Effect on maximum bond stress of ribbed bars with change in diameter of rebars

L (mm)	D (mm)	Maximum bond stress (MPa)					Average %
		60 MPa	70 MPa	80 MPa	90 MPa	100 MPa	
50	10	26.90	28.96	30.60	32.58	34.13	-
	12	26.13	28.89	30.13	31.44	32.65	
	16	21.09	22.64	24.18	25.63	27.14	
	20	20.35	21.70	22.93	24.00	24.87	
% Decrease	10 to 12	2.87	0.25	1.54	3.50	4.34	2.50
	12 to 16	19.29	21.64	19.75	18.48	16.88	19.21
	16 to 20	3.51	4.16	5.17	6.36	8.37	5.51
75	10	23.39	24.79	26.70	27.86	28.92	-
	12	21.70	23.27	24.54	26.13	27.06	
	16	18.72	20.05	21.27	22.54	23.48	
	20	18.59	19.84	21.09	22.02	22.54	
% Decrease	10 to 12	7.23	6.14	8.09	6.21	6.44	6.82
	12 to 16	13.74	13.84	13.33	13.74	13.23	13.58
	16 to 20	0.70	1.08	0.87	2.33	4.03	1.80
100	10	20.88	22.65	23.95	25.23	26.17	-
	12	19.30	20.49	21.81	23.01	23.66	
	16	17.18	18.55	19.84	20.83	19.07	
	20	17.25	18.38	19.65	20.71	17.97	
% Decrease	10 to 12	7.57	9.54	8.94	8.80	9.60	8.89
	12 to 16	10.99	9.47	9.04	9.48	19.40	11.68
	16 to 20	0.41	0.92	0.96	0.58	5.77	1.56

6.3.1.4 Comparison of numerical analysis with experimental results

The results of the bond stress of the ribbed bar obtained from ATENA are compared with the results of the pullout experiments in Chapter 6. The results of the bond stress of ribbed bars for different embedment lengths (L), bar diameter (D), and compressive strength from numerical analysis and pullout experiments are given in Table 6.7. The percentage deviation between experimental and numerical results is also shown in Table 6.7. An average percentage difference of 7.5%, 9.03%, and 7.14% was observed in the case of 60, 80, and 100 MPa concrete respectively for different bar diameters and embedment lengths.

Table 6.6: Effect on maximum bond stress of plain bars with change in diameter of rebars

L (mm)	D (mm)	Maximum bond stress (MPa)					Average %
		60 MPa	70 MPa	80 MPa	90 MPa	100 MPa	
50	10	5.09	5.51	5.86	6.19	6.54	-
	12	4.69	5.08	5.43	5.71	6.00	
	16	3.34	3.6	3.85	4.07	4.26	
	20	2.22	2.36	2.52	2.79	2.97	
% Decrease	10 to 12	7.86	7.81	7.34	7.76	8.34	7.82
	12 to 16	28.79	29.14	29.10	28.73	28.95	28.94
	16 to 20	33.54	34.45	34.55	31.45	30.29	32.86
75	10	4.46	4.78	5.13	5.41	5.66	-
	12	3.87	4.19	4.46	4.73	4.99	
	16	2.94	3.17	3.39	3.6	3.77	
	20	1.85	2.06	2.28	2.39	2.51	
% Decrease	10 to 12	13.23	12.35	13.07	12.57	11.84	12.61
	12 to 16	24.04	24.35	24.00	23.90	24.45	24.15
	16 to 20	37.08	35.02	32.75	33.62	33.43	34.38
100	10	4.05	4.34	4.64	4.9	5.35	-
	12	3.46	3.72	3.97	4.2	4.44	
	16	2.54	2.75	2.93	3.11	3.23	
	20	1.57	1.68	1.769	1.939	2.06	
% Decrease	10 to 12	14.57	14.29	14.44	14.29	17.01	14.92
	12 to 16	26.59	26.08	26.20	25.96	27.26	26.42
	16 to 20	38.19	38.91	39.63	37.66	36.23	38.12

Table 6.7: Difference between experimental and numerical results

D (mm) -L (mm)	Experimental Maximum bond stress (MPa)			Numerical Maximum bond stress (MPa)			% Deviation		
	60 MPa	80 MPa	100 MPa	60 MPa	80 MPa	100 MPa	60 MPa	80 MPa	100 MPa
12-30	34.66	37.24	39.68	33.72	35.14	38.07	2.72	5.64	4.05
12-60	24.06	25.47	27.84	24.23	26.02	27.37	0.73	2.14	1.68
12-100	17.87	18.59	20.32	19.3	21.81	23.66	8.00	17.33	16.44
16-40	30.07	32.61	33.47	25.84	27.95	31.92	14.07	14.29	4.63
16-80	19.52	23.07	24.94	18.27	20.57	24.07	6.40	10.84	3.49
16-150	15.03	15.69	17.42	15.34	17.53	19.07	2.10	11.71	9.50
20-50	26.32	27.88	29.14	20.35	22.93	24.87	22.68	17.75	14.65
20-100	16.24	19.68	23.10	17.25	19.65	21.56	6.22	0.15	6.67
20-150	13.26	15.69	17.42	13.87	15.92	17.97	4.58	1.45	3.18
Average %							7.50	9.03	7.14

6.3.1.5 Comparison of bond behaviour between plain and ribbed bars

The three basic stages which contribute to overall bond behaviour are:

I. Chemical adhesion

II. Mechanical interlock and

III. Friction.

Among these, the mechanical interlock is exclusive only to deformed bars due to the presence of ribs. The ribs present in these bars provide extra gripping strength during the pull, thus increasing the overall bond capacity of the ribbed bars. This advantage is not available in plain bars, where the initial bond strength is provided by chemical adhesion followed by surface friction of plain bars. Referring to the results of the bond behaviour of the plain bar, it can be observed that the ascending curve represents the influence of chemical adhesion on the bond capacity of the bar followed by a constant line which shows friction contribution.

On the other hand, mechanical interlock provides a sufficient contribution to overall bond capacity in the intermediate stage represented by the descending portion of the curve of bond stress vs slip as observed in the results of bond behaviour of ribbed bars. The percentage increase in maximum bond strength of ribbed bar compared to plain bar is presented in Table 6.8.

Table 6.8: Comparison of maximum bond stress between ribbed bars and plain bars

D (mm)-L (mm)	Maximum bond strength (MPa)														
	60 MPa			70 MPa			80 MPa			90 MPa			100 MPa		
	Ribbed	Plain	% Increase	Ribbed	Plain	% Increase	Ribbed	Plain	% Increase	Ribbed	Plain	% Increase	Ribbed	Plain	% Increase
10 - 50	26.9	5.09	428.49	28.96	5.51	425.6	30.6	5.86	422.18	32.58	6.19	426.3	34.13	6.54	421.87
10 - 75	23.39	4.46	424.44	24.79	4.78	418.6	26.7	5.13	420.47	27.86	5.41	415	28.92	5.66	410.95
10 - 100	20.88	4.05	415.56	22.65	4.34	421.9	23.95	4.64	416.16	25.23	4.9	414.9	26.17	5.35	389.16
12 - 50	26.13	4.69	457.14	28.89	5.08	468.7	30.13	5.43	454.88	31.44	5.71	450.6	32.65	5.995	444.62
12 - 75	21.7	3.87	460.72	23.27	4.19	455.4	24.54	4.46	450.22	26.13	4.73	452.4	27.06	4.99	442.28
12 - 100	19.3	3.46	457.80	20.49	3.72	450.8	21.81	3.97	449.37	23.01	4.2	447.9	23.66	4.44	432.88
16 - 50	21.09	3.34	531.44	22.64	3.6	528.9	24.18	3.85	528.05	25.63	4.07	529.7	27.14	4.26	537.09
16 - 75	18.72	2.94	536.73	20.05	3.17	532.5	21.27	3.39	527.43	22.54	3.6	526.1	23.48	3.77	522.81
16 - 100	17.18	2.74	527.01	18.55	2.96	526.7	19.84	3.17	525.87	20.83	3.36	519.9	21.55	3.55	507.04
16 - 150	15.34	2.54	503.94	16.5	2.75	500	17.53	2.93	498.29	18.53	3.11	495.8	19.07	3.23	490.40
20-50	20.35	2.22	816.67	21.7	2.36	819.5	22.93	2.52	809.92	24	2.79	760.2	24.87	2.97	737.37
20-75	18.59	1.85	904.86	19.84	2.06	862.9	21.09	2.28	824.78	22.02	2.39	821.1	22.54	2.51	797.81
20-100	17.25	1.57	998.73	18.38	1.68	994	19.65	1.769	1010.80	20.71	1.939	968.1	21.56	2.119	917.46
20-150	13.87	1.37	912.41	14.89	1.58	842.4	15.92	1.74	814.94	17.02	1.89	800.5	17.97	2.06	772.33
Average (%)			598.28	Average (%)		589.1	Average (%)		582.38	Average (%)		573.5	Average (%)		558.86

6.3.2 Phase-B: Beam End Bond Behaviour

The phase B results are used to develop an identical analytical model for the prediction of the bond strength of GPC. The following methodology is used for the development of an analytical model for the bond strength of GPC.

6.3.2.1 Development of an analytical model on bond strength for GPC

Numerical simulation is performed for various combinations of variable parameters influencing the maximum bond stress as shown in Table 6.9 and Table 6.10. Similar to pullout bond behaviour, beam end analysis also showed that an increase in embedment length to bar diameter ratio led to a decrease in bond stress. As the concrete cover-to-bar diameter ratio increases, there is a corresponding increase in bond stress. With an increase in the grade of concrete, the bond stress increased. As in the case of pullout bond strength, concrete is in compression and steel is in tension while in the case of beam end specimen, concrete surrounding the steel is in tension which is a more practical scenario that can be observed in traditional beams. A total of 324 beam end specimens are analysed to create a good data set. An analytical model was developed based on numerical analysis of phase B results as beam end specimens provide bond strength that is closer to practical beam conditions. Most of the codes of practice across the world predict bond strength as a function of the grade of concrete. In the present simulation, an equation incorporating embedment length to rebar diameter ratio and concrete cover to rebar diameter ratio along with the grade of concrete form a part of the numerical simulation results. Multiple nonlinear regression analysis was performed on the data set available by considering the parameters le/d, c/d and f_{ck} as independent variables. Maximum bond stress (τ_{max}) was the dependent variable on the parameters mentioned. It can be observed from the numerical analysis that the le/d ratio is inversely proportional to the bond stress, while, the c/d ratio and compressive strength are directly proportional to bond stress. Considering the above parameters and the nature of the dependency of bond stress on the independent variables, the equation for predicting the maximum bond strength is formulated as given in Eq 6.1.

$$\tau_{max} = \left(P + \frac{Q}{\frac{l_e}{d}}\right) * \left(R + S * \frac{c}{d}\right) * {f_{ck}}^{T} \qquad \text{Eq 6.1}$$

In the above equation, P, Q, R, S and, T are constants that are needed for minimizing the normalised error while performing nonlinear regression statistical analysis on the results obtained from numerical data for the best curve fit between the dependent and independent

variables. Non-linear regression analysis conducted based on a non-linear regression equation has the following form:

$$Y' = f(X, k) + \varepsilon$$

Here Y' = a predicted vector

X= a vector of ρ predictors,

K= a vector of q parameters.

f(-)= a known regression function.

ε = an error term.

Multiple nonlinear regression analysis was performed based on ordinary least squares, assuming errors are normally distributed with zero mean and constant variance. The function was fit such that the sum of squares of difference of observed(Y) and predicted (Y') values could be minimized.

Minimize $\sum(Y - Y')^2$

$$Y = Y' + \varepsilon$$

Based on this, multiple iterations have been performed to minimize normalised error and determine a vector of ρ predictors. Excel solver was used for performing the multiple non-linear regression analysis and the values for the constant terms P, Q, R, S and T were determined. The proposed analytical equation for the prediction of maximum bond strength for normal, standard and high strength is shown by Eqs 6.2 and 6.3

For compressive strength 10 to 50 MPa	$\tau_{max} = \left[\left(-0.085 + 0.511\frac{c}{d}\right)\frac{d}{l_e} + 0.627\right] f_{ck}^{0.616}$	Eq 6.2
For compressive strength above 50 MPa	$\tau_{max} = \left(0.38 + \frac{1.82}{\frac{l_e}{d}}\right) \text{x} \left(0.375 + 0.124 \times \frac{c}{d}\right) \text{x } f_{ck}{}^{0.76}$	Eq 6.3

Where,

τ_{max} = Maximum bond strength in MPa

c = Concrete Cover (mm)

le = Embedment length (mm)

d = Diameter of reinforcement bar (mm)

f_{cc} = Characteristic cube compressive strength (MPa)

Table 6.9: Beam end results of normal and standard strength of GPC from ATENA

l_e/d	c/d	Maximum Bond Strength τ_{max} (MPa)			
		20 MPa	30 MPa	40 MPa	50 MPa
9	1	4.45	5.37	5.46	7.11
9	1.5	4.79	5.80	6.38	6.72
9	2	4.83	6.10	7.18	7.55
9	2.5	5.04	6.15	8.44	9.28
9	3	5.36	6.47	8.49	9.65
9	3.5	5.31	6.50	8.00	9.06
9	4	5.34	6.60	7.81	9.06
9	4.5	5.89	7.04	8.86	9.84
9	5	6.43	7.35	9.75	12.28
7	1	5.06	6.07	5.68	6.47
7	1.5	5.27	6.50	6.65	6.71
7	2	5.22	6.89	7.55	8.27
7	2.5	5.61	6.98	8.26	10.58
7	3	5.93	7.22	8.80	10.59
7	3.5	5.69	7.20	8.17	9.05
7	4	5.70	7.21	8.22	9.09
7	4.5	6.22	7.52	9.02	10.42
7	5	6.59	7.92	10.58	12.79
5	1	4.76	6.09	5.66	6.39
5	1.5	4.73	6.45	6.65	8.34
5	2	5.48	6.64	7.94	9.40
5	2.5	5.72	6.67	9.91	12.20
5	3	5.85	7.03	9.90	12.27
5	3.5	5.57	7.02	8.38	10.84
5	4	5.62	7.08	8.26	10.84
5	4.5	6.17	7.55	9.91	12.24
5	5	6.97	8.09	12.15	14.56
3	1	4.48	6.60	6.76	8.97
3	1.5	5.24	7.56	8.55	9.28
3	2	6.29	8.12	10.67	11.78
3	2.5	7.73	8.43	13.44	16.16
3	3	7.77	8.85	13.66	16.51
3	3.5	6.96	8.41	11.62	13.74
3	4	6.90	8.47	11.15	13.69
3	4.5	7.76	9.64	13.49	16.64
3	5	9.34	10.72	16.09	20.12

Table 6.10: Beam end results of high strength GPC from ATENA

l_e/d	c/d	Maximum Bond Stress τ_{max} (MPa)				
		60 MPa	70 MPa	80 MPa	90 MPa	100 MPa
9	1	6.53	7.34	8.12	8.89	9.65
9	1.5	7.34	8.25	9.13	9.99	10.83
9	2	8.15	9.16	10.14	11.09	12.01
9	2.5	8.96	10.08	11.15	12.19	13.20
9	3	9.77	10.99	12.16	13.3	14.41
9	3.5	10.58	11.9	13.17	14.4	15.59
9	4	11.39	12.81	14.18	15.5	16.77
9	4.5	12.21	13.72	15.19	16.61	17.98
9	5	13.02	14.63	16.2	17.71	19.16
7	1	7.18	8.07	8.93	9.77	10.59
7	1.5	8.07	9.07	10.04	10.98	11.89
7	2	8.96	10.07	11.15	12.19	13.19
7	2.5	9.85	11.07	12.26	13.4	14.49
7	3	10.74	12.08	13.37	14.62	15.83
7	3.5	11.63	13.08	14.48	15.83	17.13
7	4	12.52	14.08	15.58	17.04	18.46
7	4.5	13.42	15.08	16.69	18.26	19.79
7	5	14.31	16.08	17.8	19.47	21.09
5	1	8.34	9.38	10.38	11.35	12.29
5	1.5	9.38	10.54	11.67	12.76	13.81
5	2	10.42	11.71	12.96	14.17	15.34
5	2.5	11.45	12.87	14.25	15.58	16.86
5	3	12.49	14.04	15.54	16.99	18.39
5	3.5	13.52	15.2	16.83	18.4	19.91
5	4	14.56	16.37	18.12	19.81	21.44
5	4.5	15.6	17.53	19.41	21.22	22.96
5	5	16.63	18.7	20.69	22.63	24.52
3	1	11.06	12.44	13.77	15.05	16.28
3	1.5	12.44	13.98	15.47	16.92	18.33
3	2	13.81	15.53	17.18	18.79	20.36
3	2.5	15.18	17.07	18.89	20.66	22.38
3	3	16.56	18.62	20.6	22.53	24.41
3	3.5	17.93	20.16	22.31	24.4	26.43
3	4	19.31	21.71	24.02	26.27	28.46
3	4.5	20.68	23.25	25.73	28.14	30.48
3	5	22.05	24.79	27.44	30.01	32.50

6.3.2.1 Comparison of numerical analysis with codal provisions and analytical methods

The results obtained from numerical analysis using ATENA (Červenka et al., 2005) are compared with existing analytical equations in the literature and a correlation between these is studied. The models shown in Table 2.2 are considered for comparison with the numerical results. Figure 6.10 and Figure 6.11 show the correlation of maximum bond stress τ_{max} between

different existing models and numerical bond behaviour results of normal, standard and high strength GPC obtained from ATENA. It can be noted that the analytical equations based on considering the parameters viz; embedment length, diameter of the bar and minimum cover for predicting maximum bond stress, have shown good correlation. This confirms that the bond behaviour is more empirically established when embedment length, bar diameter, cover of concrete to bar diameter, and compressive strength are considered for prediction.

Among all the proposed equations, the equation developed shows a better correlation with $R^2 = 0.88$ for numerical results. The other analytical equations and codal provisions seem to underestimate the bond behaviour of geopolymer concrete while the analytical model proposed by Esfahani and Rangan (Rangan, 1998), which considers the tensile strength of concrete without embedment length, resulted in a lower correlation compared to numerical results. Similarly, the equation based on AS 3600 (AS 3600, 2009), has exhibited a lower correlation with numerical results. Among all the models considered, the equation proposed by fib MC 2000 (Walraven, 2012) and Z.Dahou et al., 2016 (Dahou et al., 2016) showed the lowest correlation, since the prediction of maximum bond strength is based purely on the compressive strength of concrete.

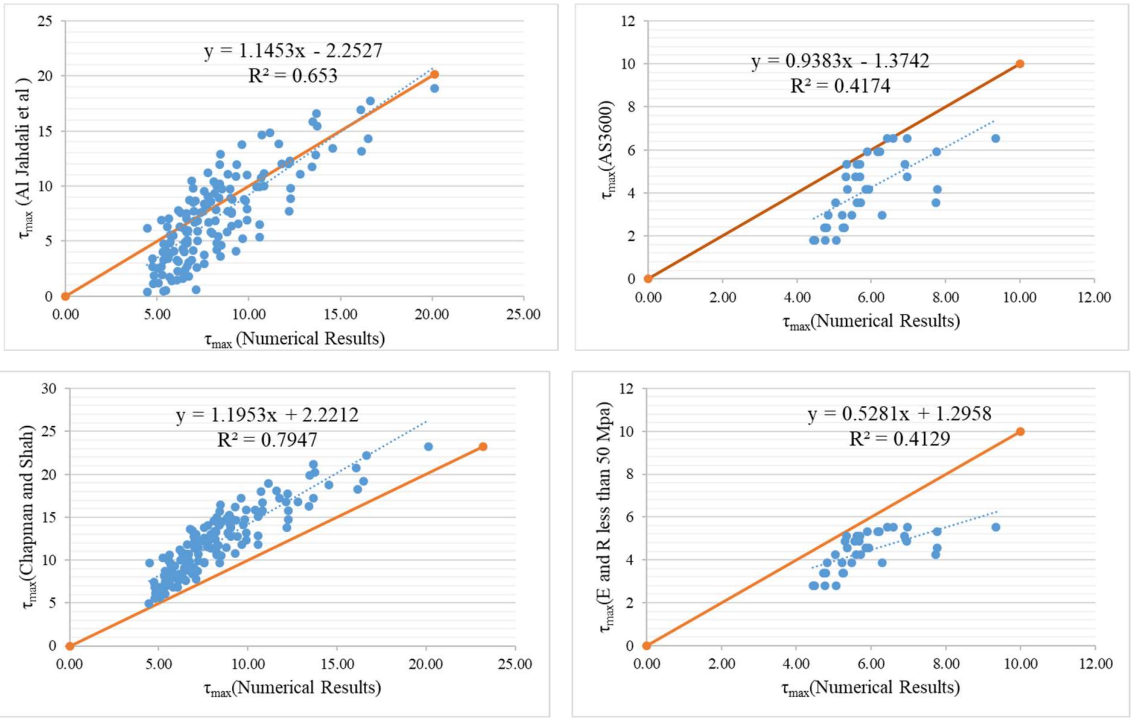

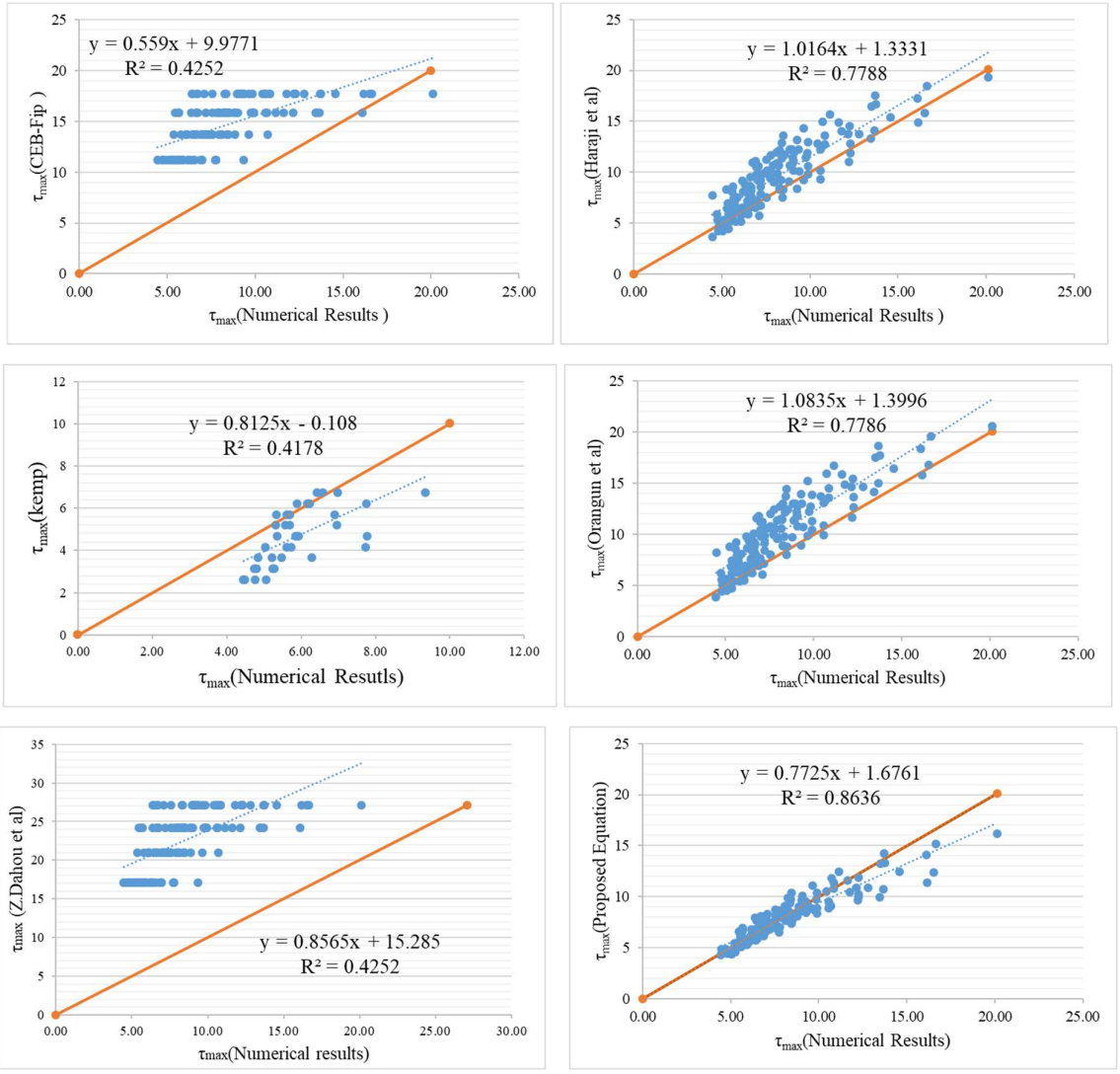

Figure 6.10: Correlation of maximum bond stress of normal and standard GPC (τ_{max}) between the numerical results and existing analytical models.

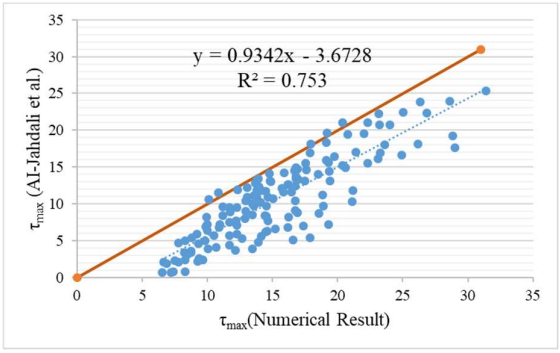
y = 0.9342x - 3.6728
R² = 0.753
τmax (Al-Jahdali et al.)
τmax(Numerical Result)

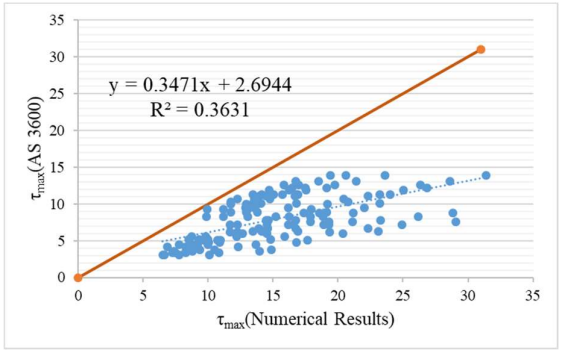
y = 0.3471x + 2.6944
R² = 0.3631
τmax(AS 3600)
τmax(Numerical Results)

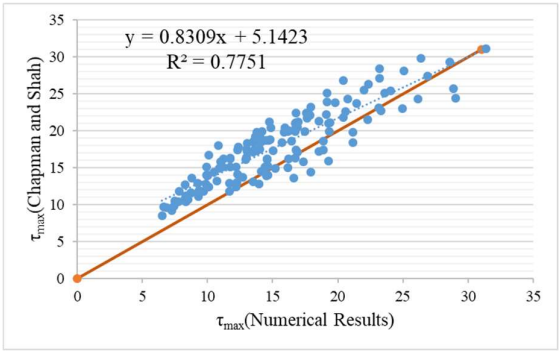
y = 0.8309x + 5.1423
R² = 0.7751
τmax(Chapman and Shah)
τmax(Numerical Results)

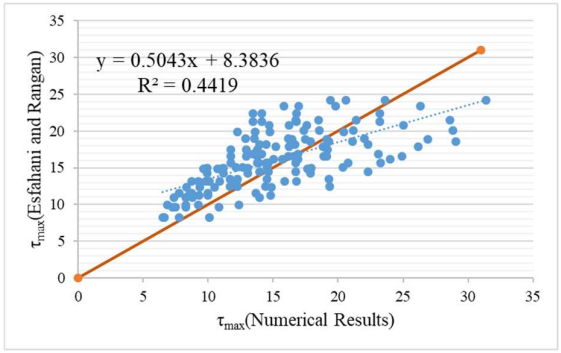
y = 0.5043x + 8.3836
R² = 0.4419
τmax(Esfahani and Rangan)
τmax(Numerical Results)

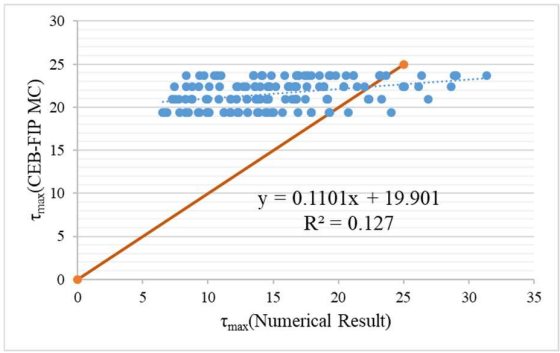
y = 0.1101x + 19.901
R² = 0.127
τmax(CEB-FIP MC)
τmax(Numerical Result)

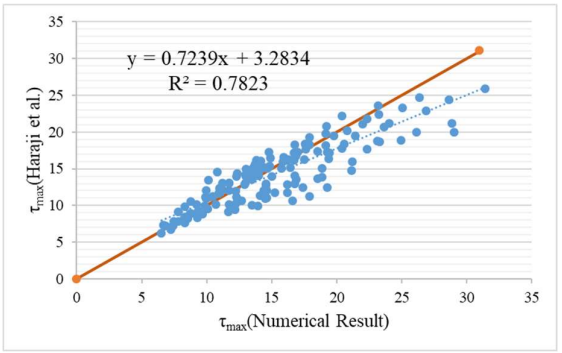
y = 0.7239x + 3.2834
R² = 0.7823
τmax(Haraji et al.)
τmax(Numerical Result)

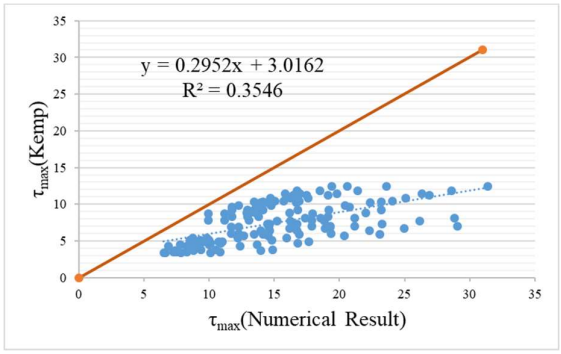
y = 0.2952x + 3.0162
R² = 0.3546
τmax(Kemp)
τmax(Numerical Result)

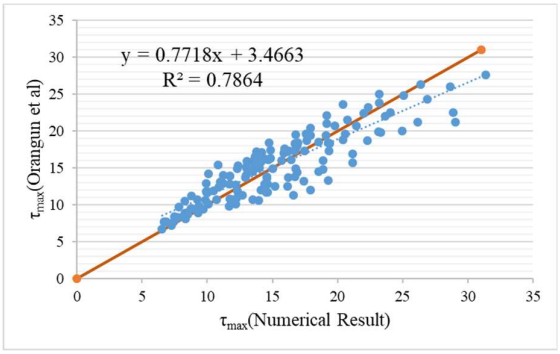
y = 0.7718x + 3.4663
R² = 0.7864
τmax(Orangun et al.)
τmax(Numerical Result)

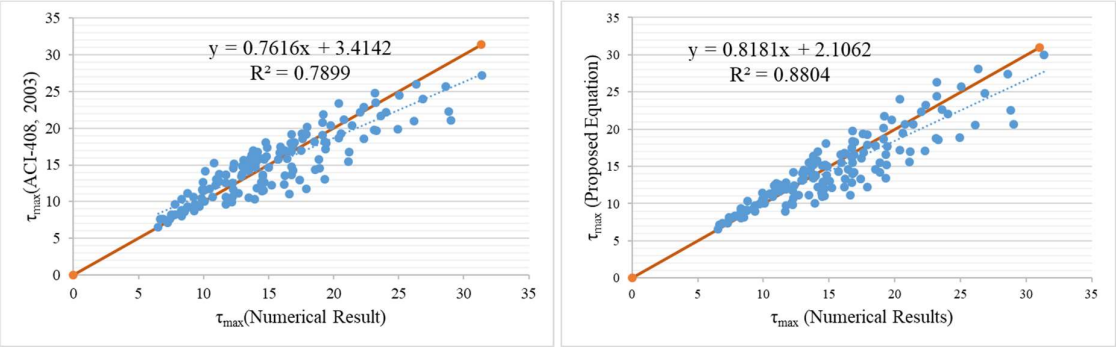

Figure 6.11: Correlation of maximum bond stress of HSGPC (τ_{max}) between the numerical results and existing analytical models.

6.4 Remarks based on the Numerical Analysis

The bond performance of normal, standard and high-strength GPC through numerical analysis of pullout and beam end tests was investigated in this phase of work. The parameters under numerical pullout analysis included concrete compressive strength (20, 30, 40, 50, 60, 70, 80, 90 and 100 MPa), bar diameter (D = 10, 12, 16 and 20 mm) and embedment length (50, 75, 100 and 150 mm). For numerical analysis of flexural beam end specimen, the parameters concrete compressive strength (20, 30, 40, 50, 60, 70, 80, 90 and 100 MPa), cover to bar diameter ratio (1 to 5 at an increment of 0.5), embedment length to bar diameter ratio (3, 5, 7 and 9) were considered. Based on multiple nonlinear regression analyses of numerical data analytical models are proposed for the prediction of maximum bond strength for normal, standard and high-strength geopolymer concrete. From this phase of work, the following conclusions can be drawn:

1. Similar to experimental results, the bond strength in HSGPC concrete increases with the compressive strength of concrete, and cover, and decreases with bar diameter and embedded length. This phenomenon is similar for all grades of concretes (60, 70, 80, 90 and 100 MPa).
2. Similar to HSGPC, the normal and standard grades of GPC showed that the bond strength increases with the compressive strength of concrete and cover, and decreases with embedded length and bar diameter. This phenomenon is similar for all grades of concretes (20, 30, 40 and 50 MPa).
3. The numerical bond behaviour of high-strength GPC is in line with experimental investigations and showed similar variation with changes in compressive strength,

embedment length, bar diameter and cover to bar. The difference between the experimental and numerical results of maximum bond strength was lower than 15% in case of pullout bond behaviour of HSGPC.

4. There is an average of 546% increase in bond strength with the use of ribbed bars compared to plain bars. This behaviour is identical for all grades of concrete for different embedment lengths and bar diameters.
5. An equation to predict the maximum bond strength of geopolymer concrete for a range of GPC grades 20, 30, 40, and 50 MPa is proposed based on the results of the present study. The relation is given by:

$$\tau_{max} = \left[\left(-0.085 + 0.511\,\frac{c}{d}\right)\frac{d}{l_e} + 0.627\right] f_{ck}^{0.616}$$

Where, τ_{max}= Bond Strength (MPa) C = Concrete Cover (mm) l_e= Embedment length (mm) d= Diameter of reinforcement bar (mm) f_{ck}= Characteristic cube compressive strength (MPa)

6. An equation for predicting the maximum bond stress considering the cover-to-diameter ratio, embedment length-to-diameter ratio and compressive strength, is proposed for a range of GPC grades at 60, 70, 80, 90 and 100 MPa.

$$\tau_{max} = \left(0.38 + \frac{1.82}{\frac{l_e}{d}}\right) \times \left(0.375 + 0.124 \times \frac{c}{d}\right) \times {f_{ck}}^{0.76}$$

7. There is a satisfactory correlation of the proposed analytical equation with the numerical simulation based on similar parameters. The correlation coefficient is 0.86 and 0.88 for NSGPC, and HSGPC respectively.

CHAPTER 7
CONCLUSIONS AND SCOPE FOR FUTURE WORK

7.1 General

High-strength geopolymer concrete mixes 60, 80 and 100 MPa are developed using multi-component binders and particle packing approach. A detailed experimental investigation of strength, chemical resistance and structural aspects of developed HSGPC mixes was performed. The mechanical properties such as modulus of elasticity, stress-strain behaviour, flexural and splitting tensile strength were investigated. The resistance to chemical attack was evaluated through the Dimensional Loss Factor (DLF), Mass Loss Factor (MLF), and Strength Loss Factor (SLF). The structural aspects viz., anchorage and flexural bond behaviour were determined through experimental investigations based on pullout (IS 2770 (Part-1), BIS 2007) and hinged beam tests (RILEM Fip-Ceb-RC5-TC9). Numerical analysis is adopted to study the bond behaviour through a wide range of parameters. Analytical models are proposed to predict maximum bond strength for normal, standard and high-strength GPC using multiple non-linear regression analysis.

7.2 Conclusions

1. Gradation based on the Modified Toufar Model (MTM) exhibited a higher packing density of 0.712 while the J D Dewar Model (JDD) method showed a packing density of 0.69. The ratio of CA: FA ratio is 55:45 as per the MTM method.
2. A 100 MPa compressive strength is achieved with ambient curing with a 10% alccofine along with other binders like flyash, GGBS, and silica fume. From SEM analysis, it is evident that GPC samples (with alccofine along with other binders) exhibited a dense structure. This can be attributed to polymerisation and polycondensation, resulting in higher compressive strength.
3. From the elemental composition, based on the ratio of Si to Al and Na to Al, it is possible to form a 3D network of polysialate-siloxo and polysialate-disiloxo. Mix with 10% alccofine (along with other binders) and 16 M NaOH showed a higher rate of gain of strength.

4. A constitutive model for predicting the stress-strain behaviour of alccofine-based high-strength GPC was established. The modulus of elasticity of GPC was lower than that of conventional concrete.

$$\sigma = \sigma' \ \frac{\epsilon}{\epsilon 0}\left[\frac{A}{A-1+\left(\frac{\epsilon}{\epsilon_0}\right)^B}\right],$$

Where, $A=\frac{Ec}{262792.3}+6.45$, $E_c= 2391.85 \text{ x } (fck)^{0.476}$, $\epsilon_0 = 6.161 \text{ x } 10^{-4} \text{ x } \sigma'^{0.424}$ and $B = \frac{2768.633}{\sigma\prime - 29.55}$

5. For 90 days of exposure to HCl, H_2SO_4, $MgSO_4$ and NaCl, 60 MPa concrete exhibited lower chemical resistance compared with 80 and 100 MPa. This is evident from the lower values of DLF, MLF, SLF, and ADLF. The reason could be attributed to a higher percentage of siliceous compounds. The extent of deterioration is in the order of H_2SO_4 > HCl > $MgSO_4$ > NaCl.

6. Pullout bond and flexural bond strengths increase with increase in the grade of concrete and decreases with increase in bar diameter and embedment length. Also, the increase in cover concrete improved the flexural bond strength.

7. The slip corresponding to maximum bond stress decreased with increase in compressive strength, bar diameter, embedment length and cover of concrete.

8. The fracture energy which indicates the ability of materials to absorb post-crack energy, decreased with increase in compressive strength of concrete, bar diameter and embedment length. The percentage decrease in fracture energy decreases with an increase in the grade of concrete.

9. The failure mode shifted from pullout failure to splitting failure for a lower grade of concrete, higher bar diameter and longer embedment lengths, as it provides higher radial tensile stresses than the splitting tensile strength of concrete.

10. An equation to predict the bond strength of geopolymer concrete for a range of GPC grades 20, 30, 40, and 50 MPa is proposed based on the results of the present study. The relation is given by:

$$\tau_{max} = \left[\left(-0.085 + 0.511\frac{c}{d}\right)\frac{d}{l_e} + 0.627\right] f_{ck}^{0.616}$$

Where, τ_{max}= Bond Strength (MPa) C = Concrete Cover (mm) l_e= Embedment length (mm) d= Diameter of reinforcement bar (mm) f_{ck}= Characteristic cube compressive strength (MPa)

11. An equation for predicting the maximum bond stress considering the cover-to-diameter ratio, embedment length-to-diameter ratio and compressive strength is proposed for a range of GPC grades 60, 70, 80, 90 and 100 MPa.

$$\tau_{max} = \left(0.38 + \frac{1.82}{\frac{l_e}{d}}\right) \times \left(0.375 + 0.124 \times \frac{c}{d}\right) \times {f_{ck}}^{0.76}$$

12. The proposed analytical equation for HSGPC has a good correlation with the experimental results with a coefficient correlation of 0.88.

7.3 Specific Contributions of the Research Work

The major contributions of the present study are:

1. The high-strength geopolymer concrete is developed using multicomponent binder and particle packing concepts. The correlation equations for mechanical properties are proposed along with the constitutive model for HSGPC.
2. Studies on the chemical resistance of HSGPC subjected to 5% concentrated HCl, H_2SO_4, $MgSO_4$ and NaCl were carried out.
3. Studies on the experimental bond behaviour of HSGPC through pullout and hinged beam tests were carried out. Parameters such as compressive strength of concrete (60, 80 and 100 MPa), embedment length (2.5D, 5D and FD), bar diameter (12,16 and 20 mm), and cover of concrete (16/20 and 40 mm) were considered for evaluation of bond behaviour of HSGPC
4. The numerical validation of parameters affecting the bond behaviour of HSGPC was determined through a pullout test. The parameters such as compressive strength (20, 30, 40, 50, 60, 70, 80, 90, and 100 MPa), embedment length (50, 75, 100 and 150 mm), bar diameter (10, 12, 16 and 20 mm), type of bar (Plain and ribbed bar) were considered.
5. The numerical evaluation of flexural bond strength through beam end test was carried out and an analytical model for normal, standard and high-strength geopolymer concrete using multiple nonlinear regression analysis is proposed to predict the maximum bond strength. The parameters such as compressive strength of concrete (20, 30, 40, 50, 60,

70, 80, 90, and 100 MPa), cover-to-bar diameter ratio varied from 1 to 5 at an increment of 0.5, and the embedment length to bar diameter ratio (3, 5, 7 and 9) were considered.

7.4 Scope for Future Research

Future research can examine some of the aspects given below:

1. The influence of fibres on bond behaviour of HSGPC for different span-to-depth ratios (a/d).
2. Investigation on the Torsion, Flexural, and Shear behaviour of HSGPC.
3. Durability performance of HSGPC through chloride ion penetration test and carbonation test.
4. Microstructure changes in HSGPC when exposed to chemical attack.

REFERENCES

ACI 318-11. (2011). Requirements for structural concrete. *U.S. Standard*.

ACI 408R-03. (2003). Bond and Development of straight reinforcing bars in tension. *Reported by ACI Committee*.

ACI-2015. (2015). Manual of concrete practice index-2015. 1–73. www.concrete.org

Adak, D., & Mandal, S. (2019). Strength and durability performance of flyash–based process-modified geopolymer concrete. *Journal of Materials in Civil Engineering*, *31*(9).

Ahmet Emin, Kurtoglu., Radhwan, Alzeebaree., Omar Aljumaili. (2018). Mechanical and durability properties of flyash and slag based geopolymer concrete. *Advances in Concrete Construction*, *6*(4), 345–362.

Al-Azzawi, M., Yu, T., & Hadi, M. N. S. (2018). Factors affecting the bond strength between the flyash-based geopolymer concrete and steel reinforcement. *Structures*, *14*, 262–272. https://doi.org/10.1016/j.istruc.2018.03.010

Albitar, M., Visintin, P., Ali, M. S. M., Lavigne, O., & Gamboa, E. (2017). Bond slip models for uncorroded and corroded steel reinforcement in class-F flyash geopolymer concrete. *Journal of Materials in Civil Engineering*, *29*(1). https://doi.org/10.1061/(asce)mt.1943-5533.0001713

Alexander, A. E., & Shashikala, A. P. (2022). Studies on the microstructure and durability characteristics of ambient cured FA-GGBS based geopolymer mortar. *Construction and Building Materials*, *347*. https://doi.org/10.1016/j.conbuildmat.2022.128538

Al-Jahdali, F. A., Wafa, F. F., & Shihata, S. A. (1994). Development length for straight deformed bars in high-strength concrete. *Special Publication*, *149*, 507–522.

Al-Majidi, M. H., Lampropoulos, A., Cundy, A., & Meikle, S. (2016). Development of geopolymer mortar under ambient temperature for in situ applications. *Construction and Building Materials*, *120*, 198–211. https://doi.org/10.1016/J.CONBUILDMAT.2016.05.085

Ambily, P. S., Ravisankar, K., Umarani, C., Dattatreya, J. K., & Iyer, N. R. (2014). Development of ultra-high-performance geopolymer concrete. *Magazine of Concrete Research*, *66*(2), 82–89. https://doi.org/10.1680/MACR.13.00057/ASSET/IMAGES/SMALL/MACR66-0082-F7.GIF

Amin, M., Elsakhawy, Y., Abu el-hassan, K., & Abdelsalam, B. A. (2022). Behavior evaluation of sustainable high strength geopolymer concrete based on fly ash, metakaolin, and slag. *Case Studies in Construction Materials*, *16*. https://doi.org/10.1016/j.cscm.2022.e00976

Andersen, P. J. (1995). Particle packing and concrete properties. *Materials Science of Concrete II*, 111–146.

Andrew, R. M. (2018). Global CO_2 emissions from cement production. *Earth System Science Data*, *10*(1), 195–217. https://doi.org/10.5194/ESSD-10-195-2018

Arioglu, N., Canan Girgin, Z., & Arioglu, E. (2006). Evaluation of ratio between splitting tensile strength and compressive strength for concretes up to 120 MPa and its application in strength criterion. *103*(1), 18–24. https://doi.org/10.14359/15123

Arunachelam, N., Maheswaran, J., Chellapandian, M., Murali, G., & Vatin, N. I. (2022). Development of high-strength geopolymer concrete incorporating high-volume copper slag and micro silica. *Sustainability*, *14*(13), 7601. https://doi.org/10.3390/su14137601

AS 3600-2009. (2009). Concrete Structures. *Standards Australia*.

ASTM-A944. (2004). Standard test method for comparing bond strength of steel reinforcing bars to concrete using beam-end specimens. *Concrete* (Issue Reapproved 2004).

ASTM C469-02. (2006). Standard test method for static modulus of elasticity and poisson's ratio of concrete in compression.

ASTM C618-03. (2003). Standard specification for coal flyash and raw or calcined natural pozzolan for use in concrete.

Bakharev, T. (2005). Durability of geopolymer materials in sodium and magnesium sulfate solutions. *Cement and Concrete Research*, *35*(6), 1233–1246. https://doi.org/10.1016/j.cemconres.2004.09.002

Bellum, R. R., Muniraj, K., Indukuri, C. S. R., & Madduru, S. R. C. (2020). Investigation on performance enhancement of flyash-GGBFS based graphene geopolymer concrete. *Journal of Building Engineering*, *32*. https://doi.org/10.1016/j.jobe.2020.101659

Bellum, R. R., Muniraj, K., & Madduru, S. R. C. (2020). Influence of activator solution on microstructural and mechanical properties of geopolymer concrete. *Materialia*, *10*, 100659.

Bharat Bhushan Jindal; Dhirendra Singhal; Sanjay K. Sharma; Deepankar K. Ashish; Parveen. (2017). Improving compressive strength of low calcium flyash geopolymer concrete with alccofine. *Advances in Concrete Construction*, *5*(1), 17–29.

Brouwers, H. J. H., & Radix, H. J. (2005). Self-compacting concrete: the role of the particle size distribution. *First International Symposium on Design, Performance and Use of SCC,* Hunan, China, 109–118.

BS EN 12390-13:2021. (2021). Testing hardened concrete-Determination of secant modulus of elasticity in compression. *BSI*.

Castel, A., & Foster, S. J. (2015). Bond strength between blended slag and Class F flyash geopolymer concrete with steel reinforcement. *Cement and Concrete Research*, *72*, 48–53. https://doi.org/10.1016/j.cemconres.2015.02.016

CEBFIP. (2012). Comite euro-international du beton-federation international de la pre-contrainte (CEB-FIP)*, model code 2010*. Thomas Telford Publishing, London, UK, vol. 1.

Červenka, V., Jendele, L., & Červenka, J. (2005). ATENA Program Documentation Part 4-2 Tutorial for Program ATENA 3D. *Cervenka Consulting*, 1–165.

Çevik, A., Alzeebaree, R., Humur, G., Niş, A., & Gülşan, M. E. (2018). Effect of nano-silica on the chemical durability and mechanical performance of flyash based geopolymer concrete. *Ceramics International*, *44*(11), 12253–12264. https://doi.org/10.1016/j.ceramint.2018.04.009

Chapman, R. A., & Shah, S. P. (1987). Early-age bond strength in reinforced concrete. *Materials Journal*, *84*(6), 501–510.

Chindaprasirt, P., Chareerat, T., & Sirivivatnanon, V. (2007). Workability and strength of coarse high calcium fly ash geopolymer. *Cement and Concrete Composites*, *29*(3), 224–229.

Chitrala, S., Jadaprolu, G. J., & Chundupalli, S. (2018). Study and predicting the stress-strain characteristics of geopolymer concrete under compression. *Case Studies in Construction Materials*, *8*, 172–192. https://doi.org/10.1016/J.CSCM.2018.01.010

Cong, X., Zhou, W., & Elchalakani, M. (2020). Experimental study on the engineering properties of alkali-activated GGBFS/FA concrete and constitutive models for performance prediction. *Construction and Building Materials*, *240*. https://doi.org/10.1016/j.conbuildmat.2019.117977

Cui, Y., Gao, K., & Zhang, P. (2020). Experimental and statistical study on mechanical characteristics of geopolymer concrete. *Materials 2020, Vol. 13, Page 1651*, *13*(7), 1651. https://doi.org/10.3390/MA13071651

Dahou, Z., Castel, A., & Noushini, A. (2016). Prediction of the steel-concrete bond strength from the compressive strength of Portland cement and geopolymer concretes. *Construction and Building Materials*, *119*, 329–342. https://doi.org/10.1016/j.conbuildmat.2016.05.002

Dao, D. S., Son, T., Ta, H. D., & Nguyen, K. T. (2022). Investigation of bond performance of reinforced fly ash-based Geopolymer concrete using experiments and numerical analysis. *Journal of Materials and Engineering Structures*, *9*(4), 521–529.

Davidovits, J. (1993). Geopolymer cements to minimize carbon dioxide greenhouse warming. *Ceramic Transactions.*, *37*(1), 165–182.

Davidovits, J. (1994a). High-alkali cements for 21st century concretes. *Special Publication*, *144*, 383–398.

Davidovits, J. (1994b). Properties of geopolymer cements. *First International Conference on Alkaline Cements and Concretes*, *1*, 131–149.

Davidovits, J. (1999). Chemistry of geopolymeric systems, terminology. *Geopolymer*, *99*(292), 9–39.

Deb, P., Nath, P., & Sarker, P. (2013). Properties of flyash and slag blended geopolymer concrete cured at ambient temperature. *New Developments in Structural Engineering and Construction*, 571–576.

De Larrard, F. (1999). Concrete mixture proportioning: a scientific approach. CRC Press.

de Larrard, F., & Sedran, T. (1994). Optimization of ultra-high-performance concrete by the use of a packing model. *Cement and Concrete Research*, *24*(6), 997–1009. https://doi.org/10.1016/0008-8846(94)90022-1

De Silva, P., Sagoe-Crenstil, K., & Sirivivatnanon, V. (2007). Kinetics of geopolymerization: role of Al_2O_3 and SiO_2. *Cement and Concrete Research*, *37*(4), 512–518.

Dewar, J. D. (1986). Ready-mixed concrete mix design. *Municipal Engineering*, *3*, 35–43.

Diaz-Loya, E. I., Allouche, E. N., & Vaidya, S. (2011). Mechanical properties of fly-ash-based geopolymer concrete. *ACI Materials Journal*, *108*(3), 300.

Diksha, Dev, N., & Goyal, P. K. (2023). Prediction of compressive strength of alccofine-based geopolymer concrete. *Iranian Journal of Science and Technology, Transactions of Civil Engineering*. https://doi.org/10.1007/s40996-023-01308-2

Doguparti, R. S. (2015). A study on bond strength of geopolymer concrete. *International Journal of Civil and Environmental Engineering*, *9*(3), 355–358.

Dong, M., Elchalakani, M., & Karrech, A. (2020). Development of high strength one-part geopolymer mortar using sodium metasilicate. *Construction and Building Materials*, *236*, 117611. https://doi.org/10.1016/j.conbuildmat.2019.117611

Dong, M., Feng, W., Elchalakani, M., Li, G. (Kevin), Karrech, A., & May, E. F. (2017). Development of a high strength geopolymer by novel solar curing. *Ceramics International*, *43*(14), 11233–11243. https://doi.org/10.1016/j.ceramint.2017.05.173

Farhan, N. A., Sheikh, M. N., & Hadi, M. N. S. (2018). Experimental investigation on the effect of corrosion on the bond between reinforcing steel bars and fibre reinforced geopolymer concrete. *Structures*, *14*(March), 251–261. https://doi.org/10.1016/j.istruc.2018.03.013

Fennis, S. (2011). Design of ecological concrete by particle packing optimization.

Fine, G., & Stolper, E. (1986). Dissolved carbon dioxide in basaltic glasses: concentrations and speciation. *Earth and Planetary Science Letters*, *76*(3), 263–278. https://doi.org/https://doi.org/10.1016/0012-821X(86)90078-6

Ganeshan, M., & Venkataraman, S. (2021). Durability and microstructural studies on fly ash blended self-compacting geopolymer concrete. *European Journal of Environmental and Civil Engineering*, *25*(11), 2074–2088. https://doi.org/10.1080/19648189.2019.1615991

Glavind, M., & Pedersen, E. (1999). Packing calculations applied for concrete mix design. *Utilizing Ready Mix Concrete and Mortar, Thomas Telford Publishing*, 121–130.

Hadi, M. N. S. (2008). Bond of high strength concrete with high strength reinforcing steel. *Construction and Building Materials*.

Hamidi, R. M., Man, Z., & Azizli, K. A. (2016). Concentration of NaOH and the effect on the properties of flyash based geopolymer. *Procedia Engineering*, *148*, 189–193. https://doi.org/10.1016/J.PROENG.2016.06.568

Harajli, M. H. (1994). Development/splice strength of reinforcing bars embedded in plain and fiber reinforced concrete. *Structural Journal*, *91*(5), 511–520.

Hardjito, D., Wallah, S. E., Sumajouw, D. M. J., & Rangan, B. V. (2004). On the development of fly ash-based geopolymer concrete. *Materials Journal*, *101*(6), 467–472.

Haruna, S., Mohammed, B. S., Wahab, M. M. A., & Liew, M. S. (2020). Effect of paste aggregate ratio and curing methods on the performance of one-part alkali-activated concrete. *Construction and Building Materials*, *261*, 120024. https://doi.org/10.1016/j.conbuildmat.2020.120024

Hatem, M., Pusch, R., Al-Ansari, N., & Knutsson, S. (2012). Optimization of concrete by minimizing void volume in aggregate mixture system. *Journal of Advanced Science and Engineering Research*, *2*(3), 208–222.

Hsu, J. P., & Nacu, A. (2005). Preparation of submicron-sized $Mg(OH)_2$ particles through precipitation. *Colloids and Surfaces A: Physicochemical and Engineering Aspects*, *262*(1–3), 220–231. https://doi.org/10.1016/J.COLSURFA.2005.04.038

IS: 383-2016. (2016). Indian standard coarse and fine aggregate for concrete- specification. *Bureau of Indian Standards,* New Delhi, India, January, 1–21.

IS: 516 Part 5. (2018). Non-destructive testing of concrete- hardened concrete-methods of test. *Bureau of Indian Standard*.

IS: 2770-1: 1967(R2017). (1967). Methods of testing bond in reinforced concrete. *Bureau of Indian Standards,* New Delhi.

IS 9103: 1999. (1999). Specification for Concrete Admixtures. *Bureau of Indian Standards,* New Delhi, 1–22.

IS: 12089-1987. (1987). Specification for granulated slag for the manufacture of Portland slag cement. *Bureau of Indian Standard,* New Delhi, 1–14.

IS: 12269:2013. (2013). Ordinary Portland Cement, 53 Grade-Specification. *Bureau of Indian Standards*.

IS 13311 (Part 2) : 1992. (1992). Non-destructive testing of concrete-methods of test. *Bureau of Indian Standards*.

IS: 15388. (2003). Silica Fume-Specification. *Bureau of Indian Standards,* New Delhi, India, 1–13.

Issa, C. A., & Masri, O. (2015). Numerical simulation of the bond behavior between concrete and steel reinforcing bars in specialty concrete. *International Journal of Civil and Environmental Engineering*, *9*(6), 767–774.

Jena, S., Panigrahi, R., & Sahu, P. (2019). Mechanical and durability properties of flyash geopolymer concrete with silica fume. *Journal of The Institution of Engineers (India): Series A*, *100*(4), 697–705. https://doi.org/10.1007/s40030-019-00400-z

Jendele, L., & Cervenka, J. (2006). Finite element modelling of reinforcement with bond. *Computers & Structures*, *84*(28), 1780–1791. https://doi.org/10.1016/J.COMPSTRUC.2006.04.010

Jones, M. R., Zheng, L., & Newlands, M. D. (2002). Comparison of particle packing models for proportioning concrete constituents for minimum voids ratio. *Materials and Structures/Materiaux et Constructions*, *34*(249), 301–309. https://doi.org/10.1007/BF02482136/METRICS

Joseph, B., & Mathew, G. (2012). Influence of aggregate content on the behavior of flyash based geopolymer concrete. *Scientia Iranica*, *19*(5), 1188–1194. https://doi.org/10.1016/J.SCIENT.2012.07.006

Kabir, S. M. A., Alengaram, U. J., Jumaat, M. Z., Sharmin, A., & Islam, A. (2015). Influence of molarity and chemical composition on the development of compressive strength in POFA based geopolymer mortar. *Advances in Materials Science and Engineering*, *2015*, 1–15. https://doi.org/10.1155/2015/647071

Kanagaraj, B., Anand, N., Andrushia, A. D., & Lubloy, E. (2022). Investigation on engineering properties and micro-structure characteristics of low strength and high strength geopolymer composites subjected to standard temperature exposure. *Case Studies in Construction Materials*, *17*, e01608. https://doi.org/10.1016/j.cscm.2022.e01608

Karadumpa, C. S., & Pancharathi, R. K. (2021). Influence of particle packing theories on strength and microstructure properties of composite cement–Based mortars. *Journal of Materials in Civil Engineering*, *33*(10). https://doi.org/10.1061/(ASCE)MT.1943-5533.0003848

Kaze, R. C., Beleuk à Moungam, L. M., Cannio, M., Rosa, R., Kamseu, E., Melo, U. C., & Leonelli, C. (2018). Microstructure and engineering properties of Fe_2O_3(FeO)-Al_2O_3-SiO_2 based geopolymer composites. *Journal of Cleaner Production*, *199*, 849–859. https://doi.org/10.1016/J.JCLEPRO.2018.07.171

Kemp, E. L. (1986). Bond in reinforced concrete: behavior and design criteria. *Journal Proceedings*, *83*(1), 50–57.

Kermeli, K., Edelenbosch, O. Y., Crijns-Graus, W., van Ruijven, B. J., Mima, S., van Vuuren, D. P., & Worrell, E. (2019). The scope for better industry representation in long-term energy models: Modeling the cement industry. *Applied Energy*, 240, 964–985. https://doi.org/10.1016/J.APENERGY.2019.01.252

Khalaf, A. A., & Kopecskó, K. (2022). Modelling of modulus of elasticity of low-calcium-based geopolymer concrete using regression analysis. *Advances in Materials Science and Engineering*, *2022*, 1–11. https://doi.org/10.1155/2022/4528264

Kim, J. S., & Park, J. H. (2014). An experimental evaluation of development length of reinforcements embedded in geopolymer concrete. *Applied Mechanics and Materials*, *578–579*, 441–444. https://doi.org/10.4028/www.scientific.net/AMM.578-579.441

Kumar, S., & Santhanam, M. (2003). Particle packing theories and their application in concrete mixture proportioning: A review. *Indian Concrete Journal*, *77*(9), 1324–1331.

Lee, N. K., & Lee, H. K. (2013). Setting and mechanical properties of alkali-activated fly ash/slag concrete manufactured at room temperature. *Construction and Building Materials*, *47*, 1201–1209. https://doi.org/10.1016/J.CONBUILDMAT.2013.05.107

Le, T. A., Nguyen, T. N., & Nguyen, K. T. (2022). Experimental, numerical, and theoretical studies of bond behavior of reinforced flyash-Based geopolymer concrete. *Applied Sciences*, *12*(15), 7812. https://doi.org/10.3390/app12157812

Ling, Y., Wang, K., Li, W., Shi, G., & Lu, P. (2019). Effect of slag on the mechanical properties and bond strength of flyash-based engineered geopolymer composites. *Composites Part B: Engineering*, *164*, 747–757. https://doi.org/10.1016/j.compositesb.2019.01.092

Liu, Y., Shi, C., Zhang, Z., Li, N., & Shi, D. (2020). Mechanical and fracture properties of ultra-high performance geopolymer concrete: Effects of steel fiber and silica fume. *Cement and Concrete Composites*, *112*, 103665. https://doi.org/10.1016/j.cemconcomp.2020.103665

Ma, C. K., Awang, A. Z., & Omar, W. (2018). Structural and material performance of geopolymer concrete: A review. *Construction and Building Materials*, *186*, 90–102. https://doi.org/10.1016/j.conbuildmat.2018.07.111

Mangulkar, M., & Jamkar, S. (2013). Review of particle packing theories used for concrete mix proportioning. *Contributory Papers*, *141*.

Mayhoub, O. A., Nasr, E.-S. A. R., Ali, Y., & Kohail, M. (2021). Properties of slag based geopolymer reactive powder concrete. *Ain Shams Engineering Journal*, *12*(1), 99–105. https://doi.org/10.1016/j.asej.2020.08.013

Ma, Z., Yue, Q., & Chen, Z. (2023). A Beam test study on the bond performance between epoxy-coated reinforcement and geopolymer concrete. *Buildings*, *13*(2), 430. https://doi.org/10.3390/buildings13020430

Mehta, A., & Siddique, R. (2017). Sulfuric acid resistance of flyash based geopolymer concrete. *Construction and Building Materials*, *146*, 136–143. https://doi.org/10.1016/j.conbuildmat.2017.04.077

Nagajothi, S., & Elavenil, & S. (2021). Effect of GGBS addition on reactivity and microstructure properties of ambient cured flyash based geopolymer concrete. *Silicon*, *13*, 507–516. https://doi.org/10.1007/s12633-020-00470-w/Published

Nath, P., & Sarker, P. K. (2014). Effect of GGBFS on setting, workability and early strength properties of fly ash geopolymer concrete cured in ambient condition. *Construction and Building Materials*, *66*, 163–171. https://doi.org/10.1016/J.CONBUILDMAT.2014.05.080

Nath, P., & Sarker, P. K. (2017). Flexural strength and elastic modulus of ambient-cured blended low-calcium fly ash geopolymer concrete. *Construction and Building Materials*, *130*, 22–31. https://doi.org/10.1016/J.CONBUILDMAT.2016.11.034

Nguyen, H.-A., Chang, T.-P., & Shih, J.-Y. (2018). Engineering properties and bonding behavior of self-compacting concrete made with no-cement binder. *Journal of Materials in Civil Engineering*, *30*(3), 04017294. https://doi.org/10.1061/(asce)mt.1943-5533.0002136

Noushini, A., Aslani, F., Castel, A., Gilbert, R. I., Uy, B., & Foster, S. (2016). Compressive stress-strain model for low-calcium fly ash-based geopolymer and heat-cured Portland cement concrete. *Cement and Concrete Composites*, *73*, 136–146. https://doi.org/10.1016/J.CEMCONCOMP.2016.07.004

Olivia, M., & Nikraz, H. (2012). Properties of fly ash geopolymer concrete designed by Taguchi method. *Materials & Design (1980-2015)*, *36*, 191–198.

Orangun, C. O., Jirsa, J. O., & Breen, J. E. (1977). A re-evaluation of test data on development length and splices. *Journal Proceedings*, *74*(3), 114–122.

Ou, Z., Feng, R., Mao, T., & Li, N. (2022a). Influence of mixture design parameters on the static and dynamic compressive properties of slag-based geopolymer concrete. *Journal of Building Engineering*, *53*. https://doi.org/10.1016/j.jobe.2022.104564

Ou, Z., Feng, R., Mao, T., & Li, N. (2022b). Influence of mixture design parameters on the static and dynamic compressive properties of slag-based geopolymer concrete. *Journal of Building Engineering*, *53*. https://doi.org/10.1016/j.jobe.2022.104564

Pandurangan, K., Thennavan, M., & Muthadhi, A. (2018). Studies on effect of source of flyash on the bond strength of geopolymer concrete. *Materials Today: Proceedings*, *5*(5), 12725–12733. https://doi.org/10.1016/j.matpr.2018.02.256

Parveen, Singhal, D., Junaid, M. T., Jindal, B. B., & Mehta, A. (2018). Mechanical and microstructural properties of fly ashbased geopolymer concrete incorporating alccofine at ambient curing. *Construction and Building Materials*, *180*, 298–307. https://doi.org/10.1016/j.conbuildmat.2018.05.286

Pavithra, P., Srinivasula Reddy, M., Dinakar, P., Hanumantha Rao, B., Satpathy, B. K., & Mohanty, A. N. (2016a). A mix design procedure for geopolymer concrete with fly ash. *Journal of Cleaner Production*, *133*, 117–125. https://doi.org/10.1016/J.JCLEPRO.2016.05.041

Pavithra, P., Srinivasula Reddy, M., Dinakar, P., Hanumantha Rao, B., Satpathy, B. K., & Mohanty, A. N. (2016b). Effect of the Na2SiO3/NaOH Ratio and NaOH molarity on the synthesis of flyash-based geopolymer mortar. *Geo-Chicago 2016*, 336–344. https://doi.org/10.1061/9780784480151.034

Perná, I., Hanzlíček, T., & Šupová, M. (2014). The identification of geopolymer affinity in specific cases of clay materials. *Applied Clay Science*, *102*, 213–219. https://doi.org/10.1016/J.CLAY.2014.09.042

Prachasaree, W., Limkatanyu, S., Hawa, A., Sukontasukkul, P., & Chindaprasirt, P. (2020). Manuscript title: Development of strength prediction models for flyash based geopolymer concrete. *Journal of Building Engineering*, *32*, 101704.

https://doi.org/10.1016/j.jobe.2020.101704

Ramadoss, P., & Nagamani, K. (2008). Tensile strength and durability characteristics of high-performance fiber reinforced concrete. *Arabian Journal for Science & Engineering (Springer Science & Business Media BV)*, *33*.

Rangan, M. R. E. & B. V. (1998). Bond between normal strength and High-Strength Concrete (HSC) and reinforcing bars in splices in beams. *ACI Structural Journal*, *95*(3). https://doi.org/10.14359/545

Rees, C. A., Provis, J. L., Lukey, G. C., & van Deventer, J. S. J. (2007). Attenuated total reflectance Fourier transform infrared analysis of fly ash geopolymer gel aging. *Langmuir*, *23*(15), 8170–8179. https://doi.org/10.1021/LA700713G/SUPPL_FILE/LA700713G-FILE002.PDF

Rilem-Fip-Ceb-RC5-TC9. (1973). Bond test for reinforcing steel 1- Beam test (7-II-28 D); 2- Pullout test (7-11- 128): tentative recommendations. *Materials and Structures*, *32*(6), 95–105.

Sakthidoss, D. D., & Senniappan, T. (2020). A study on high strength geopolymer concrete with alumina-silica materials using manufacturing sand. *Silicon*, *12*(3), 735–746. https://doi.org/10.1007/s12633-019-00263-w

Samantasinghar, S., & Singh, S. P. (2019). Fresh and hardened properties of flyash–slag blended geopolymer paste and mortar. *International Journal of Concrete Structures and Materials*, *13*(1), 1–12. https://doi.org/10.1186/S40069-019-0360-1/FIGURES/12

Sarker, P. K. (2011). Bond strength of reinforcing steel embedded in flyash-based geopolymer concrete. *Materials and Structures/Materiaux et Constructions*, *44*(5), 1021–1030. https://doi.org/10.1617/s11527-010-9683-8

Scrivener, K. L. (2004). Backscattered electron imaging of cementitious microstructures: understanding and quantification. *Cement and Concrete Composites*, *26*(8), 935–945. https://doi.org/10.1016/J.CEMCONCOMP.2004.02.029

Shadnia, R., & Zhang, L. (2017). Experimental study of geopolymer synthesized with Class F fly ash and low-calcium slag. *Journal of Materials in Civil Engineering*, *29*(10), 4017195.

Shariatmadari, N., Hasanzadehshooiili, H., Ghadir, P., Saeidi, F., & Moharami, F. (2021). Compressive strength of sandy soils stabilized with alkali-activated volcanic ash and slag. *Journal of Materials in Civil Engineering*, *33*(11). https://doi.org/10.1061/(ASCE)MT.1943-5533.0003845

Shehab, H. K., Eisa, A. S., & Wahba, A. M. (2016). Mechanical properties of flyash based geopolymer concrete with full and partial cement replacement. *Construction and Building Materials*, *126*, 560–565. https://doi.org/10.1016/j.conbuildmat.2016.09.059

Siempu, R., & Kumar Pancharathi, R. (2022). Numerical study on the bond behaviour of plain and ribbed bars in self-compacting concrete. *Materials Today: Proceedings*, *51*, 2587–2591. https://doi.org/10.1016/j.matpr.2021.12.417

Singh, B., Ishwarya, G., Gupta, M., & Bhattacharyya, S. K. (2015). Geopolymer concrete: A review of some recent developments. *Construction and Building Materials*, *85*, 78–90. https://doi.org/10.1016/J.CONBUILDMAT.2015.03.036

Sofi, M., Van Deventer, J. S. J., Mendis, P. A., & Lukey, G. C. (2007). Bond performance of reinforcing bars in inorganic polymer concrete (IPC). *Journal of Materials Science*, *42*(9), 3107–3116. https://doi.org/10.1007/s10853-006-0534-5

Tang, Z., Hu, Y., Tam, V. W. Y., & Li, W. (2019). Uniaxial compressive behaviors of flyash/slag-based geopolymeric concrete with recycled aggregates. *Cement and Concrete Composites*, *104*, 103375. https://doi.org/10.1016/j.cemconcomp.2019.103375

Tekle, B. H., Khennane, A., & Kayali, O. (2017). Bond behaviour of GFRP reinforcement in alkali activated cement concrete. *Construction and Building Materials*, *154*, 972–982. https://doi.org/10.1016/j.conbuildmat.2017.08.029

Thomas, R. J., & Peethamparan, S. (2015). Alkali-activated concrete: Engineering properties and stress-strain behavior. *Construction and Building Materials*, *93*, 49–56. https://doi.org/10.1016/j.conbuildmat.2015.04.039

Thunuguntla, C. S., & Gunneswara Rao, T. D. (2018). Mix design procedure for alkali-activated slag concrete using particle packing theory. *Journal of Materials in Civil Engineering*, *30*(6). https://doi.org/10.1061/(ASCE)MT.1943-5533.0002296

Topark-Ngarm, P., Chindaprasirt, P., & Sata, V. (2015). Setting time, strength, and bond of high-calcium flyash geopolymer concrete. *Journal of Materials in Civil Engineering*, *27*(7). https://doi.org/10.1061/(asce)mt.1943-5533.0001157

Vafaei, M., & Allahverdi, A. (2017). Durability of geopolymer mortar based on waste-glass powder and calcium aluminate cement in acid solutions. *Journal of Materials in Civil Engineering*, *29*(10). https://doi.org/10.1061/(ASCE)MT.1943-5533.0002053

Verma, M., & Dev, N. (2021). Effect of liquid to binder ratio and curing temperature on the engineering properties of the geopolymer concrete. *Silicon*. https://doi.org/10.1007/s12633-021-00985-w

Walraven, J. C. (2012). Model Code 2010. *Volume 1* (Vol. 65). fib Fédération internationale du béton.

Xie, G., Liu, L., Suo, Y., Zhu, M., Yang, P., & Sun, W. (2024). High-value utilization of modified magnesium slag solid waste and its application as a low-carbon cement admixture. *Journal of Environmental Management*, *349*, 119551. https://doi.org/10.1016/j.jenvman.2023.119551

Xin, L., Jin-yu, X., Weimin, L., & Erlei, B. (2014). Effect of alkali-activator types on the dynamic compressive deformation behavior of geopolymer concrete. *Materials Letters*, *124*, 310–312.

Xu, B. W., & Shi, H. S. (2009). Correlations among mechanical properties of steel fiber reinforced concrete. *Construction and Building Materials*, *23*(12), 3468–3474. https://doi.org/10.1016/J.CONBUILDMAT.2009.08.017

Yip, C. K., Lukey, G. C., & van Deventer, J. S. J. (2005). The coexistence of geopolymeric gel and calcium silicate hydrate at the early stage of alkaline activation. *Cement and Concrete Research*, *35*(9), 1688–1697. https://doi.org/10.1016/J.CEMCONRES.2004.10.042

Yunsheng, Z., Wei, S., & Zongjin, L. (2010). Composition design and microstructural characterization of calcined kaolin-based geopolymer cement. *Applied Clay Science*, *47*(3–4), 271–275. https://doi.org/10.1016/J.CLAY.2009.11.002

Zhang, H. Y., Kodur, V., Wu, B., Yan, J., & Yuan, Z. S. (2018). Effect of temperature on bond characteristics of geopolymer concrete. *Construction and Building Materials*, *163*, 277–285. https://doi.org/10.1016/j.conbuildmat.2017.12.043

APPENDIX-I

PARTICLE PACKING METHODS

1. Optimization of aggregate proportions using MTM

A) Binary blending of single-sized aggregates using modified toufar model

Trial 1

For 12.5-10 mm and 4.75-0.15 mm

$$\Phi_{binary} = \frac{1}{\left\{\left(\frac{Y_1}{\Phi_1}\right)+\left(\frac{Y_2}{\Phi_2}\right)-Y_2\left(\frac{1}{\Phi_2}-1\right)\times K_d \times K_s\right\}}$$

d_1	0.84	k_d	0.860233
d_2	11.18	Φ_2	0.528148

Table A.I.1: Binary packing density of mono-sized aggregates for 12.5-10 mm & 4.75-0.15 mm

Y_1	Y_2	Φ_1	Φ_2	x	k_s	k_d	Φ_{binary}	U
0	1	0.59547	0.52815	0	0	0.86023	0.52815	0.8934
0.05	0.95	0.59547	0.52815	0.09893	0.08112	0.86023	0.5484	0.82349
0.1	0.9	0.59547	0.52815	0.20886	0.17126	0.86023	0.57028	0.75352
0.15	0.85	0.59547	0.52815	0.33172	0.27201	0.86023	0.59396	0.68362
0.2	0.8	0.59547	0.52815	0.46993	0.38534	0.86023	0.6197	0.61368
0.25	0.75	0.59547	0.52815	0.62657	0.49909	0.86023	0.64424	0.55222
0.3	0.7	0.59547	0.52815	0.80559	0.60274	0.86023	0.66448	0.50494
0.35	0.65	0.59547	0.52815	1.01216	0.69202	0.86023	0.67898	0.4728
0.4	0.6	0.59547	0.52815	1.25315	0.76671	0.86023	0.68765	0.45423
0.45	0.55	0.59547	0.52815	1.53795	0.82762	0.86023	0.69097	0.44724
0.5	0.5	0.59547	0.52815	1.87972	0.87613	0.86023	0.68979	0.44972
0.55	0.45	0.59547	0.52815	2.29744	0.91381	0.86023	0.6851	0.45964
0.6	0.4	0.59547	0.52815	2.81958	0.94231	0.86023	0.67783	0.4753
0.65	0.35	0.59547	0.52815	3.49091	0.96321	0.86023	0.66882	0.49517
0.7	0.3	0.59547	0.52815	4.38602	0.97796	0.86023	0.65872	0.5181
0.75	0.25	0.59547	0.52815	5.63916	0.98788	0.86023	0.64806	0.54307
0.8	0.2	0.59547	0.52815	7.51888	0.9941	0.86023	0.6372	0.56937
0.85	0.15	0.59547	0.52815	10.65175	0.99763	0.86023	0.62639	0.59645
0.9	0.1	0.59547	0.52815	16.91749	0.99933	0.86023	0.61578	0.62396
0.95	0.05	0.59547	0.52815	35.7147	0.99992	0.86023	0.60546	0.65164
1	0	0.59547	0.52815	-	-	-	0.59547	0.67935
						Φ_{max}	0.69097	

Trial 2

For 10-4.75 mm and 4.75-0.15 mm

d_1	0.84	k_d	0.782665
d_2	6.89	Φ_2	0.512593

Table A.I.2: Binary packing density of mono-sized aggregates for 10-4.75 mm & 4.75-0.15 mm

Y_1	Y_2	Φ_1	Φ_2	x	k_s	k_d	Φ_{binary}	U
0	1	0.59547	0.51259	0	0	0.78266	0.51259	0.95088
0.05	0.95	0.59547	0.51259	0.09295	0.07622	0.78266	0.53095	0.88342
0.1	0.9	0.59547	0.51259	0.19623	0.16091	0.78266	0.55068	0.81594
0.15	0.85	0.59547	0.51259	0.31167	0.25557	0.78266	0.57193	0.74847
0.2	0.8	0.59547	0.51259	0.44153	0.36205	0.78266	0.59488	0.68101
0.25	0.75	0.59547	0.51259	0.5887	0.47338	0.78266	0.61775	0.61878
0.3	0.7	0.59547	0.51259	0.7569	0.57727	0.78266	0.63747	0.5687
0.35	0.65	0.59547	0.51259	0.95098	0.66842	0.78266	0.65253	0.5325
0.4	0.6	0.59547	0.51259	1.1774	0.74599	0.78266	0.66262	0.50916
0.45	0.55	0.59547	0.51259	1.44499	0.81028	0.78266	0.66799	0.49703
0.5	0.5	0.59547	0.51259	1.7661	0.86225	0.78266	0.66923	0.49425
0.55	0.45	0.59547	0.51259	2.15857	0.9032	0.78266	0.66709	0.49905
0.6	0.4	0.59547	0.51259	2.64915	0.9346	0.78266	0.66237	0.50973
0.65	0.35	0.59547	0.51259	3.2799	0.95792	0.78266	0.65579	0.52488
0.7	0.3	0.59547	0.51259	4.1209	0.97458	0.78266	0.648	0.54321
0.75	0.25	0.59547	0.51259	5.29831	0.9859	0.78266	0.63947	0.5638
0.8	0.2	0.59547	0.51259	7.06441	0.99308	0.78266	0.63058	0.58584
0.85	0.15	0.59547	0.51259	10.00791	0.99721	0.78266	0.6216	0.60875
0.9	0.1	0.59547	0.51259	15.89492	0.99921	0.78266	0.61269	0.63215
0.95	0.05	0.59547	0.51259	33.55594	0.99991	0.78266	0.60397	0.65571
1	0	0.59547	0.51259	-	-	-	0.59547	0.67935
						Φ_{max}	0.66923	

B) Binary blending of polydispersed aggregates using modified toufar model

For 12.5 mm nominal size of aggregate

Trial 1

d_{upper} FA	10	d_1	6.892024	d_{upper} CA	12.5	d_2	11.18034
d_{lower} FA	4.75			d_{lower} CA	10		

Table A.I.3: Binary packing density of polydispersed aggregates for 12.5-10 mm & 10-4.75 mm

Y_1	Y_2	Φ_1	Φ_2	x	k_s	k_d	Φ_{binary}
0	1	0.512593	0.528148	0	0	0.237286	0.528148
0.05	0.95	0.512593	0.528148	0.1149276	0.094239	0.237286	0.532679
0.1	0.9	0.512593	0.528148	0.2426248	0.198949	0.237286	0.537289
0.15	0.85	0.512593	0.528148	0.3853453	0.315978	0.237286	0.541979
0.2	0.8	0.512593	0.528148	0.5459059	0.442571	0.237286	0.546495
0.25	0.75	0.512593	0.528148	0.7278745	0.561172	0.237286	0.549889
0.3	0.7	0.512593	0.528148	0.9358387	0.662239	0.237286	0.551763
0.35	0.65	0.512593	0.528148	1.1757973	0.745526	0.237286	0.552246
0.4	0.6	0.512593	0.528148	1.455749	0.812397	0.237286	0.551554
0.45	0.55	0.512593	0.528148	1.7866011	0.864896	0.237286	0.549928
0.5	0.5	0.512593	0.528148	2.1836236	0.90524	0.237286	0.54759
0.55	0.45	0.512593	0.528148	2.6688732	0.935562	0.237286	0.544733
0.6	0.4	0.512593	0.528148	3.2754353	0.957796	0.237286	0.541517
0.65	0.35	0.512593	0.528148	4.0553009	0.973632	0.237286	0.538064
0.7	0.3	0.512593	0.528148	5.0951216	0.984509	0.237286	0.534469
0.75	0.25	0.512593	0.528148	6.5508707	0.991632	0.237286	0.5308
0.8	0.2	0.512593	0.528148	8.7344942	0.995998	0.237286	0.527107
0.85	0.15	0.512593	0.528148	12.373867	0.998422	0.237286	0.523423
0.9	0.1	0.512593	0.528148	19.652612	0.999562	0.237286	0.519769
0.95	0.05	0.512593	0.528148	41.488848	0.999949	0.237286	0.516157
1	0	0.512593	0.528148	-	-	-	0.512592
						Φ_{max}	0.552246

Trial 2

d_{upper} FA	2.36	d_1	0.594979	d_{upper} CA	4.75	d_2	3.348134
d_{lower} FA	0.15			d_{lower} CA	2.36		

Table A.I.4: Binary packing density of polydispersed aggregates for 4.75-2.36 mm & 2.36-0.15 mm

Y_1	Y_2	Φ_1	Φ_2	x	k_s	k_d	Φ_{binary}
0	1	0.541509	0.530943	0	0	0.698219	0.530943
0.05	0.95	0.541509	0.530943	0.110017897	0.090213	0.698219	0.546825
0.1	0.9	0.541509	0.530943	0.232260006	0.19045	0.698219	0.563686
0.15	0.85	0.541509	0.530943	0.368883538	0.30248	0.698219	0.58162
0.2	0.8	0.541509	0.530943	0.522585013	0.424984	0.698219	0.600105
0.25	0.75	0.541509	0.530943	0.696780017	0.543115	0.698219	0.616145
0.3	0.7	0.541509	0.530943	0.895860022	0.645214	0.698219	0.627423
0.35	0.65	0.541509	0.530943	1.12556772	0.730448	0.698219	0.63383
0.4	0.6	0.541509	0.530943	1.393560034	0.799706	0.698219	0.635822
0.45	0.55	0.541509	0.530943	1.710278223	0.854681	0.698219	0.634138
0.5	0.5	0.541509	0.530943	2.090340051	0.897361	0.698219	0.629603
0.55	0.45	0.541509	0.530943	2.554860062	0.929744	0.698219	0.622993
0.6	0.4	0.541509	0.530943	3.135510076	0.953701	0.698219	0.614976
0.65	0.35	0.541509	0.530943	3.882060094	0.970905	0.698219	0.606082
0.7	0.3	0.541509	0.530943	4.877460118	0.982813	0.698219	0.596714
0.75	0.25	0.541509	0.530943	6.271020152	0.990668	0.698219	0.587162
0.8	0.2	0.541509	0.530943	8.361360202	0.995515	0.698219	0.577625
0.85	0.15	0.541509	0.530943	11.84526029	0.998223	0.698219	0.568233
0.9	0.1	0.541509	0.530943	18.81306046	0.999505	0.698219	0.559061
0.95	0.05	0.541509	0.530943	39.71646096	0.999942	0.698219	0.55015
1	0	0.541509	0.530943	-	-	-	0.541509
						Φ_{max}	0.635822

Trial 3

d_{upper} FA	4.75	d_1	0.844097	d_{upper} CA	12.5	d_2	7.705518
d_{lower} FA	0.15			d_{lower} CA	4.75		

Table A.I.5: Binary packing density of polydispersed aggregates for 12.5-4.75 mm & 4.75-0.15 mm

Y_1	Y_2	Φ_1	Φ_2	x	k_s	k_d	Φ_{binary}
0	1	0.635822	0.552246	0	0	0.802541	0.552246
0.05	0.95	0.635822	0.552246	0.102094768	0.083716	0.802541	0.572365
0.1	0.9	0.635822	0.552246	0.215533398	0.176735	0.802541	0.594005
0.15	0.85	0.635822	0.552246	0.34231775	0.280696	0.802541	0.617346
0.2	0.8	0.635822	0.552246	0.484950146	0.395397	0.802541	0.642113
0.25	0.75	0.635822	0.552246	0.646600195	0.512128	0.802541	0.666065
0.3	0.7	0.635822	0.552246	0.831343108	0.615457	0.802541	0.685377
0.35	0.65	0.635822	0.552246	1.044508007	0.703647	0.802541	0.699362
0.4	0.6	0.635822	0.552246	1.29320039	0.77679	0.802541	0.70806
0.45	0.55	0.635822	0.552246	1.587109569	0.835965	0.802541	0.711995
0.5	0.5	0.635822	0.552246	1.939800585	0.882728	0.802541	0.711953
0.55	0.45	0.635822	0.552246	2.370867381	0.918803	0.802541	0.708797
0.6	0.4	0.635822	0.552246	2.909700877	0.945908	0.802541	0.703344
0.65	0.35	0.635822	0.552246	3.6024868	0.965658	0.802541	0.696304
0.7	0.3	0.635822	0.552246	4.526201364	0.979515	0.802541	0.688247
0.75	0.25	0.635822	0.552246	5.819401754	0.988774	0.802541	0.679613
0.8	0.2	0.635822	0.552246	7.759202339	0.994558	0.802541	0.670717
0.85	0.15	0.635822	0.552246	10.99220331	0.997826	0.802541	0.661778
0.9	0.1	0.635822	0.552246	17.45820526	0.99939	0.802541	0.652937
0.95	0.05	0.635822	0.552246	36.85621111	0.999928	0.802541	0.644273
1	0	0.635822	0.552246	-	-	-	0.635822
						Φ_{max}	0.711995

2. Optimization of aggregate proportions using JDD

A) Binary blending of single-sized aggregates

For sizes 4.75 - 2.36 mm and 2.36 - 0.15

d_{upper} CA	4.75	d_{upper} FA	2.36		
d_{lower} CA	2.36	d_{lower} FA	0.15		
d_i	3.348	d_i	0.595	r =	0.178
U0(CA)	0.924	U1(FA)	0.869		

For 4.75-2.36 mm & 2.36-0.15 mm

Void Ratio Diagram points	Sacing Factor, m	K_{int}	K_p	Z	U0"	U1"	U	Fine Volume Fraction, n
A(n=0)	0							
B	0.3	0.12	0.6	0.164	1.249	2.473	0.654	0.265
C	0.7	0.06	0.65	0.120	1.736	1.436	0.598	0.416
D	3	0.015	0.8	0.072	5.935	0.945	0.712	0.753
E	7.5	0	0.9	0.052	23.431	0.882	0.816	0.926
F(n=1)	infinity							

Umin	0.598
n	0.416
nx	0.441
nnext	0.753
Unext	0.712
Ux	0.606
Φ	0.623

For sizes 12.5 - 10 mm and 10 - 4.75

d_{upper} CA	12.5	d_{upper} FA	10		
d_{lower} CA	10	d_{lower} FA	4.75		
d_i	11.180	d_i	6.892	r =	0.616
U_o(CA)	1.001	U_1(FA)	1.077		

For 12.5-10 mm & 10-4.75 mm

Void Ratio Diagram points	Sacing Factor, m	K_{int}	K_p	Z	U_0"	U_1"	U	Fine Volume Fraction, n
A(n=0)	0							
B	0.3	0.12	0.6	0.225	2.330	2.243	0.938	0.418
C	0.7	0.06	0.65	0.206	4.871	1.458	0.969	0.665
D	3	0.015	0.8	0.182	45.300	1.107	1.058	0.956
E	7.5	0	0.9	0.168	354.900	1.080	1.074	0.994
F(n=1)	infinity							

U_{min}	0.938
n	0.418
n_x	0.443
n_{next}	0.665
U_{next}	0.969
U_x	0.941
Φ	0.515

B) Binary blending of polydispersed aggregates using JDD

For sizes 12.5 - 10 mm and 10 - 4.75

d_{upper} CA	12.5		d_{upper} FA	4.75	
d_{lower} CA	4.75		d_{lower} FA	0.15	
d_i	7.706		d_i	0.844	r = 0.110
U_0(CA)	0.94094		U_1(FA)	0.606	

For 12.5-4.75 mm & 4.75-0.15 mm

Void Ratio Diagram points	Sacing Factor, m	K_{int}	K_p	Z	U_0"	U_1"	U	Fine Volume Fraction, n
A(n=0)	0							
B	0.3	0.12	0.6	0.154	1.139	2.034	0.555	0.273
C	0.7	0.06	0.65	0.105	1.423	1.125	0.451	0.401
D	3	0.015	0.8	0.055	3.552	0.688	0.467	0.678
E	7.5	0	0.9	0.034	10.732	0.622	0.540	0.869
F(n=1)	infinity							

U_{min}	0.451
n	0.401
n_x	0.426
n_{next}	0.678
U_{next}	0.467
U_x	0.453
Φ	0.688

APPENDIX-II

NUMERICAL SIMULATION IN ATENA-GID

The various steps involved in the modelling of the pullout specimen have been listed below.

1. Design of geometrical model using tools of GiD software.
2. Assignment of material properties to the geometrical model.
3. Assignment of boundary conditions to the geometrical model.
4. Assignment of Monitor points.
5. Assignment of proper element type and meshing to the model.
6. Define proper step increments and intervals for the ATENA solver.

1. Design of geometrical model using tools of GiD software

After assigning the static problem to ATENA, points, lines and surfaces are created with the help of the create command. The obtained surface is extruded to obtain the geometrical model. The screenshot of the step has been presented in Figure A.II.1.

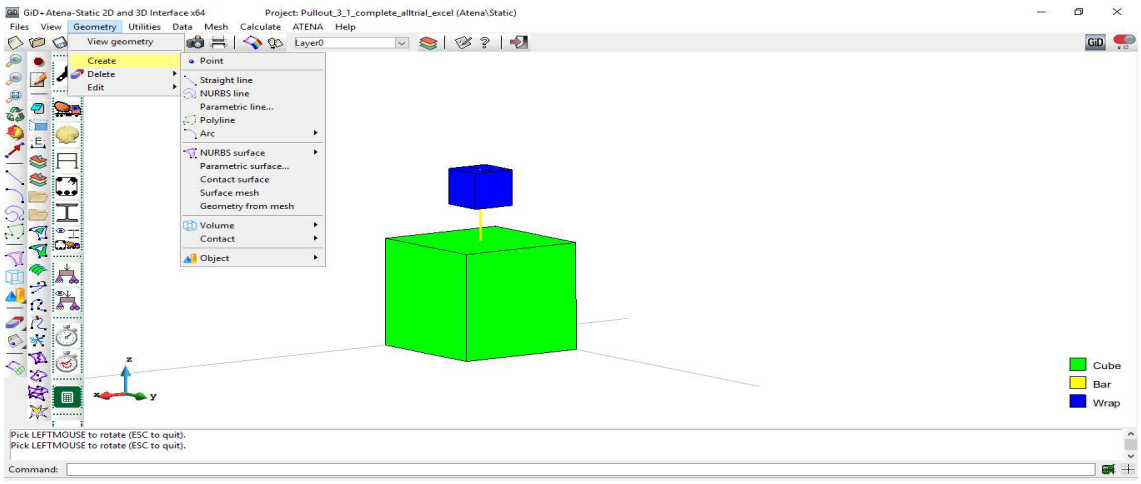

Figure A.II.1 Design of the geometrical model using tools of GiD software

2. Assignment of material properties to the geometrical model

The properties of the cube namely grade of concrete, modulus of elasticity, and tensile strength are inputted and then the other parameters are generated automatically. Similarly, respective

bar properties and properties of the wrap are generated. The screen of this step has been presented in Figure A.II.2.

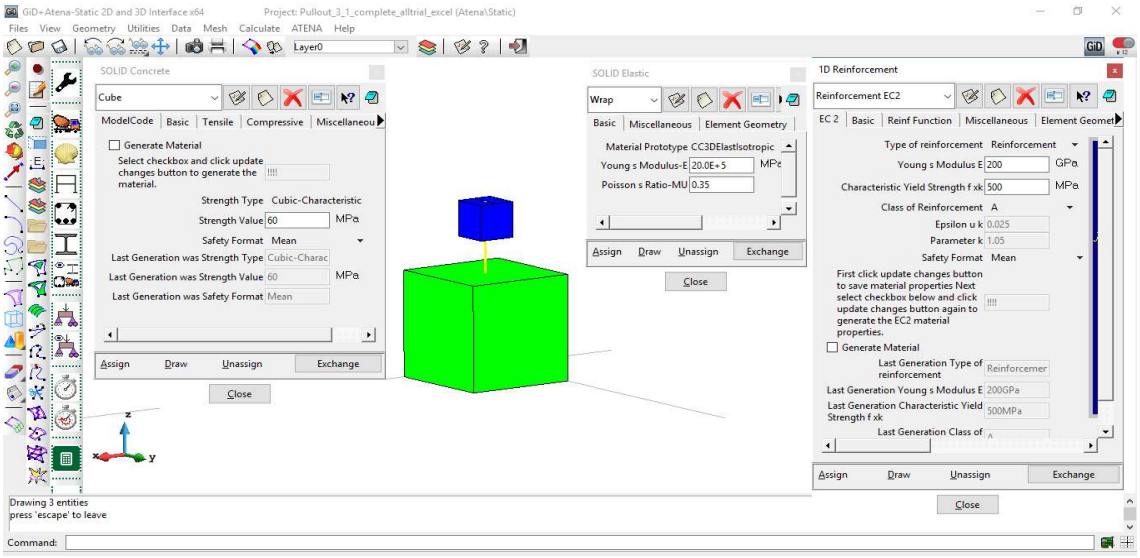

Figure A.II.2 Assignment of material properties to the geometric model

3. Assignment of boundary conditions to the geometrical model

After the assignment of the material properties, suitable boundary conditions to simulate the experimental pullout test are selected. The top of the cube is restrained against translation as well as rotation. The wrap is restrained in the x and y direction while displacement is applied at the top point of the wrap. This step is presented in Figure A.II.3.

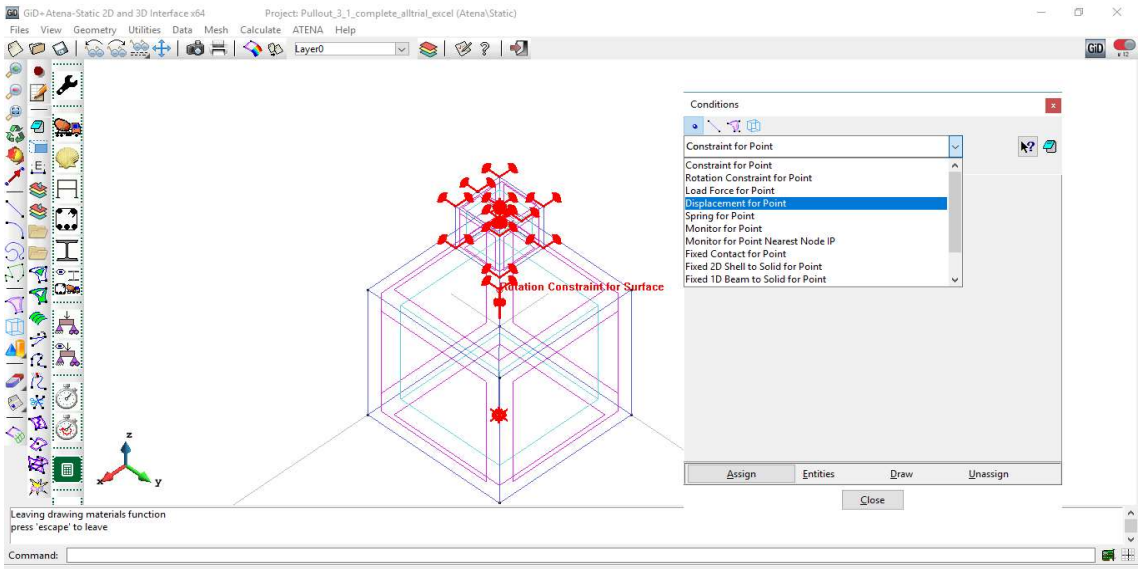

Figure A.II.3 Assignment of boundary conditions to the geometrical model

4. Assignment of Monitor points

To record the reaction and displacement at strategic points, monitor points are allocated to the specific nodes as presented in Figure A.II.4.

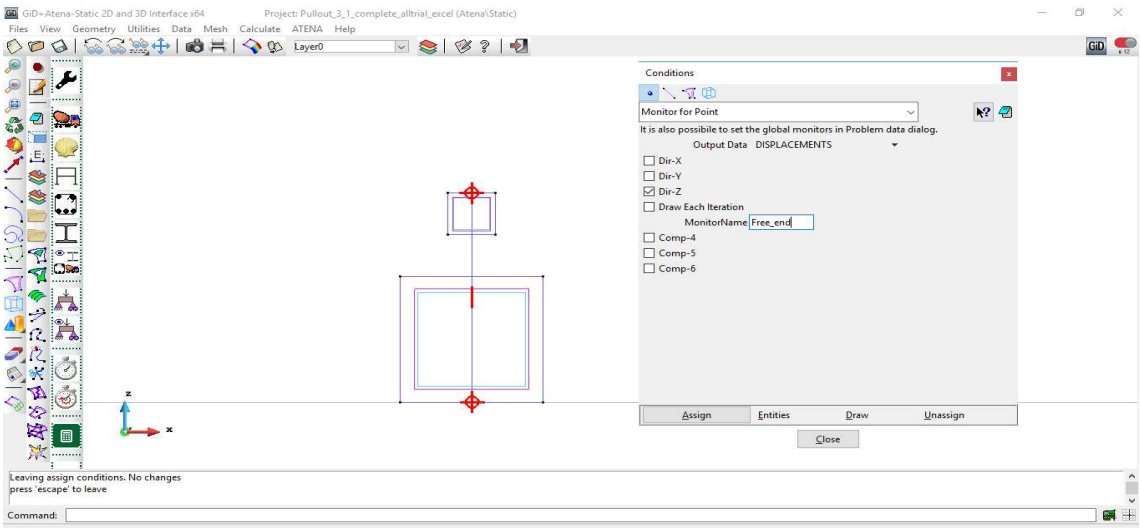

Figure A.II.4 Assignment of monitor points

5. Assignment of proper element type and meshing to the model

Cube is assigned a structured hexahedral mesh with 125 elements while bar is assigned a single linear structured element. A wrap is provided as a semi-structured tetrahedral meshing with 175 elements. The screenshot of the step is presented in Figure A.II.5.

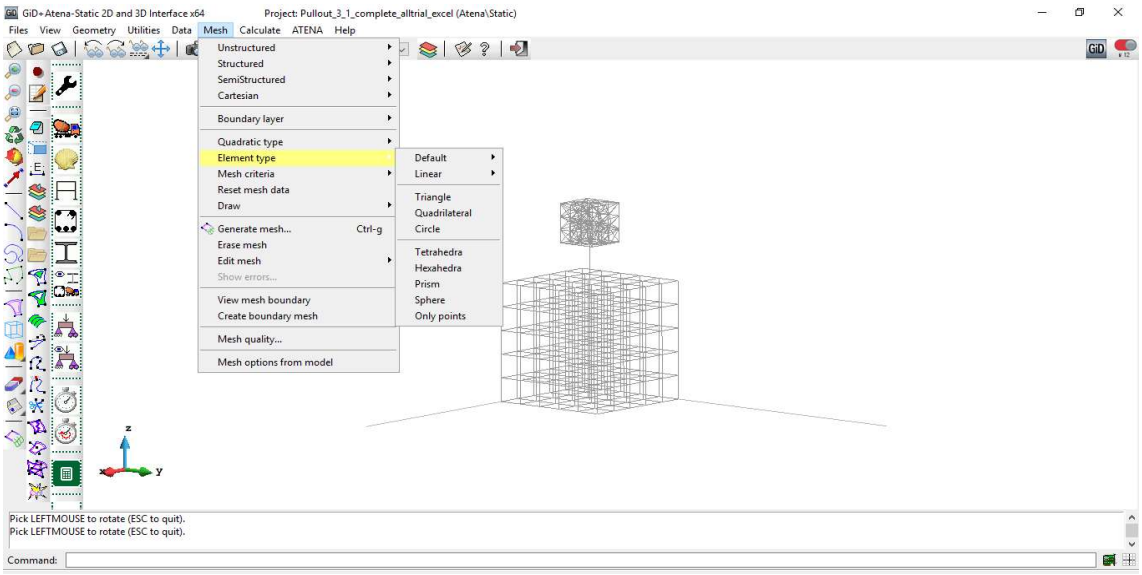

Figure A.II.5 Assignment of proper element type and meshing to the model

6. Define proper step increment and interval for the ATENA solver

Before analysis, a suitable step interval and solver type for the smooth running of the program is selected and the solver is run. The screenshot of the step is presented in Figure A.II.6 and Figure A.II.7.

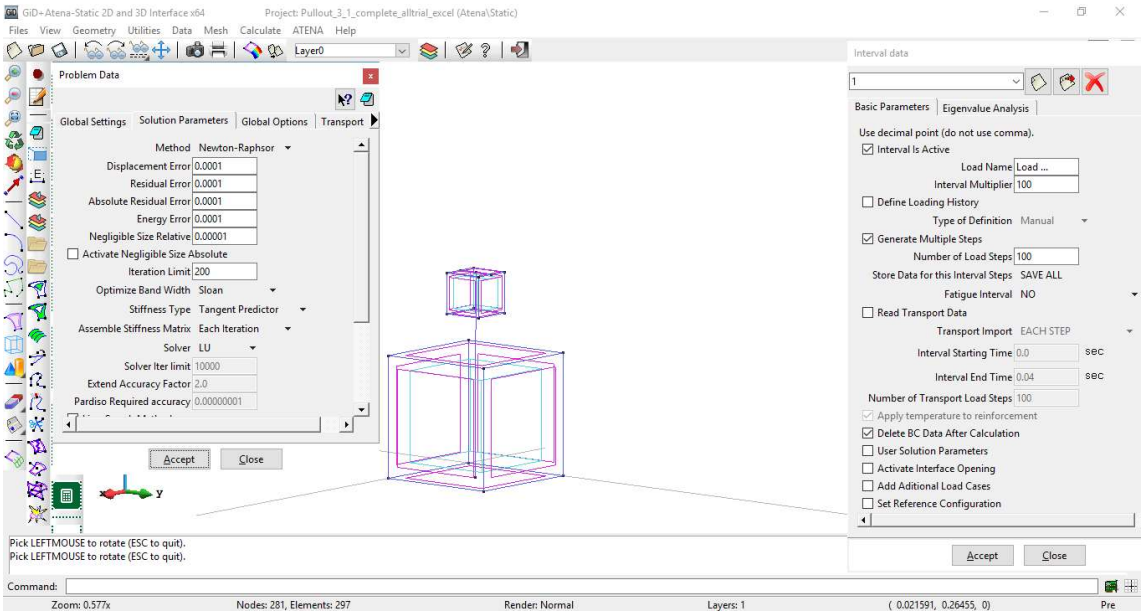

Figure A.II.6 Assignment of interval data

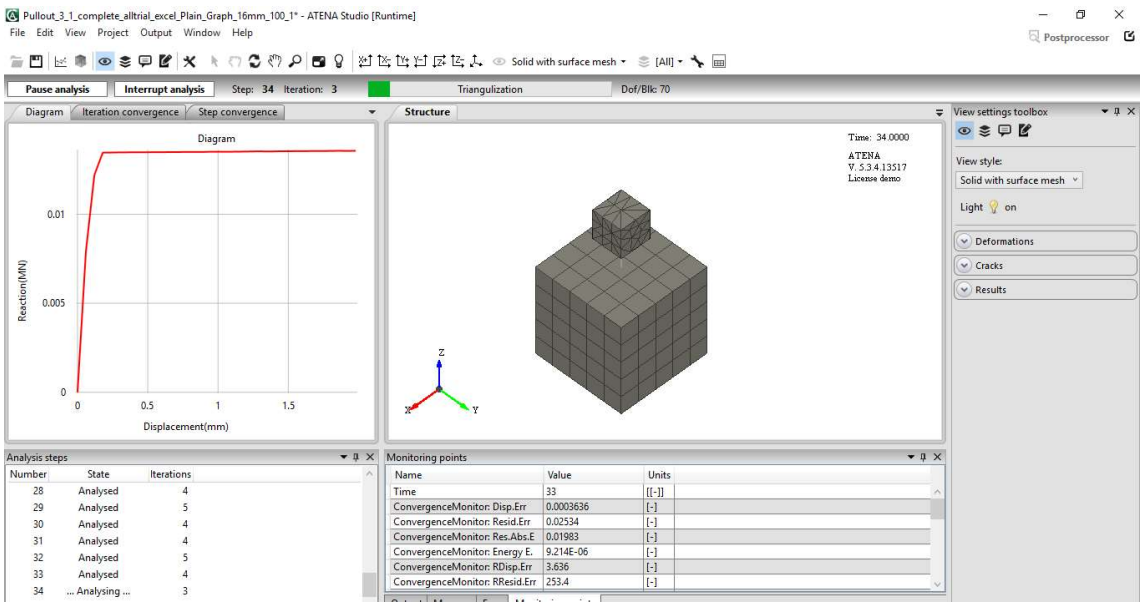

Figure A.II.7 Running analysis in Solver

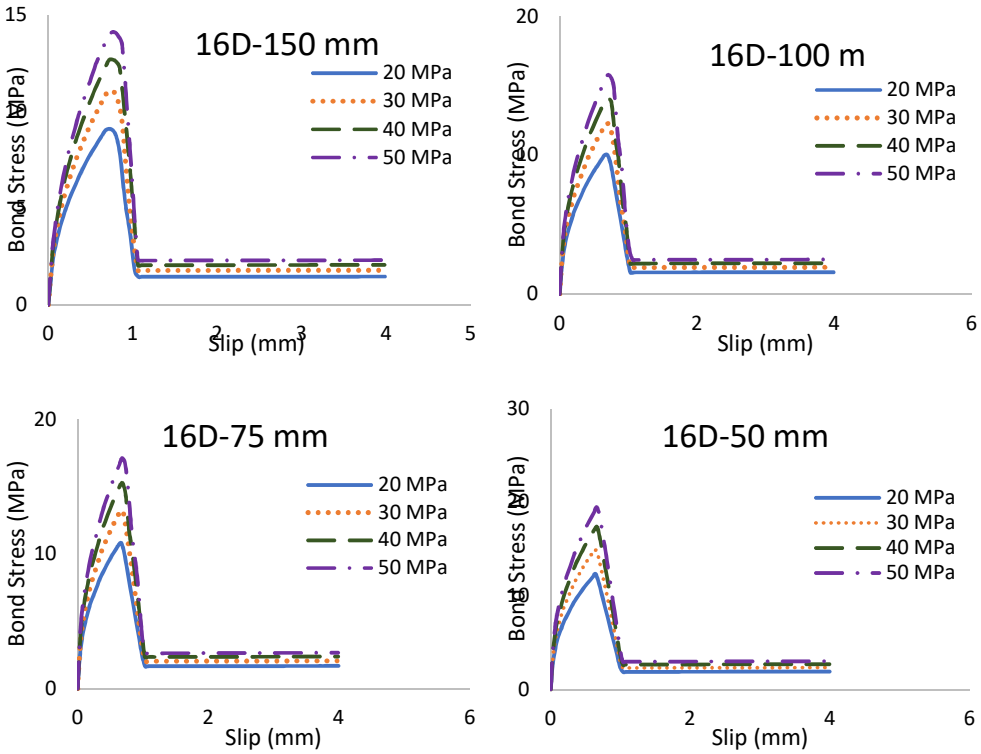

Figure A.II.8: Bond vs Slip of 16 mm diameter ribbed bar with different grades of concrete

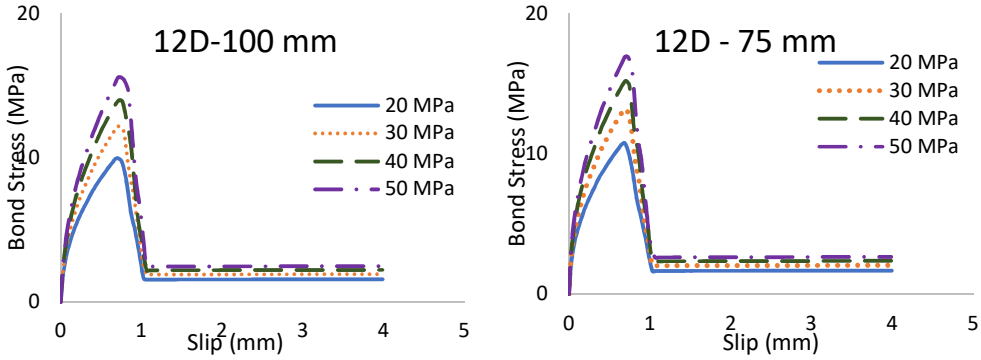

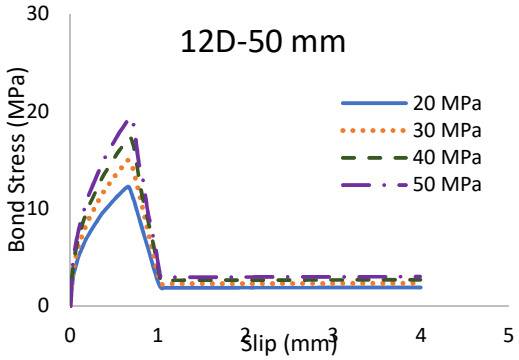

Figure A.II.9: Bond vs Slip of 12 mm diameter ribbed bar with different grades of concrete

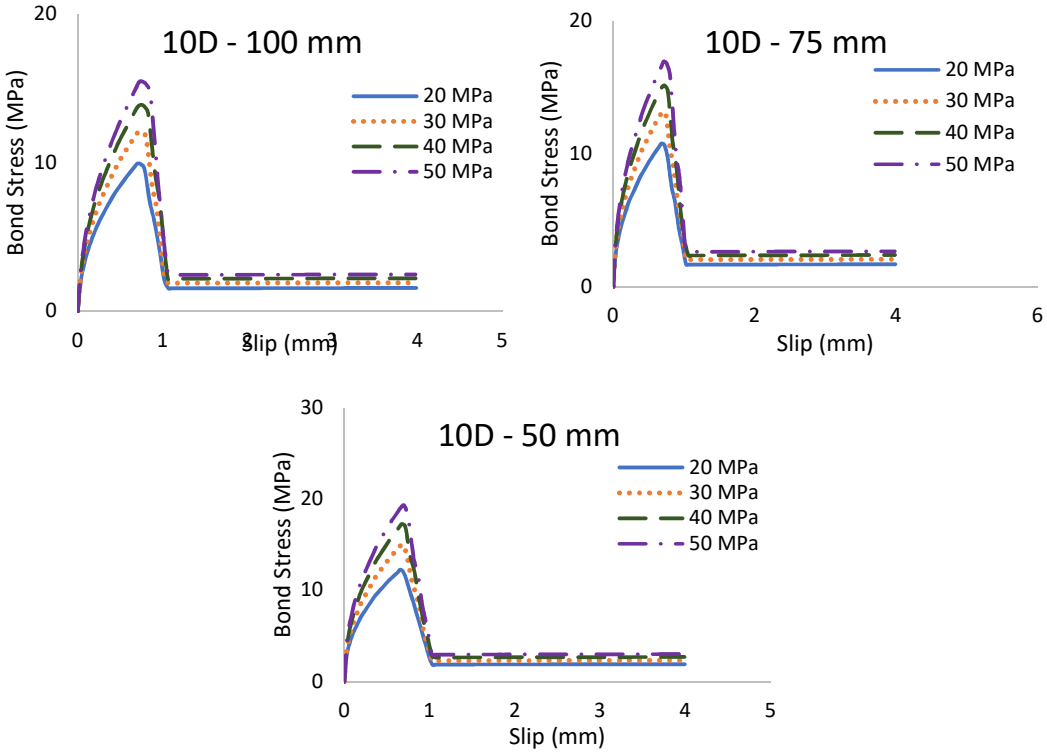

Figure A.II.10: Bond vs Slip of 10 mm diameter ribbed bar with different grades of concrete

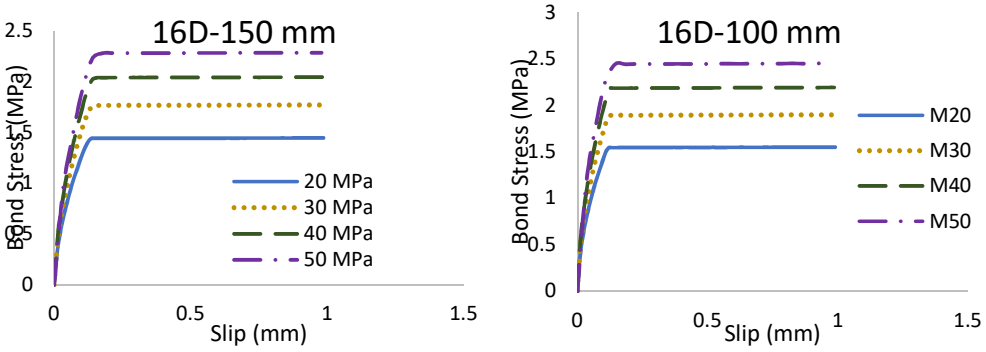

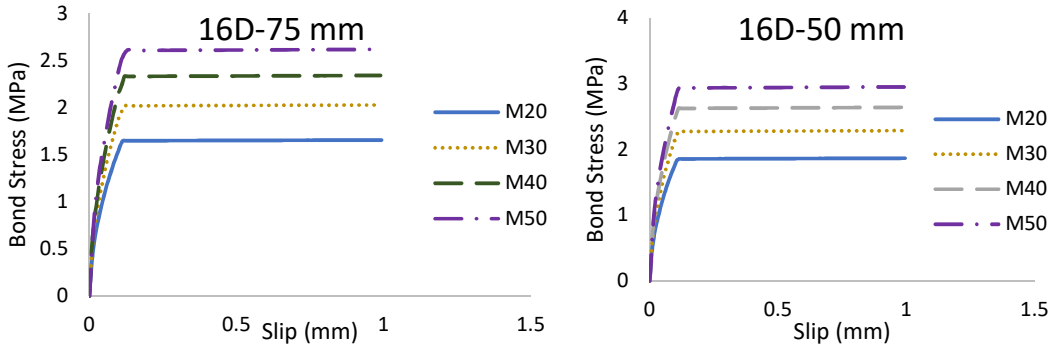

Figure A.II.11: Bond vs Slip of 16 mm diameter plain bar with different grades of concrete

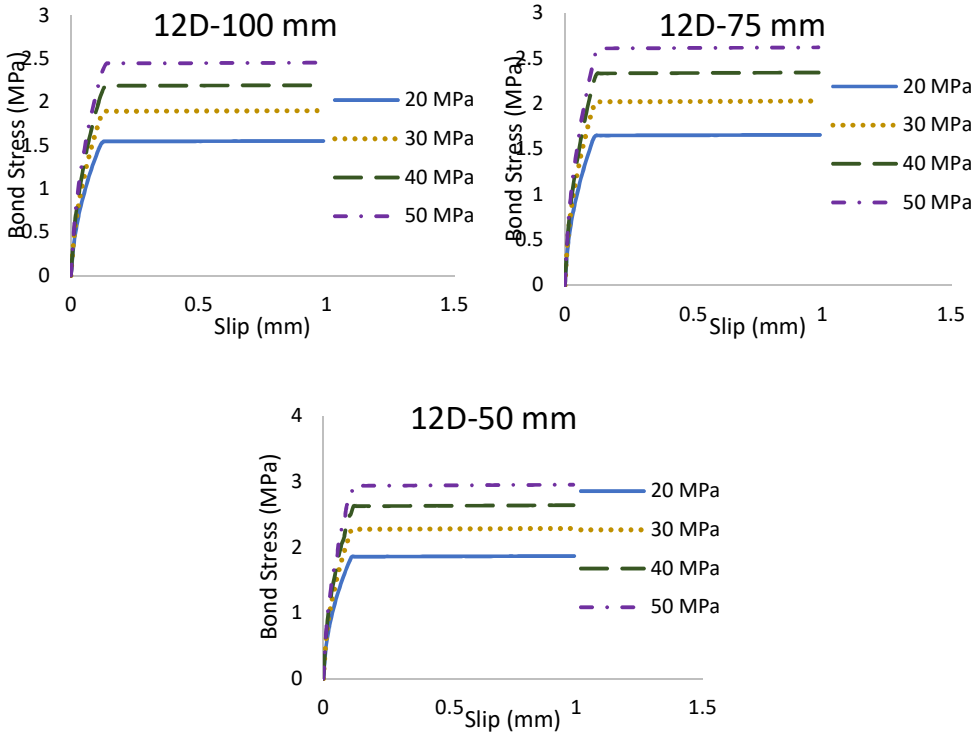

Figure A.II.12: Bond vs Slip of 12 mm diameter plain bar with different grades of concrete

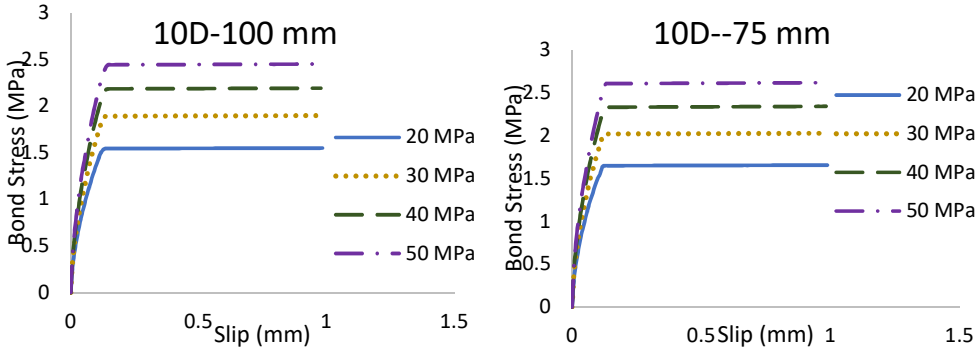

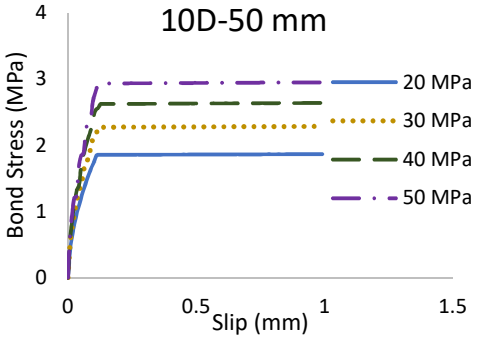

Figure A.II.13: Bond vs Slip of 10 mm diameter plain bar with different grades of concrete

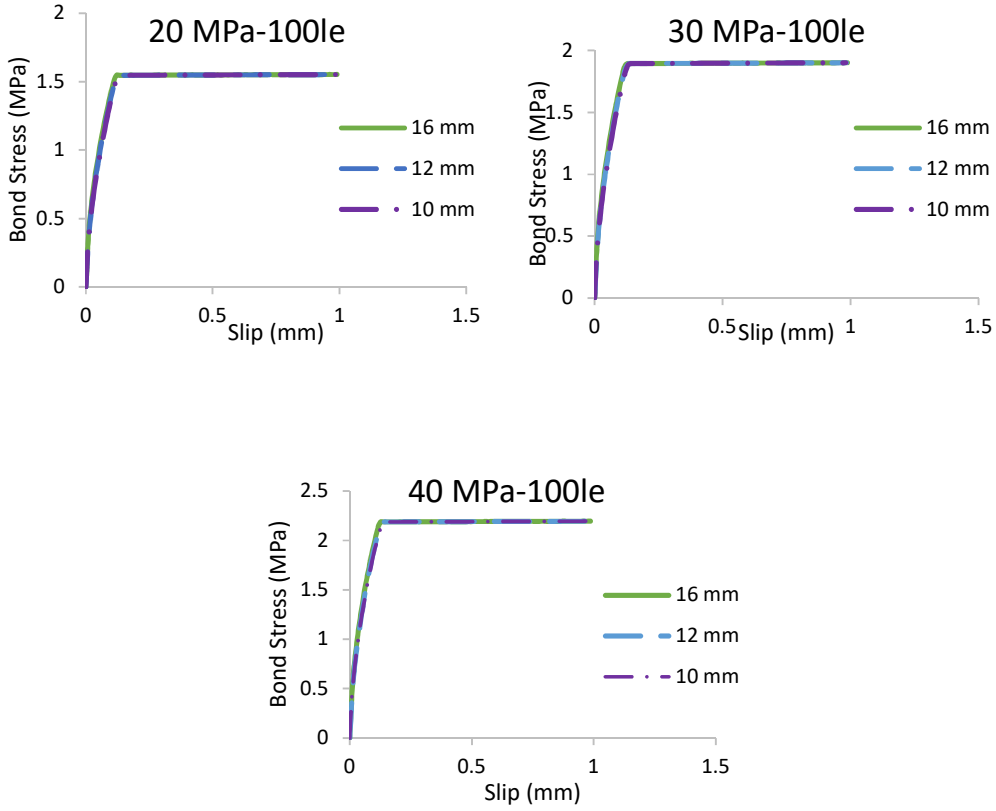

Figure A.II.14: Bond vs Slip of 100 mm embedment length with different grades of concrete

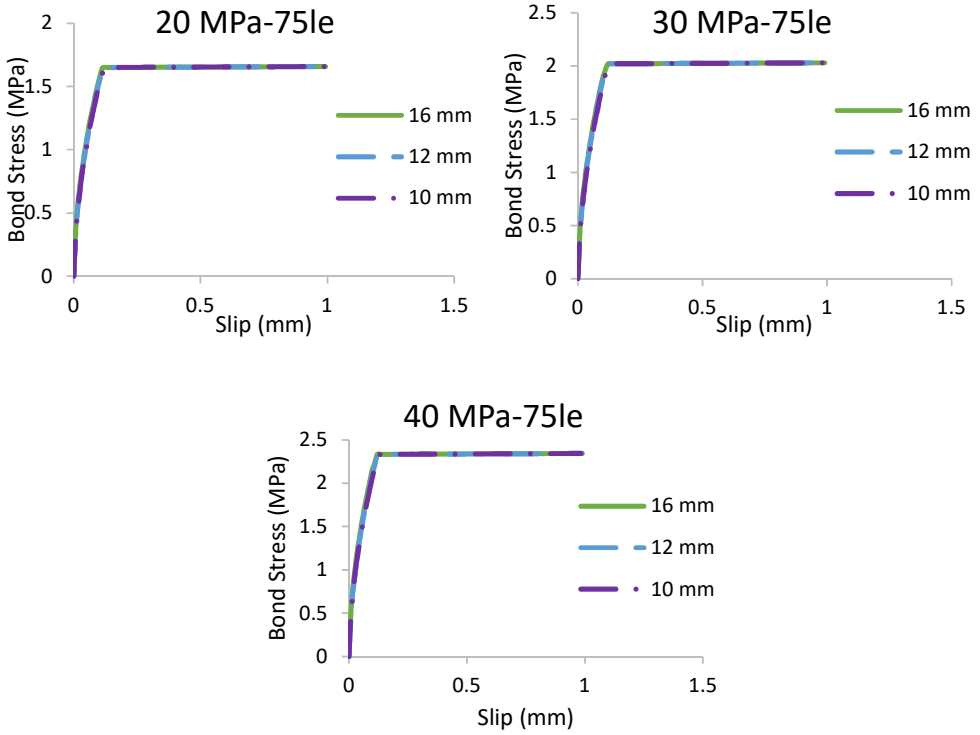

Figure A.II.15: Bond vs Slip of 75 mm embedment length with different grades of concrete

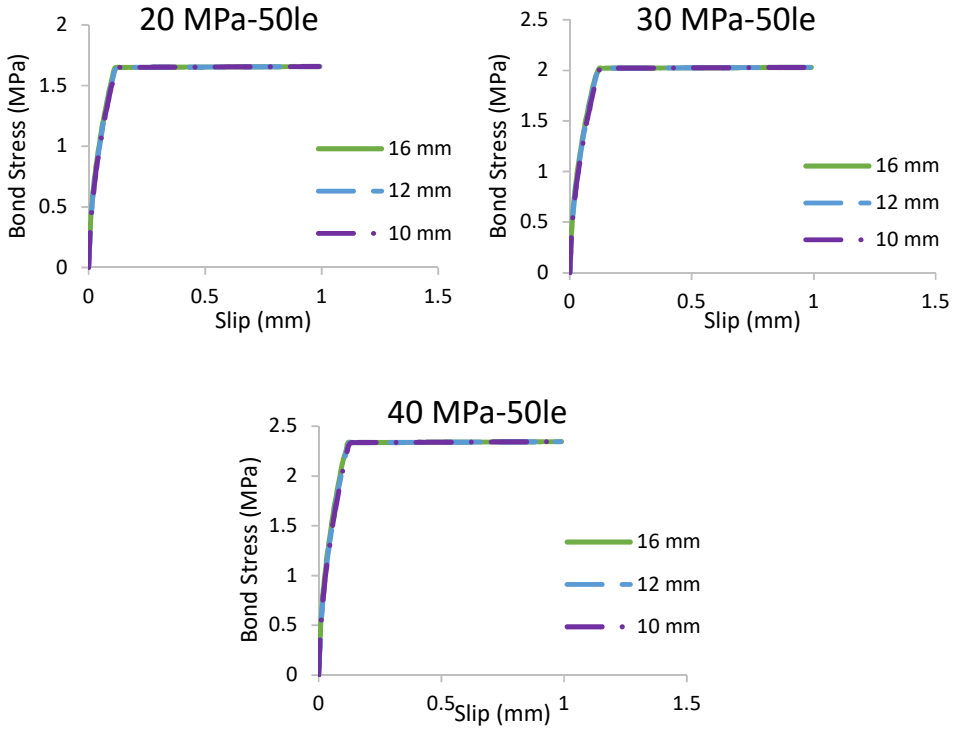

Figure A.II.16: Bond vs Slip of 50 mm embedment length with different grades of concrete

Table A.II.1: Effect on maximum bond stress with change in compressive strength of normal and standard grade of GPC for plain and ribbed bar

Diameter (mm)	Embedment length (mm)	Grade of Concrete	Bond Strength (MPa)		Percentage change (%)	
			Ribbed Bar	Plain Bar	Ribbed Bar	Plain Bar
16	150	20 MPa	9.10	1.45	-	-
		30 MPa	11.06	1.77	21.55	22.51
		40 MPa	12.69	2.05	14.71	15.45
		50 MPa	14.11	2.29	11.14	11.79
	100	20 MPa	10.02	1.55	-	-
		30 MPa	12.29	1.90	22.66	22.46
		40 MPa	14.10	2.20	14.72	15.49
		50 MPa	15.78	2.45	11.93	11.77
	75	20 MPa	10.80	1.66	-	-
		30 MPa	13.23	2.03	22.57	22.48
		40 MPa	15.25	2.34	15.20	15.43
		50 MPa	17.11	2.62	12.23	11.83
	50	20 MPa	12.34	1.87	-	-
		30 MPa	14.94	2.29	21.03	22.48
		40 MPa	17.32	2.64	15.99	15.48
		50 MPa	19.45	2.95	12.26	11.77
12	100	20 MPa	9.95	1.55	-	-
		30 MPa	12.15	1.90	22.09	22.47
		40 MPa	14.00	2.20	15.17	15.47
		50 MPa	15.57	2.45	11.23	11.80
	75	20 MPa	10.75	1.66	-	-
		30 MPa	13.16	2.03	22.33	22.48
		40 MPa	15.20	2.34	15.55	15.46
		50 MPa	16.93	2.62	11.39	11.81
	50	20 MPa	12.21	1.87	-	-
		30 MPa	14.98	2.29	22.70	22.43
		40 MPa	17.27	2.64	15.28	15.50
		50 MPa	19.43	2.95	12.52	11.78
10	100	20 MPa	9.95	1.55	-	-
		30 MPa	12.12	1.90	21.82	22.47
		40 MPa	13.91	2.20	14.73	15.47
		50 MPa	15.47	2.45	11.25	11.81
	75	20 MPa	10.76	1.66	-	-
		30 MPa	13.18	2.03	22.49	22.47
		40 MPa	15.12	2.34	14.69	15.47
		50 MPa	16.94	2.62	12.02	11.80
	50	20 MPa	12.26	1.87	-	-
		30 MPa	15.00	2.29	22.38	22.54
		40 MPa	17.27	2.64	15.11	15.48
		50 MPa	19.27	2.95	11.59	11.73

Table A.II.2: Effect on maximum bond stress with change in embedment length plain and ribbed bar

Diameter (mm)	Grade of Concrete	Embedment length (mm)	Bond Strength (MPa)		Percentage change (%)	
			Ribbed Bar	Plain Bar	Ribbed Bar	Plain Bar
16	20 MPa	150	9.10	1.45	-	-
		100	10.02	1.55	10.08	7.30
		75	10.80	1.66	7.76	6.78
		50	12.34	1.87	14.29	12.67
	30 MPa	150	11.06	1.77	-	-
		100	12.29	1.90	11.08	7.26
		75	13.23	2.03	7.68	6.79
		50	14.94	2.29	12.86	12.67
	40 MPa	150	12.69	2.05	-	-
		100	14.10	2.20	11.09	7.30
		75	15.25	2.34	8.14	6.73
		50	17.32	2.64	13.63	12.72
	50 MPa	150	14.11	2.29	-	-
		100	15.78	2.45	11.87	7.28
		75	17.11	2.62	8.43	6.80
		50	19.45	2.95	13.66	12.66
12	20 MPa	100	9.95	1.55	-	-
		75	10.75	1.66	8.05	6.77
		50	12.21	1.87	13.55	12.73
	30 MPa	100	12.15	1.90	-	-
		75	13.16	2.03	8.26	6.77
		50	14.98	2.29	13.89	12.68
	40 MPa	100	14.00	2.20	-	-
		75	15.20	2.34	8.62	6.77
		50	17.27	2.64	13.62	12.73
	50 MPa	100	15.57	2.45	-	-
		75	16.93	2.62	8.77	6.78
		50	19.43	2.95	14.77	12.69
10	20 MPa	100	9.95	1.55	-	-
		75	10.76	1.66	8.18	6.77
		50	12.26	1.87	13.88	12.70
	30 MPa	100	12.12	1.90	-	-
		75	13.18	2.03	8.77	6.78
		50	15.00	2.29	13.78	12.76
	40 MPa	100	13.91	2.20	-	-
		75	15.12	2.34	8.73	6.77
		50	17.27	2.64	14.19	12.77
	50 MPa	100	15.47	2.45	-	-
		75	16.94	2.62	9.49	6.77
		50	19.27	2.95	13.75	12.69

List of Publications

1. Padakanti Rakesh, Venkateswara Rao Sarella, Rathish Kumar Pancharathi, and Ankush Jha. 2022. "Study on the Bond Behaviour of High-Strength Geopolymer Concrete'. Asian Journal of Civil Engineering 23 (2): 269–88. https://doi.org/10.1007/s42107-022-00422-2.
2. Padakanti Rakesh, Venkateswara Rao Sarella, Rathish Kumar Pancharathi, "A study on the prediction of bond strength of ambient cured geopolymer concrete" Journal of Structural Engineering, Vol 49, No. 2, June-July 2022, PP 138-161.
3. Padakanti Rakesh, Venkateswara Rao Sarella, Rathish Kumar Pancharathi "A Study on Flexural Bond Behaviour of Multi-component Alkali-activated Concrete (AAC) System" (under review- Construction and Building materials, Elsevier).
4. Padakanti Rakesh, Venkateswara Rao Sarella, Rathish Kumar Pancharathi "A Study on Pullout bond behaviour of multi-component high strength geopolymer concrete", (about to submit)

Conferences:

1. Padakanti Rakesh, Venkateswara Rao Sarella, Rathish Kumar Pancharathi "A Comparative study on bond behavior of ternary blended geopolymer concrete and conventional concrete", International conference on Cement and Building Koncrete for a sustainable and Resilient infrastructure (CBKR2023) 28 – 29th March, National institute of technology Warangal.

Book Chapters:

1. Padakanti Rakesh, Venkateswara Rao Sarella, Rathish Kumar Pancharathi "A Comparative study on bond behavior of ternary blended geopolymer concrete and conventional concrete", lecture notes in Civil Engineering, Springer, https://doi.org/10.1007/978-981-99-7464-1_34.